



# Corrosion of copper alloys in natural seawater – Effects of hydrodynamics and pH

Maria Carvalho

## ► To cite this version:

Maria Carvalho. Corrosion of copper alloys in natural seawater – Effects of hydrodynamics and pH. Chemical Sciences. Université Pierre et Marie Curie, 2014. English. NNT : . tel-01089313

**HAL Id: tel-01089313**

**<https://hal.science/tel-01089313>**

Submitted on 1 Dec 2014

**HAL** is a multi-disciplinary open access archive for the deposit and dissemination of scientific research documents, whether they are published or not. The documents may come from teaching and research institutions in France or abroad, or from public or private research centers.

L'archive ouverte pluridisciplinaire **HAL**, est destinée au dépôt et à la diffusion de documents scientifiques de niveau recherche, publiés ou non, émanant des établissements d'enseignement et de recherche français ou étrangers, des laboratoires publics ou privés.

**THESE DE DOCTORAT DE  
L'UNIVERSITÉ PIERRE ET MARIE CURIE**

Spécialité  
Chimie Physique et Chimie Analytique

Présentée par  
Maria Leonor DE CASTRO REBELO DE AZEVEDO CARVALHO

Pour obtenir le grade de  
*DOCTEUR DE L'UNIVERSITE PIERRE ET MARIE CURIE*

Sujet de la thèse :

**Corrosion of copper alloys in natural seawater – Effects of hydrodynamics  
and pH**

Soutenue le : 29 septembre 2014

devant le jury composé de :

Mme. Nadine Pébère	Directrice de recherche, CNRS	Rapporteur
Mme. Judit Telegdi	Professeur, RCNS - HAS	Rapporteur
M. Bernard Tribollet	Directeur de recherche, CNRS	Examineur
M. Philippe Marcus	Directeur de recherche, CNRS	Examineur
Mme. Pierangela Cristiani	Chercheur, RSE SpA	Examineur
Mme. Isabelle Frateur	Chargée de recherche, CNRS	Directrice de thèse

---

## ACKNOWLEDGEMENTS

First and foremost I would like to express my sincere appreciation to my advisors Isabelle FRATEUR and Pierangela CRISTIANI for giving me an opportunity to work on this interesting topic and for providing me great guidance and support through the course of this research work. I am also thankful to Philippe MARCUS for encouraging my research and for allowing me to work at his laboratory.

I would like to express my special thanks to Sandrine ZANNA for the XPS training and Antoine SEYEUX for the ToF-SIMS training, from the research group Physical Chemistry of Surfaces (LPCS), Chimie-Paristech. They were my primary resource for getting my surface analysis questions answered. Special thanks also to Blanca TORRES BAUTISTA for welcoming me at LPCS, helping me polishing samples, sharing scientific results and having good time during our “formulas”.

I am grateful to Bernard TRIBOLLET and the Laboratory of Interfaces and Electrochemical Systems (LISE) for the scientific advices, knowledge, many insightful discussions and suggestions. I will definitely get stuck in EIS results without your help.

Special thanks also to Iwona BEECH, Magdalena SZTYLER and Jemimah DOMA from the University of Portsmouth, UoP, to have helping me performing all the genetic studies.

I also want to thank all current colleagues from RSE, SpA: Angelo PREVITALLI, Anna TOPPETTI, Claudia IMPOSIMATO, Claudio VANNINI, Dany CAM, Edoardo GUERRINI, Fiorella GRASSO, Flavia TULLI, Leonardo NERICCIO, Lidia FERRAVANTE and Michela TRIBUZIO. They provided a great atmosphere and lots of fun. Thank you for your motivation and support. A special thanks also to Giorgio PERBONI, from CESI. I thank you for your patience in helping me and nice travels to Piombino!

The research leading to these results has received funding from the Marie Curie European Community's Seventh Framework Programme (FP7/2007–2013) under grant agreement n°238579, BIOCOR Initial Training Network ([www.biocor.eu/ip7](http://www.biocor.eu/ip7)).

The BIOCOR project gave me this incredible opportunity to collaborate with research institutes across Europe and to work with the greatest experts within the field of biocorrosion. All that was possible thanks to an excellent project coordination and management and I want to thank for that Régine BASSEGUY, Vincent BIRRIEN and Jennifer STEPHENSON. My sincere thanks also goes to all my BIOCOR colleagues, all senior scientists and professors.

---

Last but not least, I can never add enough words to express how grateful I am for the endless support of my family. My father Antonio CARVALHO and also Ana COELHO have always provided me with unconditional love, support and motivation. Without their faith in me, I could not have made it this far (Obrigada pai!).

Finally, and most importantly, I would like to express much gratitude and love to my beloved husband Giovanni VARGIU. Without his patience, invaluable support, encouragement and “editing assistance”, I would not have been able to complete this work.

---

This thesis is lovingly dedicated to my mother, who will always be missed.

I love you mommy!

---

## TABLE OF CONTENTS

<b>CHAPTER 1 – SCIENTIFIC BACKGROUND</b>	<b>1</b>
1.1 Cooling water systems in power supply facilities	1
1.1.1 Types of condensers	2
1.1.2 Types of cooling waters	3
1.1.3 Constituent materials of cooling water systems	4
1.1.4 Cooling water systems operating problems	6
1.1.5 Cooling circuits tubes cleaning methods	9
1.1.6 Chlorination	9
1.2 Corrosion of copper and its alloys in aqueous environments	11
1.2.1 Galvanic corrosion	19
1.2.2 Pitting corrosion	20
1.2.3 Dealloying	20
1.2.4 Ammonia attack	21
1.2.5 Sulfide attack	21
1.2.6 Erosion-corrosion	22
1.2.7 Microbiologically influenced corrosion (MIC)	23
1.3 Effect of different parameters on the corrosion behavior of 70Cu-30Ni alloy and Al brass	25
1.3.1 Effect of iron and nickel	26
1.3.2 Effect of temperature	27
1.3.4 Effect of pH	27
1.3.4 Effect of oxygen content	29
1.3.5 Effect of polluted seawater	29
1.3.6 Effect of water velocity	30
1.3.7 Effect of seawater treatments	30
1.3.8 Effect of suspended particles and mud	31
1.3.9 Effect of biomolecules	32
1.4 Aim of this thesis and research strategy	32
1.5 Thesis outline	33
<b>CHAPTER 2 – MATERIALS AND METHODS</b>	<b>36</b>
2.1 Studied metallic materials and electrolytes	36
2.1.1 Metallic materials	37
2.1.1.1 Field experiments - electrodes and surface preparation	39
2.1.1.2 Laboratory experiments - electrodes and surface preparation	40
2.1.2 Electrolytes	42
2.1.2.1 Field experiments	42
• Natural seawater (NSW)	42
• Treated natural seawater (TNSW)	43
2.1.2.2 Laboratory experiments	43
• Filtered natural seawater (FNSW)	43
• Artificial seawater (ASW)	43
• Artificial seawater + BSA (ASW+BSA)	43
2.2 Experimental methods	43
2.2.1 Field experiments	43
2.2.1.1 On-line measurements	43
• Electrochemical cell	44
• Corrosion potential ( $E_{corr}$ ) vs immersion time	45
• Linear Polarization Resistance (LPR)	46
2.2.1.2 Off-line measurements	47

	• Weight loss measurements.....	47
	• Genetic studies.....	48
2.2.2	Laboratory experiments.....	51
2.2.2.1	Electrochemical measurements.....	51
	• Electrochemical cells.....	51
	• Corrosion potential ( $E_{corr}$ ) vs immersion time.....	53
	• Polarization curves.....	53
	• Levich and Koutecky-Levich methods.....	54
	• Electrochemical Impedance Spectroscopy (EIS).....	59
2.2.2.2	Surface analysis.....	66
	• X-ray Photoelectron Spectroscopy (XPS).....	67
	• Time-of-Flight Secondary Ion Mass Spectroscopy (ToF-SIMS).....	71

### CHAPTER 3 - COPPER ALLOYS IN REAL INDUSTRIAL CONDITIONS: CORROSION AND MICROBIOLOGY .....

		75
3.1	Power plants characteristics.....	76
3.1.1	Tests on the Tyrrhenian coast.....	76
3.1.2	Tests on the Adriatic coast.....	78
3.2	Electrochemical tools.....	79
3.2.1	Corrosion rate.....	80
3.2.2	Biofilm growth.....	80
3.2.3	Chlorination treatments.....	85
3.2.4	Other physico-chemical parameters.....	86
3.3	Results of the monitoring campaign.....	86
3.3.1	70Cu-30Ni alloy – Online measurements.....	86
3.3.2	Al brass – Online measurements.....	93
3.3.3	70Cu-30Ni alloy and Al brass - Off-line measurements.....	97
3.3.3.1	Visual observations.....	97
3.3.3.2	Weight loss measurements.....	98
3.3.3.3	Microbiological analyses.....	100
3.4	Conclusions.....	103

### CHAPTER 4 – EFFECT OF SOLUTION AND BIOMOLECULE CONCENTRATION.....

4.1	Results.....	105
4.1.1	Electrochemical measurements.....	105
4.1.1.1	Corrosion potential ( $E_{corr}$ ) vs time.....	105
4.1.1.2	Cathodic and anodic polarization curves.....	105
4.1.1.3	Electrochemical Impedance Spectroscopy.....	107
4.1.2	Surface analysis.....	108
4.1.2.1	Equations necessary for XPS data processing.....	108
4.1.2.2	Results.....	113
4.2	Discussion.....	121
4.2.1	Surface layers models (combined XPS and ToF-SIMS).....	121
4.2.2	Composition of the organic layers (XPS).....	123
4.2.3	Corrosion mechanism.....	128
4.2.4	Impedance model for 70Cu-30Ni and EIS data fitting.....	130
4.3	Conclusions.....	139

### CHAPTER 5 – EFFECT OF HYDRODYNAMICS.....

5.1	Static conditions vs under flow and stirring - Results.....	141
5.1.1	Electrochemical measurements.....	141
5.1.2	Surface analysis.....	143
5.1.2.1	Surface layers models (combined XPS and ToF-SIMS).....	145

5.2	Electrochemical measurements using a RRE .....	146
5.2.1	Theory for a Rotating Ring Electrode .....	146
5.2.2	Results .....	149
5.2.2.1	70Cu-30Ni .....	149
5.2.2.1.1	Corrosion potential ( $E_{corr}$ ) vs time .....	149
5.2.2.1.2	Cathodic polarization curves .....	150
5.2.2.1.3	Levich and Koutecky-Levich curves .....	152
5.2.2.1.4	Anodic polarization curves .....	153
5.2.2.1.5	Electrochemical Impedance Spectroscopy .....	155
5.2.2.1.6	EIS data fitting .....	156
5.2.2.2	Al brass .....	164
5.2.2.2.1	Corrosion potential ( $E_{corr}$ ) vs time .....	164
5.2.2.2.2	Cathodic and anodic polarization curves .....	165
5.2.2.2.3	Electrochemical Impedance Spectroscopy .....	166
5.2.2.2.4	Impedance model for Al brass and EIS data fitting .....	167
5.3	Conclusions .....	172
<b>CHAPTER 6 – EFFECT OF PH</b>	.....	<b>174</b>
6.1	70Cu-30Ni .....	174
6.1.1	Electrochemical measurements .....	174
6.1.1.1	Corrosion potential ( $E_{corr}$ ) vs time .....	174
6.1.1.2	Cathodic polarization curves .....	174
6.1.1.3	Anodic polarization curves .....	175
6.1.1.4	Electrochemical Impedance Spectroscopy .....	175
6.1.1.5	EIS data fitting .....	176
6.1.2	Surface analysis .....	181
6.1.2.1	Results .....	181
6.1.2.2	Surface layers models (combined XPS and ToF-SIMS) .....	187
6.1.2.3	Composition of the organic layers (XPS) .....	187
6.2	Al brass .....	191
6.2.1	Electrochemical measurements .....	191
6.2.1.1	Corrosion potential ( $E_{corr}$ ) vs time .....	191
6.2.1.2	Cathodic polarization curves .....	191
6.2.1.3	Anodic polarization curves .....	191
6.2.1.4	Electrochemical Impedance Spectroscopy .....	192
6.2.1.5	EIS data fitting .....	193
6.2.2	Surface analysis .....	197
6.2.2.1	Introduction .....	197
6.2.2.2	Results .....	201
6.2.2.3	Surface layers models (combined XPS and ToF-SIMS) .....	207
6.3	Conclusions .....	208
<b>GENERAL CONCLUSIONS</b>	.....	<b>211</b>
REFERENCES	.....	216
ANNEX A – CHAPTER 4	.....	228
ANNEX B – CHAPTER 5	.....	229
LIST OF FIGURES	.....	234
LIST OF TABLES	.....	243

---

## INTRODUCTION

This work was carried out in the frame of a Marie Curie European project (BIOCOR ITN - Initial Training Network on Biocorrosion), in close collaboration between industrial and academic partners. The researcher leading to these results has received funding from the European Community's Seventh Framework Programme (FP7/2007-2013) under grant agreement n°. 238579 (project website: [www.biocor.eu/ip7\(RSP3\)](http://www.biocor.eu/ip7(RSP3))). The core aim of BIOCOR ITN was to study biocorrosion issues by bringing together researchers with different scientific backgrounds in the area of biocorrosion.

Corrosion is the degradation of metallic materials due to electrochemical and chemical reactions. Analogous processes also occur for non-metallic materials, such as plastics, ceramics and concrete. Corrosion can lead to component failure in a variety of industrial environments. A study showed that the direct cost of corrosion was \$276 billion in the United States for 2002, which was approximately 3.1% of their Gross National Product [1]. From an economical point of view, some of the corrosion damages cannot be completely avoided, but many losses can be reduced.

Corrosion occurs in two forms: uniform corrosion and localized corrosion. Uniform corrosion is characterized by the attack that takes place over the entire surface area of a metallic surface. Localized corrosion has some selectivity and occurs on small areas or zones of a metallic surface in contact with a corrosive medium (as seawater). Some of the more widespread forms of localized corrosion are pitting corrosion, crevice corrosion, galvanic corrosion and erosion-corrosion. Compared to uniform corrosion, localized corrosion is more problematic since it can cause severe and deep failures in short time and could be very difficult to detect and predict. This is because localized corrosion morphologies are usually small in size and the corrosion spots, as pits, are often covered with corrosion products. Moreover, localized corrosion is difficult to measure gravimetrically due to the small weight loss of the corroding material [2].

Due to their corrosion and biofouling resistance in seawater environments, mechanical ductility, excellent electrical and thermal conductivity, copper alloys are used extensively as condenser and heat exchanger tubing materials in marine power plants. Copper has a good resistance to corrosion in most cases; however, it still undergoes corrosion such as pitting corrosion, crevice corrosion and stress corrosion cracking [3].

Cooling circuits of industrial plants are ideal incubators for microorganisms because they offer plenty of water, are maintained at temperatures between 30 and 60°C, at pH of 6

---

to 9, and provide a continuous source of nutrients, such as inorganic or organic compounds. The microorganisms present in cooling water circuits can be divided into planktonic and/or sessile cells. Sessile ones attach to surfaces and form what is known as biofilm. The development of a biofilm is considered to be a multistage process involving the following major steps: a) formation of an organic conditioned film on the solid surface by adsorption of biomolecules such as proteins, b) transport of microorganisms from the water to the surface, c) adhesion of microorganisms onto the surface, d) replication of the attached cells and production of exopolymers, e) detachment of parts of the biofilm that are swept along by the flowing water to repeat the process of biofilm formation elsewhere. Biofouling is hence a consequence of biofilm formation. The significant negative effects of biofouling are the blockage of water free flow in the cooling circuit and consequent mechanical damage to pumps, clogging of condenser tubes, reduction of the heat transfer efficiency and microbially induced corrosion (MIC) also called biocorrosion.

Microorganisms influence corrosion by changing the electrochemical conditions at the alloy/solution interface, creating an environment that is completely different from that of the bulk medium in terms of pH, dissolved oxygen, organic and inorganic species concentrations.

Chlorination is still the most common treatment to control biofouling of cooling circuits of power plants fed with seawater, provoking harmful effects to the aquatic environment. Once the toxicity of chlorination by-products for human health and environment became a concern, the allowed chlorine concentration was drastically reduced all over the industrialized world (0.2 mg/L) and performing effective treatments became more difficult than in the past. An environmental-friendly way to re-modulate chlorination treatments is thus highly desired.

For this reason, it is essential to carry out further research on the corrosion of copper alloys in chlorinated seawater environments. There are some possible involved mechanisms that are still under investigation:

- a) the negative biofilm action: biofilm may inhibit the growth of a protective oxide layer on the metallic surface, by locally changing the pH or by creating differential aeration cells;
- b) the positive chlorine action: the chlorine inhibits the biofilm growth which in turn stops the inhibition of a protective oxide layer growth (biocide effect), and it may passivate the metallic material (oxidizing effect).

The research described in this manuscript deals with the corrosion behavior of two copper alloys: 70Cu-30Ni (68.5% Cu, 30% Ni, 0.7% Fe and 0.8% Mn; wt. %) and aluminum

---

brass (76% Cu, 22% Zn and 2% Al; wt. %) in seawater environments. The study was carried out by combined electrochemical measurements and surface analysis. In this work, the selected electrochemical methods were:

- a) corrosion potential monitoring as a function of immersion time, in free corrosion conditions (no external voltage or current source);
- b) potentiodynamic with a given scan rate and steady-state polarization curves (external voltage source, current recorded as a function of potential);
- c) electrochemical impedance spectroscopy (EIS).

For surface analysis, X-ray photoelectron spectroscopy (XPS) and time-of-flight secondary ions mass spectrometry (ToF-SIMS) were used to estimate the surface chemical composition and the thickness of layers developed on the surface of the samples.

This PhD manuscript is divided into six chapters. Following this introductory section, the scientific background of the study is addressed in Chapter 1. That chapter presents an introduction to cooling water systems in power supply facilities, including their importance in power plants, the types of cooling water systems, and the materials commonly used in the manufacture of cooling circuits. Chapter 1 also presents an introduction to corrosion of copper and copper alloys associated with cooling circuits, and the effect of different parameters on the corrosion behavior of 70Cu-30Ni alloy and aluminum brass.

Chapter 2 details the metallic materials and electrolytes which were studied, as well as the experimental methods and the procedures used in this PhD.

Chapter 3 presents the results related to field experiments. In this chapter, the on-line monitoring of the corrosion behavior of 70Cu-30Ni alloy and Al brass in real industrial conditions is reported as well as off-line measurements (weight loss measurements and genetic studies).

In Chapter 4, the influence of solution (natural seawater vs artificial seawater) and of biomolecule concentration on the electrochemical behavior of 70Cu-30Ni alloy and on the chemical composition of oxide layers is discussed. For that purpose, filtered natural seawater (FNSW) and artificial seawater (ASW), either without any biomolecule or added with bovine serum albumin (BSA), were chosen. An impedance model for the 70Cu-30Ni/seawater system at the corrosion potential ( $E_{corr}$ ) is presented.

In Chapter 5, the effect of hydrodynamics (static conditions, under flow and stirring, and using a rotating ring electrode (RRE)) on the electrochemical behavior of 70Cu-30Ni and Al brass alloys in ASW and FNSW, and on the surface chemical composition is discussed.

---

Impedance models for the Al brass/seawater system, in static conditions and using the RRE, are presented.

At last, Chapter 6 deals with the effect of pH (ranging from 3.7 to 8.0) on the electrochemical behavior of both alloys in static FNSW and on the chemical composition of oxide layers.

This manuscript also presents two annexes. The procedure for converting marker concentrations into mass concentrations (%) of model constituents in an organic phase is presented in Annex A; whereas in Annex B, the mathematical development leading to the impedance model for the anodic dissolution of pure copper in chloride media is detailed.

## CHAPTER 1 – SCIENTIFIC BACKGROUND

### 1.1 COOLING WATER SYSTEMS IN POWER SUPPLY FACILITIES

This PhD manuscript focuses on the study of the corrosion of copper alloys used in the production of piping material for the electricity-generating plants, like fossil fuel, nuclear, hydroelectric, cogeneration and geothermal power plants.

In thermal generating plants, the chemical energy in the fuel is converted into thermal energy to heat water, making steam. The steam turns an engine (turbine), creating mechanical energy to run a generator. Magnets turn inside the generator, producing electric energy (Figure 1-1). To make thermal electricity, nuclear fissile fuel, coal, oil, waste and gas are used.

A very important part of the process occurs in the condensers and cooling water system. The steam exits the turbines and passes over cool tubes in the condensers. The condensers capture the exhausted steam and transform it back to water, at very low pressure. The cooled water is then pumped back to the boiler to repeat the heating process. At the same time, water is piped from a reservoir or a river or sea to keep the condensers constantly cool. This cooling water, now warm from the heat exchange in the condensers, is released from the plant.

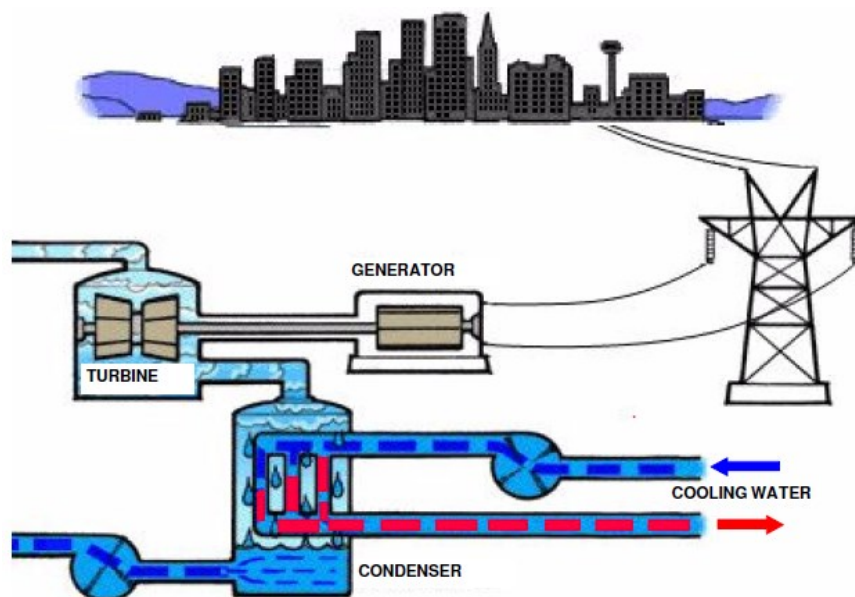


Figure 1-1: Open circuit power plant.

The condenser is a particular critical component in a power plant, because condenser tube leaks can affect many other components in the steam-water cycle and besides mechanical problems, the most frequent cause for tube leaks is corrosion [4].

### 1.1.1 TYPES OF CONDENSERS

Condensers are heat exchangers, *i.e.*, the essential heat transferring elements in cooling systems. It is the device used for transfer heat between two or more fluids at different temperatures and in thermal contact [5]. The fluids can be either liquids or gases, and are ideally separated by a heat transfer surface [6].

Heat exchangers could be classified in many different ways such as according to transfer processes, number of fluids, surface compactness, flow arrangements, heat transfer mechanisms, type of fluids and industry.

Common flow arrangements of the fluids in a heat exchanger are classified in single or multiple pass (Fig. 1-2). When a heat exchanger's fluids pass each other more than once, a heat exchanger is called a multi-pass heat exchanger. If the fluids pass each other only once, the heat exchanger is called a single-pass heat exchanger. The choice of a particular flow arrangement is dependent on the required exchanger effectiveness, available pressure drops, minimum and maximum velocities allowed, fluid flow paths, packaging envelope, allowable thermal stresses, temperature levels, piping and plumbing considerations, and other design criteria.

Considering the type of coolant, condensers may be cooled by water, air or water spray. A water-cooled condenser is a heat exchanger that removes heat from refrigerant steam and transfers it to the water flowing inside it. Thus, the refrigerant steam condenses on the outside surface of a tube and gives up heat to the water flowing inside the tube.

An air-cooled condenser is a direct dry cooling system where the steam is condensed inside finned tubes, and the cooling media (air) is blown outside the finned tubes. As there is no intermediate surface condenser like indirect dry cooling, the overall performances are better. Usually this type of condenser is used in small plants.

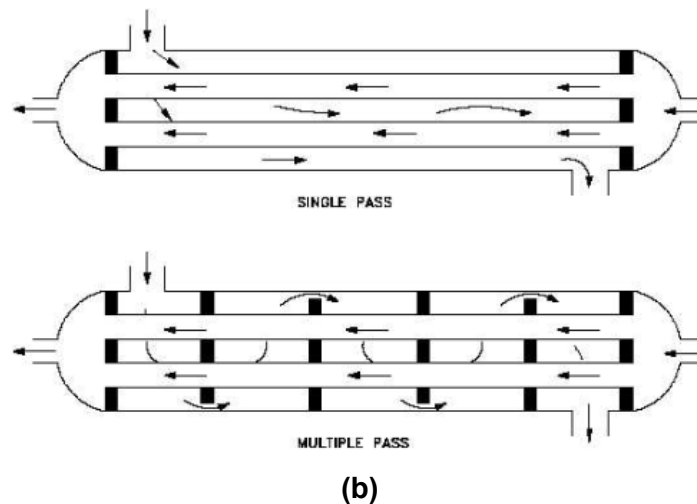
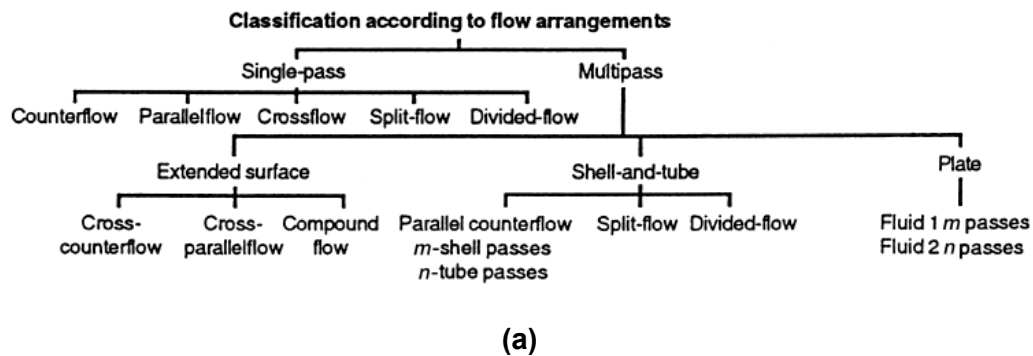


**Figure 1-2:** Classification of heat exchangers according to flow arrangements (a) and example of single and multiple pass heat exchangers (b) (adapted from John Willey [7]).

Like water-cooled condensers, evaporative-cooled condensers first transfer heat to the water and then from the water to the outdoor air. The evaporative condenser combines the functions of a cooling tower (transfer waste heat to the atmosphere through the cooling of a water stream to a lower temperature) and a condenser in one package. The condenser water evaporates directly off the tubes of the condenser.

### 1.1.2 TYPES OF COOLING WATERS

Different water resources are normally used in water-cooled condensers, depending of their availability: freshwater, seawater and brackish water<sup>1</sup>. Seawater-based cooling is mainly used in refineries and large power plants. Seawater is an excellent cooler: huge amounts are available and it is usually very clean. It presents high salinity (mainly due to sodium chloride) and electric conductivity, from 40.0 to 50.0 mS.cm<sup>-1</sup> which is at least about 200 times higher than the conductivity of a river water.

<sup>1</sup> Brackish water is water that has more salinity than freshwater, but not as much as seawater. It may be a mix of seawater and freshwater.

The pH of seawater is dependent on the predominance of aqueous  $\text{CO}_2$ , bicarbonate ( $\text{HCO}_3^-$ ) or carbonate ( $\text{CO}_3^{2-}$ ) ions. Usually, the pH of seawater is alkaline, between 7.9 and 9.0. For non polluted waters, it ranges from 8.0 to 8.4 and decreases with an increase of temperature [8]. At this pH, the  $\text{HCO}_3^-$  ions predominate. Carbonate ions concentration increases with increasing pH, and when more  $\text{CO}_2$  dissolves in seawater, the pH becomes more acidic (Figure 1-3).

When  $\text{CO}_2$  from the atmosphere reacts with seawater, it immediately forms carbonic acid ( $\text{H}_2\text{CO}_3$ ), which in itself is unstable. This further dissociates to form bicarbonate and carbonate ions. The bicarbonate and carbonate ions are responsible for the buffering capacity of seawater, *i.e.* seawater can resist drastic pH changes even after the addition of weak bases or acids. The carbonate ions can react with calcium ions ( $\text{Ca}^{2+}$ ), which are in excess in seawater, to form calcium carbonate ( $\text{CaCO}_3$ ), the material out of which the shells of mussels, the skeleton of corals and the exoskeleton of some microalgae is made of.

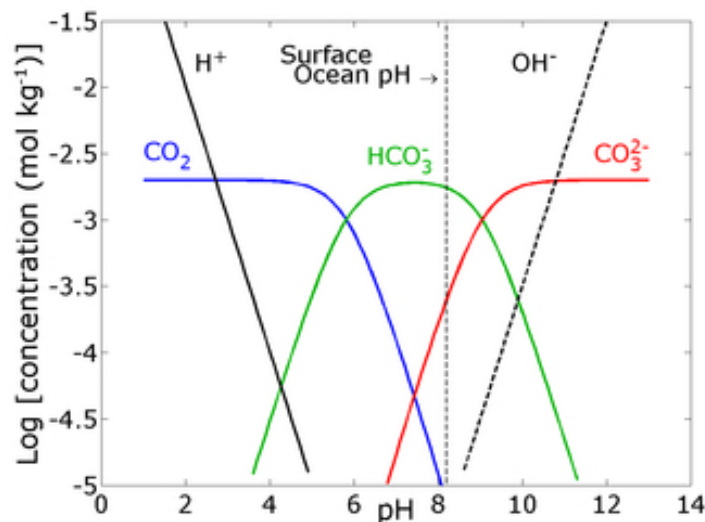


**Figure 1-3:** Distribution of  $\text{CO}_2$ ,  $\text{HCO}_3^-$  and  $\text{CO}_3^{2-}$  concentrations as a function of pH. Seawater has a pH value around 8.2.

### 1.1.3 CONSTITUENT MATERIALS OF COOLING WATER SYSTEMS

The selection of materials in cooling systems is a complex process. It must be a compromise between the requirements due to the chemistry of the water and the operational requirements of the system. A variety of materials have been used for feed-water heater and condenser tubes.

In seawater, the most common include coated carbon steel, titanium, copper alloys (aluminum brass, 90Cu-10Ni and 70Cu-30Ni copper-nickel alloys [9]), admiralty brass and Monel (70% nickel, 30% copper), sometimes also 304 stainless steel is used. Condenser tubes are often made of cuprous materials.

Titanium has been now largely used, in power plants surfaces condensers, desalination plants, chemical process and refinery heat exchangers. Titanium is known to offer an exceptional resistance to corrosion, attributed to its surface oxide film, 5-10 nm thickness, formed immediately on exposure to air. The natural titanium oxide film is dense and stable anatase ( $\text{TiO}_2$ ) and protects the inner metal from further oxidation [10-12]. There are no case histories that document microbial induced corrosion of titanium and its alloys [10, 13, 14].

Stainless steels consist of a group of iron-based alloys which contain a minimum of 10.5% and maximum 30% of chromium and are one of the most widely used materials and have many different applications; they are divided in four main groups based on their microstructure: ferritic, austenitic, martensitic and austenitic-ferritic (duplex). Other elements may be summed up to provide specific characteristics to the alloy, such as nickel, molybdenum, copper, titanium, aluminum, silicon, niobium and nitrogen; e.g. austenitic stainless steels that is usually alloyed with Ni, for example 18Cr-Ni (AISI 304) [15, 16]. The corrosion resistances of stainless steels are due to the formation of a thin passive film of chromium-rich oxide which works as a barrier against ion diffusion between the alloy and the ambient phase; this protective layer chromium-oxide develops during routine exposure to the oxygen content in the atmosphere. The passivity of stainless steel can break down under the following environments: a) dilute and concentrated HCl, HBr, and HF, and salts that hydrolyze these acids; b) oxidizing chlorides such as  $\text{FeCl}_3$ ,  $\text{CuCl}_2$ , or  $\text{NaOCl}$ ; c) seawater, except for brief exposures or when cathodically protected; and c) some organic acids including oxalic, lactic, and formic acids [14, 16, 17].

Copper and copper alloys are commonly used in condensers and heat exchangers due to their high thermal and electrical conductivity, mechanical workability and good resistance to corrosion and macrofouling. Those criteria have lead for a long time to the selection of copper alloys such aluminum brass, 70Cu-30Ni alloy or 90Cu-10Ni alloy, to be used in seawater [10, 14, 18, 19]. Alloying nickel and small amounts of iron into copper improves the corrosion resistance; therefore Cu-Ni alloys are preferred in marine environments due to the formation of a thin, adherent, protective surface film which forms naturally and quickly upon exposure to clean seawater. That surface film is complex and predominantly made up of cuprous oxide, often containing nickel and iron oxides, cuprous

hydroxychloride and cupric oxide [18, 19]. Nickel provides passivity in acidic solutions while Cu is protective in more alkaline solutions [20]. Additionally, Cu-Ni alloys are also chosen in seawater because of its resistance to macrofouling; the reason for their antifouling behavior is still not fully understood, but it may be result from the action of a low level of steady discharge of cupric ions [21]. Despite copper's reputation for toxicity, copper alloys are vulnerable to microbial induced corrosion, especially when long periods of stagnation are involved or flow is intermittent. Differential aeration, selective leaching, under-deposit corrosion, and cathodic depolarization have been reported as mechanisms for MIC of copper alloys [14, 19, 20]. The application fields of copper and its alloys can be classified into five sections as shown in Table 1-1.

**Table 1-1:** Application fields of copper and its alloys (adapted from Cieslewicz and Schweitzer [22]).

Applications	Examples	Approximate corrosion rate
Construction	Roofing, building fronts, hand rails and door knobs.	Atmosphere: 0.5~2.5 $\mu\text{m}/\text{year}$
Fresh water	Fresh water supply line and plumbing fittings.	Atmosphere: 0.5~2.5 $\mu\text{m}/\text{year}$
Marine	Seawater supply line, shafting, valve stems and marine hardware.	Seawater: about 50 $\mu\text{m}/\text{year}$
Industrial	Heat exchanger, condenser and chemical plant process equipments.	Variable (depends upon environment)
Electrical	Electrical wiring, connectors, printed circuit boards and semiconductor packages.	Variable

#### 1.1.4 COOLING WATER SYSTEMS OPERATING PROBLEMS

The major problems associated with cooling systems are: scaling, fouling, biofouling and corrosion. If these problems are not properly controlled, they can have a direct, negative impact on the value of the entire process or operation [13].

- **Scaling**

Scale refers a dense coating of predominantly inorganic material formed on the surface of equipment in the presence of water; it takes place when dissolved ions in the water exceed the solubility of a given mineral. Such a process frequently occurs when surfaces are overheated. The common precipitates are calcium carbonates, sulfates or silicates. The principal factors determining whether scale is forming are temperature, pH, water quality, concentration of scale-forming material present, hydrodynamic conditions and influence of other dissolved materials, which may or may not be scale-forming. In cooling

systems, the most frequent type of scale found is a deposit of calcium carbonate [23]. Scale formation damage the heat transfer and reduces flow velocities inside the condenser tubes, its solution, normally requires costly chemical softeners [24].

- **Fouling and biofouling**

The accumulation of solid material, other than scale, in a way that hampers the operation of plants equipment or contributes to its deterioration deposition of suspended material in heat exchange equipment is called fouling. Foulants can come from external sources such as dust around a cooling tower or internal sources such as by-products of corrosion. Examples are: dirt and silt, sand, corrosion products, natural organics, microbial masses, aluminum phosphates, iron phosphate. The factors that influence fouling in a cooling system are the water characteristics, temperature, flow velocity, microbial growth, corrosion and contamination [25].

Cooling circuits of power plants are ideal incubators for microorganisms because they offer plenty of water, are maintained at temperatures between 30°C to 60°, at pH of 6 to 9, have good aeration and provide a continuous source of nutrients, such as inorganic or organic compounds; microorganisms are those organisms that cannot be seen individually with the unaided human eye. The microorganisms present in cooling water circuits can be divided into planktonic or sessile cells. Sessile ones attach to surfaces and form what is known as biofilm.

The development of a biofilm is a multistage process involving the following major steps (Fig. 1-4): a) formation of an organic conditioned film on the solid surface by adsorption of biomolecules such as proteins, b) transport of microorganisms from the water to the surface, c) adhesion of microorganisms onto the surface, d) replication of the attached cells and production of exopolymers, e) detachment of parts of the biofilm that are swept along by the flowing water to repeat the process of biofilm formation elsewhere. Biofouling is a consequence of biofilm formation and is able to change the electrochemical properties of the metal-water interface, both in aerobic and anaerobic environments; the significant negative effects of biofouling are the blockage of water free flow in the cooling circuit and consequent mechanical damage to pumps, clogging of condenser tubes, reduction of the heat transfer efficiency (having a direct effect on the efficiency of the thermal cycle of power plants), and microbiologically influenced corrosion (MIC) also called biocorrosion.

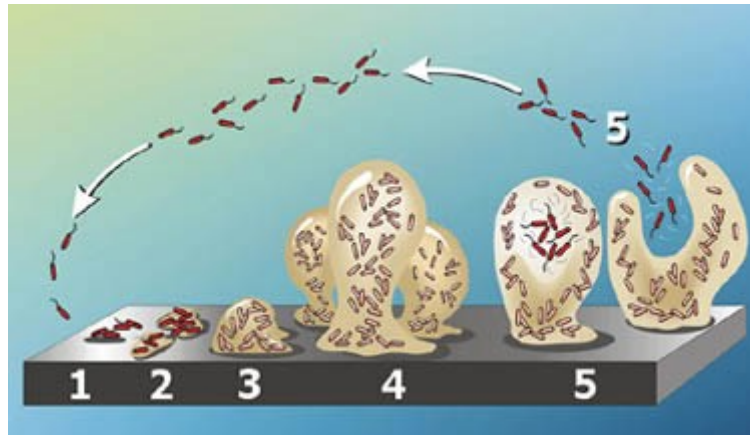


**Figure 1-4:** Principal steps in the biofilm development: 1) Initial reversible attachment of free swimming micro-organisms to surface, 2) Permanent chemical attachment, single layer, bacteria begin making slime, 3) Early vertical development, 4) Multiple towers with channels between, maturing biofilm, 5) Mature biofilm with seeding/dispersal of more free swimming micro-organisms (Graphic by Peg Dirckx and David Davies, 2003 Center for Biofilm Engineering Montana State University).

## • Corrosion

Several definitions of corrosion have been given. Despite different definitions, it can be observed that corrosion is basically the result of chemical or electrochemical interaction between a metal and environments; in cooling water circuits, this result in the gradual loss of metal thickness or even penetration of tube wall, which can cause leakage of process fluids into the cooling water or vice-versa. The main factors that affect corrosion are the oxygen and other dissolved gases, the dissolved and suspended solids, the pH, the velocity, the temperature and the microbial activity [21, 26]. Table 1-2 shows the corrosion mechanisms that are encountered in cooling water systems.

**Table 1-2:** Corrosion mechanisms that have caused problems in power plant cooling water systems under certain conditions (adapted from Syrett *et al.* [4]).

Alloy	Severity and location of attack (a)						
	Erosion-Corrosion	Sulfide attack	Dealloying	Pitting/crevice corrosion	Galvanic corrosion	Environmental cracking (b)	NH <sub>3</sub> attack
90Cu-10Ni	W	W	w	w(c)	w(d)	N	s
70Cu-30Ni	W	W	N	w(c)	w(d)	N	s
Al brass	W	W	w	W(c)	W	WS	S
304 and 316 SS	N	N	N	W	N(e)	W	N
Titanium	N	N	N	N	N(e)	N(f)	N

(a) W: water side problem; S: steam side problem; WS: both sides; N: not a problem; w: small sensibility on water side; s: small sensibility on steam side; (b) Includes stress-corrosion cracking and hydrogen embrittlement; (c) Possible problem only if sulfides are present; (d) Problems have occurred for similar alloys; (e) Induced in adjacent copper alloys, iron, and carbon steels when used in seawater or other highly conductive waters; (f) Brittle titanium hydride may form and crack if excessively high cathodic protection currents are applied.

As the objective of this work is to study the corrosion behavior of copper alloys (70Cu-30Ni and Al brass) in seawater environments, only the corrosion mechanism associated with these two materials will be considered (section 1.2).

### **1.1.5 COOLING CIRCUITS TUBES CLEANING METHODS**

All types of cooling waters can have different tendencies to corrode condenser materials and to introduce organic fouling and mineral scaling. This is why a strong control of the water is so important. It will prevent the formation of mineral scale, organic growth and corrosion.

In the case of seawater, care must be taken to control biological fouling, scale (particularly in heat exchangers), and the tendency to corrode many materials.

There are several kinds of condenser tubes cleaning procedures: physical screening, physical cleaning and chemical dosing [27], and almost all have been adopted in a large field of industries. High pressure cleaning, with a water flow pressure higher than 600 bar, is necessary to remove consistent macrofouling and calcareous settlements. In this case, oxide layers are completely removed from the metal surface. The in service continuous mechanical cleaning systems (like Taprogge system) are effective for the prevention of microfouling and it is one of the recommendable methods as Best Available Technologies [28] for cooling water circuits. In this case, sponge rubber balls, with the same density as water and a diameter slightly larger than the bore of the condenser tubes, circulate inside the pipes. This method can be effective enough for freshwater when macrofouling risk is low. But in the case of seawater, for which aggressiveness is highest and macrofouling settlement is an important issue, it has to be associated with a chemical treatment. In this case, as well as in all the cases for which a chemical solution is necessary to control macrofouling in the cooling tubes, the best solution often consists of a mechanical in-service cleaning associated with a chemical low-dosage treatment [29].

The most practical and efficient method applied to prevent and control biofilms and microbial activity in cooling water is the use of biocides. Biocides are single compounds (or a mixture of compounds) capable of killing microorganisms or inhibiting microbial growth.

### **1.1.6 CHLORINATION**

Chlorine is the most common oxidizing biocide and is introduced either through the electrolysis of seawater or the injection of sodium hypochlorite solution. Chlorination treatments can be carried out either intermittently, keeping the residual chlorine level below

0.3 to 0.5 ppm [30, 31], or by using the so called shock method, *i.e.* 2-3 ppm chlorine at intervals of 1 hour for a limited period. Since high chlorine levels increase the susceptibility of copper alloys to erosion-corrosion, continuous low level chlorination is to be preferred [31].

When chlorine is added to water, it reacts to form a pH dependent mixture of chlorine, hypochlorous acid and hydrochloric acid [32]:



Depending on pH, hypochlorous acid partly dissociates to hydrogen and hypochlorite ions:



In acidic solution, the major species are  $\text{Cl}_2$  and  $\text{HOCl}$ , while in alkaline solution only  $\text{ClO}^-$  is present. Very small concentrations of  $\text{ClO}_2^-$ ,  $\text{ClO}_3^-$ ,  $\text{ClO}_4^-$  are also found [33].

In the case of seawater, where the concentration of bromide is naturally as high as 70  $\text{mg.L}^{-1}$ , the oxidative power of chlorine dosed is quickly transferred to bromide, because the equilibrium of the reaction (1.3) moves to the products on the right, converting the “chlorination” in a “bromination”.



The equilibrium of dissociation (reaction 1.4) differs strongly between hypochlorite and hypobromite at the seawater pH (8.0-8.4); while the hypochlorite is 80% dissociated, the hypobromite is 80% un-dissociated at pH higher than 8, based on the dissociation constants values at standard conditions (10-8.6 for hypobromite acid and 10-7.53 for hypochlorite acid [34].



The biocide action of un-dissociated hypochlorite and hypobromite acids forms are strongly higher than that of ionic forms, due to the lower polarity of un-dissociated molecules favors their passage across the biological membranes. This fact, in association to the transfer of oxidant power from chlorine to bromide in seawater (reactions 1.3 and 1.4) makes chlorination working (as biocide) at concentration lower than 1  $\text{mg.L}^{-1}$ , besides the relatively high seawater pH.

While the organic matter is broken down mainly into oxidized decomposition products, a small amount (1-2 %) of the chlorine forms carbon-chlorine bonds. This reaction creates a variety of chlorinated organic by-products. In the case of seawater, where are substantial amounts of bromide ions present, some of these by-products will be brominated. The most

important ones are trihalomethans (THMs) that are suspected carcinogen and/or mutagenic compounds and persist in the water with the exhaust residual oxidant [35]. The by-products production is the concern that mainly limits the extensive use of chlorination in the recommendation for the risk assessment of biocorrosion.

The US Environmental Protection Agency (US EPA) considers as different THMs members: chloroform ( $\text{CHCl}_3$ ), bromoform ( $\text{CHBr}_3$ ), dibromochloromethane ( $\text{CHClBr}_2$ ) and dichlorobromomethane ( $\text{CHCl}_2\text{Br}$ ). Many studies on the byproducts of disinfecting drinking water have demonstrated the toxicity of these by-products since the 1970's [36].

Chlorinated by-products (CBPs) comprise other organohalogenated non-oxidizing secondary products such as haloacetonitriles and compounds from their hydrolysis [37], which concentration is usually negligible at the discharge of industrial cooling circuits.

On the other hand, bromoforms, were actually detected in cooling circuits during chlorination with dosing concentrations above  $1 \text{ mg.L}^{-1}$  [38]. Subsequent works demonstrated that chlorination treatment with oxidant concentration equal or less than  $0.2 \text{ mg.L}^{-1}$  do not give significant concentrations of halomethans [39, 40]. However, the use of chlorination is discouraged by regulations all over the world. The standard limit of chlorine concentration at the discharge into natural water bodies is generally  $0.2 \text{ mg.L}^{-1}$  all over the industrialized world [34].

As a conservative rule, the dosage of chlorine is generally set in order to have less than  $0.2 \text{ mg.L}^{-1}$  residual oxidant. In the case it is not enough to prevent/remediate biofilm development and higher dosages must be adopted, a de-chlorination treatment can be applied, with dosages of reductants such as sodium metabisulfite or sulfur dioxide. Usually, there is no specific limitation at the discharge concerning the chemicals reductants used, nevertheless, attention must be paid in the dosage because an overdosage may deplete the dissolved oxygen concentration or modify the pH of receiving streams.

## 1.2 CORROSION OF COPPER AND ITS ALLOYS IN AQUEOUS ENVIRONMENTS

Corrosion is basically the result of chemical or electrochemical interaction between a metal and environments; in cooling water circuits, this result in the gradual loss of metal thickness or even penetration of tube wall, which can cause leakage of process fluids into the cooling water or vice-versa. The main factors that affect corrosion are the oxygen and other dissolved gases, the dissolved and suspended solids, the pH, the velocity, the temperature and the microbial activity [21, 26].

Currently, the prime motive for research in corrosion is provided by the economic factor. According to a study published in 2001 by the Electric Power Research Institute (EPRI) on the cost of corrosion in the electric power industry [41], the cost to consumers of corrosion was about \$17 billion. The same study also estimated that about 22% of the corrosion costs would have been avoided by practical cost effective measures, e.g., improved selection of materials, design and fabrication, and water chemistry. A more recent survey on the costs of corrosion showed that the direct cost of corrosion was \$276 billion in the United States for 2002, which was approximately 4% of their Gross National Product [1].

In Europe, figures are not yet known, but it is expected that costs associated to corrosion will be at least as big as in the United States. From a study in Italy, in ENEL plants [42], an estimation close to tens of millions of US \$ is given for the prevention and control of fouling and microbial corrosion. Authors affirmed that 50% of corrosion cases in condenser tubes might be prevented by a better cleaning during the plant operation. In some cases, corrosion problems have been solved by adopting more noble materials such as titanium and super-ferritic stainless steels.

Copper and its alloys are subject to almost all kinds of corrosion attacks depending upon the environment. From a study conducted by the North American Electric Reliability Council between 1996 and 2000 in 1476 fossil units, 168 show that condensers were responsible for 25,955 forced and scheduled outages and deratings, costing the units 53,869 GWh<sup>2</sup> [4]. The main components responsible for these losses are the condenser tubes. And the main problems are frequently caused by corrosion or erosion.

Metals corrode in aqueous environments by an electrochemical process, in which the actual metal loss occurs by dissolution of charged metallic ions,  $M^{n+}$  ("n"= valency), and the production of electrons as follows.



In the case of copper, it gives:



Any reaction which releases electrons, as above, is called "anodic reaction". In order for the corrosion process to continue, the electrons released by the anodic reaction must be consumed by a cathodic reaction occurring simultaneously over the metallic surface, which involves chemical species present in the surrounding aqueous environment. An anodic and a cathodic reaction must occur to have corrosion.

---

<sup>2</sup> GWh = Gigawatt hour = one billion ( $10^9$ ) watt hour

- **Anodic reaction**

The anodic reaction of metal dissolution produce compound that act in different way in the corrosion process:

- a) go into the solution and the rate of metal loss may be high, as a consequence, serious operational problems can occur;
- b) or stay on the metallic surface as oxide or hydroxide (insoluble film); if they form an adherent, non-porous film, they can protect the metal from rapid corrosion.

In seawater, the main initial corrosion product on copper is cuprous chloride, CuCl, formed by the following reaction:



Cuprous chloride is slightly soluble in diluted sodium chloride and reacts to produce cuprous oxide, also called cuprite ( $\text{Cu}_2\text{O}$ , main constituent of thick scales), that, in the presence of seawater, will be later oxidized to cupric hydroxide ( $\text{Cu}(\text{OH})_2$ ), atacamite ( $\text{Cu}_2(\text{OH})_3\text{Cl}$ ) or malachite ( $\text{CuCO}_3 \cdot \text{Cu}(\text{OH})_2$ ).

Thermodynamic principles can help explain corrosion in terms of the stability of the chemical species and reactions associated to it. The Pourbaix diagram [43] for the Cu-H<sub>2</sub>O system at 25 °C (Fig. 1-5) can give us some information about copper behavior in aqueous environments. Between the two dashed lines a and b, there is a stable domain for water. It can be seen that the immunity domain of copper partly overlaps the stability domain of water. It suggests that copper will not corrode in water without oxygen being present. For most metals in a de-aerated environment, corrosion takes place and the anodic reaction is the dissolution of the metal while the cathodic reaction is the evolution of hydrogen gas from the electrolyte. However, if oxygen is present, copper is susceptible to corrosion as indicated by the corrosion domains in Figure 1-5. In other words, the primary cathodic reaction for copper corrosion in aqueous systems is the reduction of oxygen to form hydroxide ions.

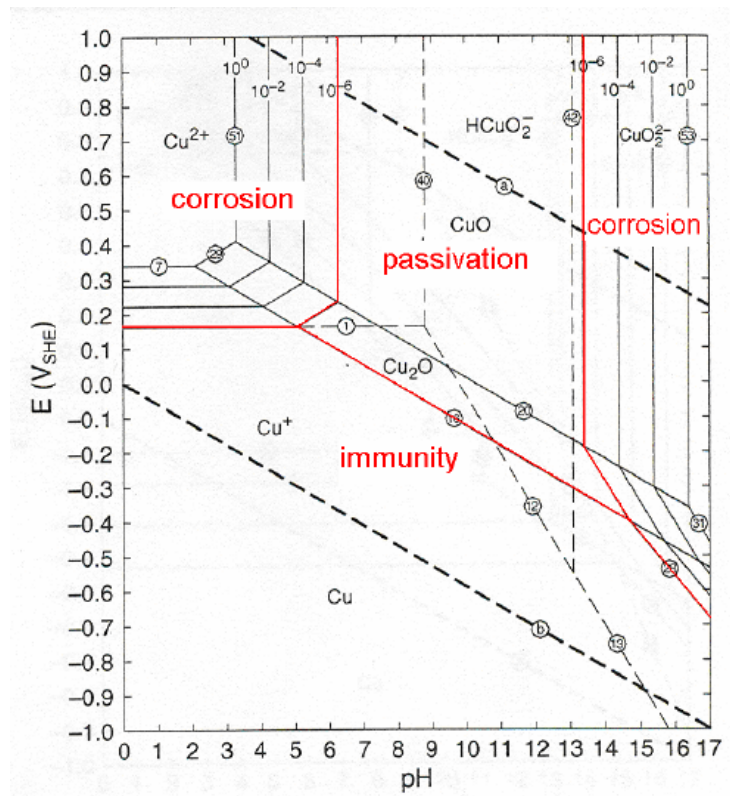


**Figure 1-5:** Pourbaix diagram for the Cu-H<sub>2</sub>O system at 25 °C [43].

The circled numbers on the diagram indicate a chemical or an electrochemical reaction, and the activity of dissolved species for which the lines were calculated is indicated by the other numbers. Bianchi and Longhi [44] determined the Pourbaix diagrams for copper in seawater at 25 °C. Figure 1-6 is an example of one of these diagrams. Compared with Figure 1-5, Figure 1-6 considers the reactions between chloride ions and copper as well as between copper and water. As a result, it can be seen that there are two new chemical species in the figure,  $\text{Cu}_2(\text{OH})_3\text{Cl}$  and  $\text{CuCl}$ . In addition, the stability domain for each species is different due to the existence of these new compounds.

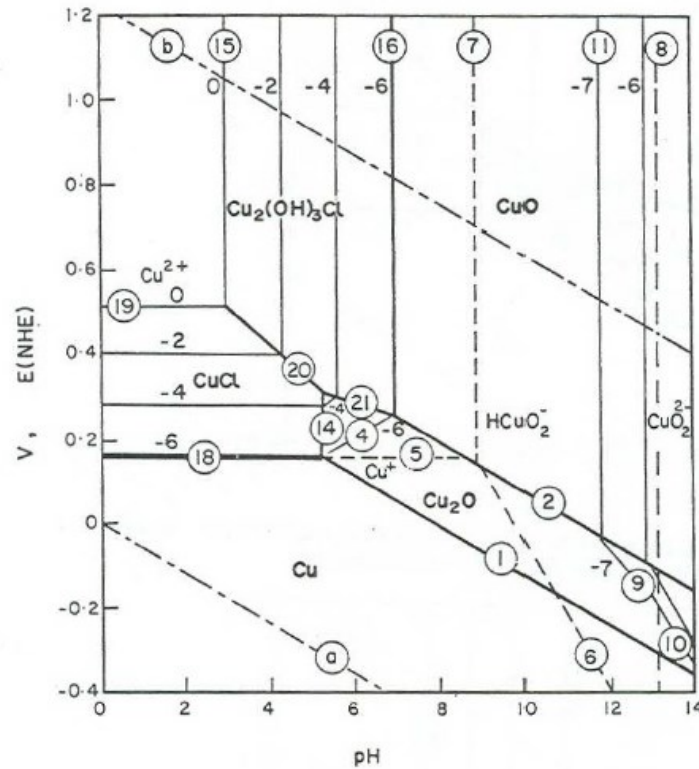


**Figure 1-6:** Pourbaix diagram for copper in seawater at 25 °C [44].

Due to its complexity, the anodic polarization behavior of pure copper in chloride media has received considerable attention in the literature. The reactions are considered to be reversible and all are universally assumed to be under mixed control (electrochemical reactions limited by both charge transfer and mass transport) close to the corrosion potential [45], where the different mechanisms for the formation of  $\text{CuCl}^-$  are presented in Table 1-3.

**Table 1-3:** Anodic partial reactions of pure copper in chloride media.

Mechanism 1	$\text{Cu} + 2\text{Cl}^- \leftrightarrow \text{CuCl}_2^- + \text{e}^-$	Direct formation of $\text{CuCl}_2^-$ species from the metal
Mechanism 2	$\text{Cu} \leftrightarrow \text{Cu}^+ + \text{e}^-$	Dissolution of copper as cuprous ion in a 1 <sup>st</sup> step
	$\text{Cu}^+ + 2\text{Cl}^- \leftrightarrow \text{CuCl}_2^-$	
Mechanism 3	$\text{Cu} + \text{Cl}^- \leftrightarrow \text{CuCl} + \text{e}^-$	Formation of $\text{CuCl}_2^-$ species from the $\text{CuCl}$
	$\text{CuCl} + \text{Cl}^- \leftrightarrow \text{CuCl}_2^-$	

The diffusion control in the electro dissolution of Cu was ascribed either to  $\text{Cl}^-$  transport from the bulk solution to the electrode surface or to the transport of  $\text{CuCl}_2^-$  from the electrode to the bulk solution [46].

Anodic polarization of copper in chloride electrolytes results in  $E$  vs  $\log i$  curves (Fig. 1-7) that can be split into three main regions of potential [45]:

- Section I: a region of Tafel behavior where the reaction is assumed to be totally limited by charge transfer.
- Section II: a potential window of film formation leading to a maximum peak current density and subsequent limiting current density. The maximum peak, minimum and limiting current density responses are produced as the formation of CuCl becomes faster than either its complexation by the chloride ion or mass transport of the cuprous dichloride complex into the bulk solution. The maximum peak current, therefore, is followed by a minimum current as the surface coverage by CuCl reaches its maximum.
- Section III: a potential domain for which any increase in current density is due to the formation of Cu(II) species.

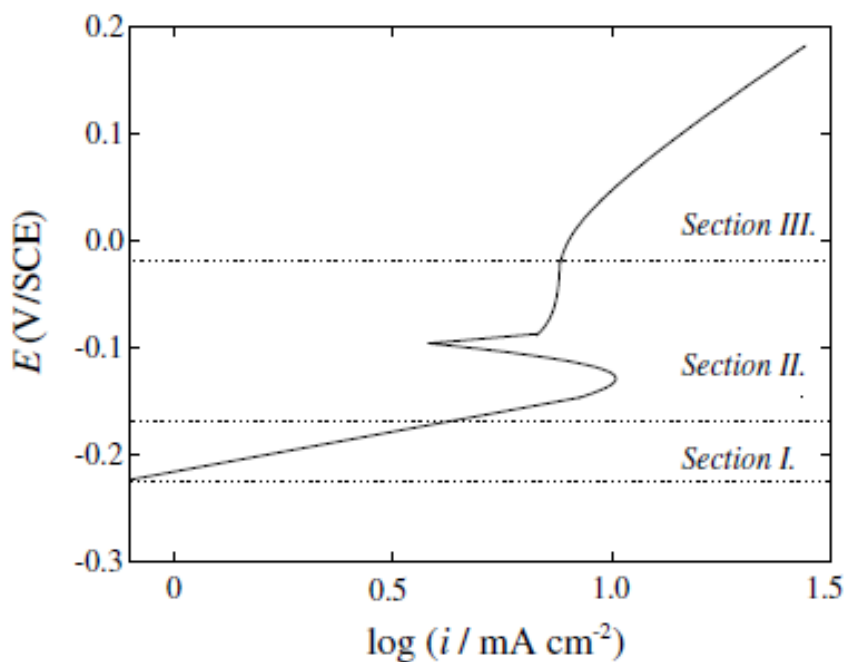
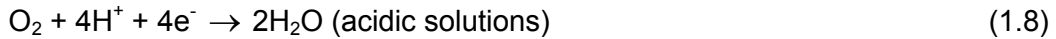


**Figure 1-7:** Typical anodic polarization curve of copper in aqueous chloride solution (adapted from Kear *et al.* [45]).

In summary, close to the corrosion potential, the anodic reaction is under mixed kinetics (charge transfer and mass transport) where the mass transport limiting step is the rate of movement of a cuprous chloride complex away from the electrode surface to the bulk electrolyte.

- **Cathodic reaction**

In aerated medium, the cathodic reaction coupled to the anodic dissolution of copper is the reduction of dissolved oxygen. The global reaction for the reduction of oxygen involves an exchange of four electrons, resulting in the production of hydroxyl ions (or water molecules at low pH). This reduction may occur in one step, with a transfer of four electrons (reaction (1.8) for acidic solutions and reaction (1.9) for neutral and alkaline solutions), or in two steps, each one involving two electrons (reactions (1.10) and (1.11)):



Hydroxyl ions or water molecules can be produced by a single four-electron step or by cumulative two-electron steps where oxygen is reduced to hydrogen peroxide, which is in turn reduced to hydroxyl ions. Figure 1-8 shows a general scheme describing the mechanism of oxygen reduction.

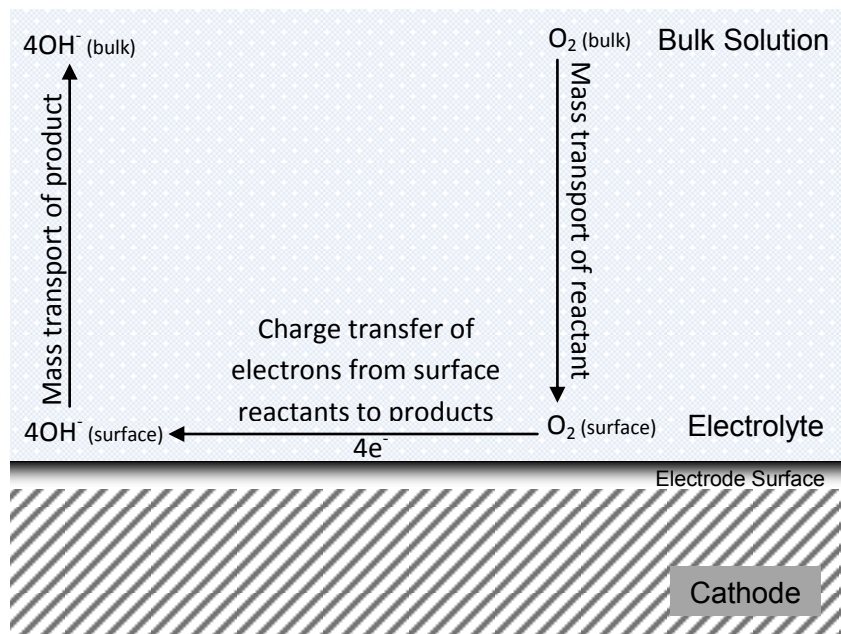


**Figure 1-8:** Steps involved during the reduction of oxygen consisting of mass transport to and from the electrode surface and electron transfer reaction (adapted from Kear *et al.* [47]).

During the first step, oxygen has to be transported to the electrode surface and this process depends on the convection, in other words on fluid velocity or electrode speed. Once

the oxygen molecules reach the electrode surface, they react to produce hydrogen peroxide then hydroxyl ions, or directly hydroxyl ions. This step is controlled by the electron transfer rate. The kinetics of oxygen reduction is expected to be very specific to the electrochemical system under study: it depends on the metallic material, its surface state, the electrolyte, and the temperature [45, 47]. Once the product ( $\text{OH}^-$ ) is formed, its removal from the electrode surface depends again on mass transport.

The cathodic reaction is dominated by the irreversible reduction of oxygen via either a two- or a four-electron exchange which is charge transfer limited at potentials close to the corrosion potential.

To have corrosion, an anodic and a cathodic reaction must occur. The anodic and cathodic reactions have to balance over the entire metallic surface. The anodic reaction cannot occur any faster than the overall cathodic reaction. In most instances of corrosion, both the anodic and cathodic reactions occur on the surface of a single metal or alloy. When a metallic material is corroding actively, the actual corrosion rate is often critically dependent upon the progress of the cathodic reaction. This means that the supply of dissolved oxygen to the metallic surface very often controls the corrosion rate. Thus, aqueous environments of high oxygen content are more corrosive than de-oxygenated ones.

Another important factor is that the diffusion of dissolved oxygen molecules in water is relatively slow. Consequently, for any given oxygen content, flowing water will cause higher corrosion rates than static conditions because the former situation will facilitate rapid oxygen supply to the metallic surface.

- **Nature of the protective film**

Unlike a passive metallic material, copper cannot produce a passive film. But the corrosion products formed on copper and its alloys, to some extent; provide a protection against corrosion. In most cases, the protective oxide film on copper is  $\text{Cu(I)}$  oxide in aqueous environments at room temperature. This adherent and relatively impervious film acts as a diffusion barrier, but it is easily affected by change in hydrodynamic conditions.

The good corrosion resistance of Cu alloys in seawater is related to the formation of a protective film of corrosion products in the early stages of exposure. It is generally considered that the inner part of the film is made of cuprous oxide ( $\text{Cu}_2\text{O}$ ) with cupric oxide ( $\text{CuO}$ ) appearing in the outer part of the film, and that the film contains metallic ions together with chlorides, hydroxides and carbonates [48]. Although this film will start developing during initial contact with oxygenated water, it may take several weeks for the film to be fully protective. When the film is fully developed and reaches steady-state, the corrosion rate is

usually very low. In unpolluted seawater, a loosely adherent porous cupric hydroxychloride ( $\text{Cu}_2(\text{OH})_3\text{Cl}$ ) corrosion product scale forms over a thin, tightly adherent layer of cuprous oxide ( $\text{Cu}_2\text{O}$ ) that increases corrosion resistance with increasing exposure time [49, 50]. The inner film is normally reddish. The outer film may be greenish, brown or yellow brown. Although  $\text{Cu}_2\text{O}$  oxide is the principal component of the film, the lattice usually includes other metallic ions, e.g. iron, nickel, aluminum, calcium, silicon, and sometimes other species. Principal anions include chlorides, hydroxides [51], carbonates and bicarbonates.

Once a protective surface film is formed, the corrosion rate will continue decreasing over a period of years, related to the classical parabolic growth rate of protective layers. For this reason, it has always been difficult to predict the life time of copper-nickel based alloys based on short-term results. Usually, general corrosion rates of 0.02-0.002 mm/yr or 20 to 2  $\mu\text{m}/\text{year}$  are anticipated [52].

Formation, structure and chemical composition of the protective layer are complex and have been the subject of many investigations [53-56]. The complexity of the films on Cu-Ni alloys in marine conditions was studied by Kato *et al.* [55, 56]. From exposure of 90Cu-10Ni samples to air-saturated 3.4% NaCl solution and analysis of the corrosion product layers by SEM and X-ray diffraction, authors concluded that the protective films, formed under open-circuit corrosion conditions, had the following features:

- a) thick outer layer, mainly cuprous hydroxy-chloride [ $\text{Cu}_2(\text{OH})_3\text{Cl}$ ], and inner layer containing appreciable amounts of chloride, oxygen, copper and some nickel;
- b) rich in chloride throughout the film with a maximum concentration along a plane located within the inner layer near the inner layer/outer layer interface;
- c) relatively poor in Ni and Fe in the inner layer, compared to levels in the outer layer, and, in early stages of growth, outer interface surface consisting of a cuprous compound (probably  $\text{Cu}_2\text{O}$ ) which, with time, gives rise to carbonate and finally to cuprous hydroxy-chloride [ $\text{Cu}_2(\text{OH})_3\text{Cl}$ ] compounds.

### 1.2.1 GALVANIC CORROSION

An electrochemical potential almost always exists between two different metals when they are immersed in a conductive solution. If two different metals are in electrical contact with each other and immersed in a conductive solution, as seawater, a potential results that enhances the corrosion of the more electronegative metal of the couple (anode) and protects the more electropositive one (cathode).

Usually, copper alloys are more cathodic than other metals (due to their position in galvanic series) such as steel and aluminum. Copper alloys usually corrode preferentially when coupled with high-nickel alloys, titanium or graphite.

The seawater high conductivity gives rise to the possibility of formation of galvanic cells with the cathodic and the anodic areas at some meters from each other, giving rise to highly localized corrosion processes.

Accelerated damage due to galvanic effects is usually the most important near the junctions, where the electrochemical current density is the highest [57]. Another factor that affects this kind of corrosion is area ratio; it happens when the cathodic area is large and the anodic one is small.

### **1.2.2 PITTING CORROSION**

Pitting is the usual form of corrosive attack at surfaces on which there are incomplete protective films, non-protective deposits, or extraneous deposits of dirty or other substances. Pitting of copper and its alloys always occurs under relatively low flow velocity, usually less than 0.6 to 0.9 m/s, and has long been associated with chloride ions [58].

Once a pit is initiated, it may propagate at a significant rate because of the development of a macro-cell, the surrounding surface and the inside of the pit. Due to the difference in electrode potential between the large passive surface area (more anodic) and the small active pit (more cathodic), the pit acts as a small anode and the external surface as a large cathode.

Copper alloys do not corrode primarily by pitting, but due to metallurgical and environmental factors that still need to be clearly understood, is a common problem detected. In order to prevent a copper alloy from pitting, the correct choice of copper alloy for the environment is necessary. For example, aluminum brass is the best choice for protection against pitting attack, while the high-copper alloys are somewhat more inclined to pitting [57].

### **1.2.3 DEALLOYING**

Dealloying is a corrosion process in which the more active metal is selectively removed from an alloy, leaving behind a spongy layer of the more noble metal. Copper-Zinc alloys containing more than 15% of Zn are susceptible to a dealloying process called dezincification [57]. In the dezincification of brass, selective removal of zinc leaves a relatively porous layer of copper and copper oxide. It can be readily observed with naked

eyes because the alloy develops a reddish color that contrasts with its original yellowish color.

Generally, there are two types of dealloying. Uniform or layer dealloying commonly occurs in high zinc alloys where the outer layer is de-alloyed and becomes dark while the inside is not affected; plug dealloying is typical of low zinc alloys and is characterized by the presence of de-alloyed dark plugs in the unaffected matrix of low zinc alloys [59].

Two theories have been proposed for dealloying of brass. One states that there is simultaneous anodic dissolution of both copper and zinc, while dissolved copper ions precipitate plate back from the solution on the remaining brass surface as a porous layer; the other states that the less noble alloying elements vs selectively dissolved, leaving vacancies in the brass lattice resulting in skeletal copper with poor mechanical integrity [59]. In the past decade, many alloying elements, as arsenic (As), have been used to minimize the dezincification and corrosion of brass alloys.

#### **1.2.4 AMMONIA ATTACK**

Ammonia can affect strongly the corrosion behavior of Cu-base alloys condenser tubes by forming soluble copper-amine complex that causes metal loss and pitting in the tubes [60]. At the condenser tube water side, ammonia compounds are produced in case of stagnant water, due to the fermentation processes occurring in presence of high organic compounds and biofilms. Nevertheless, ammonia attack may also affect the vapor side, as the water of thermal cycle of power plant is treated with hydrazine or other reducing compounds to control pH and the oxygen content.

Ammonia can also cause stress corrosion cracking in some copper alloys. In the presence of air and ammonia, aluminum brass is subject to stress corrosion cracking. Aluminum bronze is more resistant and copper nickels are highly resistant to ammonia stress corrosion cracking [61].

#### **1.2.5 SULFIDE ATTACK**

Sulfides are present in polluted seawater and can also be produced under static conditions due to the decomposition of organic matter. Copper-nickel alloys corrode in the presence of sulfide, sulfur, polysulfides, or combinations of these species. Thus, essentially non-corrosive or slow corrosion systems in de-aerated seawater turn into highly corrosive systems [62], and the effect of sulfur-containing compounds is to interfere with the formation of surface film, producing a black film made up of cuprous oxide and sulfide.

Sulfide ions have been shown to significantly increase the corrosion rate of Cu-Ni alloys [63-66]. In sulfide-containing environments, a porous copper sulfide layer forms on the surface of the alloys, which does not protect against corrosion [65]. This layer also prevents the formation of a protective copper oxide layer. During the enhanced corrosion in sulfide containing environments, preferential copper dissolution is observed [64, 66].

Eiselstein *et al.* [67] proposed two different mechanisms for Cu-Ni corrosion in sulfide-polluted seawater. One for the de-aerated seawater, where sulfide ions react with Cu(I): the decrease in the Cu(I) concentration will cause the anodic reaction to be shifted to lower potentials. In the case of aerated seawater, Eiselstein claimed that  $S^{2-}$  reacts with both Cu(I) and oxygen. In consequence, a shift of the anodic and cathodic reactions will occur in such a way that the intersection of the two polarization curves at the corrosion potential occur at higher corrosion currents.

### 1.2.6 EROSION-CORROSION

Copper alloys are relatively sensitive to erosion-corrosion when they are exposed to water with high flow velocity, and especially when turbulences occur. It is a common water-side phenomenon that is only a problem for copper alloy condenser tubes [9]. It occurs above a critical local flow intensity (Fig. 1-9), creating local energy densities which are high enough to break down protective scales, layers or films on the metallic surface. With the increase of seawater flow rate, corrosion rates remain low due to the tenacity of the protective surface film. However, when the velocity exceeds a critical value for a given geometry, the shear stress acting on the film can lead to its breakdown resulting in high corrosion rates. A critical velocity is found at which localized corrosion occurs [68].

The flow rate of the electrolyte also affects the corrosion behavior of Cu-Ni alloys. In the presence of high turbulence, a unique corrosion morphology, the so-called horse-shoe corrosion develops [58, 69].

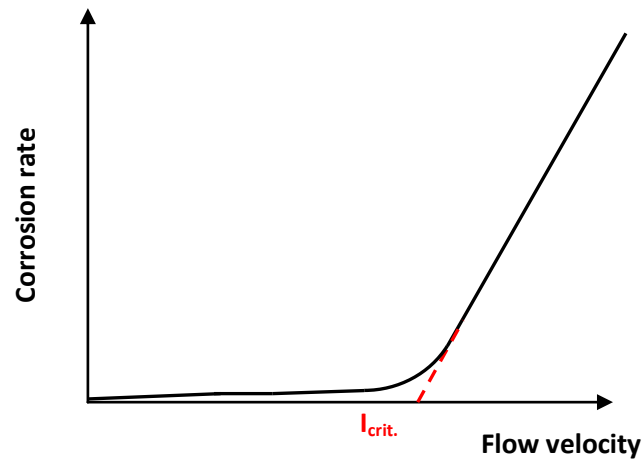


**Figure 1-9:** Critical local flow velocity.

In order to avoid corrosion problems, some suggested maximum cooling water flow velocities are shown in Table 1-4. Minimum flow rates of more than 1 m/s are usually preferred to avoid sediment build up [70]. The effect of the water velocity on the corrosion of Cu-based alloys is discussed on section 1.3.6.

**Table 1-4:** Recommended maximum water flow velocities for condenser tube alloys in seawater. Adapted from [9].

Material	Maximum velocity
	m/s
Copper	0.9
Admiralty brass	1.5
Aluminum brass	2.4
90Cu-10Ni	3.0
70Cu-30Ni	3.7
Stainless steels and titanium	No limit

### 1.2.7 MICROBIOLOGICALLY INFLUENCED CORROSION (MIC)

The well-known toxicity of cuprous ions towards living organisms does not mean that the copper-based alloys are immune to biological effects on corrosion. The electrochemical nature of the metallic corrosion still remains present in the microbial corrosion. There is an anodic process of metallic dissolution and a complementary cathodic process that is dependent of the metal-biofilm characteristics (pH, aeration, chemical composition...), as the reduction of dissolved oxygen (in aerated environments and neutral pH) or the reduction of

water (no-aerated environments). Microorganisms can change the metal/solution interface to induce, accelerate or inhibit the anodic and or cathodic reactions of the corrosion process.

The biological process is illustrated by a microbial colony growing up on the metallic substrate (Fig. 1-10). An anaerobic region is formed under the microbial colony, due to the oxygen consumption by the microbial respiration (in case of aerobic microbes) and another region, where more oxygen reaches the external part of the colony, in contact with the aerated liquid.

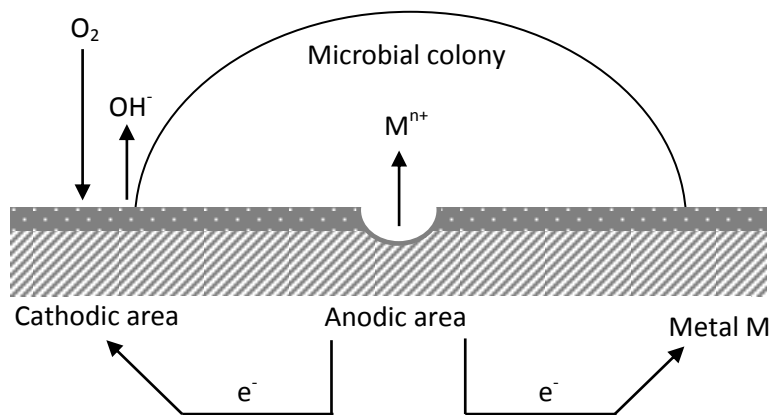


**Figure 1-10:** Scheme for microbial corrosion (metal under a microbial colony).

Any material in contact with natural waters is rapidly colonized by microbial species growing in a complex micro-environment named biofilm. Despite the good performance of copper alloys in seawater, the formation of biofilm on surfaces of heat exchangers and the subsequent settlement of macrofouling induce microbiologically-influenced corrosion (MIC), also called microbial corrosion or biocorrosion. Thus, these phenomena modify the integrity and functionality of metallic materials employed in condensers cooled with seawater [71, 72]. When immersed, copper alloys are swiftly covered by colonies of bacteria which, unlike macrofouling organisms, are not affected by the toxicity of copper, since there are protected by a mucopolysaccharide matrix [73]. The first stage in the biofilm formation is the adsorption of biomolecules, such as proteins, and other organic matter dispersed in seawater. Then, bacterial adhesion occurs and bacteria colonies are formed, together with corrosion products, algae and other microorganisms, resulting in a big complex microfouling that adheres to the metallic surface [74]. Since microfouling modifies the chemical and physical characteristics of the surface and facilitates the development of corrosion processes, an undesirable resistance to the heat exchange is introduced [75].

Biofilms are capable to modify the electrochemical characteristics of metallic surfaces [76, 77], modifying the kinetics of corrosion processes occurring at the metal-biofilm interface.

Some species of *Pseudomonas*, *Sphingomonas*, *Sphingomonas paucimobilis*, *Rhodotorula*, *Flavobacterium*, *Acidovorax delafieldii*, *Cytophaga johnsonae*, *Micrococcus kristinae*, *Acidovorax* and *Sphingomonas* have been identified in biofilms responsible for MIC in copper pipes with drinking water [78-81]. Genus of *Pseudomonas* have been shown to colonize copper surfaces [82] and to accelerate corrosion of copper and copper alloys [83].

The influence of marine aerobic *Pseudomonas* strain on the corrosion behavior of 70Cu-30Ni alloy was investigated by S.J.Yuan *et al.* [84]. A potential shift towards more cathodic value, in the presence of *Pseudomonas* bacteria was confirmed. Their results showed that, in the presence of *Pseudomonas*, the cathodic Tafel constant increases ( $d_c$ ) while  $E_{corr}$  shift in the cathodic direction and the absolute corrosion current increase. However, if *Pseudomonas* were not present,  $E_{corr}$  shifted slightly to more anodic values and the current density was reduced. At the same time, the anodic Tafel constant ( $b_a$ ) shift to higher values. The impedance spectra shown that the alloy surface, in the sterile medium, was comprised of an outer organic compound conditioning layer and an inner compact and protective oxide film layer; while in the *Pseudomonas* inoculated medium, a duplex layer of an outer porous, heterogeneous and non-protective biofilm layer and an inner porous oxide film layer was present. Their results also demonstrated a growth of the outer film with immersion time (impedance increase).

Methods used to prevent MIC, should aim in either inhibit the growth and/or metabolic activity of microorganism, or modify the environment in which the corrosion process takes place in order to avoid adaptation of microorganisms to the existing conditions. These methods can be divided in: a) cleaning procedures, b) biocides, c) coatings and, d) cathodic protection.

### **1.3 EFFECT OF DIFFERENT PARAMETERS ON THE CORROSION BEHAVIOR OF 70Cu-30Ni ALLOY AND AL BRASS**

A copper alloy is the combination of copper with one or more other metals to form a material that can improve the performance of pure copper. Doping with divalent or trivalent cations is an effective way of improving the corrosion resistance of copper.

Copper and copper based alloys can be divided into 3 groups according to the chemical composition [85]: Copper and high copper alloys (copper: Unified Numbering System UNS C10100-C15999; high-copper alloys: UNS C16000-C19999; copper nickels (Cu-Ni-Fe alloys): UNS C70000-C73499 and nickel silvers (Cu-Ni-Zn alloys): UNS C73500-C79999), brasses (Cu-Zn alloys, with or without the addition of Pb and Sn: UNS C20000-C49999) and bronzes (alloys with Sn, P, Al, or Si as the principal alloying element, UNS C50000-C69999).

Copper is the most noble metal in common use. It has excellent resistance to corrosion in the atmosphere and in fresh water. In seawater, copper and copper alloys (particularly those associated with nickel) are widely and successfully used, due to their corrosion resistance, mechanical strength and workability, excellent electrical and thermal conductivity [86] and resistance to macrofouling [87]. In practice, aluminum, zinc, tin, iron, and nickel are often used as alloying elements and reduce noticeably the corrosion rate of copper alloys.

### **1.3.1 EFFECT OF IRON AND NICKEL**

Nickel and iron present in Cu-Ni alloys improve the corrosion and erosion resistance properties of the oxide film. There is beneficial effect of incorporating iron in copper-nickel alloys and it is essential to obtain adequate corrosion resistance by assisting in protective film formation [88, 89].

Copper and its alloys do not form a truly passive corrosion product film. In aqueous environments at ambient temperature, the corrosion product predominantly responsible for protection is cuprous oxide ( $\text{Cu}_2\text{O}$ ), a p-type semiconductor. It has been established that this is the main component of the protective film formed, in the early stages of growth. The protective properties are enhanced by the incorporation of nickel and iron that leads to a decrease in both ionic and electronic conductivities [89, 90]. The corrosion process can proceed if copper ions and electrons migrate through the  $\text{Cu}_2\text{O}$  film. In order to improve the corrosion resistance of the material, the ionic and/or electronic conductivity of the film must be reduced by doping with divalent or trivalent cations [91].

Small additions of iron to copper-nickel alloys are also known to improve their resistance to erosion-corrosion [92] because iron is necessary for the occurrence of nickel enrichment in the corrosion product layer [93].

In general, the corrosion resistance of the Cu-Ni alloys increases with increasing Ni content up to approx. 30 %, above 30%, it remains constant [94] or slightly decreases [57].

According to Popplewell *et al.* [95], the nature of the corrosion film depends on the iron content of the alloy: the film on samples with 0.3 % of iron in the bulk alloy or less is bright green, that on samples with 1.5 % of iron is dark green, and that on samples with 1.5 % of iron, heat treated to precipitate an iron rich phase, is nearly black.

### 1.3.2 EFFECT OF TEMPERATURE

Generally, the corrosion of copper-based alloys in de-aerated seawater flowing from 0.9 to 2.7 m.s<sup>-1</sup> increases as the seawater is heated to 63°C. Maximum corrosion occurs at intermediate temperatures from 54 to 71°C. If seawater reaches too high temperatures (≈107°C), a significant decrease in corrosion is noted [96].

According to Ijsseling *et al.* the appearance, thickness and adherence of the oxide film, in aerated seawater, depends on the temperature of formation [97]. In flowing seawater (at 1.5 m.s<sup>-1</sup>), an adherent dark brown layer is formed at 10° C, a less adherent dark brown one is formed at 20-30°C, and a very thin, adherent, gold-brown film is visible at 40-50°C.

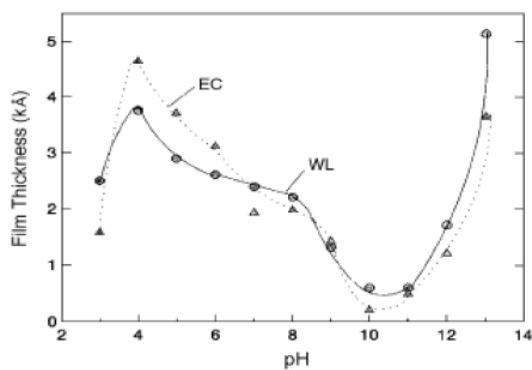
### 1.3.4 EFFECT OF PH

Depending on pH, the anodic polarization of copper may result in anodic dissolution or film formation. In acidic aqueous solutions, such as HCl or H<sub>2</sub>SO<sub>4</sub>, Cu(I) complexes are formed by bonding with Cl<sup>-</sup> or SO<sub>4</sub><sup>2-</sup>. These porous corrosion products do not prevent copper from further dissolution. As pH decreases, the corrosion rate increases. Low pH levels prevent copper-based alloys from developing or maintaining protective films and thus high corrosion rates are encountered.

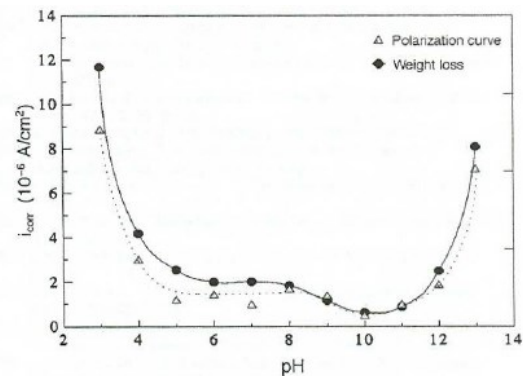
Feng *et al.* systematically investigated copper corrosion in simulated tap water over a wide pH range [98]. The results of this study are summarized in Table 1-5. The thickness of the oxide films and the dependence of corrosion rate on pH were estimated as shown in Figure 1-11. Thus, dissolution of oxide films takes place when pH is less than 4; for a pH between 4 and 10, cubic Cu<sub>2</sub>O crystals grow while the crystal size becomes smaller and the film becomes thinner; when pH is greater than 10, monoclinic CuO films start forming.

**Table 1-5:** Corrosion products, controlling mechanisms and corrosion rate of copper in aqueous solutions at various pH.

pH value	Oxide films	Morphology o corrosion products	Controlling mechanisms	Corrosion rate
3	Cu <sub>2</sub> O	Porous corrosion products	Diffusion in solution	High, due to high solution corrosiveness
4-5	Cu <sub>2</sub> O	Cubic Cu <sub>2</sub> O provides a barrier to copper dissolution	Mixed diffusion of copper ions in the oxide film and in solution	Decreases. From pH 4 to 5, the film becomes more protective
6-9	Cu <sub>2</sub> O	Cubic Cu <sub>2</sub> O is more protective	Diffusion in the oxide film	Constant. Very thin, dense and smooth Cu <sub>2</sub> O film protects the surface.
10	Cu <sub>2</sub> O	Thick and compact cubic Cu <sub>2</sub> O film	Passivation	Passivity
12-13	Cu <sub>2</sub> O	Protective monoclinic layer	Diffusion in the oxide film	Increases, due to increased solubility of CuO film



(a)



(b)

**Figure 1-11:** (a) Variation of oxide film thickness with pH estimated from electrochemical methods (EC) or weight loss method (WL); (b) corrosion current density of copper in solutions of various pH calculated from polarization curves or weight loss measurements. Copper immersed during 24 h in simulated tap water at 30°C (adapted from Feng *et al.* [98]).

The influence of metal-biofilm interface pH on aluminum brass corrosion in seawater was studied by Cristiani *et al.* [99]. According to these authors, biofilms may act on corrosion by acidification at the metal-biofilm interface. Differences have been found in corrosion current density and in surface morphology for specimens exposed to natural seawater compared to those exposed to artificial seawater (at pH 8.3).

According to Tuthill *et al.*, there is no film formation on 90Cu-10Ni in seawater below pH 6, even in the presence of oxygen (5.5-7.5 mg.L<sup>-1</sup>) [48].

It has been shown that at 65°C the erosion-corrosion attack is much more extensive and appears at lower velocities when the pH is decreased from 8 to 6.5 [100]. If the pH of warm (35°C) seawater flowing at about 2.7 m/s is adjusted to 3.6, no protective film forms on the surface of 90Cu-10Ni [101].

#### 1.3.4 EFFECT OF OXYGEN CONTENT

The oxygen content of the electrolyte has a significant effect on the corrosion resistance of copper alloys [59]. For instance, at low to moderate oxygen concentrations ( $[O_2] \leq 6.6$  mg/L), the 70Cu-30Ni alloy is more corrosion resistant than the 90Cu-10Ni ones and in saturated seawater; both alloys have similar behavior [59].

#### 1.3.5 EFFECT OF POLLUTED SEAWATER

Copper-nickel alloys corrode at increased rates in polluted waters (compared to clean waters), particularly when sulfides or other sulfur compounds are present [48, 94, 102]. Sulfides form a black corrosion product, which is less adherent and protective than the normal oxide film.

Gudas and Hack reported that 0.05 ppm of sulfide or more was necessary to cause increased corrosion of 70Cu-30Ni alloy, and even 0.01 ppm of sulfide, during one day, caused accelerated attack of 90Cu-10Ni alloy [103]. This is in agreement with the work of Alhajji and Reda who noted that sulfide was very corrosive towards the alloys with low nickel content [104].

The corrosion of Cu-Ni alloys, in flowing (1.6 m/s) seawater containing sulfides, polysulfides, or sulfur, was investigated by Anderson and Badia [105] and MacDonald *et al.* [62]. Cuprous sulphide forms as the principal corrosion product causing damage to the protective film on the metal surface. The importance of proper protective film formation on tubes and pipes must be emphasized. It is stated that if during the early life of condenser tubes clean seawater passes through, good protective films will form which are likely to withstand most adverse conditions. The ideal situation, whether in a ship or a power plant, is to re-circulate aerated, clean seawater from initial start up to a time sufficient enough to form a good protective film. If, however, polluted waters are encountered during the early life, the films formed on the condenser tubes will likely not be fully protective and the risk of premature failure will be considerably increased [102].

Yuan *et al.* showed that when 70Cu-30Ni bare metal was in contact with sulfur ions, the surface film evolves from an oxide bi-layer (formed in the absence of S-species) to S-

based layered films [84]. The authors also showed that the film was porous and not very protective in the presence of S-ions. These latter dissolve copper oxides but nickel is not affected as readily as copper. Thus, it is possible that a semi-protective film richer in nickel is formed at longer times, explaining the apparent repassivation.

### 1.3.6 EFFECT OF WATER VELOCITY

Although higher coolant flow velocities improve the efficiency of condensers and heat exchangers, the velocity cannot be increased above the endurance limit of materials.

Giuliani *et al.* [106] found that the sensitivity of Cu-Ni alloys corrosion rate to water flow rate was relatively low in  $\text{Cl}^-$  containing solution.

Based on the work carried out by Efird [107], seawater moving over a metallic surface creates a shear stress between that surface and the layer of seawater closest to the metal. As velocity increases, the corrosion rate first increases slowly, as a result of increased oxygen supply, (cathodic depolarization) and removal of the corrosion products from the metallic surface. At higher velocities, the degree of turbulence and the shear stress are such that the protective film can be locally removed and the active underlying metal can be exposed to water; at this "breakdown" velocity, the rate of attack increases dramatically. Efird [107] studied and estimated the critical shear stress for various Cu-based alloys. His research suggested that shear stresses depended on water velocity and pipe geometry. As pipe diameter increases, copper-based alloys tolerate higher nominal velocities.

Sato and Nagat [108] showed that the shear stress at the inlet-end of a condenser tube is about double that further down the tube. This explains why inlet-end erosion corrosion is such a common occurrence, and also explains the preference for copper-nickel alloys that have been developed because of their greater velocity tolerance.

At low flow velocities, sand, debris, mud, etc. may deposit, increasing the chance for the formation of macro-corrosion cells (differential aeration and concentration cells).

### 1.3.7 EFFECT OF SEAWATER TREATMENTS

#### **Ferrous sulfate**

Small and regular additions of ferrous sulfate to the cooling water can limit the deterioration of copper-based condenser tubes [109]. Its positive action, i.e. prevention of the corrosion of copper alloys, can be summarized as follows [110]: experience suggests that the further from the condenser the injection point is the less effective the treatment will be; evidence show that chlorination can cause an increased risk of corrosion at higher than

normal levels, and that ferrous sulfate can prevent these damaging effects; with copper-nickel alloys, ferrous sulfate treatment is normally unnecessary. However, there have been instances where corrosion has developed in abnormal circumstances, and the ferrous sulfate treatment has proved to be beneficial. Besides seawater situations, beneficial effects have also been observed in fresh water. Studies of the films formed as a result of ferrous sulphate treatment indicate that lepidocrocite  $\text{FeOOH}$  is sometimes present; North and Pryor showed that such film provides corrosion resistance to copper surfaces [111].

### **Chlorination**

As already referred, chlorine treatments are used to control biofouling and slime formation in coastal power plants. General experience indicates that  $\text{Cl}_2$  concentration in the range of 0.2-0.5 ppm will control biofouling with no effect on the corrosion of copper-nickel alloys [112]. Excessive chlorination, however, can damage copper alloy tubing.

In solutions containing  $\text{Cl}^-$ , the corrosion products developed on copper are mainly the chloro-complexes, which form a non-adherent layer on the metallic surface.

In chlorinated seawater, Klein et al. [113] found that 70Cu-30Ni alloy exhibited a better corrosion resistance in seawater added with 1 ppm of chlorine. In addition, in a high chlorine-containing environment (chlorine concentration = 90 ppm), the corrosion rate was found to be increase significantly.

### **1.3.8 EFFECT OF SUSPENDED PARTICLES AND MUD**

In flowing seawater, suspended particles increase the erosion-corrosion rate of Cu-Ni alloys. Sand is common in seawater and high amount can be harmful to copper alloy tubing and can damage the protective oxide film. Damage to Cu-Ni alloys increases with the size and the sharpness of the sand [114]. The presence of suspended solids will clearly represent a factor that will further damage the protection of corrosion product layers [108, 114]. The 70Cu-30Ni (C71500) has higher resistance to liquid/solid 2-phase flow than Al brass (C68700) [115].

Mud has no abrasive effect on the corrosion film, but can be very damaging for Cu-Ni alloys if allowed to deposit in tubing and remain in place over substantial periods of time. At velocities below  $1 \text{ m.s}^{-1}$ , experience has shown that corrosion failures can be expected within 6-12 months unless frequent cleaning succeeds in removing deposits before under deposit corrosion initiates [116]. What is believed to happen in deposit is, first, oxygen depletion in the inner part of the deposit next to the tube surface. The upper layer of the deposit remains aerobic with active bacteria. Secondly, after the inner layer is depleted in oxygen, sulphate

reducing bacteria become increasingly active, generating sulfides. As the sulfide concentration increases, the protective film, already weakened by the absence of oxygen, begins to break down and a general pitting type of attack follows. This is generally referred to as microbiologically influenced corrosion (MIC).

### 1.3.9 EFFECT OF BIOMOLECULES

A biomolecule is any molecule that is produced by a living organism, including large macromolecules such as proteins, polysaccharides, lipids, and nucleic acids, as well as small molecules such as primary metabolites, secondary metabolites, and natural products. Natural seawater contains biomolecules so, the influence of biomolecules adsorption, which is the first step in biofilm formation, is one important factor to be considered.

Bovine serum albumin (BSA) is a serum protein derived from cows. It is often used as model protein to study protein-surface interactions, due to its low cost and to a good knowledge of its properties. BSA is a globular protein with a molecular weight of 66,43 kDa ( $66430 \text{ g.mol}^{-1}$ ).

A number of investigations is specifically focused on the interactions between BSA and copper or other metals [117-119]. Pinto *et al.* studied BSA adsorption on copper and oxidized copper surfaces by electrochemical impedance and quartz crystal microbalance [117]. Authors concluded that the influence of BSA depends on the presence or absence of oxygen and on the applied potential (which determines the amount of copper ions released from the surface). Svare *et al.* studied the effect of proteins (alanine, bovine plasma albumin, and cystine) on the passivation of nickel and copper [118]. The results showed that the presence of cystine inhibited the passivation of nickel and improved the passivation tendency of copper. Clark and Williams studied in buffered saline solution with and without proteins (serum albumin and fibrinogen), the corrosion of the pure metals: aluminum, cobalt, copper, chromium, molybdenum, nickel, and titanium [119]. The corrosion of aluminum and titanium was unaffected by the proteins. In the presence of proteins, the corrosion rates of chromium and nickel were slightly higher, while cobalt and copper dissolved to a very much greater extent.

## 1.4 AIM OF THIS THESIS AND RESEARCH STRATEGY

This thesis is performed in the framework of the BIOCOR project, in the sub-project 3 focusing on biocorrosion problems of cooling condensers in power plants. BIOCOR ITN aims to study biocorrosion issues by bringing together researchers with different scientific

backgrounds in the area of biocorrosion, with a problem oriented approach “from the field through the lab to the field”. The research methodology is based on multidisciplinary knowledge, from chemistry, electrochemistry, material science and microbiology. The field problems due to biocorrosion are raised by industry, then related applied research work was performed in the lab, and finally, useful results are expected to solve the questions as a benefit for the industry (Figure 1-12).

This thesis was set against the background of the industry with much activity studying the performance and main problems present on cooling circuits of power plants: biofilm formation and subsequently biofouling of copper alloys used in heat exchangers and specially the mechanisms of corrosion involved on this materials used as piping material in cooling seawater systems. As a matter of fact, many failure events affecting copper alloys in heat exchanging plants were reported in the recent years due to MIC [120].

It was found that against this background it would be of interest to study 70Cu-30Ni and Al brass alloys, in which good general corrosion resistance is known, but some theoretic mechanisms must be explored. These two materials were chosen, due to their extensive use as condenser and heat exchanger tubing materials in power plants.

The objective of the thesis has been focused on some possible mechanisms potentially influencing, negatively or positively, the corrosion behavior of copper alloys:

- a) a negative biofilm action that can inhibit a protective oxide layer growth on the metallic surface by locally changing pH or by creating differential aeration cells (anodic effects);
- b) a positive oxidant action (by chlorine and bromine) that can inhibit the biofilm growth (biocide effect) allowing the formation of a protective film adherent to the metal surface;
- c) a negative action of both biofilm and chlorine that increase the cathodic reaction and, consequently, the global corrosion process of the alloy.

## **1.5 THESIS OUTLINE**

This chapter presents an introduction to cooling water systems in power supply facilities, their importance in power plants, the types of cooling water systems, and the materials commonly used in the manufacture of cooling circuits. An introduction to corrosion of copper and copper alloys associated with cooling circuits, and the effect of different

parameters on the corrosion behavior of 70Cu-30Ni alloy and Al brass completed the chapter.

After this first chapter, this thesis involves five parts, as follows (Figure 1-12):

- a) Chapter 2 details the metallic materials and electrolytes which were studied, as well as the experimental methods and the procedures used in this PhD
- b) Chapter 3 presents the results related to field experiments. In this chapter, the on-line monitoring of the corrosion behavior of 70Cu-30Ni alloy and Al brass in real industrial conditions is reported as well as off-line measurements (weight loss measurements and genetic studies).
- c) In Chapter 4, the influence of solution (natural seawater vs artificial seawater) and of biomolecule concentration on the electrochemical behavior of 70Cu-30Ni alloy and on the chemical composition of oxide layers is discussed. For that purpose, filtered natural seawater (FNSW) and artificial seawater (ASW), either without any biomolecule or added with bovine serum albumin (BSA), were chosen. An impedance model for the 70Cu-30Ni/seawater system at the corrosion potential ( $E_{corr}$ ) is presented.
- d) In Chapter 5, the effect of hydrodynamics (static conditions, under flow and stirring, and using a rotating ring electrode (RRE)) on the electrochemical behavior of 70Cu-30Ni and Al brass alloys in ASW and FNSW, and on the surface chemical composition is discussed. Impedance models for the Al brass/seawater system, in static conditions and using the RRE, are presented.
- e) At last, Chapter 6 deals with the effect of pH (ranging from 3.7 to 8.0) on the electrochemical behavior of both alloys in static FNSW and on the chemical composition of oxide layers.

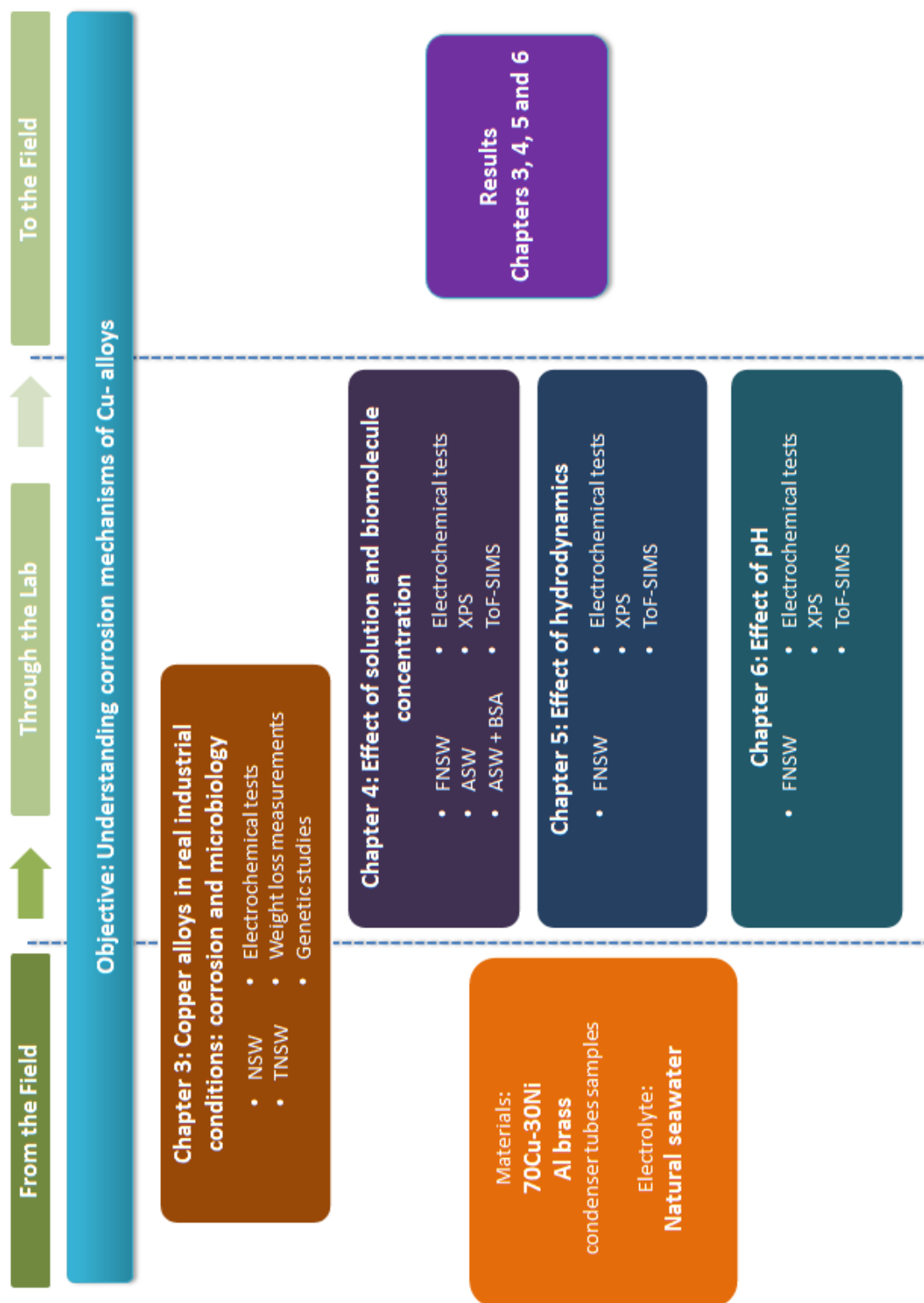


**Figure 1-12:** Outline of the thesis and objective of each chapter. This also illustrates the BIOCOR project approach: from the field, through the lab, to the field (NSW = Natural seawater without chlorination; TNSW = Treated natural seawater, with chlorination; FNSW = Filtered natural seawater; ASW = Artificial seawater; ASW+BSA = Artificial seawater with 20 mg.L<sup>-1</sup> of bovine serum albumin; XPS = X-ray photoelectron spectroscopy and ToF-SIMS = time-of-flight secondary ion mass spectrometry).

## CHAPTER 2 – MATERIALS AND METHODS

### 2.1 STUDIED METALLIC MATERIALS AND ELECTROLYTES

The metallic materials investigated in this PhD are two copper alloys which are extensively used in a variety of marine industries, especially as piping materials: 70Cu-30Ni (wt. %) and aluminum brass.

Both materials were collected from power plants as new tubes, and then cut in different shapes as a function of performed tests (seawater exposition, electrochemical measurements or surface analyses).

There are several possible approaches to study the corrosion of copper in marine environments; those selected in this PhD are presented in Figure 2-1. The experimental work was divided into two parts: field experiments and laboratory experiments. The different experiments were performed at different places, as indicated in Figure 2-1.

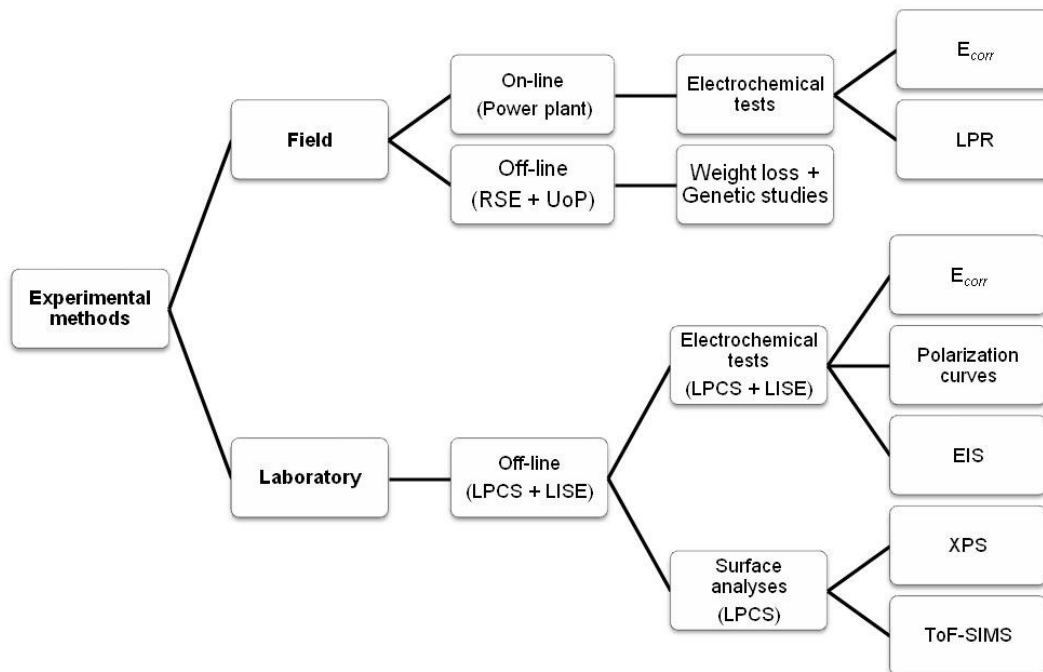


**Figure 2-1:** Experimental methods and places where the measurements were performed. (RSE SpA = Ricerca sul Sistema Energetico, Milan, Italy; UoP = University of Portsmouth, Portsmouth, UK; LPCS = Laboratoire de Physico-Chimie des Surfaces, Paris, France; LISE = Laboratoire Interfaces et Systèmes Electrochimiques, Paris, France;  $E_{corr}$  = corrosion potential; LPR = linear polarization resistance; EIS = electrochemical impedance spectroscopy; XPS = X-ray photoelectron spectroscopy and ToF-SIMS = time-of-flight secondary ion mass spectrometry).

### 2.1.1 METALLIC MATERIALS

#### 70Cu-30Ni alloy

The 70Cu-30Ni (wt. %) alloy was collected from a power plant in the form of tubes (condenser tubes; Figs. 2-2(a) and (b)) with 2.54 cm external and 2.28 cm internal diameter. The chemical composition of this alloy is reported in Table 2-1.

**Table 2-1:** Chemical composition of the 70Cu-30Ni (wt. %) alloy.

Alloy	Weight (%)						
	Cu	Zn	Ni	Al	As	Fe	Mn
70Cu-30Ni	68.5	-	30	-	-	0.7	0.8

From these tubes, different types of samples and electrodes were prepared (Fig. 2-2(c)). Table 2-2 summarizes the different samples geometries as a function of performed tests.

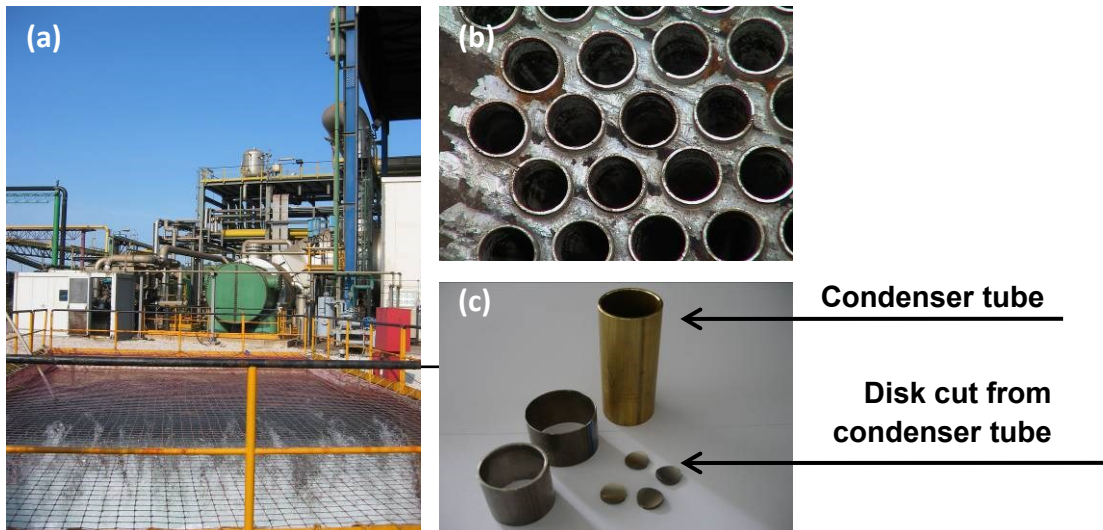
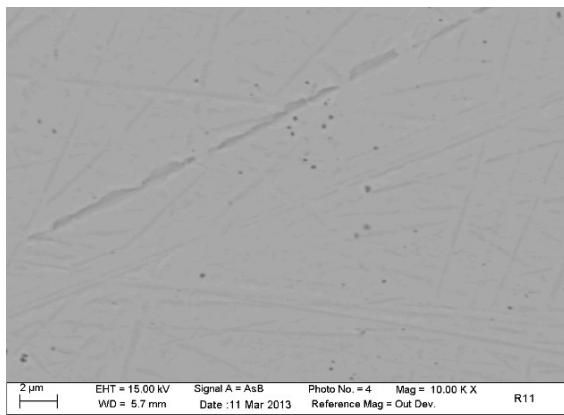


**Figure 2-2:** (a) Heat exchanger inside a power plant facility, (b) condenser tubes and (c) samples cut from condenser tubes.

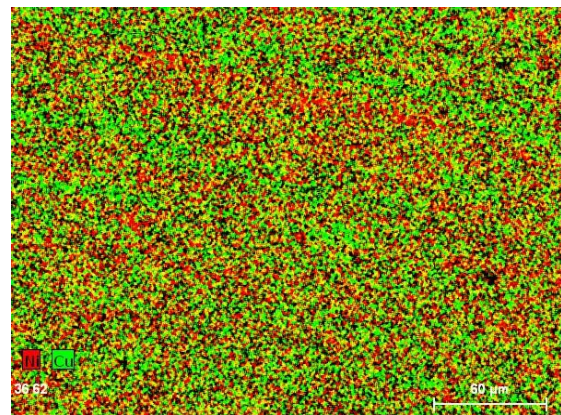
Scanning Electron Microscopy (SEM) micrographs of a 70Cu-30Ni polished sample are given in Figure 2-3. These images show a homogeneous distribution of Cu and Ni along the surface and hence a homogeneous surface chemical composition of the alloy.

**Table 2-2:** 70Cu-30Ni samples geometry, as a function of performed tests.

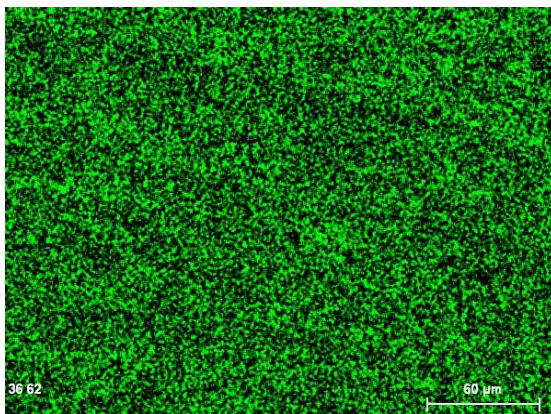
Tests	Seawater expositions	Electrochemical tests			Surface analyses		
		Field experiments	Static conditions	RRE	SEM	XPS	ToF-SIMS
<b>Samples geometry</b>	6cm-long tubes	4cm- and 6cm-long tubes	1.2 cm diameter disks (flattened)	1cm-long tubes	¼ of a tube (1cm-long)	1.2 cm diameter disks (flattened)	



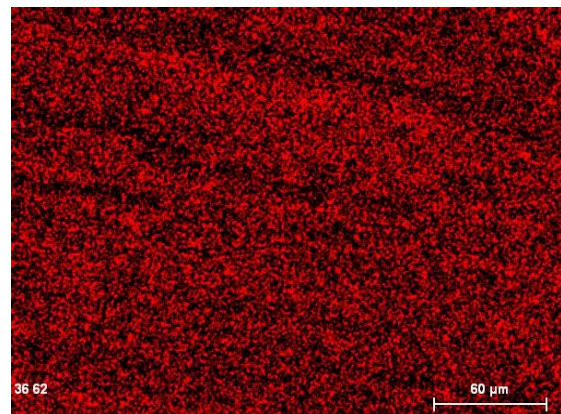
(a)



(b)



(c)



(d)

**Figure 2-3:** SEM micrographs of a 70Cu-30Ni polished sample: (a) surface overview (secondary electrons; scale: 2µm), (b) Cu and Ni distribution (scale: 60 µm), (c) Cu distribution (scale: 60 µm) and (d) Ni distribution (scale: 60 µm).

### Aluminum Brass

The Al brass alloy (76% Cu, 22% Zn and 2% Al) was collected from a power plant in the form of tubes (condenser tubes) with 2.54 cm external and 2.26 cm internal diameter. From these tubes, different types of electrodes were built (Fig. 2.2(c)), depending on the tests (surface analysis, electrochemical measurements...).

**Table 2-3:** Al brass samples geometry as a function of performed tests.

Tests	Seawater expositions	Electrochemical measurements		Surface analyses		
		Static conditions	RRE	SEM	XPS	ToF-SIMS
<b>Samples configuration</b>	6cm-long tubes	1.2 cm diameter disks (flattened)	1cm-long tubes	$\frac{1}{4}$ of a tube (1cm-long)	1.2 cm diameter disks (flattened)	

SEM analysis performed with an Al brass polished sample shows a homogeneous distribution of Cu, Zn and Al along the surface (Fig. 2-4).

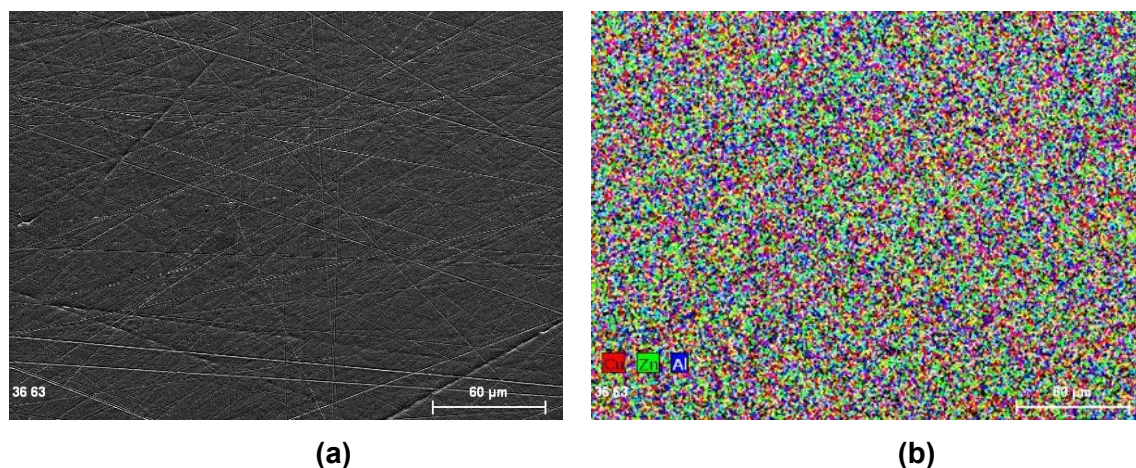


**Figure 2-4:** SEM micrographs of an Al brass polished sample: (a) surface overview (secondary electrons; scale: 60μm), (b) Cu, Zn and Al distribution (scale: 60 μm).

#### 2.1.1.1 FIELD EXPERIMENTS - ELECTRODES AND SURFACE PREPARATION

For the corrosion rate estimation, a probe with 5 tubular electrodes (3 x 6cm-long 70Cu-30Ni tubes + 2 x 4cm-long 70Cu-30Ni tubes), with an electrical connection by means of Cu wires soldered to the rear side of the samples, as shown in Figure 2.5. Before exposition to seawater, each specimen was named by letter and one number, using an

electric writing pen. The five electrodes were placed inside a plastic tube, leaving a distance of about 2 cm between each and, in order to insure tightness, stainless steel “ties” were used.

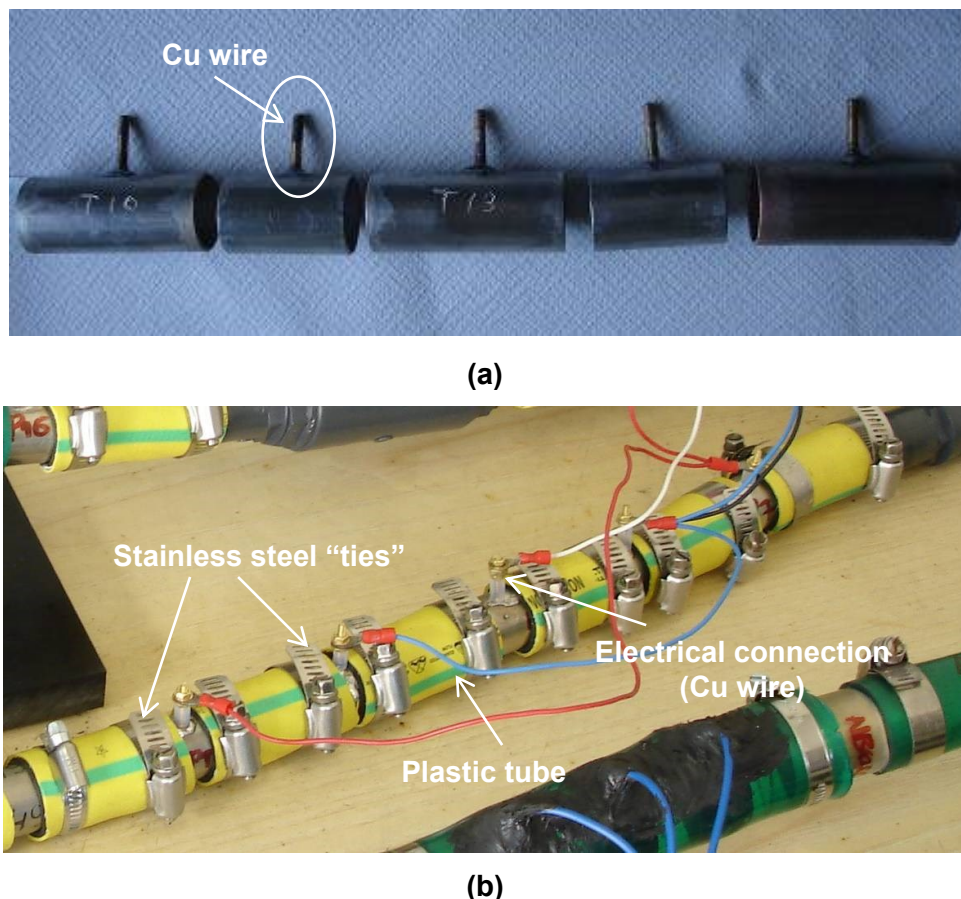


**Figure 2-5:** Five tubular electrodes used for the corrosion rate determination: (a) outside and (b) inside a plastic tube.

All samples and electrodes used in field experiments were not polished only degreased (5 min in acetone).

#### 2.1.1.2 LABORATORY EXPERIMENTS - ELECTRODES AND SURFACE PREPARATION

##### Experiments in static conditions:

Disks were cut from real condenser tubes (70Cu-30Ni and Al brass) and then flattened at Chimie ParisTech. The geometrical surface area exposed to the solution was  $0.28 \text{ cm}^2$ , and the tightness between the disk and the sample holder was ensured by a Viton® O-ring (Figure 2-6).

Before electrochemical measurements, samples were mechanically polished with SiC papers down to grade 1200, then degreased in an ultrasonic bath three times in acetone for 10 min, once in ethanol for 10 min, and once in ultra-pure water for 10 min, dried under an argon flow, and finally exposed to UV for 20 min.

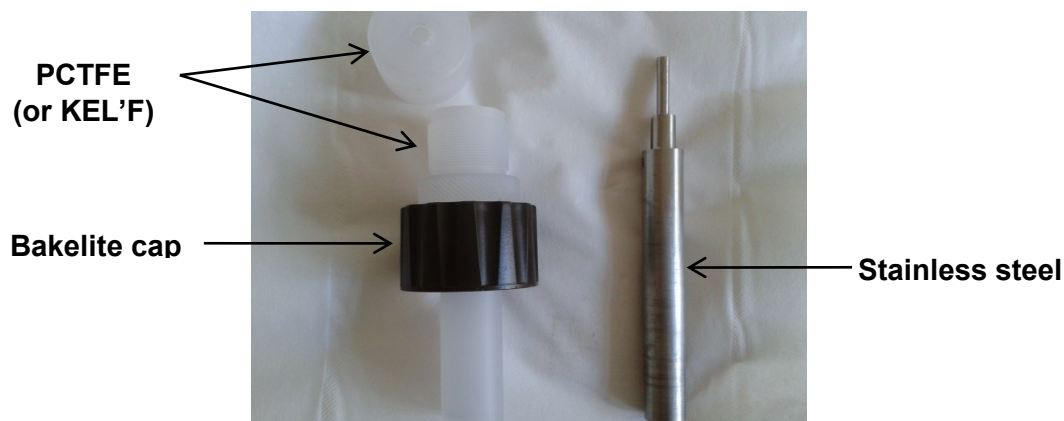


**Figure 2-6:** Sample holder used for electrochemical tests in static conditions.

#### Experiments with a Rotating Ring Electrode (RRE)

For electrochemical measurements in well-controlled hydrodynamic conditions, rotating electrodes were used. In order to work with the industrial alloys and not to buy commercial rods, rotating ring electrodes (RRE) and not rotating disk electrodes (RDE) were designed from real condenser tubes. Such RRE could be mounted on the rotating system available at LISE.

In order to protect the sidewall of the electrodes and to avoid corrosion, cataphoretic paint was deposited on the alloy surface. Cataphoresis is a process of painting by immersion, which is based on the movement of charged particles in an electric field towards an oppositely charged pole (metallic surface to be painted). Before applying the process, the electrode surface (1cm-long 70Cu-30Ni and Al brass tubes) was degreased with acetone. After deposition, the paint was heated at 140°C for 1h, to achieve polymerization. Once cooled down, the samples were mounted on an electrical copper connector and embedded in a non-conducting epoxy resin. Thus, the working electrode is the tube section exposed to the solution and its geometrical surface is 0.97cm<sup>2</sup> (Figure 2-7).

Samples were mechanically polished with SiC papers down to grade 1200, then degreased in an ultrasonic bath three times in acetone for 10 min, once in ethanol for 10 min, and once in ultra-pure water for 10 min, and finally dried under an argon flow.

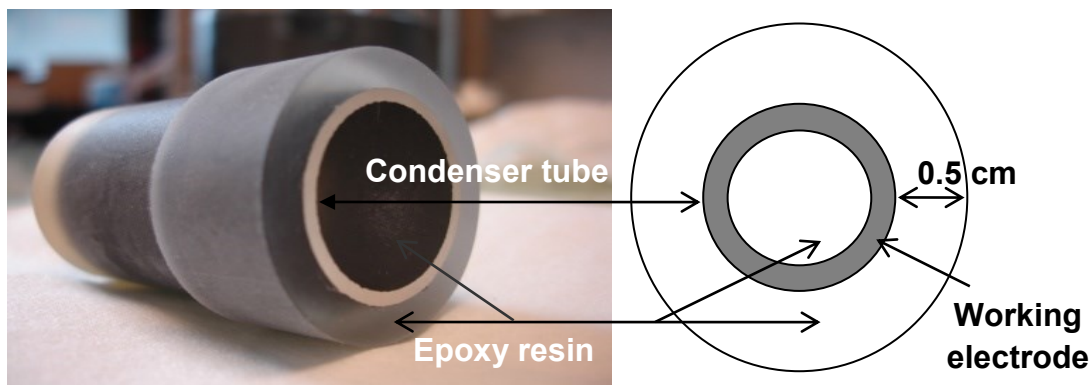


**Figure 2-7:** Rotating Ring Electrode (RRE) for the measurements in well-controlled hydrodynamic conditions.

### Surface analysis

Before surface analysis, without or with previous electrochemical treatment, samples were mechanically polished first with SiC papers down to grade 1200, then with 6  $\mu\text{m}$ , 3  $\mu\text{m}$ , and 1  $\mu\text{m}$  diamond pastes. Their subsequent treatment was the same as before electrochemical measurements.

After electrochemical treatment the samples were gently dipped in ultra-pure water three times in order to remove salts and loosely bound organic matter, and then dried with argon.

## **2.1.2 ELECTROLYTES**

All electrolytes were used in aerated conditions.

### **2.1.2.1 FIELD EXPERIMENTS**

- **NATURAL SEAWATER (NSW)**

Field experiments were performed in industrial sites, thermoelectric power plants, located in Italy. A bypass in the condenser allowed to study two different solutions: the inlet seawater (natural seawater), before any chlorination treatment or other kind of treatment and the outlet water from the condenser (treated natural seawater).

Seawater comes from the Tyrrhenian Sea and presents a pH of 8.2, maximum temperature in the plant from 32 to 39  $^{\circ}\text{C}$  and a dissolved oxygen concentration from 4 to 8 ppm. Regular analyses of seawater were not performed, with the exception of pH and conductivity, so that traces of nitrates or ammonia cannot be excluded. However, previous

analysis (as reported by plant operators) indicated nitrates and ammonia concentrations always lower than 0.1 ppm.

- **TREATED NATURAL SEAWATER (TNSW)**

An anti-fouling treatment is carried out in the cooling circuit by use of chlorine intermittent dosages: a commercial product based on sodium hypochlorite is dosed in order to achieve a total residual oxidant concentration of 0.4-0.8 mg/L in the water exiting the condenser. The dosing occurs every 6 hours, each one lasting 0.5-1 hour, depending on the season.

### **2.1.2.2 LABORATORY EXPERIMENTS**

- **FILTERED NATURAL SEAWATER (FNSW)**

Three different solutions were used in this work. Seawater was collected in the power plant previously mentioned, filtered at 1  $\mu\text{m}$  and kept in the fridge until use. This filtered water contains no more bacteria, but still biomolecules naturally present in seawater. For experiments presented in Chapter 6, seawater pH was adjusted by adding HCl at 0.1M.

- **ARTIFICIAL SEAWATER (ASW)**

Artificial seawater was used for laboratory experiments (ASW; composition (g/L): NaCl (24.615), KCl (0.783),  $\text{Na}_2\text{SO}_4$  (4.105),  $\text{MgCl}_2 (\text{H}_2\text{O})_6$  (11.060),  $\text{CaCl}_2$  (1.160),  $\text{NaHCO}_3$  (0.201); pH = 8.0; ionic strength = 0.7155 M).

- **ARTIFICIAL SEAWATER + BSA (ASW+BSA)**

In order to study the influence of biomolecules naturally present in seawater on the electrochemical behavior and the surface chemical composition of copper alloys, bovine serum albumin (BSA), which is a model protein often used to study protein-surface interactions, was added to ASW with a concentration of 20  $\text{mg}\cdot\text{L}^{-1}$  (about 99% purity (Fraction V); Sigma-Aldrich).

## **2.2 EXPERIMENTAL METHODS**

In this sub chapter, the general electrochemical approach that was used for this thesis is presented. All the experiments in laboratory were carried out on duplicate. Laboratory and field experiments were carried out at room temperature.

### **2.2.1 FIELD EXPERIMENTS**

#### **2.2.1.1 ON-LINE MEASUREMENTS**

- ELECTROCHEMICAL CELL**

Potentiostatic electrochemical techniques apply an input potential (DC or AC) and measure the output current or simply do not perturb the system and measure the natural potential also called open circuit potential (OCP) or corrosion potential ( $E_{corr}$ ). For this purpose, an electrochemical cell is needed and can consist of two, three or four electrodes immersed in an electrolytic solution. Electrodes are classified into three categories, depending on their function: working electrode, reference electrode, and auxiliary or counter electrode.

The working electrode (WE) is the sample under study. The reference electrode (RE) provides a constant potential and allows to measure or to apply the potential of the working electrode. Finally, the auxiliary or counter electrode (CE) allows the electrical current to flow through the cell; this electrode usually consists of a large surface area material, often made of platinum, corresponding to very low impedance. The simplest electrochemical cells consist of two electrodes, a working electrode and a counter electrode.

In Figure 2-8, a three-electrode electrochemical cell is shown, consisting of an electrolyte (ionic conductor), a working electrode, a counter electrode and a reference electrode. In some electrochemical cells, mass transport needs to be controlled; for that purpose, rotating working electrodes (disks, rings...) can be used, the rotation speed of which is carefully monitored [121].

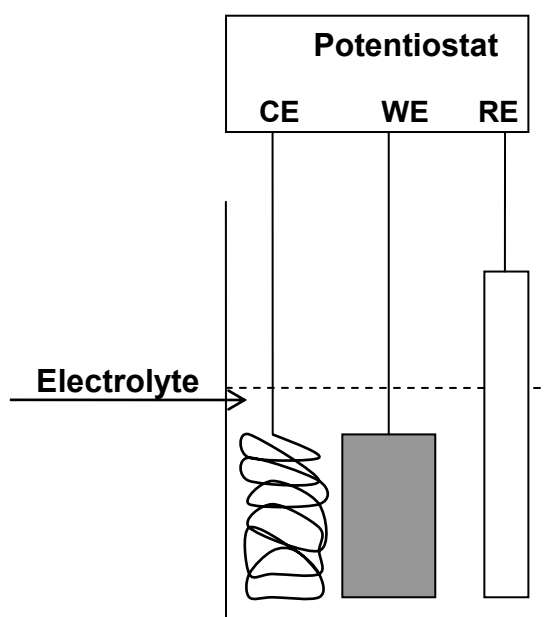


**Figure 2-8:** Three-electrode electrochemical cell.

In field experiments, the electrochemical cell is made of five new 70Cu-30Ni specimens cut from a condenser tube. It was designed to maintain a symmetric circulation of the polarization current and to keep the working electrodes in the same conditions (flow rate and geometry) as the real operating condenser tubes (Figure 2-9). It is in agreement with the ASTM G96-90(2001)-mode B and ASTM G102-89(1999) standards.

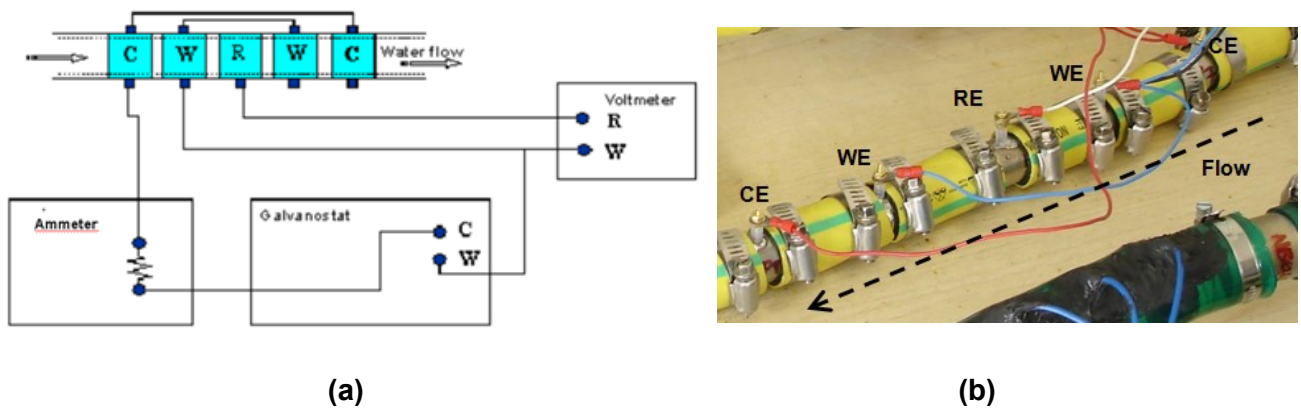


**Figure 2-9:** Electrochemical cell used for the corrosion rate determination by the Linear Polarization Resistance (LPR) method: (a) schema of the LPR method and (b) image of the electrochemical cell inserted in a test line.

- **CORROSION POTENTIAL ( $E_{CORR}$ ) VS IMMERSION TIME**

The open circuit potential or corrosion potential ( $E_{corr}$ ) is the potential difference between the material under study (WE) and a reference electrode (RE) at zero net current. Its value depends on different factors: the nature of the working electrode, the chemical composition of the electrolyte, the temperature and the hydrodynamic conditions. The corrosion potential of 70Cu-30Ni copper electrodes in natural seawater was measured, as a function of immersion time, against a “home made” Zn reference electrode, as reported in figure 2-10. Usually it is not advisable to use Zn as a reference electrode because it is a very active metal and it does not reach equilibrium. Exception can be made when used in clean and oxygenated seawater, for which the accuracy is sufficient.

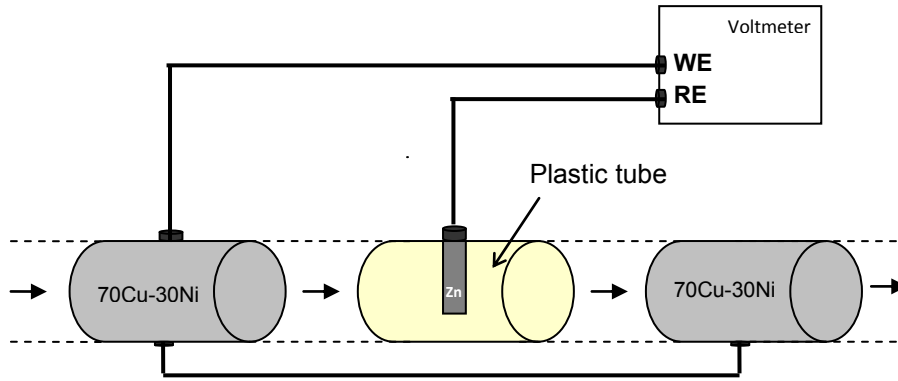


**Figure 2-10:** Electrodes configuration for the measurement of the corrosion potential vs a Zn electrode during field experiments (on-line measurements).

- **LINEAR POLARIZATION RESISTANCE (LPR)**

A polarization resistance,  $R_p$ , can be used to determine the resistance of a metal or an alloy against corrosion.

Polarization of an electrode causes current to flow due to electrochemical reactions induced at the electrode surface. The polarization resistance is defined by the following equation:

$$R_p = \left( \frac{\Delta E}{\Delta i} \right)_{E_{corr}} \quad (2.1)$$

where,  $\Delta E$  is the variation of the applied potential around the corrosion potential and  $\Delta i$  is the resulting current. The polarization resistance is defined as the inverse of the slope of the current-potential curve at open circuit or corrosion potential, and can be related to the corrosion current,  $i_{corr}$ , by the Stern-Geary relationship [122]:

$$R_p = \frac{B}{i_{corr}} \quad (2.2)$$

where for a particular system, the proportionality constant,  $B$ , can be determined either empirically (from weight loss measurements) or, as shown by Stern and Geary, from the anodic and the cathodic Tafel constants,  $b_a$  and  $b_c$ , respectively (in V/decade), as follows:

$$B = \frac{b_a b_c}{2.303(b_a + b_c)} \quad (2.3)$$

The Tafel constants can be evaluated experimentally from the polarization curves. Thus, when the anodic and the cathodic reactions are in one step and tafelian *i.e.* totally limited by charge transfer (no limitation by mass transport), the corresponding polarization curves plotted in semi-logarithmic coordinates ( $\log |i|$  vs  $E$ ) are straight lines with  $1/b_a$  and  $-1/b_c$  slopes, respectively (Tafel slopes).

The polarization resistance values were computed by analyzing polarization curves plotted from -10 to +10mV with respect to the corrosion potential, in linear coordinates. Only the linear region of the curves was taken into account. From the values of  $R_p$ , the corrosion current density was estimated by application of equation (2.2).

The software calculates the corrosion rate,  $V_{corr}$ , expressed in  $\mu\text{m/y}$  using the correlation factor  $BK = 250$ , determined experimentally by comparison between the integral of the inverse of polarization resistance ( $R_p$ ) vs time and the weight loss of the same electrode during many trials.

$$V_{corr} = \frac{250}{R_p A} [\mu\text{m} / \text{y}] \quad (2.4)$$

where  $R_p$  is expressed in  $\text{k}\Omega$  and the surface area ( $A$ ) in  $\text{cm}^2$ .

The variation of  $B$ , using different samples with increasing exposition times to seawater, is less than 20% (result taken from experiments of several previous campaigns), which is acceptable. It should be emphasized that the estimation of corrosion rates is based on the assumption that the total exposed surface of the sample corrodes uniformly.

### 2.2.1.2 OFF-LINE MEASUREMENTS

- **WEIGHT LOSS MEASUREMENTS**

The simplest way of measuring the corrosion rate of a metallic material is to expose the sample to the test medium (sea water) and to measure the loss of weight of the material as a function of time. Weight loss measurements were performed following the American Society for Testing and Materials (ASTM) standards [ASTM Standard Practice G1-X2-72]. At the end of the experiment, coupons were cleaned by immersion in a concentrated  $\text{H}_2\text{SO}_4$  solution at  $40^\circ\text{C}$ . Corrosion rates were calculated from weight losses using the following equation, deduced from Faraday's law:

$$C_r = \frac{\Delta m \times 3650}{\rho \times A \times t} [\mu\text{m} / \text{y}] \quad (2.5)$$

with:

$\Delta m$ : weight loss (g) = difference between “initial weight” and “weight after cleaning”;

$\rho$ : density of the 70Cu-30Ni alloy = 8.94 g.cm<sup>-3</sup>;

A: sample surface area exposed to solution (cm<sup>2</sup>);

t: exposure time (days).

## • GENETIC STUDIES

In order to identify and better characterize the bacteria community present in the metal tubes, samples were collected after a long period (one year) and short period (2 days) of exposure to treated natural seawater (TNSW) and natural seawater (NSW). Molecular techniques including DNA extraction, polymerase chain reaction (PCR) of 16S rRNA gene, denaturing gradient gel electrophoresis (DGGE) and sequencing were used (Figure 2-11).

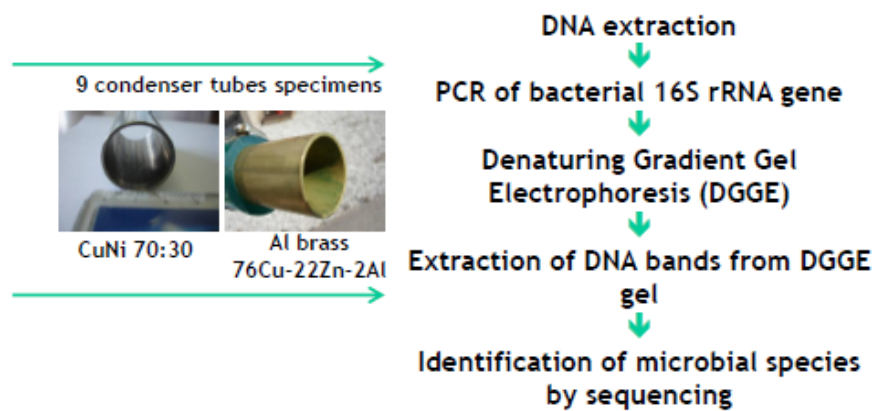


**Figure 2-11:** Microorganisms identification: molecular biology steps.

The vast majority of microbial communities in the nature has not been cultured in laboratory. Therefore, the primary source of information for these uncultured but viable organisms is their biomolecules such as nucleic acids, lipids, and proteins. Microbial community analysis is a quantitative molecular technique to assess microbial community structure and diversity. A combination of methods is used, in order to genetically characterize and compare microbial communities. It is based on the 16S rRNA gene in microbial DNA (deoxyribonucleic acid), whose sequence is used as phylogenetic and taxonomic marker.

Compared with standard culturing approach, this technique is quicker (few days vs 1-2 weeks) and all microorganisms present in the sample are observed (with culturing, only 1% or less of the present microbes can be grown and analyzed) [123].

#### DNA extraction

A combination of physical and chemical methods is used in the isolation and purification of DNA

There are several methods for purifying DNA and they must be selected depending on the nature of the DNA sample and the downstream applications. There are two to three basic steps in DNA extraction. The first step is to lyse or break open the cell. This can be achieved by lysing the cells and treating these cells with a salt solution and detergents. These solutions break down and emulsify the lipids and proteins that find in the cell membrane. Finally, ethanol is added. The alcohol causes DNA to precipitate, or settle out of the solution, leaving behind all the cellular components that are not soluble in alcohol.

Biofilm from 70Cu-30Ni and Al brass was collected by transferring the samples to sterile Petri dishes and rinsed with 0.9% NaCl. The rinsed-off solution was collected in sterile 1.5ml eppendorf tubes and centrifuged for 5 minutes at 13,000×g (Heraeus Fresco 21, Thermo Scientific, UK). Supernatant was discarded and total DNA was isolated with the PowerBiofilm™ DNA isolation kit (Mo BIO Laboratories, UK) according to the manufacturer's instructions. The kit uses a bead beating technique and incubation at 65°C for 5 minutes in aiding to breakdown biofilm extracellular polymeric substance matrix. The concentration of extracted and purified DNA was determined using a NanoDrop ND-1000 spectrophotometer (Thermo Scientific, USA). PCR was subsequently performed on the samples.

#### Polymerase Chain Reaction (PCR) for DGGE

In polymerase chain reaction (PCR) method, the total DNA, extracted from a sample, is used as a template for the characterization of microorganisms. This is a technique to amplify a fragment of DNA multiple times, generating thousands to millions of copies of a particular DNA fragment. The PCR product generated reflects a mixture of microbial gene signatures from all organisms present in the sample. PCR amplification of conserved genes such as 16S rRNA from an environmental sample has been used extensively in microbial ecology primarily because these genes (1) are ubiquitous, i.e., present in all prokaryotes, (2) are structurally and functionally conserved, and (3) contain variable and highly conserved regions [124].

The bacterial 16S rRNA gene (550bp) was amplified using universal bacterial primers: 341F+GC (5'- CGC CCG CCG CGC GCG GGC GGG GCG GGG GCA CGG GGG GCC TAC GGG AGG CAG CAG-3') and 907R (5'- CCG TCA ATT CMT TTG AGT TT-3) [12] purchased from Life Technologies, UK). PCR reactions were performed in 50 µl mixtures, containing 25 µl of 10x GoTaq® Green Master Mix (Promega, UK) and 1 µl of each primer (10 pmol/µl). Reactions for bacterial 16SrRNA 550bp gene to be amplified were initially denatured at 94°C for 4 minutes; followed by a touchdown PCR: 20 cycles of 94°C for 1 minute, 63-54°C for 1 minute and 72°C for 1 minute followed by 15 cycles of 94°C for 1 minute, 53°C for 1 minute and 72°C for 1 minute and finally elongated for 10 minutes at 72°C.

#### Agarose gel electrophoresis

In this method, DNA is forced to migrate through a highly cross-linked agarose matrix in response to an electric current. The phosphates on the DNA backbone are negatively charged, and the molecule will therefore migrate to the positive pole.

Agarose gel electrophoresis was performed after PCR to determine the size of the PCR product by running beside a DNA marker (100bp DNA ladder, Fermentas). PCR products were run on 0.9% of agarose gel on 150V for 30 minutes to 1 hour to enable proper separation. Agarose gel was stained with SYBR® Safe DNA gel stain (Invitrogen Corp., USA) and viewed under UV transillumination (Alpha Innotech Corporation, USA) and Digital Camera (Olympus C-4000 Zoom) to ensure that the correct size fragment was amplified.

#### Denaturing Gradient Gel Electrophoresis (DGGE)

DGGE is a genetic fingerprint that generates a profile of microbial communities based on direct analysis of PCR products amplified from DNA [125]. The PCR products are electrophoresed on a polyacrylamide gel containing a linear gradient of DNA denaturant such as a mixture of urea and formamide [126].

To separate the PCR-amplified products for bacterial 16S rRNA genes (550bp), 40µl of PCR-amplified products was used in an Ingeny Gel Apparatus (Ingeny, Netherlands), at a constant voltage of 90 V for 18 hours and a constant temperature of 60°C, after an initial 15 minutes at 200V. The standard gradient was formed of 6% polyacrylamide in 0.5xTAE (Trisacetic-EDTA) buffer with a gradient between 30% and 80% denaturant (7M urea and 40% formamide defined as 100% denaturant). After electrophoresis, the gel was stained with 12µl SYBR® Safe DNA gel stain (Invitrogen Corp.), allowed to stand in dark for 15minutes, viewed under UV transilluminator, and a permanent image captured by the Alpha Innotech Gel Documentation System (Alpha Innotech Corporation, USA).

### Extraction of DNA bands from DGGE gel

All visible bands were cut from the gel using a sterile scalpel blade and transferred into sterile 1.5 ml microcentrifuge tubes containing 30  $\mu$ l of ultra pure water to extract the DNA. Samples were then centrifuged at 13 000 x g for 1 minute (Heraeus Fresco 21, Thermo Scientific, UK) and 5  $\mu$ l aliquots of supernatants were used for PCR re-amplification as described above. PCR products were purified using the NucleoSpin® Extract II PCR purification kit (Macherey-Nagel, UK) and sent to the GATC Biotech UK DNA sequencing service.

## **2.2.2 LABORATORY EXPERIMENTS**

### **2.2.2.1 ELECTROCHEMICAL MEASUREMENTS**

- ELECTROCHEMICAL CELLS**

#### Experiments carried out in static conditions in ASW (without or with BSA) and FNSW

The electrochemical measurements were performed with a three-electrode cell (Figure 2-12(a) and (b)), designed and manufactured at Chimie ParisTech, with a volume of solution of about 0.1 L for static conditions and about 1 L for experiments under flow and stirring. The working electrode was the 70Cu-30Ni alloy (disk samples), the counter-electrode was a platinum wire, and the reference electrode was a saturated calomel electrode (SCE; 0.245 V vs SHE). Electrochemical measurements were performed with an EC-Lab SP-200 system from Bio-Logic.

In FNSW, the electrochemical experiments were carried out in a conventional three-electrode cell (the same as Figure 2-12), designed and manufactured at Chimie ParisTech, with a volume of solution of about 0.1 L. Disk electrodes cut from 70Cu-30Ni and Al brass condenser tubes were used as working electrodes. A saturated sulphate electrode (SSE; sat.  $\text{K}_2\text{SO}_4$  Hg/Hg<sub>2</sub>SO<sub>4</sub>; 0.645 V vs SHE) was used as the reference electrode and a platinum wire as the counter electrode. Electrochemical measurements were performed with an AUTOLAB PGSTAT30/FRA2 system from ECO CHEMIE.

#### Experiments carried out under flow and stirring in ASW and FNSW

The electrochemical experiments carried out under flow and stirring conditions were performed under the same conditions as the previous described, being the main difference the volume of solution (Figure 2-12 (c)). For that, a volume 10 times higher than in static conditions was used inside the electrochemical cell (1 L instead of 100 mL); the solution was

continuously renewed using a peristaltic pump, with a flow rate of  $\sim 0.27 \text{ mL.s}^{-1}$ , and the electrolyte inside the cell was stirred using a magnetic stirrer.

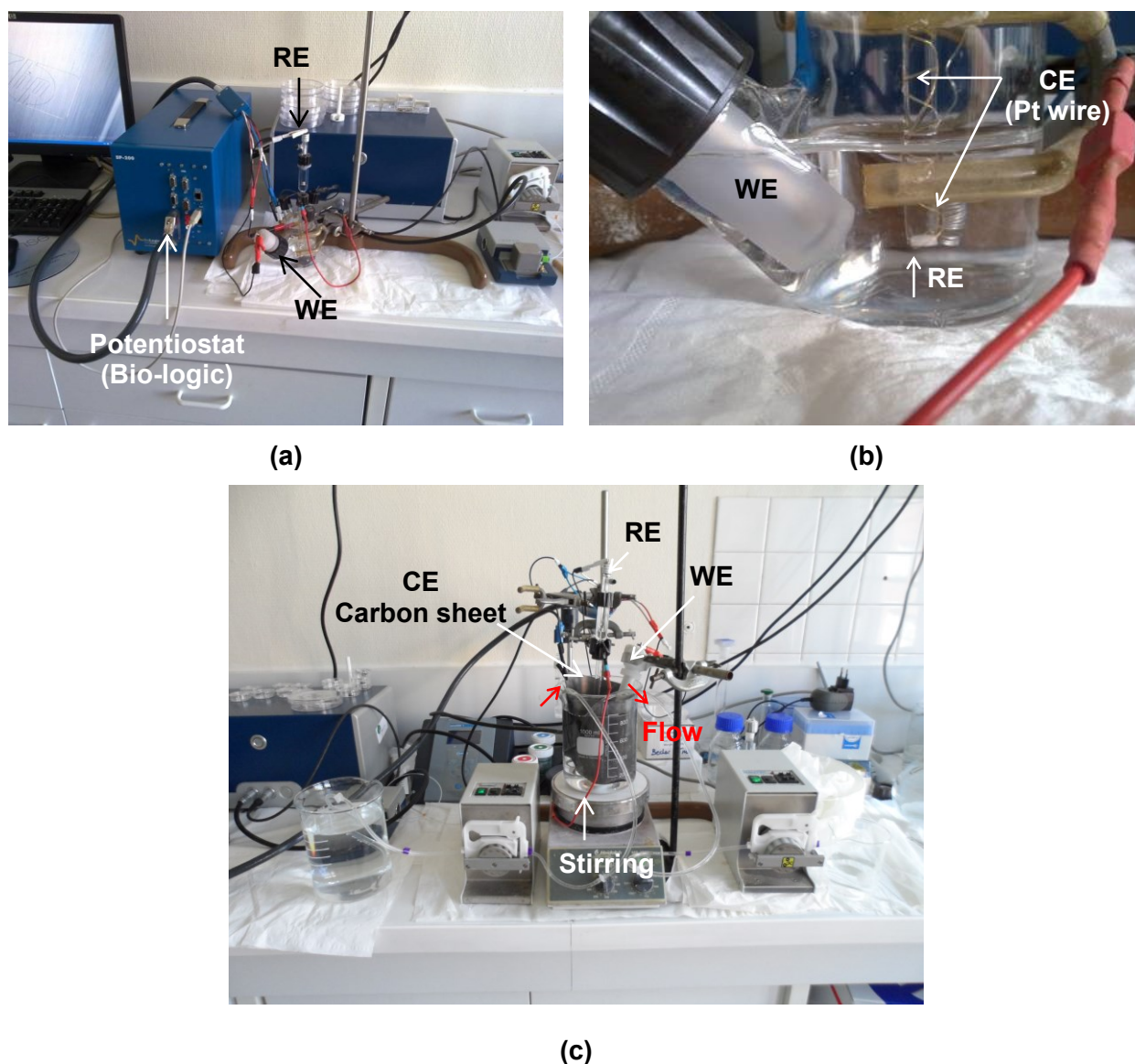


**Figure 2-12:** Electrochemical cells used for experiments carried with ASW (without or with BSA) and FNSW in: (a), (b) static conditions and (c) under flow and stirring.

#### Experiments carried out with a RRE in ASW and FNSW

The electrochemical cell is very similar to that used in static conditions. The volume of the solution was about 0.800 L. The working electrode was the 70Cu-30Ni alloy or Al brass RRE, the counter-electrode was a carbon sheet, with a large surface area, and the reference electrode was a SSE. Electrochemical measurements were performed with an SOTELEM

potentiostat (for steady-state polarization curves) or with an AUTOLAB PGSTAT30/FRA2 system from ECO CHEMIE (EIS diagrams).

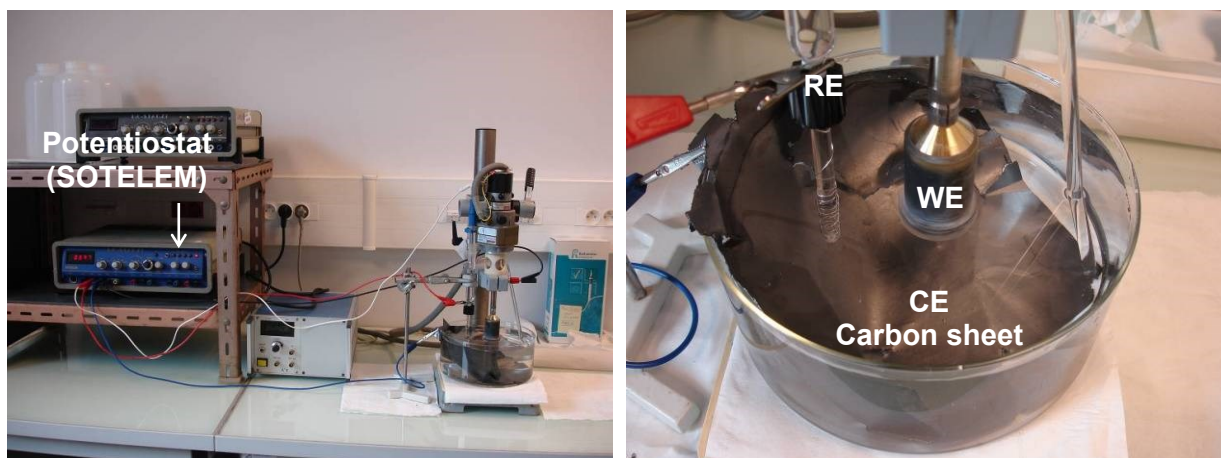


**Figure 2-13:** Electrochemical cell used for experiments carried out with a RRE in ASW and FNSW.

- **CORROSION POTENTIAL ( $E_{CORR}$ ) VS IMMERSION TIME**

The corrosion potential ( $E_{CORR}$ ) was measured during the first hour of immersion, using a SCE or a SSE as reference electrode depending on the electrochemical cell. This technique does not provide mechanistic information and it is recommended to use it with other electrochemical techniques such as polarization curves and electrochemical impedance spectroscopy.

- **POLARIZATION CURVES**

A potentiodynamic scan is a transient electrochemical method that consists of imposing between the working electrode and the reference electrode a potential ramp (discrete and successive values or linear ramp), and recording the resulting current. Thereby, a current-potential curve, also called polarization curve, can be plotted, that gives information about involved electrochemical processes. The scan rate is a key parameter for these techniques. Thus, if the scan rate is too high, important kinetic data may not be captured, but if the scan rate is too low, the experiment can become very long. In this work, a scan rate of  $0.5 \text{ mV.s}^{-1}$  was chosen to plot pseudo steady-state polarization curves.

These curves were compared to steady-state ones which were plotted point by point. In that case, each applied potential was kept constant during about 10 minutes and the corresponding current density was recorded after that stabilization time.

Cathodic and anodic polarization curves were plotted separately from the free corrosion potential,  $E_{corr}$ , by means of a potentiostat.

If the anodic and cathodic polarization curves, in semi-logarithmic coordinates, exhibit linear domains close to  $E_{corr}$ , the corrosion current density can be extracted from polarization curves in case of Tafel behavior (one step reactions totally limited by charge transfer). The intersection of the two extrapolated lines gives  $i_{corr}$  from which the corrosion rate can be determined. Table 2-4 shows values found in the literature for the Tafel constants for copper in aerated natural and artificial seawaters.

**Table 2-4:** Tafel constants for pure copper in aerated chloride media.

Electrolyte	Hydrodynamics conditions	$b_a$ (V.decade <sup>-1</sup> )	$b_c$ (V.decade <sup>-1</sup> )	Reference
NSW* and ASW**	RCE <sup>▲</sup>	0.062	-0.100	[127]
NSW	Static	0.067	-0.046	[104]
NSW ASW	RDE <sup>▼</sup>	0.063±0.001 0.066±0.002	-0.134	[45]

(\*NSW = natural seawater; \*\*ASW = artificial seawater; <sup>▲</sup>RCE = Rotating cylinder electrode; <sup>▼</sup>RDE = Rotating disk electrode)

#### • LEVICH AND KOUTECKY-LEVICH METHODS

The aim of a kinetic study is to determine the electrochemical reaction mechanisms and to quantify its characteristic parameters: charge transfer rate constants and coefficients, and mass transport parameters (diffusion coefficients). The Koutecky-Levich method is frequently used to determine the mass transport parameters [128].

Hydrodynamic devices use convection to enhance the rate of mass transport to the electrode. Forced convection usually results in increased currents and removes the small random contribution from natural convection. Figure 2-14 shows the two kinds of flow behavior through a pipe: the well-defined laminar conditions (Figure 2-14(a)) and turbulent conditions (Figure 2-14(b); flow is essentially random and unpredictable).

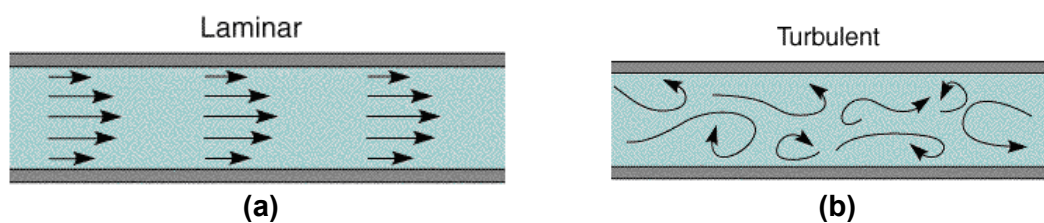


**Figure 2-14:** Flow behavior through a pipe: a) laminar and b) turbulent behavior.

The transition between laminar and turbulent flow can be predicted using the concept of the Reynolds number,  $Re$  [129]. When laminar flow prevails, the fluid dynamics within the cell can be predicted by the Navier-Stokes equations [130], and then the concentration of the reagents and the relationship between the current and the transport rate within the cell can be calculated. If  $Re > 10^5$ , the flow is considered turbulent; so, in order to work in laminar conditions,  $Re$  must be lower than  $10^5$ .

To precise the kind of flow, in the case of a RRE, the Reynolds number is defined as [131]:

$$Re = \frac{\Omega(R_0 + \Delta R)^2}{\nu} \quad (2.6)$$

where  $\Omega$  is the electrode rotation speed in  $\text{rad.s}^{-1}$ ,  $R_0$  is the ring inner radius in cm,  $\Delta R$  is the ring thickness in  $\text{cm}^2$  and  $\nu$  the kinematic viscosity of the fluid in  $\text{cm}^2.\text{s}^{-1}$  (for seawater is equal to  $10^{-2} \text{ cm}^2.\text{s}^{-1}$ , at  $20^\circ\text{C}$ ).

For 70Cu-30Ni and Al brass,  $(R_0 + \Delta R)^2$  is equal to 1.96 and 1.99 respectively and applying equation (2.6),  $\Omega$  is equal to 427 and 416  $\text{rad.s}^{-1}$ . Taking into account that  $1\text{tr.min}^{-1} = (2\pi)/60 \text{ rad.s}^{-1}$ , the rotation rate in rpm must be lower than 4081rpm for 70Cu-30Ni and 3977rpm for Al brass, in order to work in laminar conditions.

The rotating disk electrode (RDE) is the most commonly used electrode configuration in electrochemical studies since it yields a constant and homogeneous stirring near the disk and allows a perfect control of hydrodynamics.

A rotating disk electrode in laminar flow conveys a steady state stream of species from the bulk solution to the electrode surface (Fig. 2-15). While the bulk solution far away from the electrode surface remains well-stirred by the convection induced by the rotation, the portion of the solution near the electrode surface tends to rotate with the electrode. Thus, if the solution is viewed from the frame of reference of the rotating electrode surface, then the solution appears relatively static.

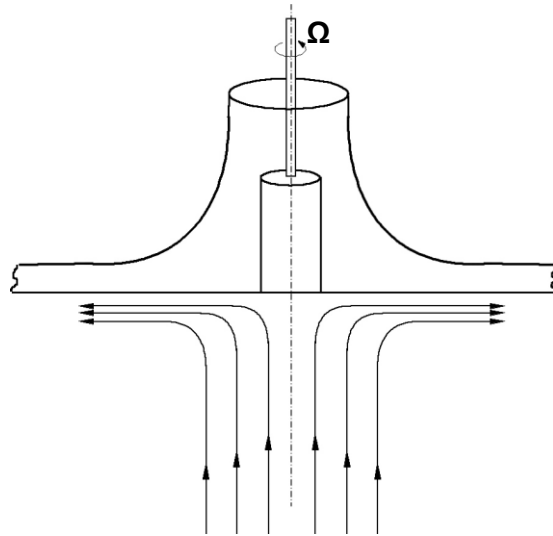


**Figure 2-15:** Flow movement induced by a rotating disk electrode.

The movement of an ion or a molecule to the electrode surface is dominated by convection in the bulk solution and diffusion across a very thin layer of solution immediately adjacent to the electrode known as the diffusion layer.

The first mathematical treatment of convective and diffusion towards a rotating disk electrode was given by Levich [132]. He showed that for a reaction totally limited by mass transport occurring on a RDE, the limiting current ( $I_L$ ) increases in absolute value with the square root of the rotation speed ( $\Omega$ ). The Levich method consists of plotting  $I_L$  as a function of  $\Omega^{1/2}$  (Levich plot). For a Rotating Ring Electrode (RRE), the oxidation limiting current of species R (anodic reaction) is given by:

$$I_L^a = n \times \frac{F\pi}{\Gamma\left(\frac{4}{3}\right)} \times (3a_0)^{1/3} \times [R]_{\infty} \times D_R^{2/3} \times \nu^{\frac{1}{3} + \frac{1}{1-n}} \times R_i^{\frac{4}{3} \times \frac{1}{3} \times \frac{1-n}{1+n}} \times \Delta R^{2/3} \times \Omega^{1/2} \quad (2.7)$$

and the reduction limiting current of species O (cathodic reaction) is given by:

$$I_L^c = -n \times \frac{F\pi}{\Gamma\left(\frac{4}{3}\right)} \times (3a_0)^{1/3} \times [O]_{\infty} \times D_O^{2/3} \times \nu^{\frac{1}{3} + \frac{1}{1-n}} \times R_i^{\frac{4}{3} \times \frac{1}{3} \times \frac{1-n}{1+n}} \times \Delta R^{2/3} \times \Omega^{1/2} \quad (2.8)$$

where  $n$  is the number of exchange electrons (4 in the case of the reduction of dissolved oxygen);  $F$  is the Faraday constant ( $96485 \text{ C} \cdot \text{mol}^{-1}$ );  $\Gamma\left(\frac{4}{3}\right)$  for a Newtonian fluid<sup>3</sup> is equal to

<sup>3</sup> Newtonian fluids are the simplest mathematical models of fluids that account for viscosity.

$\sim 0.893$ ;  $a_0$  for a Newtonian fluid is equal to 0.51021599;  $[R, O]_\infty$  the bulk concentration of species R or O;  $D_{R,O}$  the diffusion coefficient of species R or O;  $\nu$  the kinematic viscosity;  $R_i$  is the internal radius;  $R_i + \Delta R$  the external radius.

From Equations (2.7) and (2.8), the  $I_L^a$  or  $|I_L^c|$  vs  $\Omega^{1/2}$  plot result in a straight line with anodic or cathodic,  $s_{La}$  or  $s_{Lc}$  respectively, slop given by:

$$s_{La} = n \times \frac{F\pi}{\Gamma\left(\frac{4}{3}\right)} \times (3a_0)^{1/3} \times [R]_\infty \times D_R^{2/3} \times \nu^{-\frac{1}{3} \times \frac{1}{1-n}} \times R_i^{\frac{4}{3} \times \frac{1}{3} \times \frac{1-n}{1+n}} \times \Delta R^{2/3} \quad (2.9)$$

$$s_{Lc} = n \times \frac{F\pi}{\Gamma\left(\frac{4}{3}\right)} \times (3a_0)^{1/3} \times [O]_\infty \times D_O^{2/3} \times \nu^{-\frac{1}{3} \times \frac{1}{1-n}} \times R_i^{\frac{4}{3} \times \frac{1}{3} \times \frac{1-n}{1+n}} \times \Delta R^{2/3} \quad (2.10)$$

If the solution kinematic viscosity is known (usually, of the order of  $10^{-2} \text{ cm}^2 \cdot \text{s}^{-1}$  in aqueous solutions at room temperature), from the slopes of the  $|I_L^{a,c}|$  vs  $\Omega^{1/2}$  curves it is possible to determine the values of the diffusion coefficients  $D_{R,O}$ . More details will be given in Chapter 5.

In case of side oxidation or reduction reactions of the solvent or of the supporting electrolyte, the expression for the current of a reaction partially limited by mass transport (mixed kinetics) as a function of the rotation speed is given by the following general relationship [133]:

$$I = A + \frac{1}{B + C\Omega^{-1/2}} \quad (2.11)$$

with

A: non-diffusional current, independent of  $\Omega$  (protons reduction current, for example)

B: inverse of the electronic transfer current ( $I_t$  infinite  $\Omega$ )

$$B = 1/I_t = \lim_{\Omega \rightarrow \infty} 1/I \quad (2.12)$$

$C\Omega^{-1/2}$ : inverse of the diffusion-convection limiting current (infinitely fast electronic transfer)

C: inverse of the Levich coefficient ( $s_{La}^{-1}$  or  $s_{Lc}^{-1}$ )

In order to determine A, B and C at a given electrode potential, we must plot I as a function of  $\Omega^{1/2}$ , and the intercept gives the value of A (Figure 2-16).

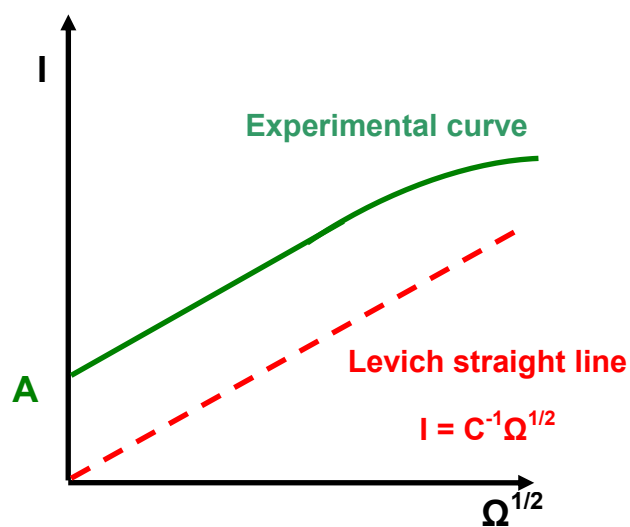


**Figure 2-16:** Levich plot ( $I = f(\Omega^{1/2})$ ).

Then, plotting  $(I-A)^{-1}$  as a function of the inverse of the square root of rotation speed ( $\Omega^{-1/2}$ ) yields a straight line with an intercept equal to B and a slope equal to C (Figure 2-17). From C it is possible to determine the value of the diffusion coefficient of the considered species.

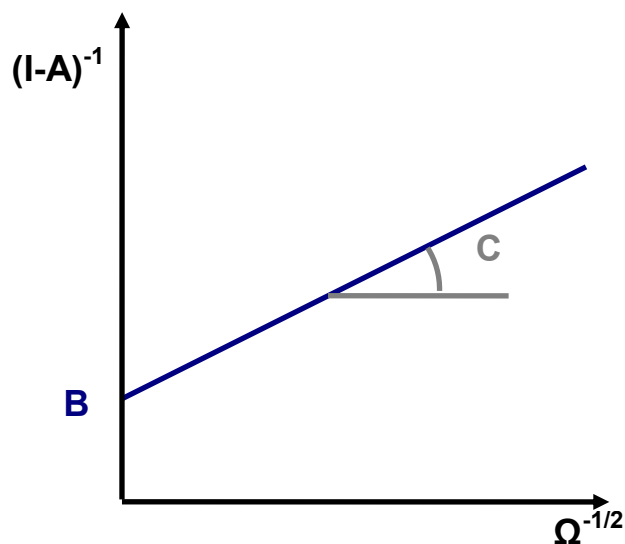


**Figure 2-17:** Koutecky-Levich plot ( $(I - A)^{-1} = f(\Omega^{-1/2})$ ).

- **ELECTROCHEMICAL IMPEDANCE SPECTROSCOPY (EIS)**

Electrochemical impedance spectroscopy (EIS) is a non-destructive technique, often used to understand the interfacial behavior of electrochemical systems, being so one of the most common techniques in corrosion studies.

Impedance definition: concept of complex impedance

Electrical resistance is the ability of a circuit element to resist the flow of electrical current. Ohm's law defines resistance in terms of the ratio between voltage,  $E$ , and current,  $I$ . The use of this relationship is limited to only one circuit element, the ideal resistor. An ideal resistor has several simplifying properties: it follows Ohm's law at all current and voltage levels, its value is independent of frequency, and AC current and voltage signals through a resistor are in phase with each other.

However, there are circuit elements that exhibit much more complex behavior, so that the simple concept of resistance must be replaced by impedance. Electrochemical impedance is usually determined by applying an AC (sinusoidal) potential or current to an electrochemical cell and then measuring the current or the potential, respectively, through the cell. The response to this perturbation potential/current signal is an AC current/potential signal that can be analyzed as a sum of sinusoidal functions (Fourier series).

Electrochemical impedance is usually measured using a small excitation signal, so that the cell response is pseudo-linear. For a linear system, the current response to a sinusoidal potential is a sinusoidal signal with the same frequency as the potential but shifted in phase (Figure 2-18).

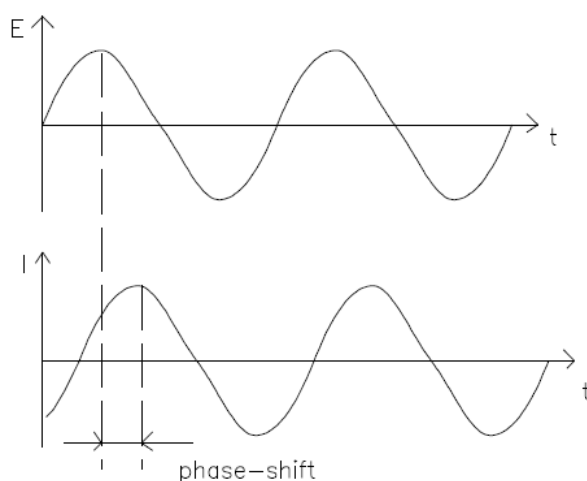


**Figure 2-18:** Sinusoidal current response of a linear system.

The excitation time signal,  $E_t$ , at a constant polarization potential, is given by:

$$E_t = E_0 \sin(\omega t) \quad (2.13)$$

Where  $E_0$  is the amplitude of the signal (independent of frequency) and  $\omega$  is the angular frequency. The relationship between the angular frequency  $\omega$  (in  $\text{rad.s}^{-1}$ ) and the frequency  $f$  (in Hz) is:

$$\omega = 2\pi f \quad (2.14)$$

For a linear system, the response signal,  $I_t$ , is given by:

$$I_t = I_0 \sin(\omega t + \varphi) \quad (2.15)$$

with  $I_0$  the amplitude (dependent on  $\omega$ ) and  $\varphi$  the phase-shift.

An expression analogous to Ohm's law allows calculating the impedance of the system which is a complex number defined at each frequency by:

$$Z(\omega) = \frac{E(\omega)}{I(\omega)} = |Z(\omega)|e^{j\varphi} = \frac{E_0}{I_0}(\cos \varphi + j \sin \varphi) \quad (2.16)$$

The impedance is therefore expressed in terms of a modulus,  $|Z|$ , and a phase shift,  $\varphi$ , or in terms of a real part,  $Z_r$ , and an imaginary part,  $Z_j$ .

$$|Z(\omega)| = Z_r(\omega) + jZ_j(\omega) \quad (2.17)$$

The combination of a phase-sensitive detector and a frequency response analyzer is the method usually used in EIS measurements today. In a three-electrode system, the potentiostat applies, at a constant DC potential, a sinusoidal potential of small amplitude. Then the current response is compared with original input signals in the analyzer. Through the response analyzer, the real and imaginary parts of the electrochemical impedance of the system under study are obtained. This method is appropriate for a frequency range between  $10^{-4}$  and  $10^6$  Hz.

If we plot the applied sinusoidal signal  $E_t$  on the X-axis of a graph and the sinusoidal response signal  $I_t$  on the Y-axis, the result is an oval (Figure 2-19). This oval is known as a "Lissajous figure". Analysis of Lissajous figures on oscilloscope screens was the accepted method of impedance measurement prior to the availability of modern EIS instrumentation.

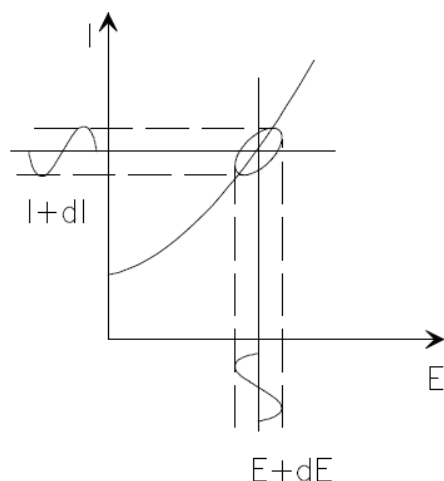


**Figure 2-19:** Origin of Lissajous Figure.

### Data representation

The expression for  $Z(\omega)$  is composed of a real and an imaginary part. If the real part is plotted on the X-axis and the opposite of the imaginary part is plotted on the Y-axis of a chart, we get a Nyquist Plot. The Nyquist plot shown in Figure 2-20(a) exhibits one semi-circle, characteristic of a single time constant. Electrochemical impedance plots often contain several semi-circles. It must be noticed that in this plot, the Y-axis is negative and each point is the impedance at one frequency.

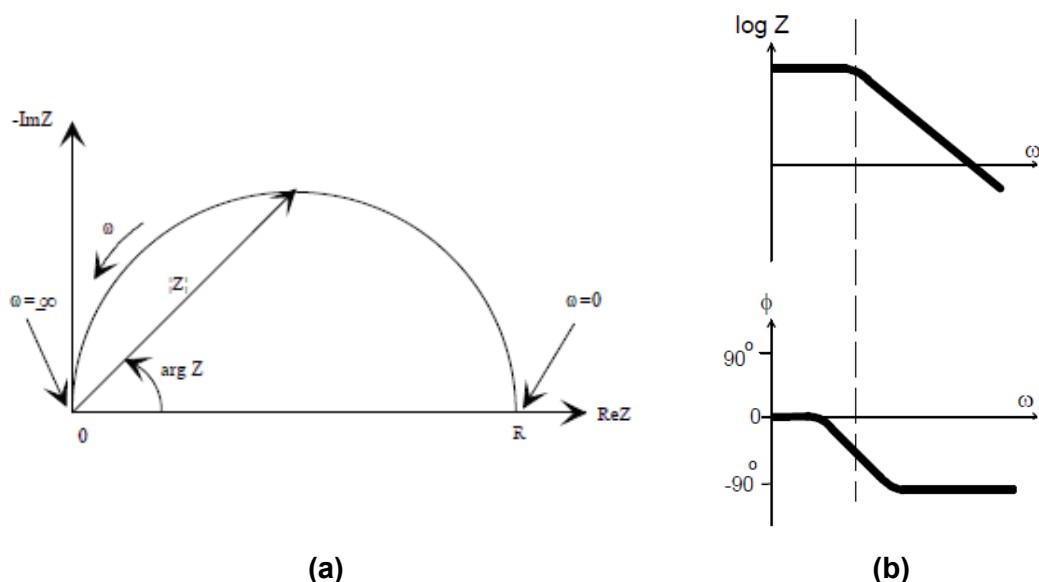


**Figure 2-20:** EIS representation: (a) Nyquist plot with impedance vector (b) Bode plots (with one time constant).

On the Nyquist plot, the impedance can be represented as a vector (arrow) of length  $|Z|$ . The angle between this vector and the X-axis, commonly called the phase angle is  $\varphi = \arg Z$ . One major shortcoming of Nyquist plots is that the frequency is an implicit parameter. Another representation of impedance data is Bode plots (Fig. 2-20(b)). The logarithm of the frequency is plotted on the X-axis and both the modulus of the impedance ( $|Z|$ ) and the phase-shift are plotted on the Y-axis.

### Analysis of EIS data

EIS data are commonly analyzed by fitting them, to an equivalent electrical circuit. Most of the elements in the model are common electrical elements such as resistances, capacitances and inductances. To be useful, the elements in the model should have a basis in the physical electrochemistry of the system. The general equivalent circuit of the electrode/electrolyte interface consists of three parts: a resistor representing the electrolyte resistance,  $R_e$ , in series with the parallel combination of a capacitor representing the double layer capacitance,  $C_{dl}$ , and a Faradic impedance,  $Z_F$ , describing the electrochemical reaction (Randles circuit).

Table 2-5 lists the common electrical elements, the equation for their current versus voltage relationship, their impedance and some characteristics.

The electrolyte resistance ( $R_e$ ), also called Ohmic resistance, is the resistance to current flow through the electrolyte. It is proportional to the electrolyte resistivity  $\rho$ , and to the thickness of the electrolyte,  $d$ , as following:

$$R_e = \rho \cdot d \quad (2.18)$$

with  $R_e$  in  $\Omega \cdot \text{cm}^2$ . This parameter depends on the cell geometry.

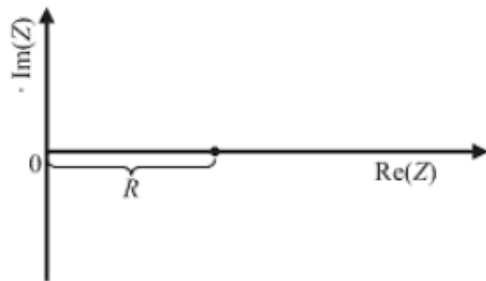
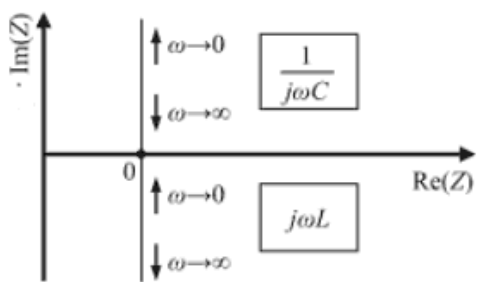
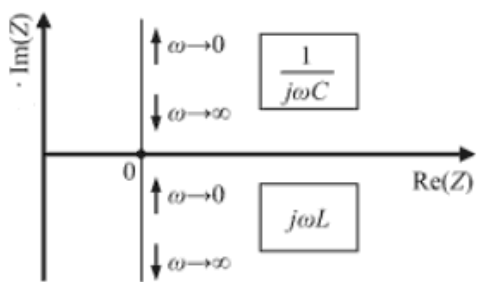
The charge transfer resistance ( $R_t$ ) is the resistance associated with the charge transfer mechanism for electrode reactions. This is the resistance to electrons crossing the interface. It is defined as the inverse of the partial derivative of the Faradaic current density ( $j_F$ ) with respect to potential ( $E$ ):

$$R_t = \left( \frac{\partial j_F}{\partial E} \right)^{-1} \quad (2.19)$$

Combinations of pure resistors, capacitors, or inductors do not necessarily describe the response of all systems. To model the behavior of real electrochemical systems,

distributed elements are used, among which the constant-phase element (CPE) and the Warburg impedance.

**Table 2-5:** Common electrical elements, equations for their current vs voltage relationship, their impedance, their characteristics and their Nyquist representation.

Element	I vs E	Z	Notes	Nyquist representation
<b>Resistor</b>	$E = IR$	$Z = R$	Z is independent of frequency, since it has no imaginary component, but only a real component. The current through a resistor stays in phase with the voltage across the resistor.	
<b>Inductor</b>	$E = L \frac{di}{dt}$	$Z = j\omega L$	Z increases with the frequency. Inductors have only an imaginary component. The current is 90 degrees phase-shifted with respect to the voltage.	
<b>Capacitor</b>	$I = C \frac{dE}{dt}$	$Z = \frac{1}{j\omega C}$	Frequency behavior of C is opposite to that of L. Z decreases with increasing frequency. Capacitors have only an imaginary component. The current is -90 degrees phase shifted with respect to the voltage.	

### Constant Phase Element (CPE)

The impedance response for electrochemical systems often reflects a distribution of reactivity that is commonly represented in equivalent electrical circuits as a constant-phase element (CPE) [134-136]. The impedance of a CPE is given by:

$$Z_{CPE} = \frac{1}{Q(j\omega)^\alpha} = \left( \frac{1}{Q\omega^\alpha} \times \left[ \cos\left(\frac{\alpha\pi}{2}\right) - j\sin\left(\frac{\alpha\pi}{2}\right) \right] \right) \quad (2.20)$$

It is defined by two parameters  $Q$  and  $\alpha$ . It can be reduced to a pure resistor, capacitor or inductor when  $\alpha = 0$ ,  $\alpha = 1$  and  $\alpha = -1$ , respectively. When  $\alpha = 1$ ,  $Q$  has units of a capacitance, *i.e.*  $F \cdot cm^{-2}$ ; when  $\alpha \neq 1$ ,  $Q$  has units of  $s^{\alpha} \Omega^{-1} cm^{-2}$ .

If plotting the absolute value of the imaginary part of the impedance ( $|Z_j|$ ) as a function of frequency ( $f$ ), in logarithmic coordinates the resulting curve is a straight line with a slope equal to  $-\alpha$ . This  $\log|Z_j|$  vs  $\log f$  representation is recommended since it allows to get rid of the electrolyte resistance.

The  $Q$  parameter can be obtained from the imaginary part of the impedance as follows:

$$Q = -\frac{1}{Z_j(f)(2\pi f)^{\alpha}} \times \sin\left(\frac{\alpha\pi}{2}\right) \quad (2.21)$$

A CPE behavior can be attributed to a distribution of time constant either along the area of the electrode (surface distribution) or along the axis normal to the electrode (normal distribution) [137]. A surface distribution could arise from surface heterogeneities (grain boundaries, crystal faces on polycrystalline electrode...), or from geometry-induced non-uniform current and potential distributions. A normal distribution may be attributed to changes in the conductivity of films or porosity.

If the CPE behavior is assumed to be associated with surface distributed time constants for charge-transfer reactions, then it is possible to apply the equation derived by Brug *et al.* to calculate the effective capacitance,  $C_{eff}$ , associated with the CPE [138, 139]:

$$C_{eff} = Q^{1/\alpha} (R_e^{-1} + R_t^{-1})^{(\alpha-1)/\alpha} \quad (2.22)$$

In the case of a blocking electrode ( $R_t \rightarrow \infty$ ) this equation becomes:

$$C_{eff} = Q^{1/\alpha} (R_e^{-1})^{(\alpha-1)/\alpha} \quad (2.23)$$

In the case of an R//CPE circuit, the CPE parameters  $\alpha$  and  $Q$  can be graphically obtained following the method presented by Orazem *et al.* [140]. The parameter  $\alpha$  is calculated from the slope of the  $\log|Z_j|$  vs  $\log f$  curve in the HF range and  $Q$  is obtained from  $\alpha$  by application of Eq. 2.21.

A double layer capacitance will present values of the order of a few tens of  $\mu F \cdot cm^{-2}$ .

Normal distributions of time-constants can be expected in systems such as oxide films, organic coatings, and human skin. They may be interpreted in terms of dielectric

properties of the material. If the dielectric response can be associated with an effective capacitance  $C_{eff}$ , the dielectric constant  $\epsilon$  and film thickness  $d$  may be obtained from:

$$C_{eff} = \frac{\epsilon \epsilon_0}{d} \quad (2.24)$$

where  $C_{eff}$  is expressed in  $F.cm^{-2}$  and  $\epsilon_0$  is the permittivity of vacuum ( $\epsilon_0 \approx 8.854 \times 10^{-14} F.cm^{-1}$ ). In the case of normal distributions, the challenge is to find a correct way to extract an effective capacitance from the CPE parameters  $\alpha$  and  $Q$ . This case is not detailed here since in this PhD work, the CPE behavior of electrochemical systems was attributed to surface distribution.

### Warburg

The Warburg impedance is associated with one-dimensional diffusion of species  $x_i$ , in an infinite stagnant medium and is given by:

$$Z_i = \frac{1}{(k_i \sqrt{j\omega})} \quad (2.25)$$

where  $k_i$  is a Warburg coefficient, dependent on many parameters such as the diffusion of species  $X_i$ , the reaction rate, the bulk concentration of species  $X_i$  and the potential.

### Equivalent circuit

One of the problems with the use of equivalent circuits is that different circuits can have the same impedance signature. This raise questions about the physical meaning of model parameters.

In this work, EIS diagrams were plotted at the corrosion potential ( $E_{corr}$ ). Thus, only the electrical circuit corresponding to a freely corroding electrode will be considered.

At  $E_{corr}$ , the anodic and cathodic currents have the same magnitude and the net current is equal to zero ( $i_t = i_a + i_c = 0$ ). When the current flowing through circuit elements is the same, but the potential drop is different, the respective impedances must be added in series ( $Z = Z_1 + Z_2$ ). On the other hand, when the current flowing through circuit elements is different, but the potential drop is the same, the respective impedances must be added in

parallel ( $Z = \left[ \frac{1}{Z_1} + \frac{1}{Z_2} \right]^{-1}$ ) [136]. Therefore, by principles of summation of currents, the anodic and cathodic Faradaic impedances,  $Z_F^a$  and  $Z_F^c$ , respectively, must be in parallel (Figure 2-21). The contribution of the double-layer capacitance  $C_{dl}$  is added in parallel. Expressions for the anodic and cathodic impedances must be developed separately, according to proposed reaction mechanisms. In the overall impedance of the electrochemical system, the electrolyte resistance  $R_e$  is added in series with  $C_{dl} // Z_F^a // Z_F^c$ .

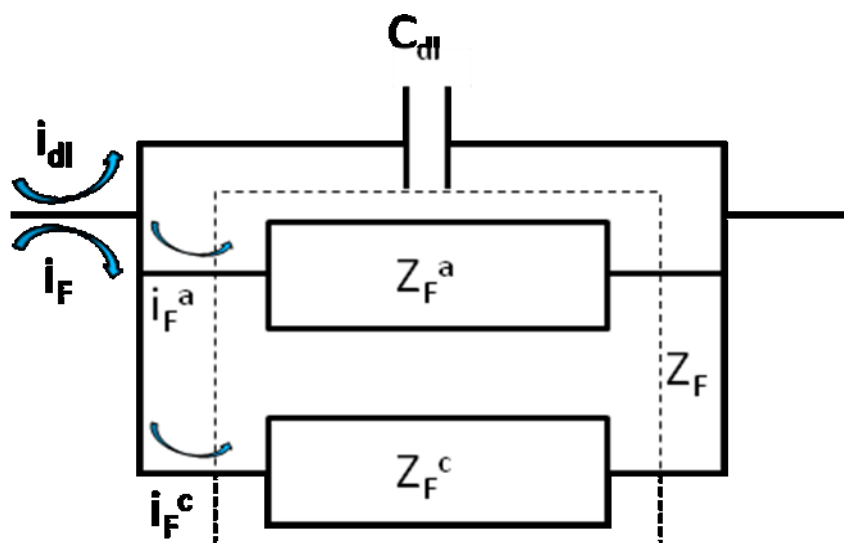


**Figure 2-21:** Equivalent electrical circuit of the interfacial impedance at the corrosion potential, where  $i_{dl}$  represents the charging current,  $i_F^a$  the anodic Faradaic current and  $i_F^c$  the cathodic Faradaic current (the electrolyte resistance is omitted).

In this work, the analysis of impedance data by regression of equivalent circuits was performed using Simad® software developed at *Laboratoire Interfaces et Systèmes Electrochimiques*.

#### 2.2.2.2 SURFACE ANALYSIS

In this chapter the spectroscopic techniques used to characterise the chemistry of the different surfaces investigated will briefly be described. The spectroscopic techniques used were: XPS (X-Ray Photoelectron Spectroscopy) and ToF-SIMS (Time of flight secondary ion mass spectrometer). These spectroscopic techniques can provide qualitative, and in certain cases quantitative, analysis of the chemistry of the surface (information depth 0.1 – 5 nm).

## • X-RAY PHOTOELECTRON SPECTROSCOPY (XPS)

Surface analysis by X-ray photoelectron spectroscopy (XPS) or electron spectroscopy for chemical analysis (ESCA) [141], allow investigating thin layers formed or adsorbed on different materials surface. It may be applied to surface chemical analysis of minerals, catalysts, metals and polymers as well as living systems such a biofilms [142, 143].

In an XPS experiment, a specimen is irradiated by low energy X-rays (usually Mg K $\alpha$  (1253.6 eV) or Al K $\alpha$  (1486.6 eV)) in ultra-high vacuum. This causes photo-ionization of the atoms: in other words, photoelectrons are emitted from energy levels determined by the electronic structure of the atom.

Photoelectron emission occurs when a photon transfers its energy to an electron, and a photoelectron can be emitted only when the photon energy is larger than the binding energy of the electron [142]. The emitted photoelectrons have kinetic energies,  $E_{kin}$ , given by:

$$E_{kin} = h\nu - E_b - F \quad (2.26)$$

where  $h\nu$  is the energy of the photon,  $E_b$  the binding energy of the atomic orbital from which the electron originates and  $F$  is the work function of the spectrometer (assuming conductive samples). As the energy of the photons and the spectrometer work function are known quantities, the measurement the electron binding energies can be obtained by measuring the kinetic energies of the photoelectrons.

The relaxation energy can dissipate either as a photonelectron or it can be given to a second electron, an Auger electron. Since the emission of x-ray photons is low in the energy range used in XPS, photoionization normally leads to two emitted electrons: a photoelectron and an Auger electron (Figure 2-22).

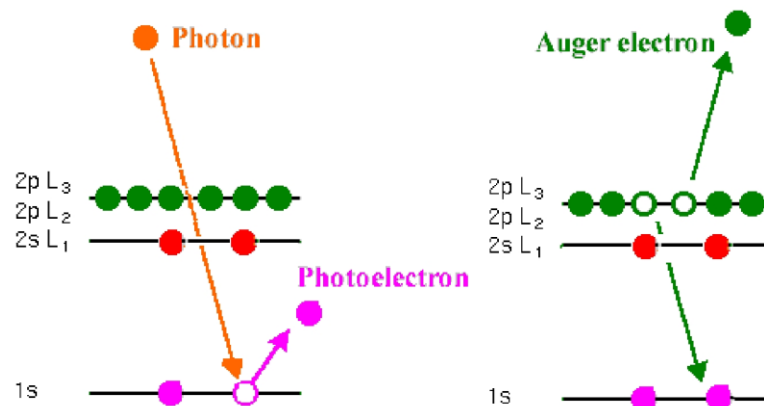


**Figure 2-22:** Schematic diagrams of (a) photoelectron emission, and (b) Auger electron emission.

Due to the relatively short inelastic mean free path for the photoelectrons and the Auger electrons (the transportation of emitted electrons, generated in the solid, to the surface can only occur from a certain depth) makes XPS a very surface sensitive analyzing method. Using XPS it is possible to detect all elements except for H and He. An XPS spectrum shows the number of photoelectrons as a function of binding energy. The spectrum will be a superposition of photoelectron and Auger lines with accompanying satellites and loss peaks and a background due to inelastic scattering in the substrate.

### Instrumentation

An XPS spectrometer is constituted of at least two chambers, one to introduce samples and a second one to proceed to the analysis, the later is always kept under ultra high vacuum. Chambers are made of stainless steel with a series of valves and windows. High vacuum is maintained, thanks to knife-edge flanges, which are compressed against copper gaskets. Electron trajectories are screened from earth magnetic field by using a metal with high magnetic permeability for internal walls of the analysis chamber. Additional chambers can also be added to allow sample pre-treatment or parking [142].

XPS analyses were performed with a Thermo Electron Escalab 250 spectrometer, this equipment consist of three different chambers: a) fast entry air lock (FEAL), b) a preparation chamber, and c) an analysis chamber. The FEAL chambers is the point at which samples are introduced into the system and it is not a UHV chamber, due to the frequent exposure to the atmosphere, but it is capable of pumping down to  $10^{-6}$  mbar using a proper turbo pump. The samples are transfer from the FEAL chamber to the preparation chamber through a sample transfer mechanisms onto which specimen holders are loaded and held by a robust spring-loaded mechanism via the gate valve. The preparation chamber is a UHV chamber equipped with three sample ports, where samples can be stored; this chamber is also equipped with a sample transfer mechanisms equivalent to the FEAL chamber, allowing move the samples to the analysis chamber via the gate valve [144].

For the XPS measurements a monochromatised Al K $\alpha$  X-ray source (1486.6 eV) was chosen. The analyser pass energy was 100 eV for survey spectra and 20 eV for high resolution spectra. The spectrometer was calibrated using Au 4f $_{7/2}$  at 84.1 eV. All spectra were referred to the C 1s peak for the carbon involved in C-C and C-H bonds, located at 285 eV. The fitting of the complex C 1s signal was based on published data [145]

### Data processing

Curve fitting of the spectra was performed with the Thermo Electron software “Avantage”. The peak fitting was performed on the recorded high resolution spectra. For that, an appropriate choice of back ground had to be applied. The Avantage data systems offer three background subtraction methods, Linear, Shirley and Tougaard. In this thesis, the selected method used was the Shirley background subtraction, which is the most widely used method.

After the definition of the peak energy range, the following step consists of separation of peaks into signal components by peak fitting. Peak fitting requires the knowledge of the energy position and shape of the individual peaks. This information can be obtained by comparison with spectra of standard compounds or by consulting the literature on XPS investigation. The peak shape as well as the peak position can be changed using the already mentioned software by the modification of the following parameters: peak centre in eV (binding energy), peak height in cps, Full Width Half Maximum in eV (FWHM), and Lorentzian/Gaussian ration in % (L/G). In addition the software offers the possibility of using asymmetric peak shape, using tailing functions. Once peak decomposition is done, the software calculates the peak intensity by the integration the area portion of the peak involved.

The integral intensity  $I_N^M$  (describing the intensity of an element N in a matrix M) of emitted photo-electrons depends on the specific parameters related with the spectrometer and the sample, This is given by the following equation [142, 144, 145]:

$$I_N^M = kT(E_k)\sigma_N \int D_N^M(z) \exp\left(\frac{-z}{\lambda_N^M \sin \theta}\right) dz \quad (2.27)$$

Where:

$k$  : Spectrometer specific constant;

$T(E_k)$ : Transmission function of the energy analyzer depending on the  $(E_k)$  of photoelectrons of the analyzed element;

$\sigma_N$  : Photo-ionization cross-section;

$D_N^M$  : Density of an element N in a matrix M;

$z$  : Depth analysis;

$\lambda_N^M$  : Attenuation length of electrons (inelastic mean free path (IMFP)) of the element N in the matrix M;

$\theta$  : Take off angle with respect to the surface normal.

Assuming homogeneous distribution of an element N with the density in a theoretical infinite thick sample, with homogeneous composition, the equation simplifies to:

$$I_N^{M,\infty} = kT(E_k)\sigma_N D_N^M \int_0^\infty \exp\left(\frac{-z}{\lambda_N^M \sin \theta}\right) dz \quad (2.28)$$

which after integration becomes:

$$I_N^M = kT(E_k)\sigma_N D_N^M \lambda_N^M \sin \theta \quad (2.29)$$

The intensity can be attenuated by the formation of a surface layer of thickness  $d$  and of a homogeneous composition. So the intensity of the substrate under a formed surface layer or thin film respectively is expressed depending on an exponential term that describes the attenuation of the signal by the surface layer.

The following equation describes the attenuation of the signal of an element N in a substrate matrix M by a thin film formed on top of thickness  $d$ .

$$I_N^{Ms} = kT_N(E_k)\sigma_N D_N^{Ms} \lambda_N^{Ms} \exp\left(\frac{-d}{\lambda_N^{MF} \sin \theta}\right) \quad (2.30)$$

$M_s$ : Substrate matrix

$M_F$ : Surface layer

The attenuation-coefficient is given by this equation:

$$A_i = \exp\left(\frac{-d_i}{\lambda_i \sin \theta}\right) \quad (2.31)$$

In this thesis, the inelastic mean free path values were calculated by the TPP2M formula [146], and the photoemission cross-sections were taken from Scofield [147].

For 70Cu-30Ni samples, in the Cu Auger line, the relative contributions from Cu<sub>2</sub>O, CuO and metallic Cu were performed with the software “CASA”. The three known reference spectra of metal and oxides were used to construct line-shapes forming the basis for a

nonlinear optimization, the results of which provides an estimate for the relative proportions of these materials. The same was done for Al brass samples, using Zn metallic and ZnO.

- **TIME-OF-FLIGHT SECONDARY ION MASS SPECTROSCOPY (ToF-SIMS)**

ToF-SIMS is a secondary-ion mass spectrometry method combined with a time-of-flight analyzer, which has been widely used in recent years for analyzing the elemental and chemical composition of surfaces. In this approach, the surface of a sample is bombarded with an energetic beam of ions (primary ions), generated by a liquid metal ion gun (LMIG). The impact of primary ion beam with the substrate leads to a collision cascade and particles (ions, electrons, neutral particles) are emitted from 1 to 3 monolayers of the substrates (Figure 2-24).

Depending on the ion dose, the technique can be separated into two modes: dynamic and static SIMS. In contrast to dynamic SIMS, static SIMS is performed with low primary ion doses [146, 148].

Only ejected ions, which are either positive or negative, are analyzed in a ToF-SIMS measurement. The yield of secondary ions are function of many factors, including the energy of primary ions. The higher energies result in increased yields, but also in increased of sample damage. The secondary ions enter the ToF analyzer, where they are mass analyzed, thanks to the time needed to travel from the entrance of the analyzer to the detector.

There are three different modes of analysis in TOF-SIMS; 1) mass spectra are acquired, with a very good mass resolution, to determine the elemental isotopic and/or molecular analysis of the surface species; 2) images are acquired, with a lower mass resolution, but a good lateral resolution (~ 200nm) to visualize the distribution of chemical elemental and/or molecular species on surface; and 3) depth profiles, generally acquired with a good mass resolution, in which the use of a sputtering gun alternatively with the primary gun, allows to determine with a very good depth resolution (function of the energy of the sputter gun), the in depth of the order of a few micrometers.

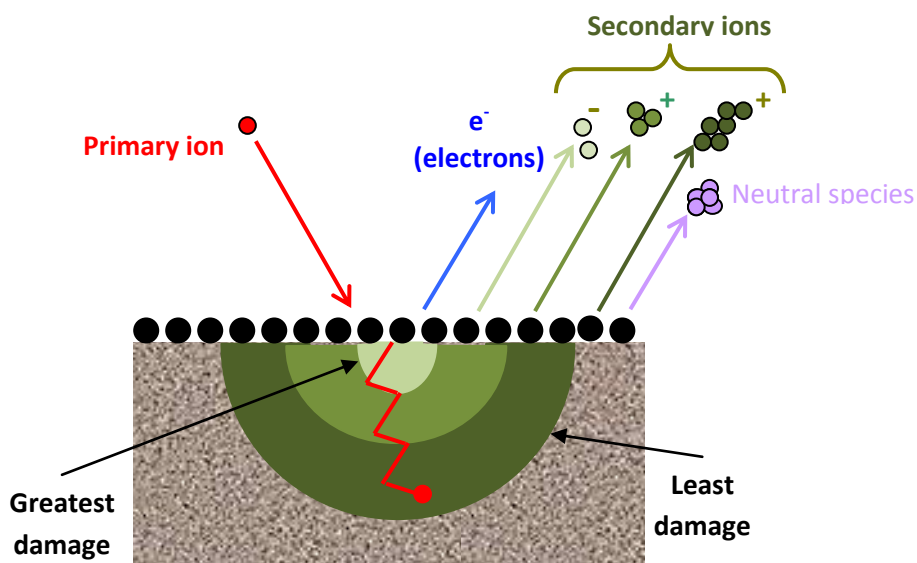


**Figure 2-23:** Schematic drawing of the secondary particles emission process initiated by the impact of the primary ion. Positive and negative ions, electrons and neutral particles are emitted. In ToF-SIMS measurements, only ions can be analyzed.

In order to characterize the thin films formed in copper alloys, after exposition to seawater environments, and better compliment XPS measurements, in this work, the analysis are performed using the depth profiling mode.

A depth profile reflects the intensity of a given mass signal as a function of sputtering time. Although ToF-SIMS is not directly quantitative technique, a profile reflects direct the variation of species abundance/concentration with depth below the surface (Figure 2-25).

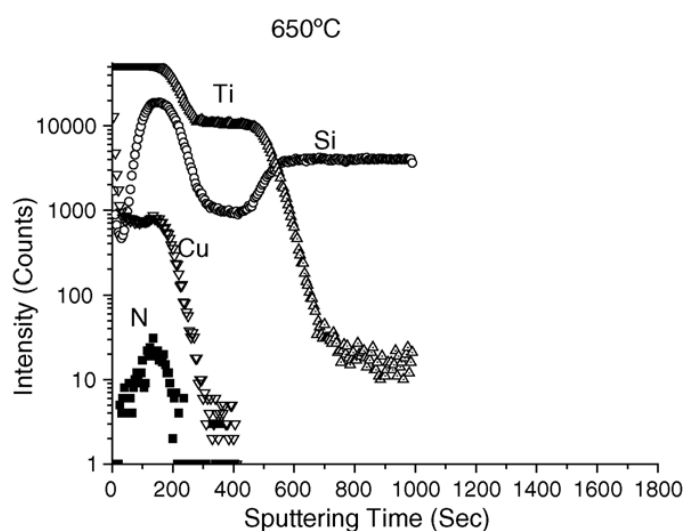


**Figure 2-24:** SIMS depth profile of Cu, Ti, Si and N after annealing for 30 min at 650°C. Copper diffused into Ti–Si–N film. (Adapted from Y.C. Ee *et al.* [149])

### Instrumentation

ToF-SIMS analyses were done using a ToF-SIMS V spectrometer (ION-TOF GmbH).

For the ToF SIMS measurements, the analysis chamber was maintained at less than  $10^{-9}$  Pa in operation conditions. The depth profiles were performed using the instrument in dual beam mode. A pulsed 25 keV  $\text{Bi}^+$  primary ion source (LMIG) at a current of 1.2 pA (high mass resolution mode), rastered over a scan area of  $100 \times 100 \mu\text{m}^2$ , was used as the analysis beam. The sputtering was performed using a 1 keV  $\text{Cs}^+$  ion beam delivering 50 nA, over a  $300 \times 300 \mu\text{m}^2$  area. The depth profiles were obtained in negative polarity meaning only negative ions were analyzed. The distribution of the ionized fragments, all measured quasi-simultaneously, were plotted versus  $\text{Cs}^+$  ion sputtering time.

### Data processing

Secondary ions yields depend on several factors and are not directly proportional to its concentration in the sample, making the quantitative SIMS analysis difficult. The yield of secondary ions can be described in terms of secondary ion current ( $i_{\text{MS}}$ ) during SIMS analysis. The yield important variables that contribute to  $i_{\text{MS}}$  include  $S$ , the yield of secondary particles per primary particle impact (sputter yield), and  $R^+$ , the probability that a given particle will be emitted as an ion (ionization probability). Often  $S$  and  $R^+$  are grouped together in a variable referred to as the transformation probability ( $P$ ).

$$i_{\text{MS}} = i_p S R^+ \theta_M^n \quad (2.32)$$

Where  $i_p$  is the primary particle flux,  $\theta_M$  is the fractional coverage of  $M$ , and  $n$  represents the transmission and detection efficiency of the analyzer system. The above equation indicates that the sensitivity of the technique for a particular secondary ion depends on its sputter yield and ionization probability.

“Matrix effects” also play a major role in SIMS quantitative analysis. The problem can be defined as the variability of ion yields as the surface composition changes. The same species will not have the same secondary ion yield in a different chemical environment, making direct comparison among samples difficult. No method has been developed to compensate for the variation in ion yields due to matrix effects [147, 150].

The majority of depth profiles reported in the literature are only qualitative or semi-quantitative. Sometimes, in an attempt to obtain a quantitative profile, the elemental intensity signals are simply converted to atomic concentrations by means of relative elemental

sensitivity factors. Likewise, sputtering time is converted to depth by estimation of a constant sputtering rate. However, these simple procedures only provide a semi-quantitative result [151].

In this work, the intensity was reported using a logarithmic scale, which emphasizes the low intensity signals. The variation of the ion intensity with sputtering time reflects the variation of the in-depth concentration but is also dependent on the matrix from which the ions are emitted. Data acquisition and processing were performed using the IonSpec software.

The thickness of the oxide layer was estimated from theoretical sputtering rate of corresponding pure metallic substrate (given in tables) in the same sputtering conditions, which is a good estimation, e. g., the thickness of pure nickel oxide was estimated from the sputtering rate of a pure metallic nickel. For mixed metal oxides, the thickness was estimated from an average sputtering rate calculated by summing the sputtering rate of pure metallic metals ponderating by the fraction of each element in the oxide.

## CHAPTER 3 - COPPER ALLOYS IN REAL INDUSTRIAL CONDITIONS: CORROSION AND MICROBIOLOGY

The aim of the present chapter was to characterize the electrochemical behavior of 70Cu-30Ni alloy and Al brass in chlorinated (treated natural seawater, TNSW) or natural seawater (NSW), under real industrial conditions (flow conditions). The monitoring was carried out in industrial plants and pilot circuits, under different sets of environmental conditions.

Both copper alloys, 70Cu-30Ni and Al brass, have been extensively used in different marine engineering structures. Their main application is heat exchangers and piping for seawater handling, where seawater must be often chlorinated. Typically, chlorine dosages (intermittent or continuous) are used taking into account the macro-fouling resistance of these materials. Recommended industrial practices suggest to treat the condenser tubes with cool and chlorinated water for some weeks before the first start of operation, while during the regular operation, it is important to use in the cooling circuits an efficient antifouling treatment.

Recent studies [152] confirmed the recommendations, documenting that microbial activity negatively affects both the formation and the stability of protective oxide layers on Cu-based alloys. The development of biofilm on 70Cu-30Ni condenser tubes in the early stages of exercise may induce localized corrosion, and it can be so extensive that the replacement of tubes is required.

From thermodynamic point of view, the strong oxidant action of chlorine should promote corrosion of copper alloys [153, 154] but it exists a good range of safety with a threshold which guarantees the best benefit and avoids the possible negative effects. Even if it must be considered the fact that the behavior of each material could be quite different.

The halogenated by-products formed during chlorination treatments have been studied due to their potential toxicity and because some highly-chlorinated substances do not degrade easily. Nowadays, it is a very important issue that leads to a drastic reduction of chlorine concentrations in industrial discharges over the world. Previous studies refer mainly on chlorine concentrations higher than  $0.2 \text{ mg.L}^{-1}$ , the maximum level currently allowed at the discharge in most of the industrialized world, and, as a consequence, sustainable treatments and a careful control of their effects (in terms of environmental impact as well as the materials performance) are currently mandatory in the operational practice of industrial cooling circuits.

According to these needs, an innovative integrated monitoring equipment, specifically set for industrial application, was designed and used to monitor several kinds of chlorination treatments and their effects on condenser tubes [152]. Experimental test facilities were set up in cooling circuits of two Italian power plants, for more than two years of operation, in two different hydraulic test lines: with and without chlorination treatment. An automatic electrochemical workstation able to monitor on-line the corrosion and the antifouling treatments (described in detail in section 3.2), equipped with a remote data control device, was used. The main monitored parameters were: the corrosion rate (by weight losses and linear polarization resistance probe - section 3.2.1), the biofilm growth (by the BIOX probe - section 3.2.2), the chlorine concentration (section 3.2.3) and other physic-chemical parameters (flow rate, temperature, turbidity, seawater, red-ox potential and corrosion potential – section 3.2.4).

The identification of bacteria inside the biofilm grown on the surface of both alloys, complements the work. In order to identify and better characterize the bacterial community present on the copper alloys, tube samples were exposed to TNSW and NSW and collected after a long period (one year) and short period (2 days) of exposure. From the collected samples, molecular techniques such as DNA extraction, polymerase chain reaction (PCR), denaturing gradient gel electrophoresis (DGGE) and identification by sequencing were performed.

## **3.1 POWER PLANTS CHARACTERISTICS**

### **3.1.1 TESTS ON THE TYRRHENIAN COAST**

The main set of investigations was carried out in a thermoelectric power plant located on the Italian Tyrrhenian coast near Piombino (Livorno; Figure 3-1).

The cooling system is composed of a fiberglass channel with a length of about 2400 m, and a diameter of 1.2 m, in which seawater flows with a flow rate of about  $10000 \text{ m}^3 \cdot \text{h}^{-1}$ . The flow velocity in the channel (inhibiting the growth of biofouling settlements along the channel) is quite high,  $2.5 \text{ m} \cdot \text{s}^{-1}$ . The steam condenser exhibits 70Cu-30Ni (ASTM B111 C71500) alloy tubes bundles. The chemical and physico-chemical characteristics of these tubes are reported in Table 2-1.

The condenser shell is covered by epoxidic coating and protected by zinc anodes. Just before the condenser, there is a rotating “Taprogge” filter able to retain and restore from the downstream all the solid bodies with significant size (bigger than 0.5 cm size). After the

condenser, seawater flows in an open pool (Figure 3-1(b)) before being discharged into the sea. Seawater characteristics are reported in Chapter 2 (section 2.1.2.1).

The plant cooling circuit is affected by significant daily/weekly influxes of slime and mud, which causes extensive microfouling accumulation in the tubes that cannot be mitigated by the operating mechanical filters.

An antifouling treatment is carried out in the cooling circuit with chlorine intermittent dosages: a commercial product based on sodium hypochlorite is dosed in order to measure a total residual oxidant concentration of 0.4-0.8 mg.L<sup>-1</sup> in the water exiting the condenser. The dosing occurs every 6 hours, each lasting 0.5-1 hour, depending on the season. This treatment has been applied since the beginning of the condenser operation in 2005.



**Figure 3-1:** Pictures of the Piombino power plant: power plant view (left side) and outlet of seawater in the pool (right side).

A bypass in the condenser (schema in Figure 3-2) was set to study two different conditions: outlet water from the condenser (treated line) and inlet seawater, before the chlorination treatment, without any kind of treatment (control line). Materials, physico-chemical characteristics and seawater treatments in the test lines are the same as inside the condenser tubes. The seawater flow velocity in the test lines was maintained at  $\sim 1.6 \text{ m.s}^{-1}$ .

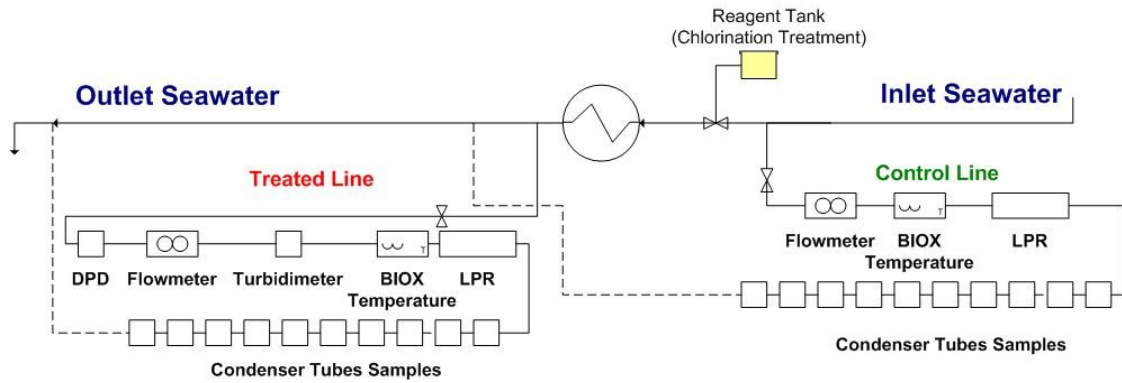


**Figure 3-2:** Schema of the two hydraulic test lines (control and treated) in the cooling circuit bypass (DPD = N,N-diethyl-p-phenyldiamine; LPR = linear polarization resistance).

### 3.1.2 TESTS ON THE ADRIATIC COAST

Monitoring tests were also carried out at a thermoelectric power plant placed in Servola (Trieste, Italy). An antifouling treatment is carried out in the cooling circuit with chlorine dioxide, that is dosed in order to measure a total residual oxidant concentration of  $0.05\text{--}0.1 \text{ mg.L}^{-1} \text{ ClO}_2$ .

Al brass alloy (ASTM B111 C68700), commonly used for condenser tubes using seawater as coolant, is the material used in this plant (Figure 3-3).

A bypass in the condenser, as the one described in Figure 3-2, was set in this power plant. Materials, physico-chemical characteristics and seawater treatments in the test lines are the same as inside the condenser tubes. The seawater flow velocity in the test lines was maintained between  $1.6$  and  $1.8 \text{ m.s}^{-1}$ .



**Figure 3-3:** Pictures of the heat exchanger at Servola power plant: inlet (left side) and outlet (right side).

## 3.2 ELECTROCHEMICAL TOOLS

Commercial devices (AMEL, model 1310CU), operating with full wireless set of probes and remote control (via GSM modem), were used to perform the test campaign in the power plant cooling circuits (Figure 3-4). Electrochemical tools, described in following subsections, are the key instruments of the monitoring system, permitting the on-line control of:

- the corrosion rate (by a tubular probe using electrochemical Linear Polarization Resistance (LPR) technique),
- the biofilm growth (by the BIOX electrochemical probe),
- the chlorination treatment (by the BIOX electrochemical probe and colorimetric device),
- the water temperature,
- other physico-chemical parameters (turbidity and corrosion potential).

Some specimens, cut from the operated condenser tubes, complete the hydraulic test lines, in order to make possible periodic visual observations, weight loss measurements and other off-line specific analyses.

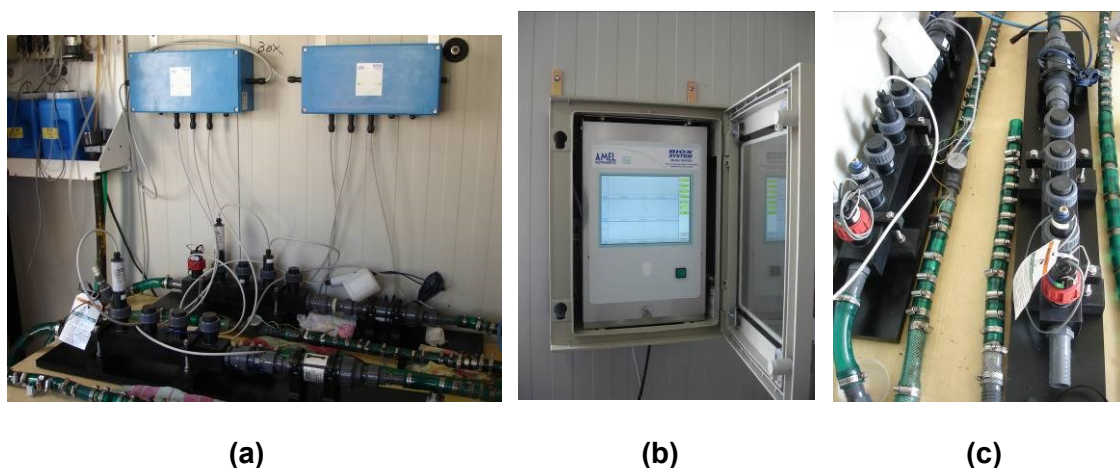


**Figure 3-4:** Monitoring system: a) Inside view of the experimental circuit, (b) computer display and (c) two hydraulic lines (Control and Treated) with 70Cu-30Ni specimens and probes.

### 3.2.1 CORROSION RATE

Corrosion rate was estimated by the Linear Polarization Resistance (LPR) method, previously described in Chapter 2 (section 2.2.1). The electrochemical cell was built using five new specimens of the selected material (70Cu-30Ni or Al brass) cut from new condenser tubes.

### 3.2.2 BIOFILM GROWTH

Biofilms can change the electrochemical characteristics of metallic surfaces [77, 155] and the involved mechanisms are linked to the kinetic changes of the corrosion processes occurring at the metal-biofilm interface and the acceleration of cathodic discharges of chemical species (e.g. oxygen in aerobic conditions) caused by bacterial activity in the biofilm. The acceleration of the oxygen reduction reaction on passive alloys, in aerobic conditions, frequently named “cathodic depolarization” [155], can cause corrosion. Based on this phenomenon, very simple electrochemical devices for biofilm monitoring are designed.

The evolution of the overall cathodic current, during the gradual development of biofilm on a Stainless Steel (SS) sample, immersed in aerated natural seawater, is presented in Figure 3-5. Curve (1) describes the oxygen reduction kinetics, measured at the beginning of the exposure to aerated seawater on a clean (no biofilm) SS surface. Curve (4) shows the cathodic curve measured on an SS sample completely covered by biofilm, whereas curves (2) and (3) describe the trend of the cathodic current in two intermediate conditions.

If, the evolution of cathodic current is only due to biofilm development, the evolution of “cathodic depolarization” from curve (1) to curve (4) can be monitored by the simple circuit of Figure 3-6(a), consisting of a SS sample coupled, through an external resistor, to a less noble material which plays the role of sacrificial anode. Although extremely simple, this electrochemical sensor shows a very high sensitivity to the biofilm growth during the early stage of its development (Figures 3-6(b) and (c)).

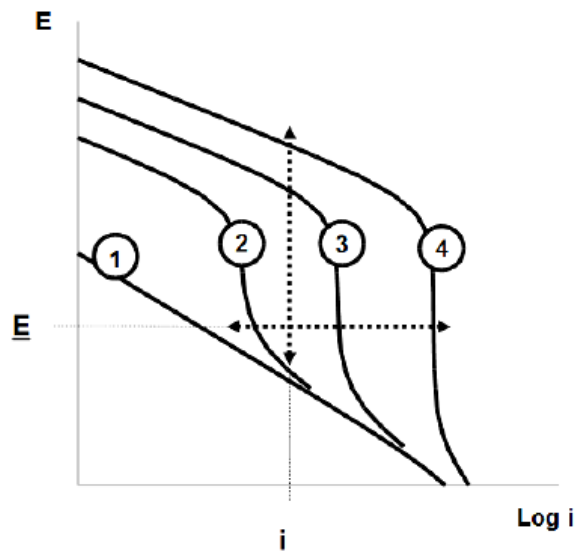


**Figure 3-5:** Evolution of the overall cathodic curve during the gradual development of biofilm on a stainless steel surface exposed to aerated natural seawater (adapted from G. Pavanello *et al.* [159]).

According to Mollica and Cristiani [156], the biofilm formation, through “cathodic depolarization” induced by biofilm growth, causes a sharp increase of the free corrosion potential of SS in passive state promoting, in so far, a higher probability of localized corrosion onset, and a higher propagation rate of localized corrosion in active state. Galvanic corrosion of less noble alloy coupled with SS is also increased when biofilm forms on SS surfaces.

The evolution of “cathodic depolarization” induced by biofilm growth can be monitored in, at least, two classical ways:

- 1) in potentiostatic way: measurement of the cathodic current on an SS sample polarized at fixed potential (depolarization is revealed by an increase of the cathodic current when SS sample is polarized at a fixed cathodic potential);
- 2) in galvanostatic/intentiostatic way: measurement of the potentials able to sustain a fixed cathodic current during the biofilm growth (depolarization is revealed by an increase of the SS potential when a fixed cathodic current is imposed on the sample).

For practical purposes the two above mentioned classical techniques can be approximated by quasi-potentiostatic and quasi-intentiostatic techniques which, in turn, can be both applied using the very simple basic circuit shown in Figure 3-6(a).

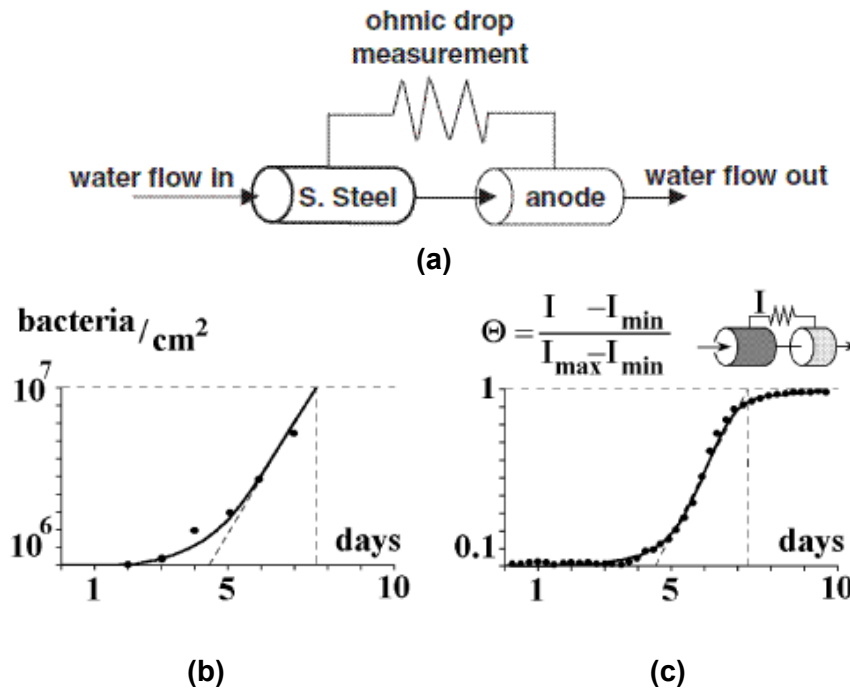


**Figure 3-6:** Biofilm growth. (a) Schema of the electrochemical sensor, (b) Evolution of the bacteria population density on SS surfaces obtained from SEM count of settled bacteria and (c) signal provided by an electrochemical probe in a test performed in flowing natural seawater [156].

As previously referred, the circuit consists of a SS sample (in form of a pipe) coupled, through an external resistor, to a less noble material which plays the role of sacrificial anode: the choice of the resistor value and of the sacrificial anode nature determines which technique (quasi-potentiostatic or quasi-intentiostatic) is applied to the SS sample playing the role of the cathodic element of the galvanic couple.

Tests were firstly performed in natural seawater using as biofilm sensor the circuit above described, arranged in order to apply a quasi-potentiostatic cathodic polarization to the SS element; for this purpose, iron was chosen as anode in order to polarize the SS sample at a potential level close to -500 mV and a low resistor value was fixed in such a way that for a cathodic current density of about  $10 \mu\text{A cm}^{-2}$  (magnitude of the maximum cathodic current observed at the above mentioned potential on SS samples when biofilm is totally developed on the surface,  $I_{\max}$ ), a maximum ohmic drop of about 10 mV is measured across the resistor.

Figure 3-6(b) shows the evolution of the mean bacterial population density on SS samples (each point plotted in Figure 3-6(b) was obtained from direct counts, by SEM, of settled bacteria observed on 50 fields of about  $300 \mu\text{m}^2$  randomly chosen on a small SS sample exposed to flowing seawater) whereas Figure 3-6 (c) shows the cathodic current,

plotted in a normalized form, delivered by the SS element of the sensor concurrently exposed to the same flowing seawater. The trend of the data plotted in these figures suggests an incubation time of about 4 days and an increase of about one order of magnitude during the following 3 days.

The electrochemical sensors show a very high sensitivity to the biofilm growth during the early stage of its development. The sensor signal moves from the base line when bacteria density overcomes a level of about  $10^6$  bacteria  $\text{cm}^{-2}$ ; it means that the sensor reveals the biofilm presence starting from a very little biofilm amount developed on a few percent of the whole SS surface. Later on, the bacteria density reaches a value close to  $10^7$  bacteria. $\text{cm}^{-2}$ , the electrical signal goes into saturation, corresponding to a signal increase of more than 0.5 V from the base value.

### **BIOX Probe**

The BIOX probe consists of a special tubular electrochemical “battery” (Fig. 3-7) whose current density increases when the biofilm colonizes its SS cathode. A quasi-intentiostatic cathodic polarization is applied to the SS element by coupling it with a zinc anode. The resistor is chosen high enough to strongly limit the galvanic current in such a way to cause an ohmic drop close to 1 V when a cathodic current density of some  $0.1 \mu\text{A cm}^{-2}$  is delivered by the stainless steel element.

Taking to account the very small galvanic current allowed to circulate between the two elements, zinc can be considered as a non-polarized anode in sulfide-poor environments, and consequently, as a sufficiently stable “reference” electrode for the measurement of the SS potential [157]. This way, the SS potential can be directly read as ohmic drop across the resistor. Owing to the “cathodic depolarization” of SS electrode due to the biofilm growth, the increase of the ohmic drop provides an index of the biofilm development on the SS surface. BIOX sensor signalizes biofilm growth by an increase of the ohmic drop across the resistor from a base line of 400–500 mV to a maximum of about 1.400 mV.

Other cathodic processes, than the oxygen reduction, that are able to ennoble the stainless steel electrode potential can be detected by the same BIOX probe increasing this way the galvanic current. These processes include the reduction of chlorine, bromide and other strong oxidants used as biocides (peracetic acid, chlorine dioxide, hydrogen peroxide, ozone, etc.) [29]. Therefore, BIOX probe offers the additional advantage of monitoring the biocide treatment in case of application of antifouling procedure based on oxidant, such as intermittent chlorination.

If the SS element of the sensor is clean *i.e.* biofilm-free (or in the initial phase of bacterial colonization), the BIOX sensor signalizes the intermittent chlorination by a spike with a height proportional to the local chlorine concentration in the range  $0.2\text{--}1\text{ mg.L}^{-1}$ .

Oxidant detection is fast while biofilm response is quite long, due to the long time required for bacteria to colonize the complete surface of the electrodes. Under regular operational conditions, the BIOX signal trend permits to distinguish in a simply way the contribution of both phenomena with respect to time (Figure 3-7(b)). The sensitivity of the BIOX sensor to the oxidant is limited by the concentration able to diffuse towards the electrode surface, depending on the cleaning conditions of the probe.

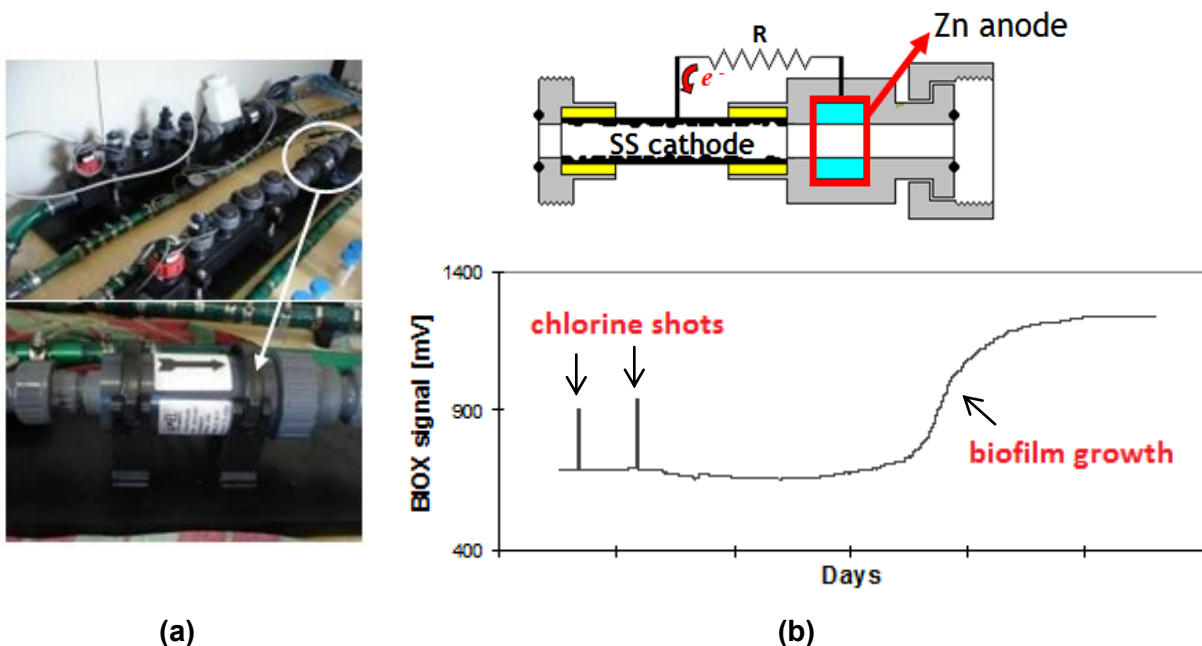


**Figure 3-7:** Biofilm growth. (a) BIOX system, (b) typical trend of BIOX signal (chlorine dosages and biofilm growth).

Compared to other commercial probes, the BIOX sensor offers the following advantages arising from the strong limitation of the cathodic current density on the SS element [158]:

- carbonate precipitation on the SS electrode is avoided, so that it is not necessary to often clean the sensor in order to maintain electrochemically active the whole SS surface;
- the BIOX probe works not only in seawater but also in solutions with a relatively high resistivity, such as river water.

As an example, Figure 3-7(b) shows the type of information that can be provided by the BIOX sensor. The initial two peaks signalize two chlorine shots and the following gradual increase of the signal indicates that, when chlorination is stopped, biofilm grows.

### 3.2.3 CHLORINATION TREATMENTS

Chlorination treatments are monitored in two ways: with the electrochemical BIOX probe (Figure 3-7) and, in comparison, with a colorimetric device able to give a more precise estimation of the oxidant concentration in the bulk water (Figure 3-8).

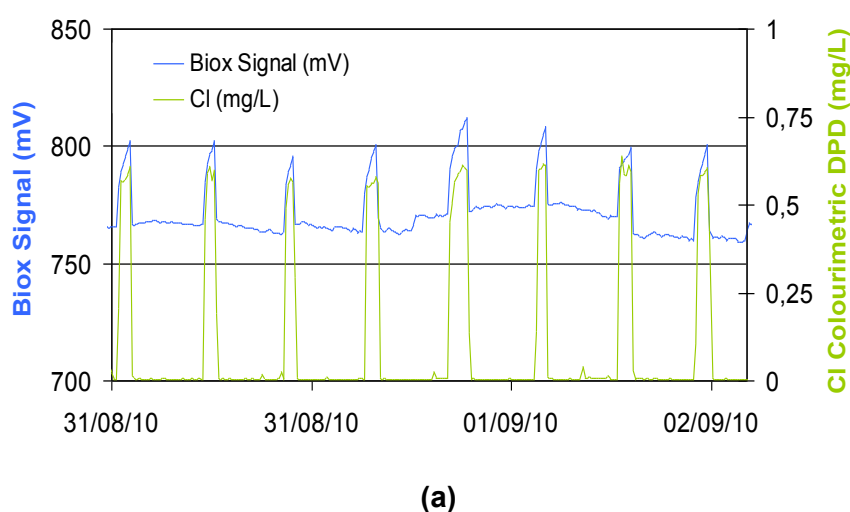


**Figure 3-8:** BIOX and chlorination treatments: (a) BIOX signal trend and residual oxidant concentration in seawater measured with the on-line instrumentation based on DPD colorimetric method, (b) AMI Codes (SWAN) colorimetric device.

In order to measure the concentration of the oxidant in the water bulk, a colorimetric device was added to the monitoring probe set. That system (AMI Codes of SWAN, Fig. 3-8 (b)) is based on DPD (N, N-diethyl-p-phenylenediamine) method (according to ISO 7393-2). The seawater reacts with N, N-diethyl-p-phenylenediamine in the presence of a suitable buffer (Potassium Citrate). The indicator, buffer, and potassium iodide are added to the seawater. Chloramines, chlorine and hypochlorites all react to produce a pink color, and this species is then measured by a spectrophotometer. In the range 0.1 – 1 mg/L of total residual oxidant in the water, the responses of the two on-line devices are in good agreement (Fig. 3-8(a)).

### 3.2.4 OTHER PHYSICO-CHEMICAL PARAMETERS

Other physico-chemical parameters, such as temperature, turbidity, corrosion potential and seawater redox potential, were also measured.

Temperature was acquired using a PT100 sensor (1310/TH AMEL; temperature range: from -10 to 120°C with a 0.1°C resolution). The operating principle is to measure the resistance of a platinum element; the PT100 has a resistance of 100  $\Omega$  at 0 ° C, and 138.4  $\Omega$  at 100 ° C.

Turbidity increases as a result of suspended solids in the water that reduce the transmission of light (suspended solids are clay, silt, and plankton). The intensity of light reflected by suspended solids, in the range of 0-100 Nephelometric Turbidity Units (NTU), and with a resolution of 0.2 NTU was measured by a nephelometer (346/TU AMEL).

The redox potential ( $E^0$ ) is used in plant mainly to establish whether aerobic or anaerobic conditions are developing in water, or oxidant biocides are present in the solution. It is a measurement of the ability of one chemical species to oxidize a second one. Under conditions of low oxygen content or when hydrogen sulfide is present, organic compounds dissolved in the water may have to be considered. A high red-ox potential suggests that bacteria are mainly aerobic but the corrosion of a metallic material exposed to the same environment can occur under a thick biofilm, at the bottom of which a prevailing anaerobic bacteria population may be present due to total consumption of dissolved oxygen. The redox potential was directly measured using a silver chloride electrode Ag/AgCl (AMEL 1310/RDX).

Open circuit potential may give information about the passive layer formed on metallic materials and the thermodynamic risk of corrosion. It can be used together with Pourbaix diagrams and can provide a useful indication of active or passive behavior of the system. It was measured with the probe previously described in section 2.2.1.1.2.

## 3.3 RESULTS OF THE MONITORING CAMPAIGN

### 3.3.1 70Cu-30Ni ALLOY – ONLINE MEASUREMENTS

The free corrosion potential  $E_{corr}$ , measured for three different 70Cu-30Ni samples vs a Zn reference electrode (-0.762 V vs SHE), is plotted as function of time (in days) in Figure 3-9. Old sample corresponds to a 70Cu-30Ni tube immersed for more than one year in TNSW, and new samples are new 70Cu-30Ni tubes just immersed.

During the first days of immersion, the corrosion potential  $E_{corr}$  increases till reaching a base-line value of  $\sim -0.24$  V vs SCE for the new sample exposed to TNSW. The peaks are associated with chlorination treatments. With time, due to the formation of an oxide film, the amplitude of these peaks becomes lower.

NSW induces a more anodic  $E_{corr}$  value of  $\sim -0.04$  V vs SCE. This increase of the corrosion potential can be correlated with the formation of a biofilm and/or oxide film on the metallic surface. When the copper oxide film reaches a relatively steady state, the partial anodic current and, therefore,  $E_{corr}$  also reaches a relatively stable value. It can be seen in Figure 3-9 that  $E_{corr}$  for the old sample presents a value of  $\sim -0.30$  to  $-0.25$  V vs SCE.

The  $E_{corr}$  of new samples exposed to TNSW show in Figure 3-9 present some peaks that are in coincidence with the dosages of chlorine. With time, the amplitude of these peaks becomes less pronounced, but still detectable. After a long time exposure to TNSW (Old sample in Figure 3-9) the peaks corresponding to chlorination treatments are barely visible.

When compared with other materials such as high alloyed stainless steels, for which corrosion potential can vary by several hundreds of mV during chlorination treatments (0-100 mV variation for 0.1-0.2 ppm free chlorine to 500-700 mV variation for 0.5-1.0 ppm free chlorine), the range of potential variations for 70Cu-30Ni alloy is narrower, revealing a behavior with significantly reduced sensitivity towards free chlorine. Therefore, the risk of localized corrosion is reduced compared to high alloyed materials.

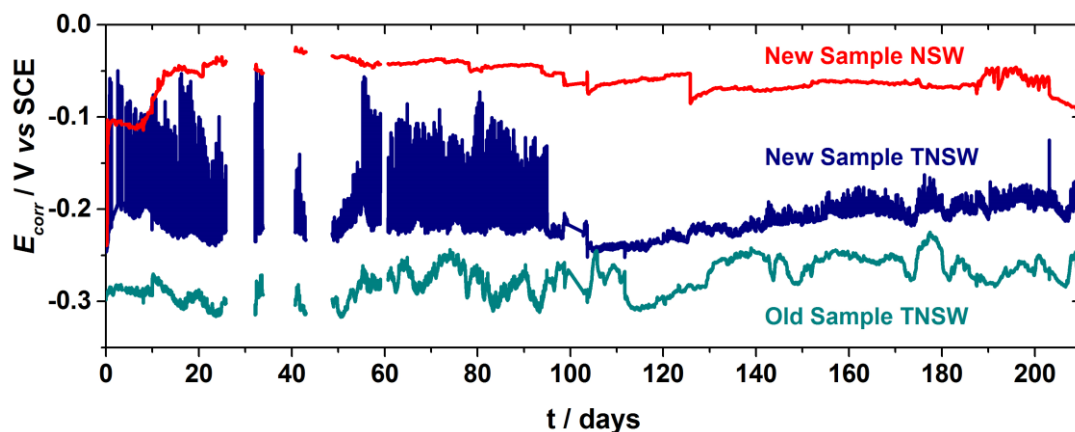
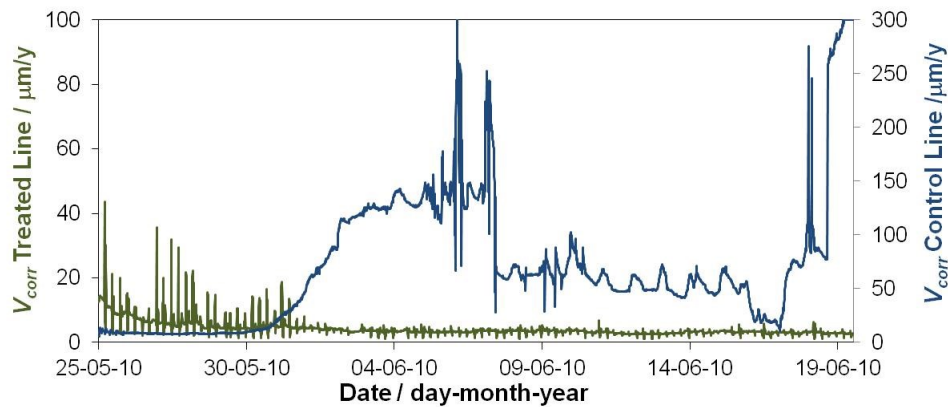


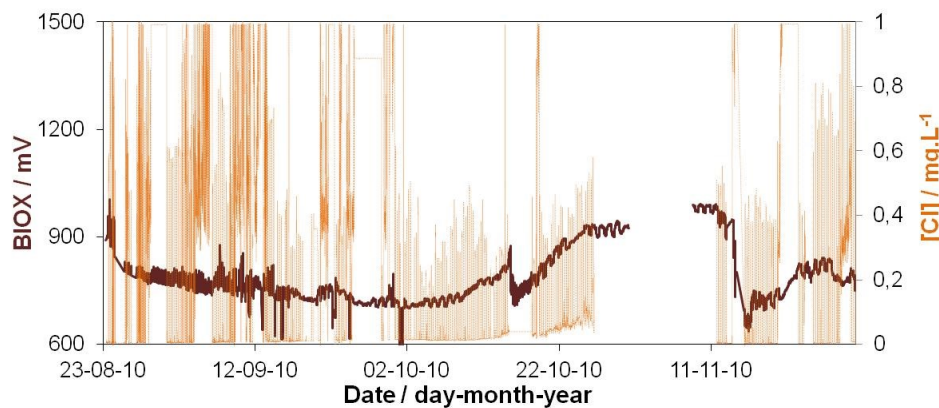
**Figure 3-9:** Corrosion potential ( $E_{corr}$ ) vs SCE of three 70Cu-30Ni samples (new and old) exposed to natural seawater (NSW) or treated natural seawater (TNSW) for a period of 210 days.

General corrosion rate ( $V_{corr}$ ) was measured by the LPR probe (Figure 2-9) in NSW and TNSW. Figure 3-10(a) shows the acquired data of new 70Cu-30Ni specimens at the beginning of exposure to seawater in both test lines, when a new biofilm starts growing. The effectiveness of the chlorination treatment is clearly shown by the low value of  $V_{corr}$  ( $< 20 \mu\text{m}/\text{year}$ ) for the sample exposed to TNSW, also by the difference in  $V_{corr}$  value between the samples exposed to NSW and to TNSW. Large variations of corrosion rates calculated from the continuous measurements in NSW are also visible (maximum value of  $V_{corr}$  of  $\sim 80 \mu\text{m}/\text{year}$  and minimum value of  $\sim 20 \mu\text{m}/\text{year}$ ). This difference between the maximum and the minimum values is believed to be due to the presence of localized corrosion.

Interruptions in graphs are due to electricity shut down in the power plant or, in the case of chlorine concentration, to chemicals depletion.



(a)



(b)

**Figure 3-10:** Monitoring system results. (a) Corrosion rate ( $V_{corr}$ ) of 70Cu-30Ni exposed to the chlorinated seawater (Treated line) and non-chlorinated seawater (Control line), and (b) BIOX signal (left side scale) and chlorine concentration (right side scale) for the 70Cu-30Ni/TNSW system in the period 22 August – 30 November 2010.

The BIOX signal increase together with the decrease of chlorine treatment is visible in Figure 3-10(b). The trend of the BIOX signal and the amplitude of the peaks shows how it is difficult to maintain a constant concentration of residual oxidant in the water and to get a total control of biofilm activity, in spite of the constant dosing of chlorine. Indeed, the chlorine demand of the water (mainly due to its reactions with the dissolved organic matter) can change during the same day, and this may explain the variability of the oxidant concentration at the surface of the BIOX probe metallic electrode.

Figure 3.11 shows the monitoring data for the period from January to March 2011.

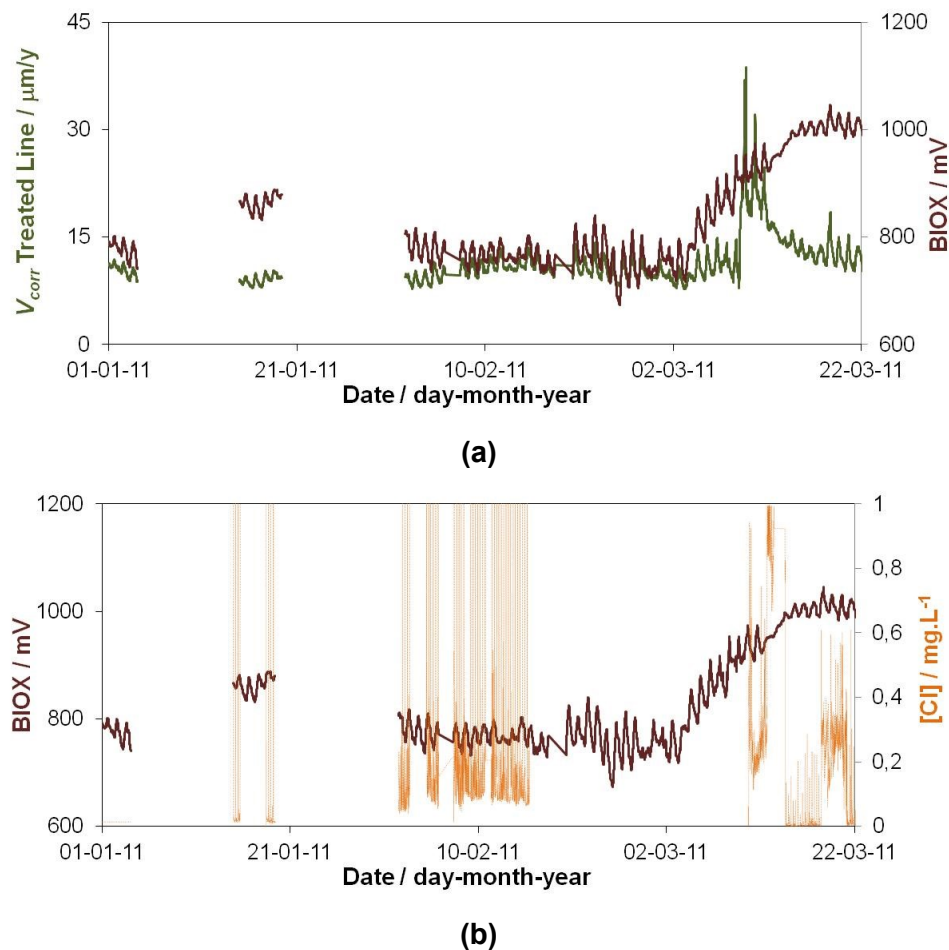


**Figure 3-11:** Monitoring system results. (a) Corrosion rate ( $V_{corr}$ ) (left side scale) and BIOX signal (right side scale) of 70Cu-30Ni exposed to chlorinated seawater in the period January-March 2011, and (b) BIOX signal (left side scale) and chlorine concentration (right side scale).

This is a critical period in which the biological activity, after the winter break, is higher. A peak can be observed on the  $V_{corr}$ , together with the increase of the BIOX signal, due to the growth of biofilm on the probe (Figure 3-11(a)). The peaks on the BIOX signal indicate

that the antifouling treatment was performed regularly, as in the winter period but it is not perfectly adjusted to the increase of biological activity. Figures 3-11(a) and (b) shows that higher concentrations of chlorine were sufficient to lower the corrosion rate of the probe, although the treatment is not effective enough to destroy the biological activity on the BIOX probe (BIOX signal remains high).

The monitoring data for the period from April to June 2011 are reported in Figure 3-12(a). Around the 20<sup>th</sup> of May, the electrodes of the corrosion probe were replaced by other samples that were previously exposed to treated seawater and chemically cleaned for weight lost measurements. Even in this case, the graph shows the effectiveness of the chlorination treatment (low corrosion rates for samples exposed to treated seawater).

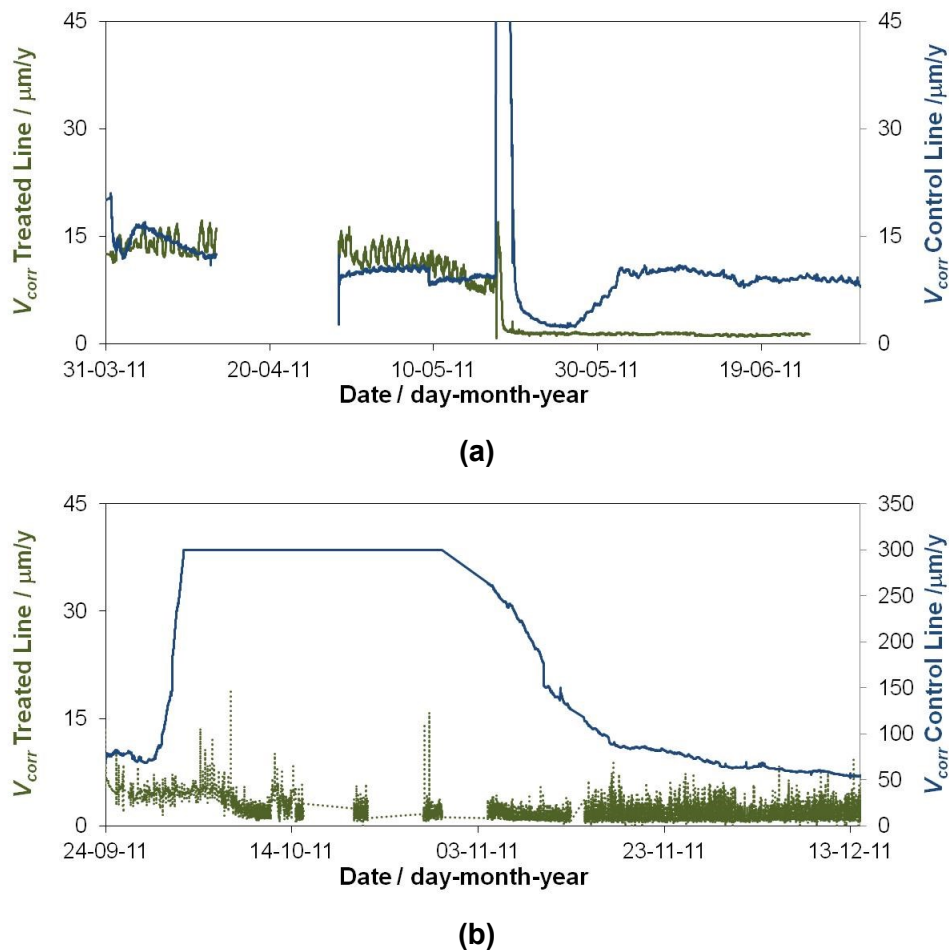


**Figure 3-12:** Monitoring system results. Corrosion rate ( $V_{corr}$ ) of 70Cu-30Ni exposed to chlorinated seawater (Treated Line) and non-chlorinated seawater (Control Line) in the period (a) April-June 2011 and (b) October-December 2011.

Figure 3-12(b) shows the monitoring data covering the period from late September to December 2011 (after the summer stop). The static conditions in the lines during the summer stop caused the increase of the corrosion rate in both lines, although limited in the treated line. The biofilm is particularly aggressive and grows very rapidly in static conditions. In stagnant waters or at very low flow rates, the oxygen can be quickly consumed by the biofilm and anoxic conditions (partial or total absence of oxygen) can occur. The pH lowers, due to microorganisms activity, and local conditions become particularly aggressive, which can lead more quickly to the puncture of the tubes.

The correlation between the BIOX signal and seawater red-ox potential is reported on Figure 3-13. Both probes were affected by the chlorination treatment (peaks), but at the end of the chloride dosage, the seawater red-ox potential is not able to return to the baseline value, unlike the BIOX signal. The low BIOX base-line signal indicates that the antifouling treatment was effective enough to destroy the biological activity on the BIOX probe.

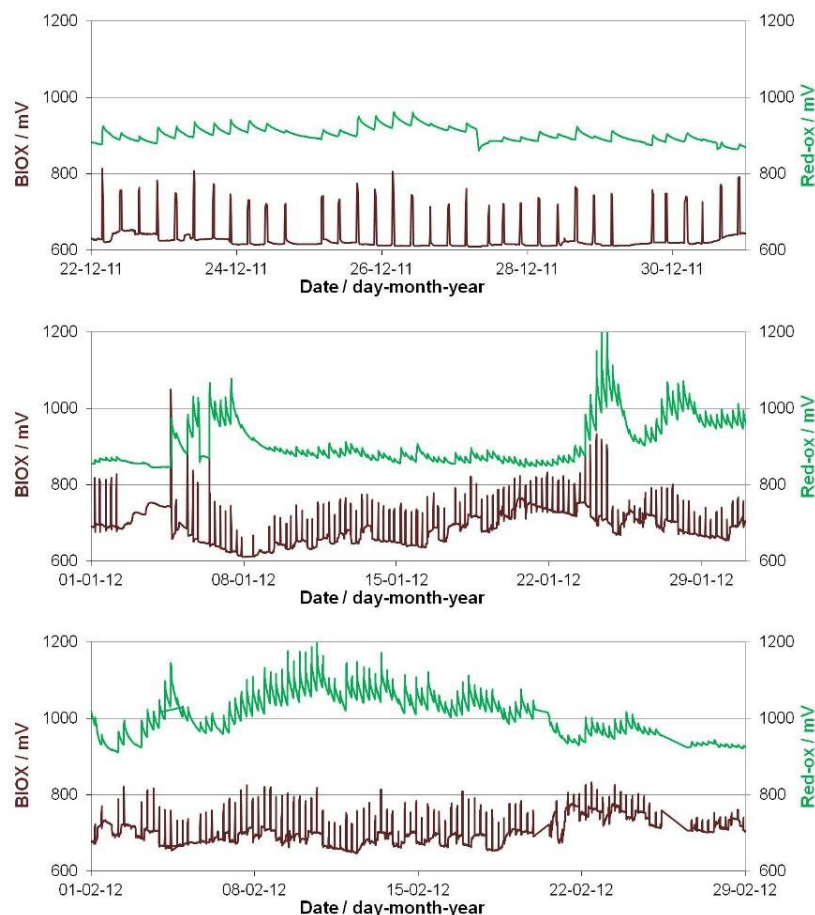


**Figure 3-13:** BIOX signal (left side scale) and chlorinated seawater (Treated Line) red-ox potential (right side scale) from end December 2011 to end February 2012.

Natural seawater red-ox potential base line is below 0.4 V (Figure 3-14(a)), to be compared to the value  $> 0.8$  V obtained in TNSW. If we look at the BIOX signal in the two solutions, during the same period, a constant saturation of the signal can be observed in the control line, indicating fouling conditions.

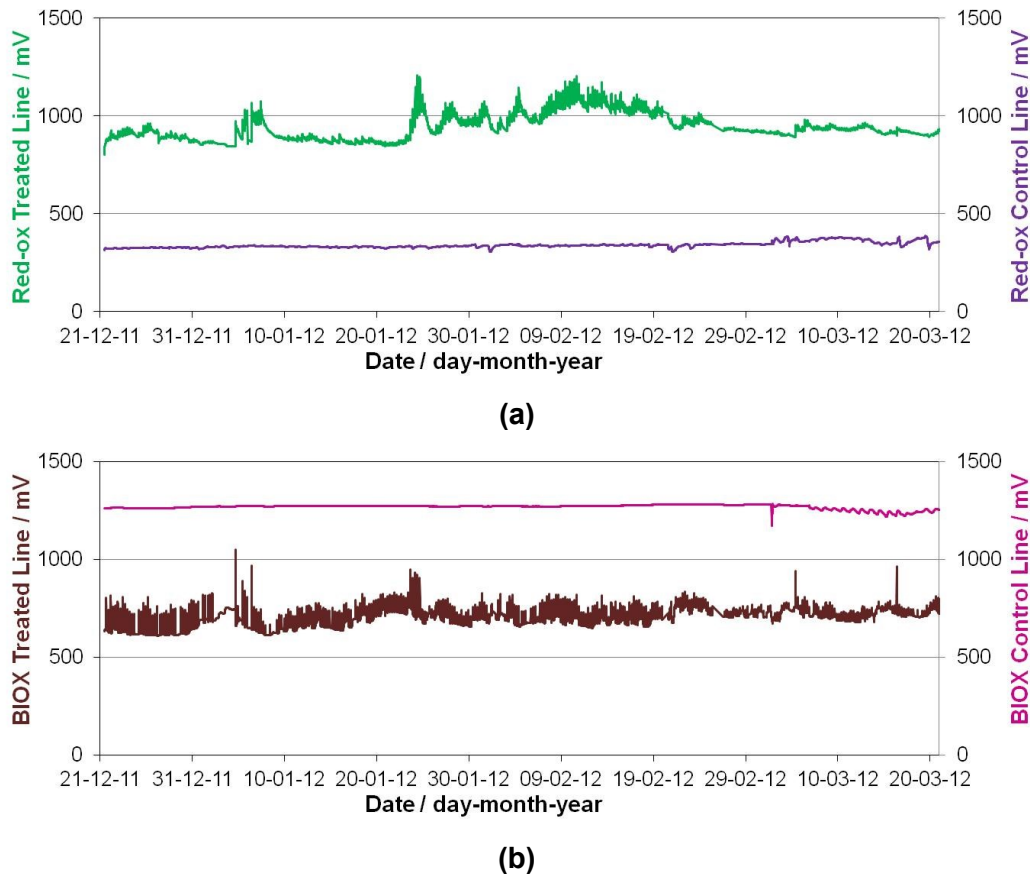


**Figure 3-14:** Monitoring system results. (a) Seawater red-ox potential in the treated line (left side scale) and in the control line (right side scale); (b) BIOX signal for the treated line (left side scale) and for the control line (right side scale), from end December 2011 to middle March 2012.

Temperature is also an important parameter to be considered. Figure 3-15(a) shows the temperature data for the two lines during the pre-spring period. In the treated line the temperature is raised, due to the passage through the heat exchanger (compared with the control line). During the winter month of February, a small increase of the BIOX signal was detected in FNSW (Fig. 3-13), together with an increase of the temperature (Fig 3-15(a)), and incoming slime (detected by the Nephelometer; Fig. 3-15(b)), indicating fouling conditions. In March, the flow disturbance in the control line is emphasized by the variation of temperature between day and night, due to static conditions inside the pipes. The increase of

the turbidity signal with time can be explained by the fouling of the sensor, and the peaks are due to occasions of real turbidity.

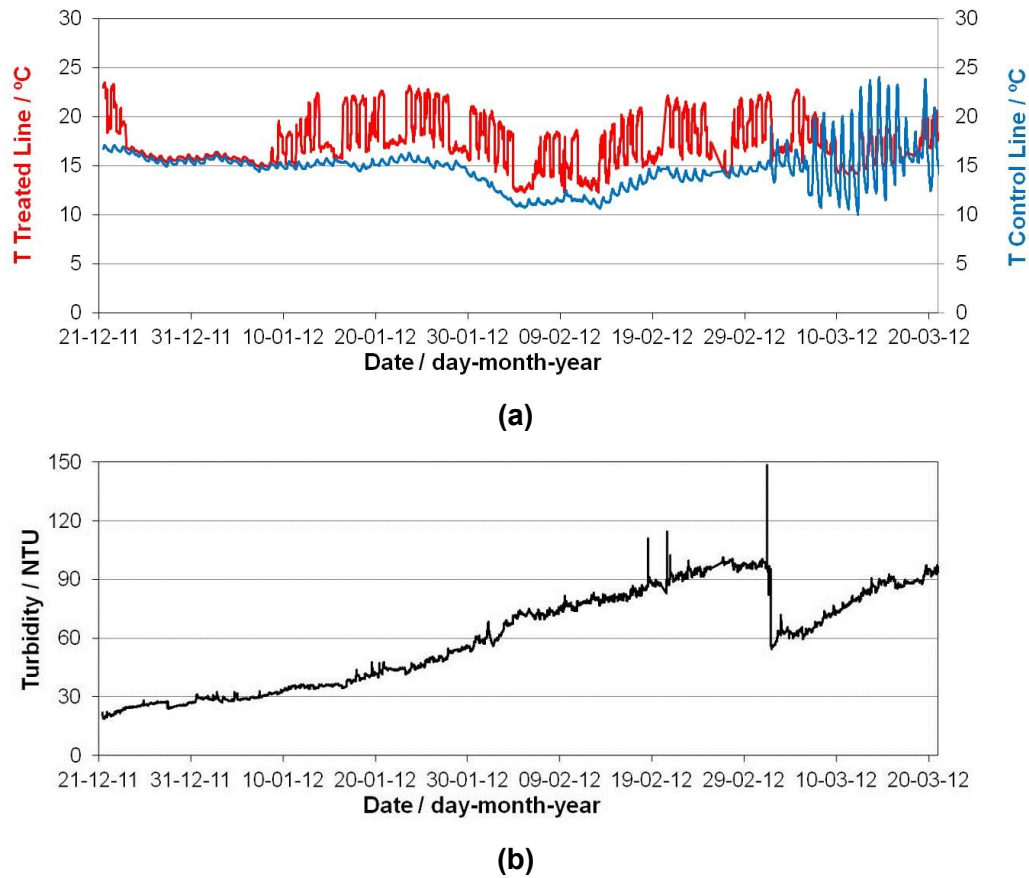


**Figure 3-15:** Monitoring system results. (a) seawater temperature in the treated line (left side scale) and in the control line (right side scale); (b) seawater turbidity for the treated line. Period from the end December 2011 to middle March 2012.

### 3.3.2 AL BRASS – ONLINE MEASUREMENTS

The major corrosion problems associated with aluminum brass are general corrosion, flow-accelerated corrosion (FAC) and stress-corrosion cracking [160]. However, it presents an excellent corrosion protection behavior due to the formation of a thin, dense and adherent shielding film which forms naturally and quickly on exposure to clean seawater. This film is complex and consists predominantly of cupric and cuprous oxides [161], which form a “barrier” between the alloy surface and the seawater. FAC and erosion corrosion (EC) are frequently used interchangeably to describe analogous material degradation processes. The differences between both are related to the mechanism by which the protective film is removed from the metal surface. In the EC process, the oxide film is mechanically removed

from a metallic substrate, whereas in the FAC process, the protective oxide film is not mechanically removed but dissolved or banned from forming, allowing corrosion of the unprotected surface. EC is a common water-side phenomenon encountered with aluminum brass condenser tubes [160]. It occurs in areas where the turbulence intensity at the metallic surface is high enough to cause mechanical or electrochemical disruption of the protective oxide film. Turbulence increases as the flow velocity increases, and it is greatly influenced by the geometry of the tubes. Usually, the turbulence intensity is much higher at the tube inlets; therefore, if erosion-corrosion is a problem, it is commonly found in the first 25 cm length of the tubes.

Ferrous salt is a normal and recommended corrosion inhibitor for Al brass [109]. It promotes the formation of a ferric oxide layer in the form of lepidocrocite ( $\text{FeO}\cdot\text{OH}$ ), that provides a good protection for this copper alloy. Turbulent water flow conditions can cause local erosion of the protective films and result in localized deep attack by a combination of corrosive and erosive action. To know if oxidizing treatments associated with ferrous ions treatments are effective if corrosion-erosion of Al brass occurs, it is very important to monitor, control and study, case by case, the effectiveness of the antifouling and anticorrosive treatments.

Smooth and stepped Al brass specimens (Figure 3-16), with steps of  $\sim 0.3$  mm depth and 1 mm width, 60 mm length and 20 mm diameter, were inserted in a test line with the same characteristics as the one previously described (Figure 3-2). The steps were dug with the aim to stress the turbulence on the metallic surface.

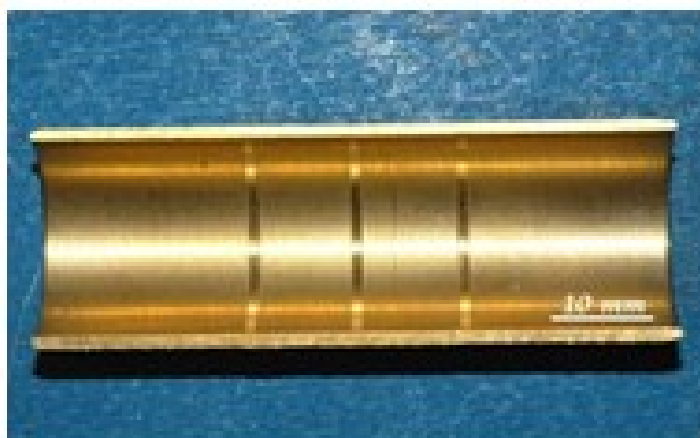


**Figure 3-16:** Longitudinal view of Al brass stepped specimens.

At the end of November 2010, in addition to the antifouling treatment applied in this plant, discontinuous treatments with  $\text{FeSO}_4$  started, with a concentration of  $0.3\text{--}0.5 \text{ mg.L}^{-1} \text{ Fe}^{2+}$  at outlet, lasting one hour every two days ( $\text{ClO}_2$  dosages suspended during  $\text{FeSO}_4$  treatments). Examples of monitoring of antifouling and anticorrosive treatments, carried out with the BIOX and corrosion probes made of Al brass, are reported in Figure 3-17.

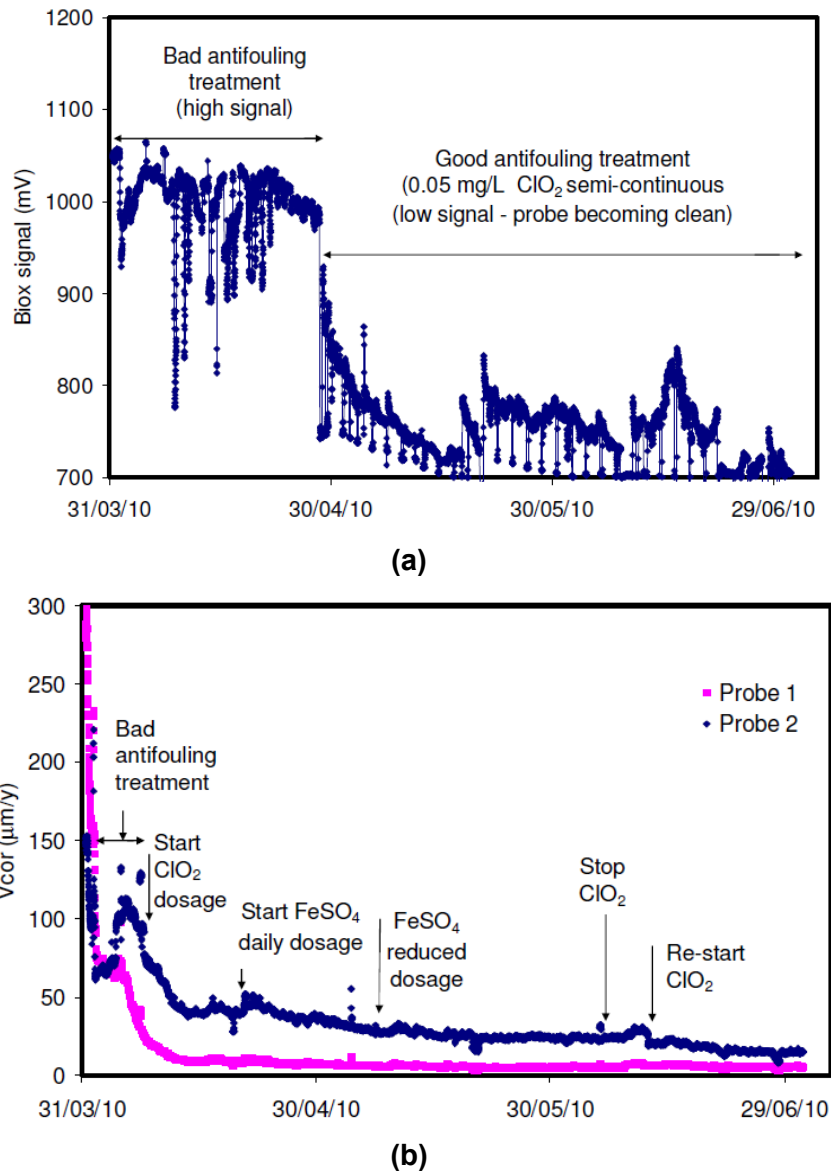
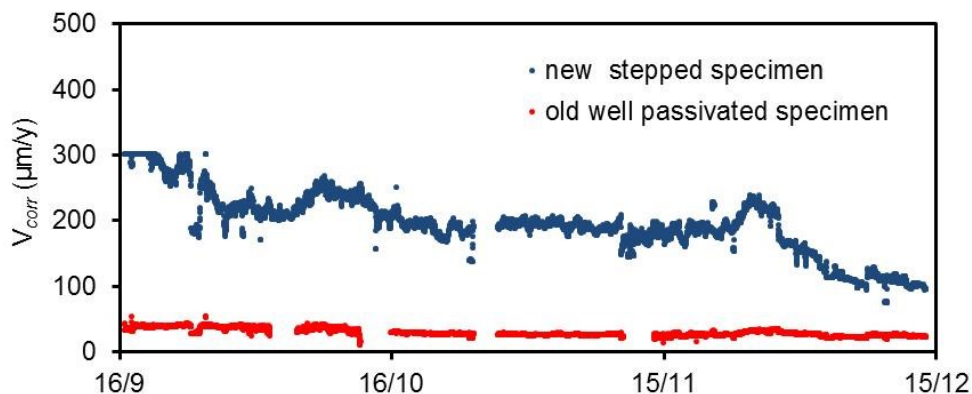


**Figure 3-17:** Monitoring results in treated natural seawater (TNSW). (a) Antifouling treatment monitored by the BIOX probe and (b) Al brass corrosion rate ( $V_{\text{cor}}$ ), estimated with two probes: probe 1 with smooth specimens; probe 2 with smooth and stepped specimens.

Up to April 29, the  $\text{ClO}_2$  treatment did not work correctly, due to lacks in the dosage system. As a consequence of the  $\text{ClO}_2$  deficiency, the BIOX signal (mV) reached the

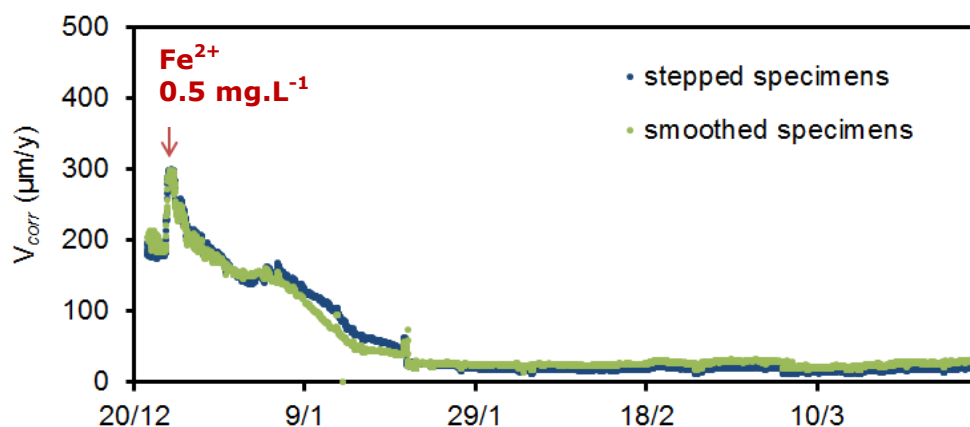
saturation value ( $> 1000$  mV), indicating the presence of biofilm covering the electrode surface. When the regular treatment was recovered, the signal drop to a baseline of  $\sim 700$  mV indicated the deactivation of the biofilm. The periodic decrease of the signal close to this baseline was due the temporary interruption of the  $\text{ClO}_2$  treatment for the dosage of ferrous ions. The complete destruction of the biofilm was reached at the end of June, when the  $\text{ClO}_2$  treatment was stopped again for few days and the BIOX signal stayed close to the baseline. Figure 3-17(b) shows the monitoring of the corrosion rate with two Al brass probes: probe 1 with not stepped specimens; probe 2 with stepped specimens. Probe 1 shows lower  $V_{\text{corr}}$  values, indicating that in the stepped specimens, besides the antifouling treatment, the oxide film is less protective.

Figure 3-18 presents the behavior of a non stepped passivated Al brass specimen (old), together with a stepped, not passivated specimen (new), during the period from September to December 2010. The graph clearly shows the low and steady-state corrosion rate of the old specimen in comparison with the high and instable corrosion rate of the new one.



**Figure 3-18:** Monitoring results. Corrosion rate trends of Al brass specimens in treated natural seawater: non stepped specimen (old) and stepped specimen (new).

At the end of December 2010, the corrosion probes were substituted by new ones and the  $\text{FeSO}_4$  dosages (1 h/day) were increased in order to have a residual concentration of  $\text{Fe}^{2+}$  of  $0.5 \text{ mg.L}^{-1}$  as total residual oxidant concentration in the water at the condenser tube outlet. Only one month was enough for reaching a good passivation of the specimens (Figure 3-19). The  $V_{\text{corr}}$  of stepped and smoothed samples is similar, indicating that the  $\text{FeSO}_4$  dosages were enough to passivate also the stepped specimens (controlled turbulence effect).



**Figure 3-19:** Corrosion rate trend of new Al brass stepped and smoothed (not stepped) specimens immersed in natural seawater with  $\text{FeSO}_4$  dosages ( $0.5 \text{ mg.L}^{-1} \text{ Fe}^{2+}$ , 1 h/day).

In March 2010, other new electrodes (smoothed + stepped) were exposed to flowing seawater treated with  $\text{Fe}^{2+}$  ( $0.5 \text{ mg.L}^{-1}$ , 1 h/day plus  $1 \text{ mg.L}^{-1}$  1 h/week). Passivation was reached within about 15 days, as shown in Figure 3-20.

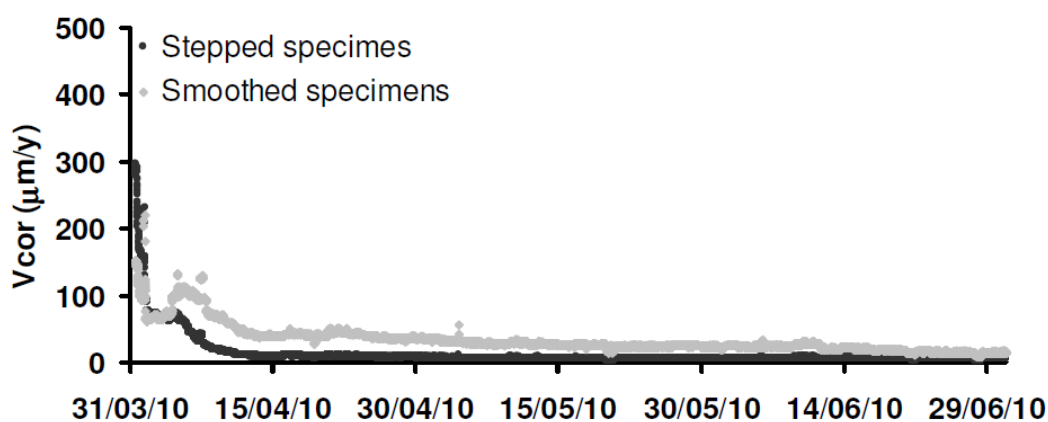


**Figure 3-20:** Corrosion rate trend of new Al brass stepped and smoothed (not stepped) specimens with  $\text{FeSO}_4$  dosages ( $0.5 \text{ mg.L}^{-1} \text{ Fe}^{2+}$ , 1 h/day +  $1 \text{ mg.L}^{-1} \text{ Fe}^{2+}$ , 1 h/week).

### 3.3.3 70Cu-30Ni ALLOY AND AL BRASS - OFF-LINE MEASUREMENTS

#### 3.3.3.1 VISUAL OBSERVATIONS

Figure 3-21 reports morphological observations of different 70Cu-30Ni samples: A24 and A9 samples were immersed in chlorinated seawater (TNSW) and A1 and T16 samples in natural seawater (NSW) for a period of 80 days (same water and treatment as reported in

sections 2.1.2.1.1 and 2.1.2.1.2). The surface of the samples exposed to TNSW are covered by a protective uniform brown/green oxide film, whereas samples exposed exhibit localized corrosion. Shining metal appears inside the attack points (after acidic cleaning; Figs. 3-21(b, d)) and the presence of non-protective red oxides is clearly visible.

Copper alloys tend to suffer pitting attack and some forms of pitting are specifically associated to biofilm, both in aerobic or anaerobic conditions [162]. Occluded pits contain red cuprous oxide crystals and the metallic surface is overlaid with exfoliating crusty corrosion products changing in color from deep green to purplish black [163]. In anaerobic condition, the pits take the form of sulfide-rich “pepper-pot” tubercles.

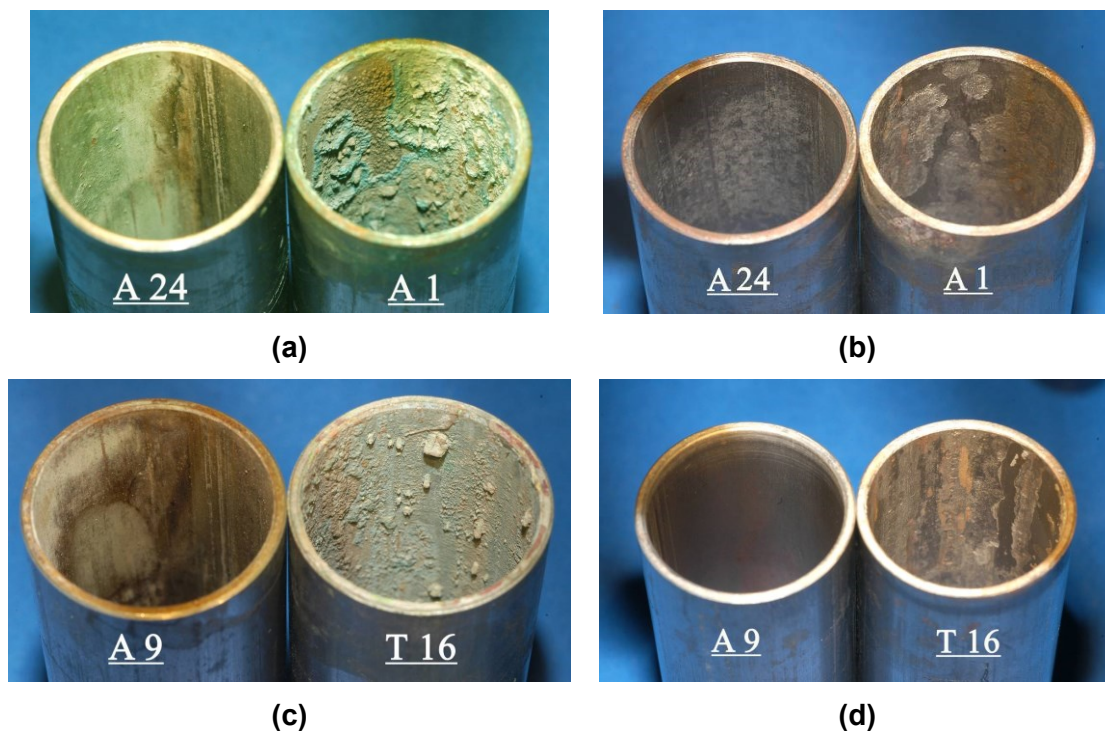


**Figure 3-21:** 70Cu-30Ni samples extracted from the hydraulic lines after 80 days of operation: A24 and A9 samples were exposed to TNSW, and A1 and T16 ones to NSW. (a,c) Before and (b, d) after acidic cleaning.

### 3.3.3.2 WEIGHT LOSS MEASUREMENTS

Gravimetric measurements were performed with a few specimens following the procedure exposed in section 2.2.1.2.1. Tables 3-1 and 3-2 present the results of weight loss measurements performed with samples at different exposure times. Figure 3-22 shows the pictures of the corrosion probes after 405 days of operation in TNSW or NSW.

Corrosion rates ( $C_r$ ) presented in Tables 3-1 and 3-2 were calculated from weight losses by application of Faraday's law Eq. 2-5.

The small amounts of deposit (difference between "initial weight" and weight after cleaning only with water, in order to remove mud and debris) indicate the absence of significant precipitation of mud and corrosion products on the samples. Weight losses and the corresponding corrosion rates are also presented in Tables 3-1 and 3-2. The continuous decrease of the corrosion rate in NSW over time indicates the tendency of the alloy to create a protective surface layer. In TNSW,  $C_r$  is similar for the different exposure times.

**Table 3-1:** Off-line measurements. Weight loss measurements performed with 70Cu-30Ni samples exposed to treated natural sweater.

Sample	Exposure time	Length (cm)	Deposit (mg.cm <sup>-2</sup> )	Weight loss (mg.cm <sup>-2</sup> )	$C_r$ (µm/year)
A9	80	6	0.036	0.322	6.018
A24	80	6	0.038	0.443	6.811
A27	164	6	0.061	0.417	4.643
A15	164	6	0.055	0.438	4.339
A6	290	6	0.073	1.979	5.251
A19	290	6	0.144	1.727	7.248
A21	290	6	0.263	1.022	10.167
Corrosion probe	T10	405	6	0.140	3.785
	T34	405	4	0.133	1.342
	T14	405	6	0.255	0.948
	T33	405	4	0.101	2.110
	T13	405	6	0.166	3.266

**Table 3-2:** Off-line measurements. Weight loss measurements performed with 70Cu-30Ni samples exposed to natural sweater.

Sample	Exposure time	Length (cm)	Deposit (mg.cm <sup>-2</sup> )	Weight lost (mg.cm <sup>-2</sup> )	$C_r$ (µm/year)
A1	80	6	0.742	1.300	159.944
T16	80	6	0.589	0.900	111.138
A2	164	6	3.094	1.499	95.588
A3	164	6	7.213	1.034	78.772
A5	290	6	3.600	0.915	35.464
A10	290	6	7.716	1.206	50.988
Corrosion probe	T9	405	6	1.080	1.033
	T35	405	4	3.445	0.690
	T23	405	6	4.242	0.994
	T36	405	4	1.401	0.660
	T19	405	6	5.765	0.849

The values obtained are in agreement with the electrochemical data, from the corrosion probes that were used to estimate the corrosion rate by the LPR technique, and show a much lower corrosion rate for samples exposed to TNSW.

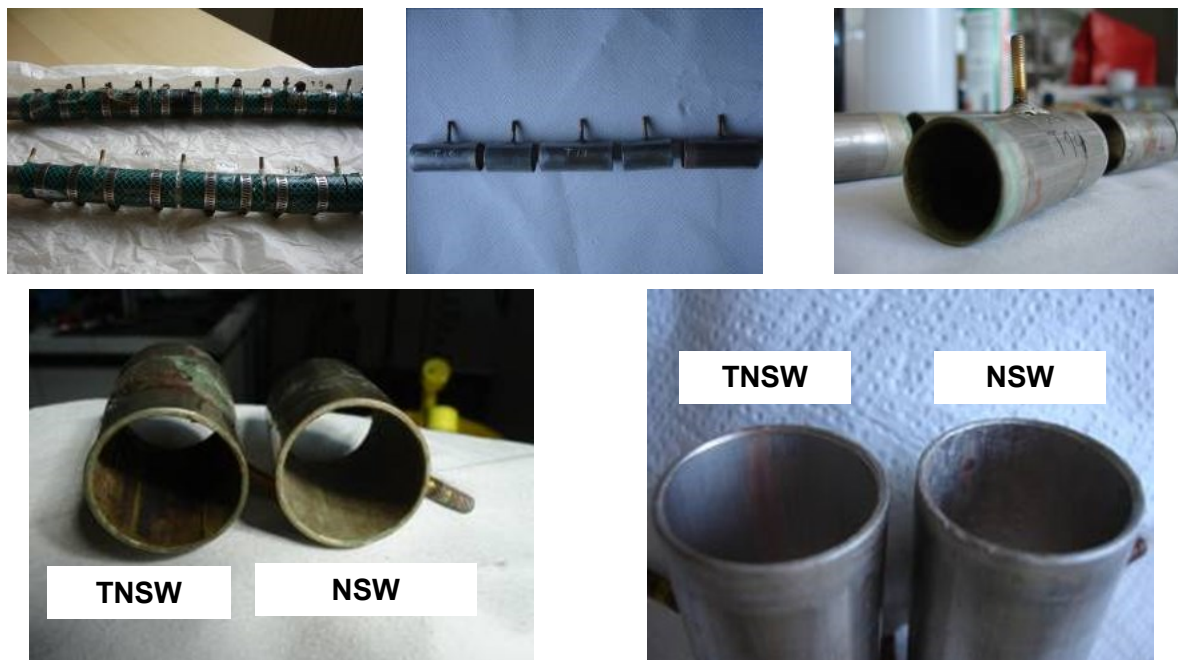


**Figure 3-22:** Off-line measurements. 70Cu-30Ni corrosion probes extracted from the hydraulic lines after 405 days of operation in treated natural seawater (TNSW) or natural seawater (NSW).

### 3.3.3.3 MICROBIOLOGICAL ANALYSES

For bacteria identification (by genetic analyses) at different stages of biofilm growth, condenser tubes samples (6-cm long) have been inserted in the hydraulic loop. A set of 9 70Cu-30Ni and Al brass samples exposed for one year to NSW (long time) or TNSW (low, stable BIOX base line and low corrosion rate) and for 2 days to NSW (high corrosion rate and low BIOX signal).

Deoxyribonucleic acid (DNA) is a molecule responsible for preserving genetic information across species and across time. It consists of a meaningful arrangement of chemicals called nucleotides that are symbolized by A (adenine), T (thymine), C (cytosine) and G (guanine). These arrangements express the story of each organism or individual, in that the code they produce, represent a detailed instruction book for that organism or individual.

Molecular biology approach is a fingerprinting methodology. First, DNA fragments from a sample containing multiple organisms are amplified (production of millions of copies of a specific DNA sequence) using the polymerase chain reaction (PCR). These amplified products generally entail sequences that are well conserved from organism to organism – for example, sequences for the 16S rDNA are a common choice. This collection of fragments is then subjected to the Denaturing Gradient Gel Electrophoresis (DGGE) component of the procedure. DGGE is a particular type of gel electrophoresis where DNA, which is negatively charged, is attracted by the positive electrode and forced to migrate through the pores of a polyacrylamide gel. Once it reaches the concentration of denaturing reagents at which it unwinds, it is said to have melted. This determines the melting domains, which are defined as stretches of base pairs with an identical melting temperature. In other words, base pairs formed by nucleotides A, T, C and G are chemically melted apart.

Among these 9 samples, 8 of them were positive for DNA as revealed by nanodrop spectroscopy and bacteria 16S PCR amplification using 341F+GC and 907R primers.

DGGE analysis of the samples indicate 24 visible bands (Figure 3-23). Attempts were made to incise all visible bands but, only a representative was acquired.

From the DNA extracted from 70Cu-30Ni and Al Brass samples, sequencing results reveal the presence of bacteria species belonging to gammaproteobacteria, such as *Marinobacter adhaerens* (99%<sup>§</sup>), *Alteromonas macleodii* (99%), and *Pseudomonas spp.* (90%).

Genus of *Pseudomonas* are known to produce extracellular polymeric substances (EPS) which contribute to the mechanical stability of biofilms, mediate their adhesion to surfaces and form a cohesive, three-dimensional polymer network that interconnects and transiently immobilizes biofilm cells [164]. These species have been shown to colonize the copper surface [82] and accelerate corrosion of copper and copper alloys [83].

In the global oceans, one of the most ever-present and assumed to have significant impact in a variety of biogeochemical cycles is the genus of *Marinobacter* [165].

The metal binding ability of bacterial EPS is very well known [170]. *Alteromonas macleodii* produces EPS with a high metal-binding ability [166] and uronic acid-rich extracellular polysaccharides [167-169]. EPS extracted from *Marinobacter* species [171] is widely employed in bioremediation of heavy metals such as Ni and Cu [171, 172].

---

<sup>§</sup> 99% indicates how similar the sequence is to the one saved in database of recognized strains.

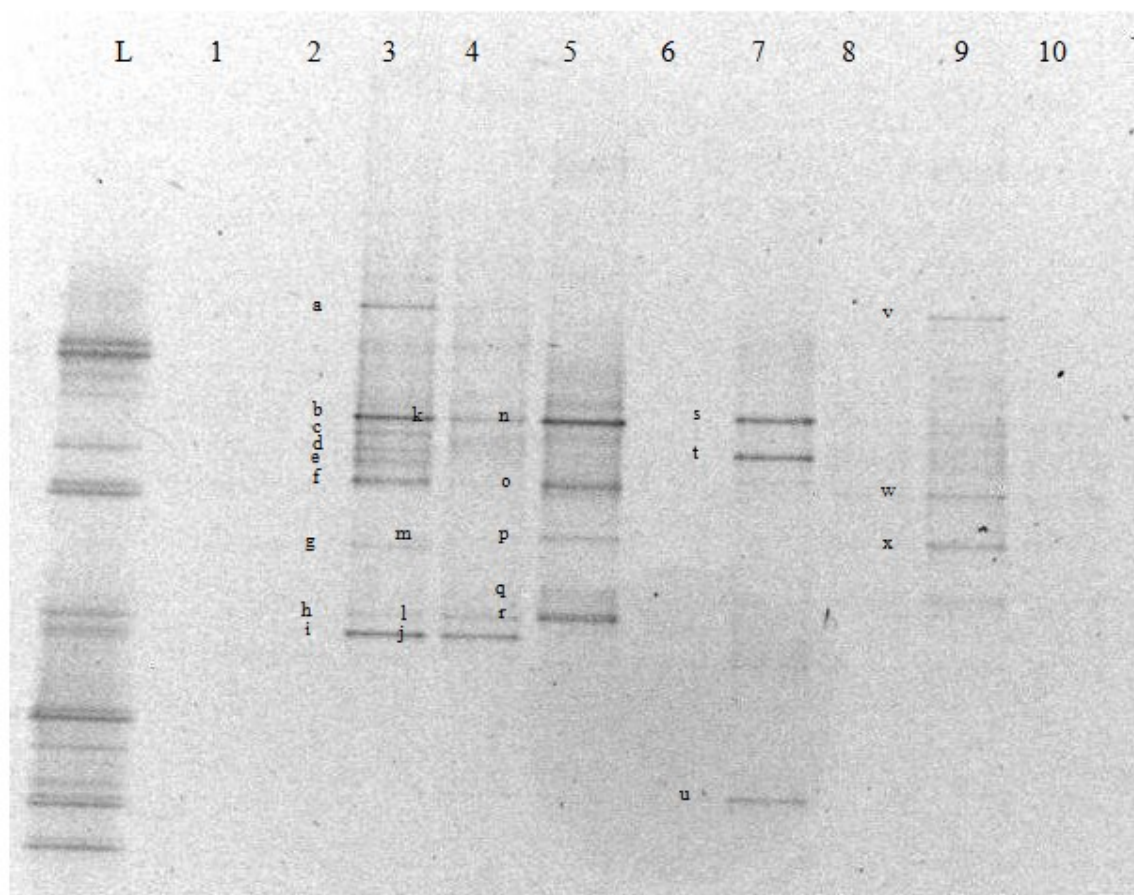


**Figure 3-23:** Six percent DGGE gel showing biodiversity data from 70Cu30Ni and Al brass samples exposed to LTTNSW (long time (one year) to treated natural seawater), LTNSW (long time to natural seawater) and 2DNSW (2 days to natural seawater). Lanes 1 and 2: 70Cu30Ni/LTNSW; lanes 3, 4 and 5: 70Cu30Ni/LTTNSW; lanes 6 and 7: Al brass/2DNSW; lane 8: Al brass/LTNSW; and lane 9 70Cu30 Ni 2D/NSW.

From the agarose gel shown in Figure 3-24, it is observed that 70Cu-30Ni and Al brass samples in lanes 1 and 2 (70Cu-30Ni exposed for long time (one year) to NSW), 6 (Al brass exposed for 2 days to NSW) and 8 (Al brass exposed for long time to NSW) were negative to the presence of bacteria. 70Cu-30Ni and Al brass samples exposed for long time to TNSW showed biodiversity (totality of genes, species, and ecosystems of a region) if compared to the polyacrylamide denaturing gel (DGGE Figure 3-23); similarities are observed in the representatives of microbial communities in the sample. Although on the polyacrylamide gel, the diversity is more in samples 3 and 5.

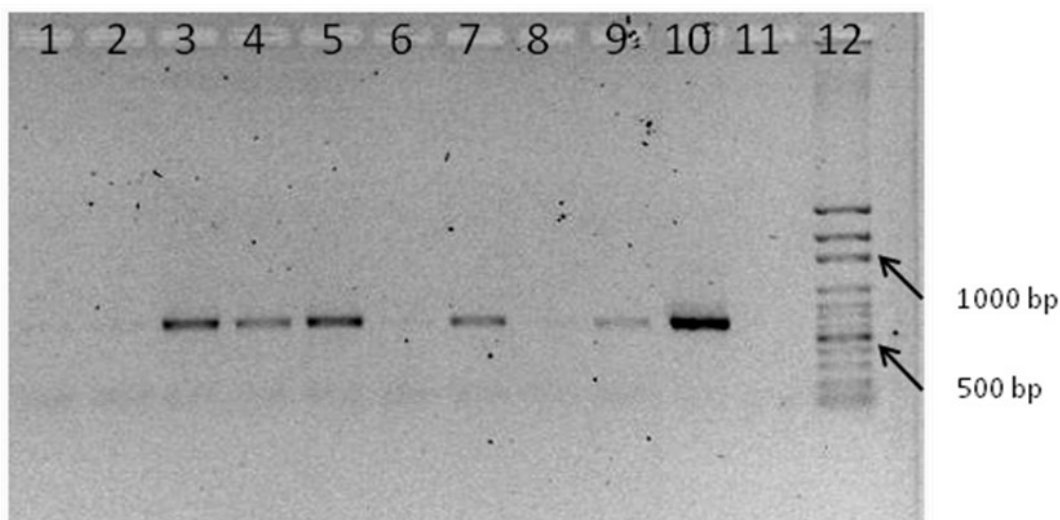


**Figure 3-24:** Bacterial 16S rRNA gene (550 bp); 70Cu30Ni and Al brass samples on 0.9% agarose gel exposed previously to LTTNSW (long time (one year) to treated natural seawater), LTNSW (long time to natural seawater) and 2DNSW (2 days to natural seawater). Lanes 1 and 2: 70Cu30Ni/LTNSW; lanes 3, 4 and 5: 70Cu30Ni/LTTNSW; lanes 6 and 7: Al brass/2DNSW; lane 8 Al brass/LTNSW; lane 9 70Cu30Ni/2DNSW; lane 10 *D. alaskensis* (positive control); lane 11 negative control (PCR water); and lane 12 100 bp DNA ladder.

From the results above, it can be drawn that while the cooling lines were treated, overtime, organisms grow in the systems. This could result from the depletion of the treatment in the system or the selection of more resistant bacterial populations.

### 3.4 CONCLUSIONS

The results are in agreement with previous monitoring campaigns [152], where the relevant role of biofouling against the formation of protective oxide layers on the surfaces of copper alloys exposed to seawater and, the positive influence of chlorination treatments on the formation of these protective oxide layers were confirmed.

For 70Cu-30Ni alloy:

- When biofilm starts growing on new samples exposed to seawater, it can be observed:
  - with chlorination: a quite constant and low value of the corrosion rate;
  - without chlorination: high values of the corrosion rate.
- The quite stable base line value of the BIOX signal confirms that chlorination treatments were enough to strictly control the biofilm growth.

- The corrosion rates monitored with the LPR probe were in agreement with weight loss measurements.

For aluminum brass:

- When operating at high flow rates (up to  $1.8 \text{ m.s}^{-1}$ ), Al brass could suffer from corrosion-erosion problems. Periodical dosages of ferrous ions with a concentration of  $0.5 - 1 \text{ mg.L}^{-1}$  to inhibit the corrosion of Al brass are recommended. When increasing the  $\text{Fe}^{2+}$  concentration, the time required for reaching passivity ( $V_{\text{corr}} < 20 \text{ }\mu\text{m/y}$ ) is reduced to few weeks.

For both alloys:

Microbiological and molecular analysis of 70Cu-30Ni and Al brass samples indicated the bacteria species found in biofilms formed on copper alloys exposed to seawater; these species were: *Marinobacter*, *Alteromonas* and *Pseudomonas*. Similar bacteria can be found in waters of different parts of the world. This fact can underline an important influence of metallic substrate chemical composition on bacteria selection. Furthermore, a biodiversity was found in samples that were exposed for long period to treated seawater.

Copper alloys condenser tubes suffer from biofouling problems that can result in serious damages. Biofouling is a consequence of biofilm formation. There are two opposite goals for the control of microbial adhesion and biofilm formation: one is the prevention of biofilms, and the other one is their promotion. Controlling the adsorption of biomolecules, which is the first step in biofilm formation, by modifying the surface properties of the material may represent a good strategy for inhibiting microbial growth. For this reason, in the next chapter, the influence of solution (FNSW vs ASW) and biomolecule concentration (biomolecules naturally present in seawater vs BSA) on the electrochemical behavior and the surface chemical composition of 70Cu-30Ni alloy in seawater, in static conditions is presented.

## CHAPTER 4 – EFFECT OF SOLUTION AND BIOMOLECULE CONCENTRATION

Copper alloys often used in cooling circuits of industrial plants can be affected by biocorrosion induced by biofilm formation. The objective of this chapter was to study the influence of solution (FNSW vs ASW) and biomolecule concentration (biomolecules naturally present in seawater vs BSA) on the electrochemical behavior and the surface chemical composition of 70Cu-30Ni alloy in seawater, in static conditions. For that purpose, electrochemical measurements performed after 1 h of immersion were combined to surface analyses.

In order to study biomolecule concentration, results obtained in ASW and FNSW were compared with those obtained in ASW with 20 mg.L<sup>-1</sup> of BSA (ASW + BSA). BSA is a model protein often used to study the protein-surface interactions due to its low cost and to a good knowledge of its properties [145, 173, 174].

### 4.1 RESULTS

#### 4.1.1 ELECTROCHEMICAL MEASUREMENTS

##### 4.1.1.1 CORROSION POTENTIAL ( $E_{CORR}$ ) VS TIME

Natural seawater was collected at the inlet of a condenser (Italian thermal power plant) and filtered with 1  $\mu$ m filter paper. Although filtration removes most of the organic matter, including bacteria, some biomolecules still remain in FNSW, but at low concentration.

Before each experiment, the corrosion potential was followed as a function of time ( $E_{corr}$  vs time). During the first hour of immersion, the corrosion potential  $E_{corr}$  decreases till reaching a steady-state value of  $-0.230 \pm 0.009$  V vs SCE in ASW. The  $E_{corr}$  value in FNSW is  $-0.231 \pm 0.013$  V vs SCE. Therefore, the  $E_{corr}$  values obtained in ASW are comparable to those obtained in FNSW. BSA induces a more anodic corrosion potential; thus, after 1 h of immersion, its value is equal to  $-0.203 \pm 0.005$  V vs SCE (difference of  $\sim 30$  mV with the value found in FNSW and in ASW without protein).

##### 4.1.1.2 CATHODIC AND ANODIC POLARIZATION CURVES

Figure 4-1(a) shows the cathodic polarization curves obtained in FNSW, and in ASW without and with 20 mg.L<sup>-1</sup> of BSA. Two current plateaus, illustrating pure mass transport

limitation, can be clearly observed in all cases. The short plateau at around -0.30 V vs SCE ( $|j| \sim 10 \mu\text{A.cm}^{-2}$ ) illustrates the first step of dissolved oxygen reduction with production of  $\text{H}_2\text{O}_2$ , that can be written at pH = 8.0 as follows [127, 175]:



The wide plateau observed for potentials ranging from -0.40 down to -1.00 V vs SCE corresponds to the second step of dissolved oxygen reduction with transfer of 4 electrons, that can be written at pH = 8.0 as follows:



The ratio between the two plateau current densities is comprised between 2 and 3 (theoretical value : 2). This observation is consistent with the presence on the alloy surface of a layer composed of reducible products (oxides) in the oxygen reduction domain.

If comparing ASW and ASW + BSA, the second plateau current density is divided by 2 in the presence of the protein ( $|j| \sim 40 \mu\text{A.cm}^{-2}$  without BSA to be compared to  $|j| \sim 20 \mu\text{A.cm}^{-2}$  with BSA). This difference in plateau current is not necessarily due to the BSA but may also be induced by a difference in natural convection from one experiment to another.

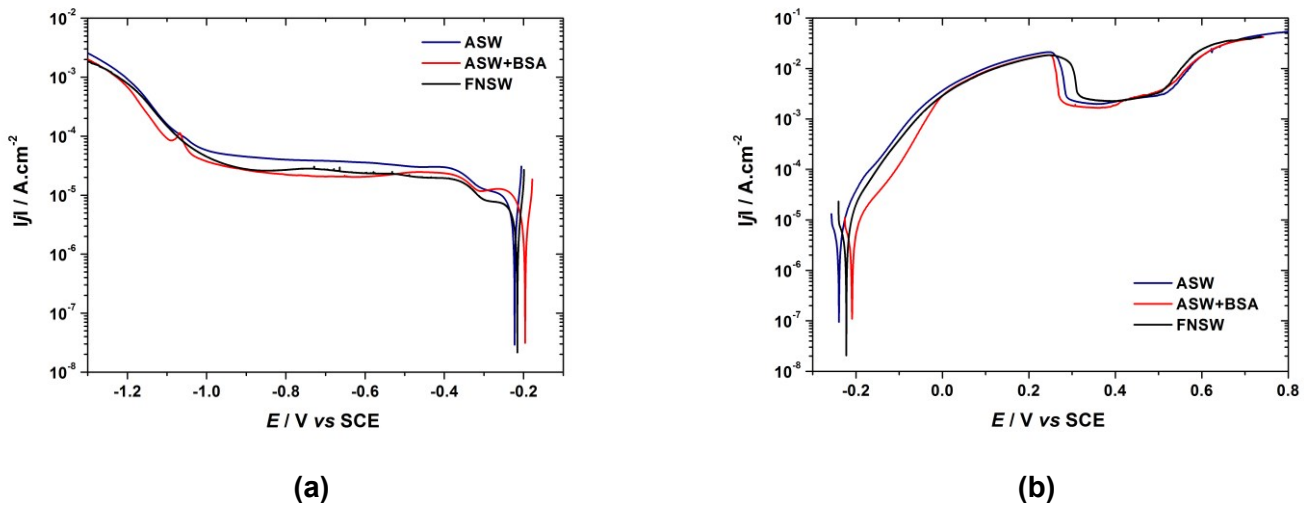


**Figure 4-1:** (a) Cathodic and (b) anodic polarization curves of 70Cu-30Ni after 1 h of immersion at  $E_{\text{corr}}$  in static aerated filtered natural seawater (FNSW), artificial seawater (ASW) without BSA and with  $20 \text{ mg.L}^{-1}$  of BSA. Scan rate:  $0.5 \text{ mV.s}^{-1}$ .

The second plateau current density for the oxygen reduction reaction in FNSW ( $|j| \sim 30 \mu\text{A.cm}^{-2}$ ) is divided by 1.33 if compared to that in ASW ( $|j| \sim 40 \mu\text{A.cm}^{-2}$ ). The same ratio is observed for the first plateau current densities. Although the natural seawater was filtered, not all the organic matter was removed from the solution; therefore, FNSW contains some

biomolecules. The lower first and second plateau current densities may be due to the presence of these biomolecules, but may also be induced by a difference in natural convection from one experiment to another.

The current increase (in absolute value) observed below -1.00 V vs SCE illustrates water reduction (hydrogen evolution reaction).

The anodic polarization curves obtained in the three solutions are presented in figure 4-1(b). In FNSW and ASW without BSA, the curves are very similar and show very high dissolution currents. In particular, a pseudo-plateau, corresponding to a current density of  $\sim 2.5 \text{ mA.cm}^{-2}$ , can be observed at around 0.4 V vs SCE; therefore, this high current density indicates poor passivity, and hence the oxide film formed on the surface is not a good protecting barrier-type film. Moreover, visual observation of the electrode surface after an anodic scan shows a green layer, the thickness of which increases with the end anodic potential. This green layer corresponding to high anodic currents may be formed by redeposition due to the saturation of the solution in copper ions. In the presence of BSA, lower current densities can be observed near  $E_{corr}$ , for potentials lower than 0.0 V vs SCE; this difference in current densities is partly due to the difference in  $E_{corr}$  values without and with BSA. Above 0.0 V vs SCE, the two anodic polarization curves overlap. Thus, only a slight influence of the protein on the anodic electrochemical behavior can be seen. Moreover, after the anodic polarization scan, the green color is not observed in ASW with BSA.

#### 4.1.1.3 ELECTROCHEMICAL IMPEDANCE SPECTROSCOPY

Figure 4-2 shows the impedance diagrams in the complex plane (Nyquist diagrams) plotted at  $E_{corr}$  after 1 h of immersion in FNSW, and in ASW without and with 20 mg.L<sup>-1</sup> of BSA. The diagrams exhibit two capacitive loops: one high frequency (HF) depressed semi-circle, and a low frequency (LF) loop. The size of the HF loop is similar in ASW and FNSW, whereas it is slightly higher in the presence of BSA. It can be concluded that the electrochemical behavior of the alloy in ASW (BSA-free) is comparable to that observed in FNSW.

As mentioned before, the impedance diagrams were plotted at the corrosion potential, which is not the same without (ASW, FNSW) and with BSA (ASW+BSA). Therefore, the analysis of data must take into account the effect of potential.

After impedance measurement at  $E_{corr}$ , there is no sign of pitting corrosion on the electrode surface whatever the solution is.

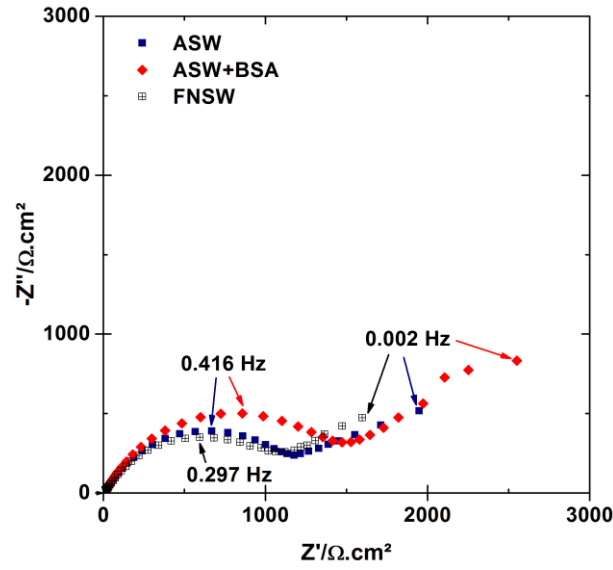


**Figure 4-2:** Experimental impedance diagrams in the complex plane (Nyquist diagrams) of 70Cu-30Ni plotted at  $E_{corr}$  after 1 h of immersion in static aerated filtered natural seawater (FNSW), artificial seawater (ASW) without and with 20 mg.L<sup>-1</sup> of BSA.

## 4.1.2 SURFACE ANALYSIS

### 4.1.2.1 EQUATIONS NECESSARY FOR XPS DATA PROCESSING

As indicated in chapter 2, from SEM micrographs it is possible to observe a homogeneous distribution of Cu and Ni along the 70Cu-30Ni sample surface.

If a continuous mixed oxide layer covering the metallic alloy is assumed (Figure 4-3), the composition and the equivalent thickness of the oxide layer ( $d_{ox}$ ) can be calculated from XPS data using the following system of equations, in which the intensities of copper and nickel in the metallic substrate and in the oxide layer are considered:

$$\text{Metallic copper (Cu}^m\text{)} \quad I_{Cu}^m = k\sigma_{Cu}\lambda_{Cu}^m D_{Cu}^m T_{Cu} \left( \exp\left(-\frac{d_{ox}}{\lambda_{Cu}^{ox}}\right) \right) \quad (4.3)$$

$$\text{Copper oxide (Cu}^{ox}\text{)} \quad I_{Cu}^{ox} = k\sigma_{Cu}\lambda_{Cu}^{ox} D_{Cu}^{ox} T_{Cu} \left( 1 - \exp\left(-\frac{d_{ox}}{\lambda_{Cu}^{ox}}\right) \right) \quad (4.4)$$

$$\text{Metallic nickel (Ni}^m\text{)} \quad I_{Ni}^m = k \sigma_{Ni} \lambda_{Ni}^m D_{Ni}^m T_{Ni} \left( \exp \left( - \frac{d_{ox}}{\lambda_{Ni}^{ox}} \right) \right) \quad (4.5)$$

$$\text{Nickel oxide (Ni}^{ox}\text{)} \quad I_{Ni}^{ox} = k \sigma_{Ni} \lambda_{Ni}^{ox} D_{Ni}^{ox} T_{Ni} \left( 1 - \exp \left( - \frac{d_{ox}}{\lambda_{Ni}^{ox}} \right) \right) \quad (4.6)$$

where:

$k$  is the spectrometer specific constant;

$\sigma_{Cu}$ ,  $\sigma_{Ni}$  are the photo-ionization cross-sections of Cu and Ni, respectively;

$\lambda_{Cu}^m, \lambda_{Cu}^{ox}, \lambda_{Ni}^m, \lambda_{Ni}^{ox}$  are the inelastic mean free paths (IMFP) of the photoelectrons emitted by the Cu and Ni core levels in the metallic alloy and in the oxide, respectively;

$T_{Cu}$ ,  $T_{Ni}$  are the transmission functions for elements Cu and Ni, respectively;

$D_{Cu}^m, D_{Cu}^{ox}, D_{Ni}^m, D_{Ni}^{ox}$  are the densities of elements Cu and Ni in the metallic alloy and in the oxide, respectively.

In this work, the take-off angle of the photoelectrons with respect to the sample surface is equal to 90°.

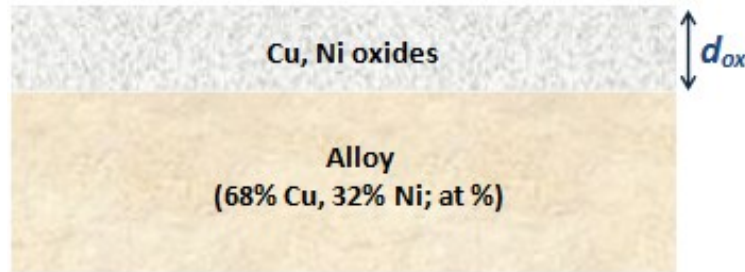


**Figure 4-3:** Layer model assumed for the analysis of XPS data (mixed oxide layer covering the metallic substrate).

Considering that:

$$D_{Cu}^m + D_{Ni}^m = 1 \quad (4.7)$$

$$D_{Cu}^{ox} + D_{Ni}^{ox} = 1 \quad (4.8)$$

the concentrations of copper and nickel in the oxide layer and beneath the oxide layer, as well as the oxide layer thickness can be calculated by solving the system of six equations (Eqs. (4.3) to (4.8)) with six unknowns ( $D_{Cu}^m, D_{Ni}^m, D_{Cu}^{ox}, D_{Ni}^{ox}, d_{ox}$  and  $k$ ).

The calculated values for the transmission function  $T$  are listed in Table 4-1.

**Table 4-1:** Transmission functions  $T(E_{kin})$  of the Escalab 250 energy analyzer, provided by Thermo Electron Corporation.

$T(E_{kin})$	Cu Auger line $L_3M_{45}M_{45}$	Cu 2p <sub>3/2</sub>	Ni 2p <sub>3/2</sub>
	3492	4265	4062

As mentioned in Chapter 2, the inelastic mean free path ( $\lambda$ ) values were taken from the QUASES-IMFP-TPP2M, a database for calculation of IMFPs by the TPP2M-formula, which is part of the QUASES-Tougaard method. These values are listed in Table 4-2.

**Table 4-2:** Inelastic mean free paths  $\lambda$  in nm – Taken from the QUASES-IMFP-TPP2M.

$\lambda$ (nm)						
$\lambda_{Cu2p_{3/2}}^{Cu^{2+}}$	$\lambda_{Cu2p_{3/2}}^{Cu^+}$	$\lambda_{Cu2p_{3/2}}^m$	$\lambda_{Cu\ Auger}^{Cu^+}$	$\lambda_{Cu\ Auger}^m$	$\lambda_{Ni2p_{3/2}}^{Ni^{2+}}$	$\lambda_{Ni2p_{3/2}}^m$
1.19	1.23	1.01	1.76	1.46	1.31	1.11

The photoionization cross-section  $\sigma_X$  values are presented in Table 4-3.

**Table 4-3:** Photo-ionization cross sections  $\sigma_X$  at 1486.6 eV.

	Cu Auger line $L_3M_{45}M_{45}^*$	Cu 2p <sub>3/2</sub>	Ni 2p <sub>3/2</sub>
$\sigma_X$	5.4	16.73	14.61

\*Value calculated by:  $\sigma_{Cu\ Auger} = \sigma_{Cu} \frac{I_{Cu\ Auger}^m}{I_{Cu2p_{3/2}}^m} \frac{\lambda_{Cu2p_{3/2}}^m}{\lambda_{Cu\ Auger}^m} \frac{T_{Cu2p_{3/2}}}{T_{Cu\ Auger}}$ , using the known intensity values

$I_{Cu2p_{3/2}}^m$  and  $I_{Cu\ Auger}^m$  of the 70Cu-30Ni alloy after polishing and sputtering (removal of oxides from the surface).

Although with the previous equations, it is possible to calculate the equivalent thickness and the composition of the oxide layer formed on the 70Cu-30Ni alloy, the decomposition of the Cu 2p<sub>3/2</sub> XPS peak presents an important difficulty. Indeed, the binding energy of Cu<sup>0</sup> and Cu<sup>+</sup> are located at the same position as shown in Table 4-4, in which the binding energy of the Cu 2p<sub>3/2</sub> core level and the kinetic energy of the L<sub>3</sub>M<sub>45</sub>M<sub>45</sub> Cu Auger line are presented for different Cu species. This difficulty is overcome by making use of the Cu

Auger line ( $L_3M_{45}M_{45}$ ), helpful for distinguishing these two species. Furthermore, the Cu Auger line was used to obtain information about the relative contributions of  $Cu_2O$ ,  $CuO$  and metallic Cu. For that purpose, the decomposition was performed with the software “CASA”, using the reference spectra of  $Cu_2O$ ,  $CuO$  and metallic Cu. The results provide the relative proportions of these compounds on the alloy surface, considering that no other species is present. However, this is not fully correct, due to the fact that other Cu species may be part of the surface film, such as  $Cu(OH)_2$ ,  $CuSO_4$  or other Cu complexes, leading to an overestimation of the percentages of  $Cu^+$  and  $Cu^{2+}$  in the Auger line ( $L_3M_{45}M_{45}$ ).

**Table 4-4:** Binding energy of Cu  $2p_{3/2}$  XPS peak and kinetic energy of  $L_3M_{45}M_{45}$  Cu Auger line for different Cu species [176-182].

Compound	Cu $2p_{3/2}$ binding energy / eV	$L_3M_{45}M_{45}$ Cu Auger line kinetic energy / eV
Cu	$932.5 \pm 0.2$	$918.7 \pm 0.3$
$Cu_2O$	$932.4 \pm 0.2$	$917.0 \pm 0.4$
$CuO$	$933.4 \pm 0.2$	$917.9 \pm 0.2$
$Cu(OH)_2$	$934.5 \pm 0.4$	$916.4 \pm 0.2$
$CuSO_4$	$935.4 \pm 0.3$	$916.0 \pm 0.1$
$Cu_2S$	$932.6 \pm 0.3$	$917.4 \pm 0.7$
$CuCl$	$932.0 \pm 0.7$	$915.5 \pm 0.3$
$CuCl_2$	$934.6 \pm 0.6$	$915.5 \pm 0.3$

As it was not possible to know precisely what other compounds (different from  $Cu_2O$  and  $CuO$ ) were involved in the formation of the oxide film, and as Auger line  $L_3M_{45}M_{45}$  references could be obtained for all the involved copper compounds, only the intensity of  $Cu^0$  obtained from the decomposition of the Cu Auger line ( $L_3M_{45}M_{45}$ ) was taken into account. Therefore, the intensity of  $Cu^0$  in the Auger line ( $I_{Cu\ Auger}^{Cu^0}$ ) was calculated from the total

intensity of the Cu Auger, and this value was converted into a  $I_{Cu2\ p_{3/2}}^{Cu^0}$  using the following equation:

$$I_{Cu2\ p_{3/2}}^m = \frac{\sigma_{Cu2\ p_{3/2}} \lambda_{Cu2\ p_{3/2}}^m T_{Cu2\ p_{3/2}} \exp\left(-\frac{d_{ox}}{\lambda_{Cu2\ p_{3/2}}^{ox}}\right)}{\sigma_{Cu\ Auger} \lambda_{Cu\ Auger}^m T_{Cu\ Auger} \exp\left(-\frac{d_{ox}}{\lambda_{Cu\ Auger}^{ox}}\right)} I_{Cu\ Auger}^m \quad (4.9)$$

The intensity of  $\text{Cu}^+$  ( $I_{\text{Cu}2p_{3/2}}^{\text{Cu}^+}$ ) was then calculated from  $I_{\text{Cu}2p_{3/2}}^m$  by:

$$I_{\text{Cu}2p_{3/2}}^{\text{Cu}^+} = I_{\text{Cu}2p_{3/2}}^{932\text{eV}} - I_{\text{Cu}2p_{3/2}}^m \quad (4.10)$$

where  $I_{\text{Cu}2p_{3/2}}^{932\text{eV}}$  corresponds to the intensity of the peak located at 932 eV in the Cu  $2p_{3/2}$  core level spectrum corresponding to  $\text{Cu}^+$  and/or  $\text{Cu}^0$ .

The intensities  $I_{\text{Cu}2p_{3/2}}^{\text{Cu}^+}$  and  $I_{\text{Cu}2p_{3/2}}^m$  can be used to solve the system of equations that will allow to calculate the equivalent thickness of the oxide layer, and the composition of the oxide film and of the substrate beneath the oxide film.

For experiments performed in ASW + BSA and in FNSW, the composition and the equivalent thickness of the oxide layer ( $d_{ox}$ ) formed in the presence of biomolecules were calculated from XPS data, using the system of equations previously presented (Eqs: (4.3) to (4.8)) and considering the intensities of copper and nickel in the metallic substrate and in the mixed oxide layer formed on the alloy surface (the presence of biomolecules leads to mixed oxide layers, as will be shown later). Figure 4-4 illustrates the layer model used for the analysis of XPS data of 70Cu-30Ni alloy after immersion in a solution containing biomolecules (ASW + BSA or FNSW) that adsorb on the surface, forming an organic film on top of the oxide layer, with an equivalent thickness  $d_{BSA}$  (for ASW + BSA) or  $d_{org}$  (for FNSW).

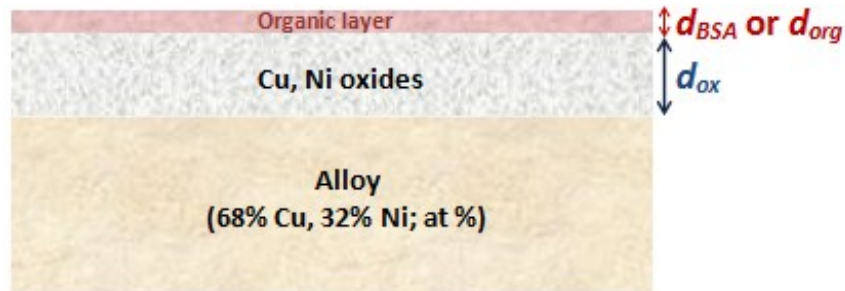


**Figure 4-4:** Layer model assumed for the analysis of XPS data (organic layer covering the mixed oxide layer formed on the metallic substrate).

The thickness  $d_{BSA}$  can be calculated from the  $\frac{I_N^{BSA}}{I_{Cu}^{ox}}$  ratio. The nitrogen signal comes

only from the protein and is therefore a fingerprint of the adsorbed protein. The N 1s intensity emitted by the adsorbed BSA is given by:

$$I_N^{BSA} = k\sigma_N\lambda_N^{BSA}D_N^{BSA}T_N \left[ 1 - \exp\left(-\frac{d_{BSA}}{\lambda_N^{BSA}}\right) \right] \quad (4.11)$$

The Cu 2p<sub>3/2</sub> intensity emitted by the oxide layer and attenuated by the adsorbed protein layer is given by:

$$I_{Cu}^{ox} = k\sigma_{Cu}\lambda_{Cu}^{ox}D_{Cu}^{ox}T_{Cu} \exp\left(-\frac{d_{BSA}}{\lambda_{Cu}^{BSA}}\right) \left( 1 - \exp\left(-\frac{d_{ox}}{\lambda_{Cu}^{ox}}\right) \right) \quad (4.12)$$

Then,

$$\frac{I_N^{BSA}}{I_{Cu}^{ox}} \times \frac{\sigma_{Cu}\lambda_{Cu}^{ox}D_{Cu}^{ox}T_{Cu}}{\sigma_N\lambda_N^{BSA}D_N^{BSA}T_N} = \frac{1 - \exp\left(-\frac{d_{BSA}}{\lambda_N^{BSA}}\right)}{\exp\left(-\frac{d_{BSA}}{\lambda_{Cu}^{BSA}}\right) \left( 1 - \exp\left(-\frac{d_{ox}}{\lambda_{Cu}^{ox}}\right) \right)} \quad (4.13)$$

The calculated value for the transmission function  $T(E_{kin})$  of the Escalab 250 energy analyzer for nitrogen (N 1s) is 3233.4, and the photo-ionization cross-section of N 1s is 1.8. The values for the inelastic mean free path are presented in Table 4-5.

**Table 4-5:** Inelastic mean free paths  $\lambda$  in nm – Taken from the QUASES-IMFP-TPP2M.

$\lambda$ (nm)		
$\lambda_{Cu2p_{3/2}}^{BSA}$	$\lambda_{Ni2p_{3/2}}^{BSA}$	$\lambda_{N1s}^{BSA}$
1.94	2.13	3.39

The values of the different parameters for Cu and Ni are given in Tables 4-1 to 4-3.

#### 4.1.2.2 RESULTS

During the XPS measurements, the following core levels were recorded: Cu 2p (and Auger line), Ni 2p, O 1s, C 1s, and N 1s. Only the Cu 2p<sub>3/2</sub> and Ni 2p<sub>3/2</sub> peaks were used in the decomposition and analysis of XPS data.

The XPS Cu 2p<sub>3/2</sub> core level spectrum of the 70Cu-30Ni alloy sample just after polishing shows the presence of a first peak at 932.2 eV corresponding to Cu<sup>+</sup> and/or Cu<sup>0</sup>, and a second peak at 933.7 eV with a satellite at higher binding energy (943.2 eV) corresponding to Cu<sup>2+</sup> (Figure 4-5(a)). The position of the Auger line (L<sub>3</sub>M<sub>45</sub>M<sub>45</sub>) at a kinetic energy of 919.1 eV indicates a major contribution of Cu<sup>0</sup> (Figure 4-5(b)). On the other hand, the Ni 2p<sub>3/2</sub> core level spectrum shows a peak at a binding energy of 852.2 eV characteristic

of  $\text{Ni}^0$ , and another peak at 855.6 eV with a satellite at 860.9 eV corresponding to nickel hydroxide ( $\text{Ni}(\text{OH})_2$ ) (Figure 4-6). The calculated thickness of the oxide layer is  $\sim 1.5$  nm and its atomic composition is: 27 at. %  $\text{Cu}_2\text{O}$  + 42 at. %  $\text{Cu}^{2+}$  ( $\text{CuO}$  and  $\text{Cu}(\text{OH})_2$ ) + 31 at. %  $\text{Ni}(\text{OH})_2$ . Enrichment in copper of the alloy beneath the oxide layer is also detected (75 at. % Cu + 25 at. % Ni to be compared to 68 at. % Cu + 32 at. % Ni for the bulk alloy).

After immersion in ASW, the XPS  $\text{Cu } 2p_{3/2}$  core level peak with a binding energy located at 932.2 eV (Figure 4-5(a)) and the Cu Auger line ( $\text{L}_3\text{M}_{45}\text{M}_{45}$ ) at a kinetic energy of 916.8 eV (Figure 4-5(b)) demonstrate, according to Table 4-4, the presence of  $\text{Cu}^+$  instead of  $\text{Cu}^0$  as observed for the sample after polishing. In the case of FNSW, the Cu  $2p_{3/2}$  core level spectrum exhibits the a first peak at  $\sim 932.2$  eV corresponding to  $\text{Cu}^+$  and/or  $\text{Cu}^0$ , and a second peak at higher binding energy ( $\sim 934$  eV) with a satellite at  $\sim 944$  eV corresponding to  $\text{Cu}^{2+}$  (Figure 4-4(a)). The position of the Auger line ( $\text{L}_3\text{M}_{45}\text{M}_{45}$ ) at a kinetic energy of 916.7 eV (Figure 4-4(b)) shows the presence of  $\text{Cu}^+$ , similarly to what is observed in ASW.

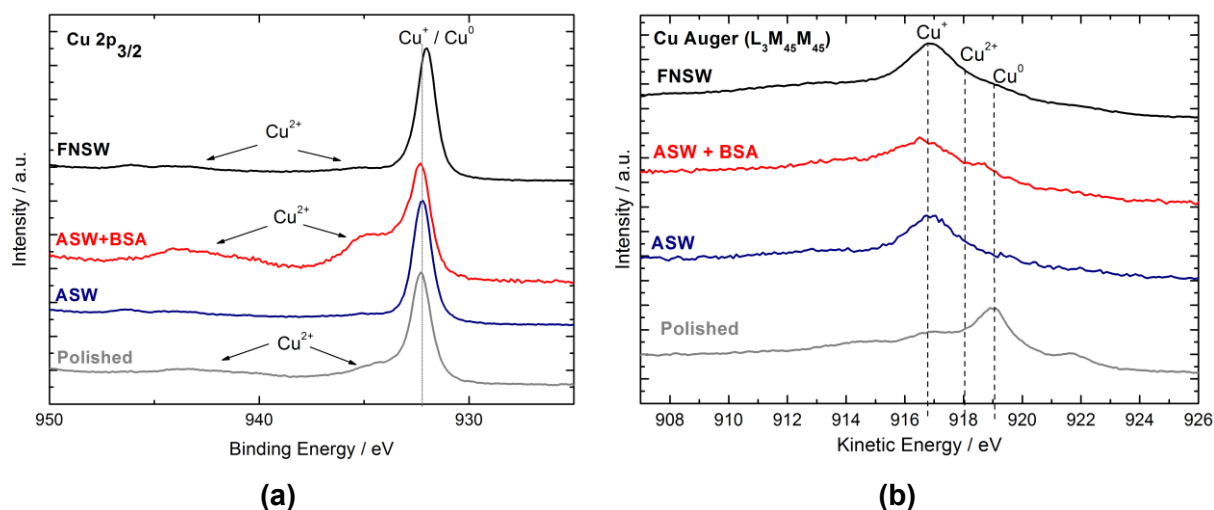


**Figure 4-5:** (a) X-ray photoelectron spectroscopy (XPS)  $\text{Cu } 2p_{3/2}$  core level spectra and (b) Cu  $\text{L}_3\text{M}_{45}\text{M}_{45}$  Auger lines of 70Cu-30Ni after polishing and after 1 h of immersion at  $E_{\text{corr}}$  in static aerated filtered natural seawater (FNSW) and artificial seawater (ASW) without and with  $20 \text{ mg.L}^{-1}$  of BSA. The intensity is expressed in arbitrary unit (a.u.).

The XPS  $\text{Ni } 2p_{3/2}$  core level spectrum of the 70Cu-30Ni alloy sample just after polishing shows the presence of a first peak at  $\sim 852.4$  eV corresponding to  $\text{Ni}^0$ , and a second peak at  $\sim 856.0$  eV with a satellite at higher binding energy (862 eV) corresponding to  $\text{Ni}(\text{OH})_2$  (Figure 4-6) [183]. From the XPS  $\text{Ni } 2p_{3/2}$  core level spectra, the presence of  $\text{Ni}(\text{OH})_2$  in the surface layer is demonstrated, after immersion in ASW as well as in FNSW, by a peak located at  $\sim 856.0$  eV and the corresponding satellite at  $\sim 862$  eV, (Figure 4-6) [183].

The XPS Cl 2p core level spectra, of the alloy exposed to ASW and FNSW (not presented here), show a peak centered at 198.6 eV. Using the intensity of the Cl 2p signal, the amount of Cl<sup>-</sup> can be calculated; a value of ~ 0.2% is found after immersion in ASW and of ~ 0.8% after immersion in FNSW.

The atomic composition of the oxide layer calculated from XPS data for 70Cu-Ni alloy after 1 h of exposure to ASW (93 at. % Cu<sub>2</sub>O + 7 at. % Ni(OH)<sub>2</sub>) indicates an enrichment in Cu<sub>2</sub>O compared to the sample just after polishing; no Cu<sup>2+</sup> compounds are detected in the oxide layer. After immersion in FNSW, the oxide layer also exhibits an enrichment in Cu<sup>+</sup>, but Cu<sup>2+</sup> compounds are found in the oxide layer as well as Ni(OH)<sub>2</sub> (55 at. % Cu<sup>+</sup> + 16 at. % Cu<sup>2+</sup> + 29 at. % Ni<sup>2+</sup>). The depth analyzed by XPS is about 10 nm. No metallic contribution is observed in the Cu 2p<sub>3/2</sub> and Ni 2p<sub>3/2</sub> core level spectra, which means that the oxide film is thicker than 10 nm; therefore, the thickness of the oxide film cannot be calculated from XPS data.

After immersion in the BSA-containing solution, the XPS Cu 2p<sub>3/2</sub> core level spectrum exhibits three peaks (Figure 4-5(a)): one located at 932.3 eV attributed to Cu<sup>0</sup> and/or Cu<sup>+</sup>, another one with a binding energy of 933.9 eV and the corresponding satellite at higher binding energy attributed to Cu<sup>2+</sup>. Moreover, the Cu Auger line at a binding energy of 916.6 eV (Figure 4-5(b)) shows the presence of Cu<sup>+</sup>. The XPS Ni 2p<sub>3/2</sub> core level spectrum recorded in the presence of BSA exhibits the same features as without protein: a peak at a binding energy of 856.0 eV and the corresponding satellite at 861.7 eV showing the presence of Ni(OH)<sub>2</sub> in the surface layer (Figure 4-6). From these XPS data, it can be concluded that the presence of BSA leads to a mixed copper oxides (Cu<sup>+</sup> and Cu<sup>2+</sup>) and nickel hydroxide layer, with the following atomic composition: 16 at. % Cu<sup>+</sup> + 33 at. % Cu<sup>2+</sup> + 51 at. % Ni(OH)<sub>2</sub>. A lower amount of Cu<sup>+</sup> and higher amounts of Cu<sup>2+</sup> and Ni(OH)<sub>2</sub> are detected compared to the results obtained in ASW without BSA.

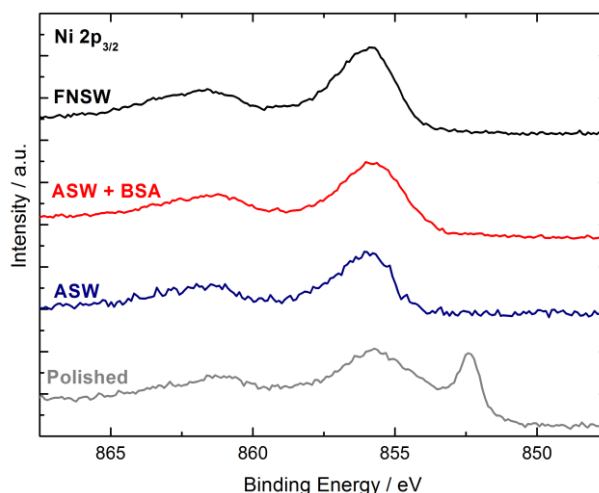


**Figure 4-6:** X-ray photoelectron spectroscopy (XPS) Ni 2p<sub>3/2</sub> core level spectra of 70Cu-30Ni after 1 h of immersion at  $E_{corr}$  in static aerated filtered natural seawater (FNSW) and artificial seawater (ASW) without and with 20 mg.L<sup>-1</sup> of BSA. The intensity is expressed in arbitrary unit (a.u.).

A characteristic ToF-SIMS depth profile (negative ions) obtained with 70Cu-30Ni alloy immersed during 1 h at  $E_{corr}$  in ASW is presented in Figure 4-7. This profile evidences a stratification of the oxide film covering the metallic surfaces. Three regions can be observed. The first one extends from 0 to 200 s of sputtering, characterized by an intense  $95^{63}\text{CuO}_2^-$  signal. As one probes deeper into this first region, a progressive increase of the  $90^{58}\text{NiO}_2^-$  signal is observed, indicating that the outer surface layer is mainly composed of copper oxide, with the presence of some Ni oxide and/or hydroxide, in agreement with XPS data. In the second region that extends from 200 s to 290 s, a sharp decrease of the  $95^{63}\text{CuO}_2^-$  signal is observed, whereas  $90^{58}\text{NiO}_2^-$  signal reaches its maximum intensity. This second region is assigned to a nickel oxide and/or hydroxide inner layer in which the presence of oxidized copper cannot be excluded. Finally, after 290 s of sputtering, one enters the third region characterized by a sharp decrease of all oxidized signals ( $18^{18}\text{O}^-$ ,  $95^{63}\text{CuO}_2^-$  and  $90^{58}\text{NiO}_2^-$ ) and a constant and intense plateau for the  $116^{58}\text{Ni}_2^-$  signal which is characteristic of the metallic substrate. It is noticeable that Cl species (represented by the  $35\text{Cl}^-$  signal on the profile) are present essentially in the outer part of the oxide layer (copper oxide). Thus, the oxide film formed on 70Cu-30Ni alloy in ASW exhibits a duplex structure with (a) a 20 nm-thick outer layer mainly composed of copper oxide and (b) a 10 nm-thick inner layer mainly composed of oxidized nickel. The possible presence of Ni hydroxide in the inner layer can be explained by the fact that the outer layer is, in fact, redeposition of copper oxide on the surface.

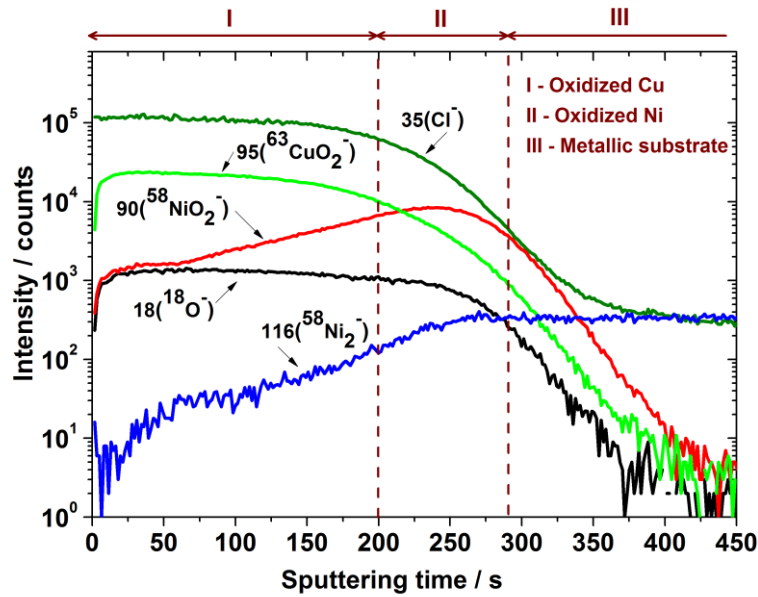


**Figure 4-7:** Characteristic time-of-flight secondary ions mass spectrometry (ToF-SIMS) negative depth profile of 70Cu-30Ni after 1 h of immersion at  $E_{corr}$  in static aerated artificial seawater (ASW).

Figure 4-8 exhibit the negative depth profile recorded after 1 h of immersion at  $E_{corr}$  in FNSW. This profile, as the one obtained in ASW, allows evidencing a possible stratification of the different compounds on the alloy surface. Three main regions can be identified. In the first region, from 0 s to 32 s of sputtering, all signals increase, particularly the  $26\text{CN}^-$ ,  $32\text{S}^-$ ,  $63\text{PO}_2^-$ ,  $90^{58}\text{NiO}_2^-$  signals, which reach a maximum value and subsequently sharply decrease. The  $95^{63}\text{CuO}_2^-$ ,  $18^{18}\text{O}^-$  signals start to slowly decrease at the end of this first region, whereas the  $116^{58}\text{Ni}_2^-$  signal keeps increasing. The second region, which goes from 32 up to 187 s of sputtering, is characterized by a new increase of the  $26\text{CN}^-$ ,  $32\text{S}^-$ ,  $63\text{PO}_2^-$ ,  $90^{58}\text{NiO}_2^-$  signals. The  $116^{58}\text{Ni}_2^-$  signal slightly increase until form a plateau at  $\sim 187$  s, when all the signals representing the oxidized components sharply decrease; at this point, the interface Cu oxide/oxidized Ni has been reached. The first region can be probably due to the presence of some islands of oxidized Ni and Cu on the oxide layer, covering an oxidized Ni oxide layer, represented by region 2. The signal  $35\text{Cl}^-$  holds its high intensity value up to 82 s of sputtering, which indicate the presence of  $\text{Cl}^-$  along the oxide layer. The  $32\text{S}^-$  signal follows the same trend as the  $90^{58}\text{NiO}_2^-$  signal, indicating the presence of sulfur throughout the inner layer. The global thickness estimated by ToF-SIMS was of  $\sim 23$  nm.

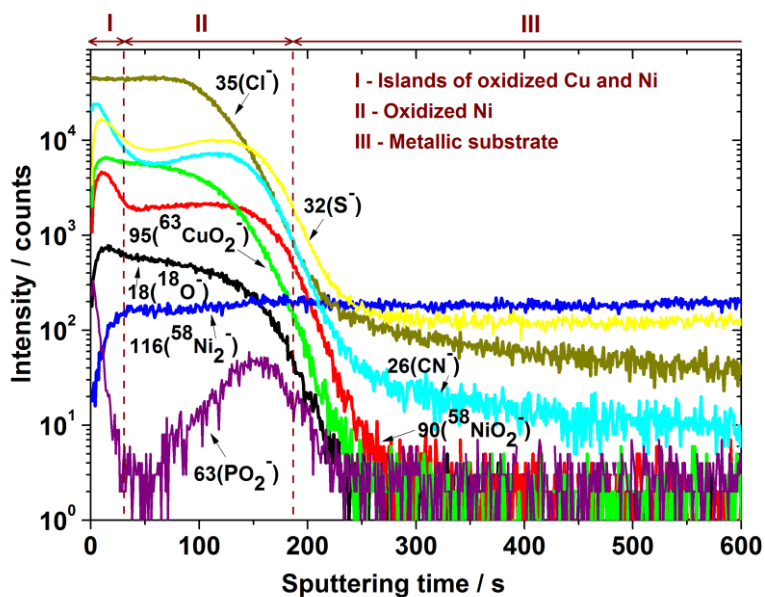


**Figure 4-8:** Characteristic time-of-flight secondary ions mass spectrometry (ToF-SIMS) negative depth profile of 70Cu-30Ni after 1 h of immersion at  $E_{\text{corr}}$  in static aerated filtered natural seawater (FNSW).

Figure 4-9 shows the ToF-SIMS negative depth profile obtained with 70Cu-30Ni after 1 h of immersion in ASW with  $20 \text{ mg.L}^{-1}$  of BSA. In this figure, it is possible to distinguish mainly four regions. The first region that goes from 0 to 10 s shows an increase of all the signals, and it is characterized by a maximum intensity in the  $35\text{Cl}^-$  and  $26\text{CN}^-$  (characteristic signal of proteins -peptidic link-) signals. From 10 s up to 25 s of sputtering the second region is observed, where the  $95^{63}\text{CuO}_2^-$ ,  $18^{18}\text{O}^-$  and  $90^{58}\text{NiO}_2^-$  signals reach their maximum value, and the  $35\text{Cl}^-$  signal and the  $26\text{CN}^-$  one sharply decrease. This region corresponds to the oxide layer beneath the BSA layer. The third region starts from 25 up to 64 s of sputtering, when the  $95^{63}\text{CuO}_2^-$ ,  $18^{18}\text{O}^-$ ,  $35\text{Cl}^-$  and the  $90^{58}\text{NiO}_2^-$  signals exhibit an inflection point, slightly increasing forming a shoulder; whereas the  $26\text{CN}^-$  signals keeps sharply decreasing and the  $116^{58}\text{Ni}_2^-$  signal gradually increase. This third region evidences an oxide layer non-cover by the BSA. Finally after  $\sim 64$  s of sputtering, oxides signal presents a sharp decrease, and the  $116^{58}\text{Ni}_2^-$  signal form a plateau indicating that the alloy/oxide interface is reached.

By ToF-SIMS, it is not possible to identify a stratification of the different compounds on the alloy surface in the presence of the protein. Therefore, the depth profiles show one mixed oxide layer (oxidized copper and nickel) with a thickness of  $\sim 10$  nm, being three times lower than that in the absence of the protein, and partly cover by the BSA layer.

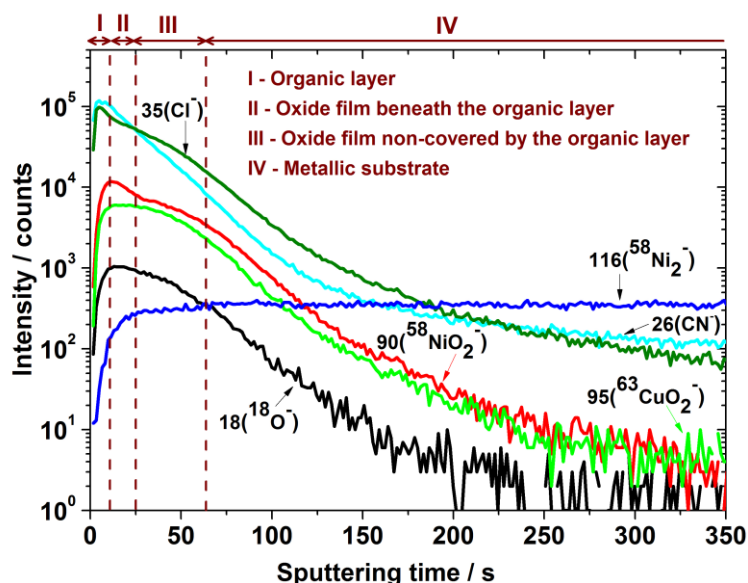


**Figure 4-9:** Characteristic time-of-flight secondary ions mass spectrometry (ToF-SIMS) negative depth profile of 70Cu-30Ni after 1 h of immersion at  $E_{corr}$  in static aerated artificial seawater with 20 mg.L<sup>-1</sup> of BSA.

The N 1s spectrum recorded after immersion in ASW with BSA (Figure 4-10 (a)) exhibits a major symmetric peak, centered at 400.2 eV, as expected for the amine or amide groups of BSA [184]. In the case of ASW, there is no protein adsorbed on the surface, and low amount of adsorbed proteins are adsorbed in FNSW. The C 1s signal obtained in the same conditions is shown in Figure 4-10 (b). It can be fitted with three contributions corresponding to well identified carbon bonds present in the BSA molecule: C<sub>1</sub>, at a binding energy of 285.0 eV, assigned to C-C and C-H; C<sub>2</sub>, at a binding energy of 286.4 eV, attributed to C-N and C-O single bonds; and C<sub>3</sub>, at a binding energy of 288.3 eV, assigned to O=C-O and O=C-N (peptide bonds) bonds [145].

From the N 1s and C 1s signals, it is possible to calculate different “nitrogen/carbon” or “carbon/carbon” atomic ratios. The values of these ratios obtained for the 70Cu-30Ni alloy immersed in static ASW without and with BSA and in FNSW, as well as those estimated in previous studies for the BSA powder [15, 146] are presented in Table 4-6. The good agreement between the values for the sample exposed to BSA and the BSA powder provides a fingerprint for the protein, and allows us to conclude that the protein is present on the surface. The thickness estimated from XPS data for this adsorbed layer is ~ 3 nm which, according to the size of the BSA molecule [174], corresponds to one monolayer.

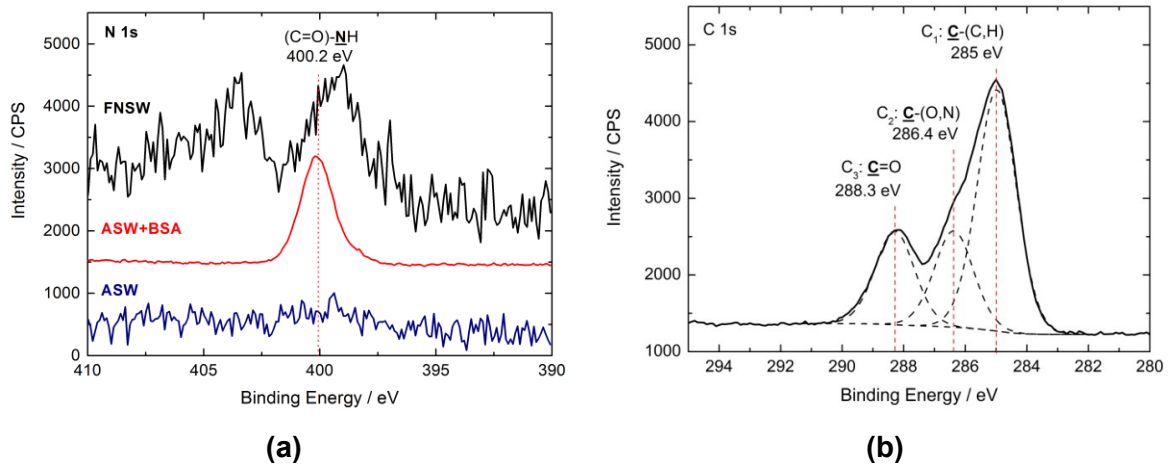


**Figure 4-10:** (a) N 1s core level spectra of 70Cu-30Ni after 1 h of immersion at  $E_{corr}$  in static aerated filtered natural seawater (FNSW) and artificial seawater (ASW) without and with 20 mg.L<sup>-1</sup> of BSA, and (b) C 1s core level spectra of 70Cu-30Ni after 1 h of immersion at  $E_{corr}$  in static aerated artificial seawater with 20 mg.L<sup>-1</sup> of BSA. Solid line: experimental spectra; dashed line: peak decomposition. The intensity is expressed in counts per second (CPS).

**Table 4-6:** Atomic ratios calculated from the XPS N 1s and C 1s core level spectra recorded for the BSA powder and for 70Cu-30Ni after 1 h of immersion at  $E_{corr}$  in static aerated artificial seawater without and with 20 mg.L<sup>-1</sup> of BSA and filtered natural seawater.

	N/C <sub>total</sub> *	N/(C <sub>2</sub> +C <sub>3</sub> ) *	C <sub>1</sub> /C <sub>total</sub> *	C <sub>2</sub> /C <sub>total</sub> *	C <sub>3</sub> /C <sub>total</sub> *
<b>BSA powder</b>	0.22	0.48	0.54	0.26	0.20
<b>ASW+BSA</b>	0.20	0.45	0.56	0.22	0.22
<b>ASW</b>	0.03	0.14	0.78	0.13	0.09
<b>FNSW</b>	0.04	0.13	0.65	0.11	0.24

<sup>(a)</sup>The atomic ratio X/Y is given by:

$$X/Y = I_X \sigma_Y \lambda_Y^{BSA} T_Y / I_Y \sigma_X \lambda_X^{BSA} T_X$$

where  $I_{X,Y}$  is the intensity of the peak (peak surface area) associated to element X or Y (X and Y equal to N or C),  $\lambda_{X,Y}^{BSA}$  the attenuation length of photoelectrons emitted by the X or Y core level in the BSA layer,  $\sigma_{X,Y}$  the photoionisation cross-section of X or Y, and  $T_{X,Y}$  the transmission factor of X or Y. The C 1s signal is fitted with three contributions C1, C2 and C3, corresponding to well identified carbon bonds present in the BSA molecule.

In FNSW the “nitrogen/carbon” ratios are similar to those obtained in ASW, but the ratios “carbon/carbon” are slightly different, especially  $C_3/C_{total}$ , assigned to O=C-O and O=C-N (peptide bonds) bonds. This can mean that FNSW, besides filtered, still have some protein compounds on its composition.

## 4.2 DISCUSSION

### 4.2.1 SURFACE LAYERS MODELS (COMBINED XPS AND TOF-SIMS)

Figure 4-11 illustrates the surface layer model deduced from the surface analysis of the 70Cu-30Ni alloy just after polishing. In this model, one mixed oxide layer, made up of  $\text{Cu}^+$ ,  $\text{Cu}^{2+}$  and  $\text{Ni}^{2+}$  compounds, covers the surface. The thickness of the oxide layer is about 1.5 nm.

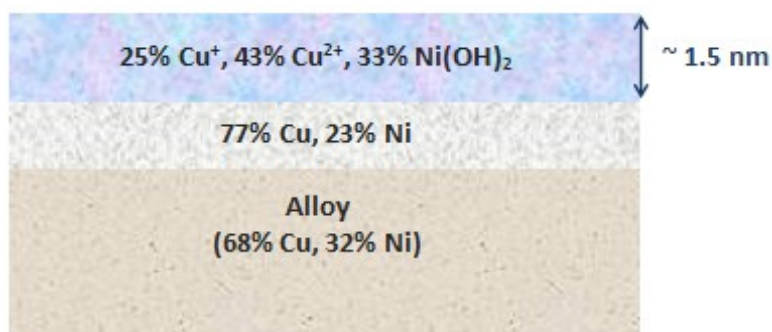


**Figure 4-11:** Model of the surface layers deduced from combined X-ray photoelectron spectroscopy (XPS) and time-of-flight secondary ions mass spectrometry (ToF-SIMS) results for 70Cu-30Ni just after polishing.

The surface layer model deduced from combined XPS and ToF-SIMS data for 70Cu-30Ni alloy after short-term immersion (1 h of exposure) at  $E_{corr}$  in static ASW is shown in Figure 4-12(a). This model shows two oxidized layers: an outer layer mainly composed of cuprous oxide ( $\text{Cu}_2\text{O}$ ) and an inner layer mainly composed of oxidized nickel; no  $\text{Cu}^{2+}$  compounds were found. A similar model with two oxidized layers is deduced for 70Cu-30Ni alloy after 1 h of immersion in static FNSW (Figure 4-12(b)). However, in this case,  $\text{Cu}^{2+}$  and  $\text{Cu}^+$  compounds were detected on the surface, and the oxidized Cu/oxidized Ni ratio in the outer oxide layer is lower than that observed in ASW.

The duplex structure observed after 1 h of immersion in static ASW and in FNSW, with a cuprous oxide-rich outer layer and an oxidized Ni-rich ( $\text{NiO}$  and/or  $\text{Ni(OH)}_2$ ) inner layer, has already been observed by Souchet *et al.* for the early stages (1-2 h) of low temperature (100-200°C) air oxidation of CuNi alloys [185,186] but this result is not well-known for the oxidation of such alloys in aqueous solution.

The  $\text{Cl}^-$  ToF-SIMS signal, visible throughout the outer layer in static ASW and FNSW, could be related to the formation of  $\text{CuCl}$ , as taken into account in the impedance model (see section 4.2.4). However, the amount of chlorides detected by XPS is lower than 1% (at. %)

after immersion in both solutions. This is because the limit of detection of ToF-SIMS is lower than that of XPS. Therefore, the main  $\text{Cu}^+$  compound formed on the surface layer is  $\text{Cu}_2\text{O}$ .

The oxide layer composition estimated from XPS data for the 70Cu-30Ni alloy after short-term immersion (1 h of exposure) at  $E_{\text{corr}}$  in ASW with  $20 \text{ mg.L}^{-1}$  of BSA is summarized in Figure 4-14(c). The presence of BSA induces the formation of a mixed oxide layer composed of  $\text{Cu}^+$ ,  $\text{Cu}^{2+}$  and  $\text{Ni}^{2+}$  compounds, but with a lower  $\text{Cu}_2\text{O}$  content, a higher  $\text{Ni}(\text{OH})_2$ , as well as a lower oxide layer thickness (if compared with ASW without BSA and FNSW).

There are basically two mechanisms of de-alloying for binary alloys proposed in the literature [127]:

- i. simultaneous dissolution of both components of the alloy followed by redeposition of one component (usually the more noble one),
- ii. selective dissolution of one element from the alloy.

Beccaria and Crousier studied the de-alloying of Cu-Ni alloys exposed to natural seawater for 660 h and found simultaneous dissolution of both components with possible redeposition of copper for nickel contents lower than 50 %, whereas for nickel concentrations higher than 50% selective dissolution of copper took place [187]. Results obtained by Mansfeld *et al.* for long-term exposure (1-3 months) in natural seawater suggest that de-alloying of 70Cu-30Ni is initially due to simultaneous dissolution of copper and nickel and subsequent redeposition of copper in agreement with the results of Beccaria and Crousier [127].

Our results obtained for short-term exposure to ASW are in agreement with the conclusions drawn by Beccaria and Crousier, and Mansfeld *et al.*; the cuprous oxide  $\text{Cu}_2\text{O}$  detected on the surface by XPS and ToF-SIMS is formed by redeposition of dissolved copper.

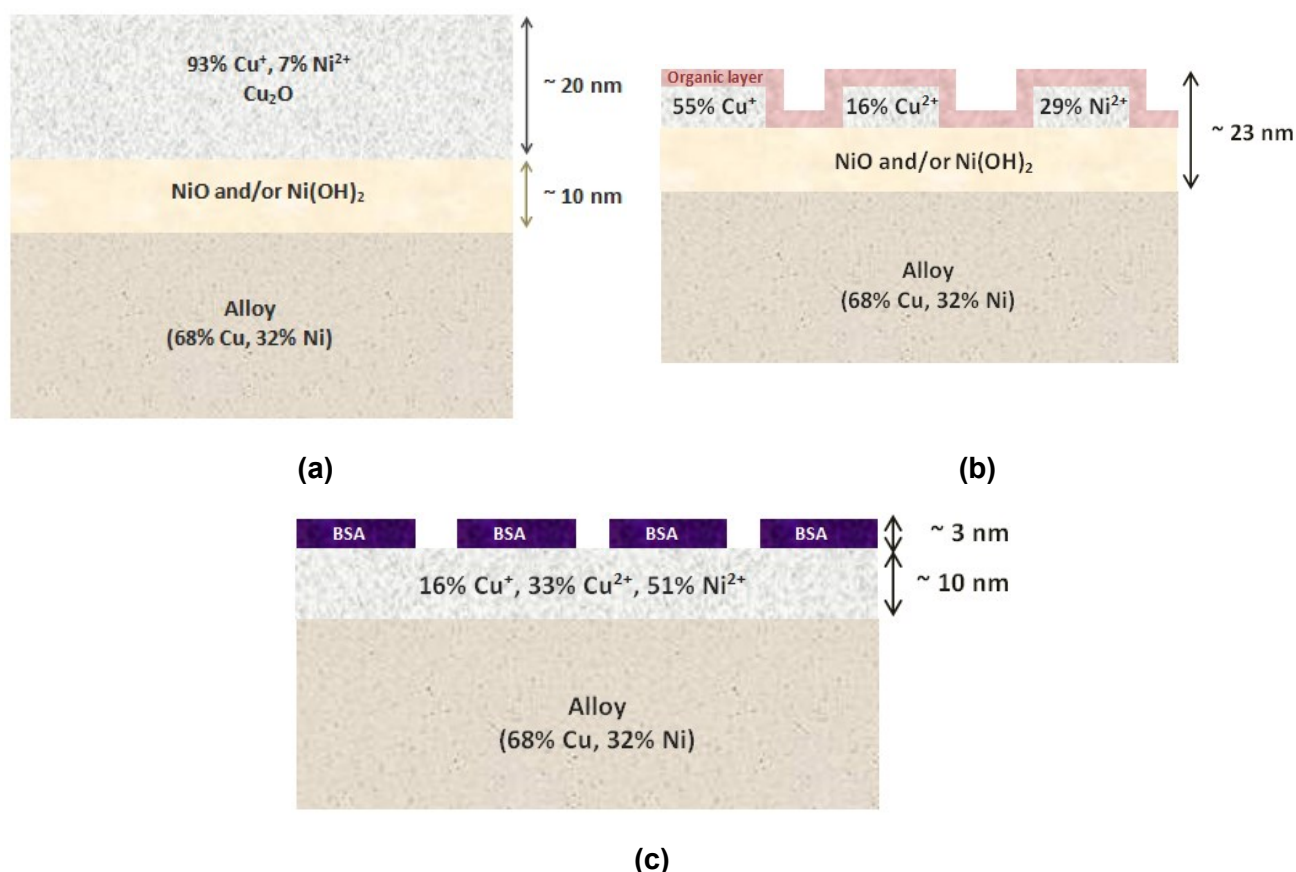


**Figure 4-12:** Models of the surface layers deduced from combined X-ray photoelectron spectroscopy (XPS) and time-of-flight secondary ions mass spectrometry (ToF-SIMS) results for 70Cu-30Ni after 1 h of immersion at  $E_{\text{corr}}$  in static (a) ASW, (b) FNSW and (c) ASW with  $20 \text{ mg.L}^{-1}$  of BSA (ASW + BSA).

#### 4.2.2 COMPOSITION OF THE ORGANIC LAYERS (XPS)

Correlations between spectral XPS data (C 1s, N 1s and O 1s) were used to generate information about the organic layer formed in FNSW and in ASW in the presence of BSA [142, 188]. As mentioned before, the C 1s peak was decomposed into three contributions (Figure 4-10). In Table 4-7 are summarized the binding energies of carbon, oxygen and nitrogen in chemical functions of biochemical compounds.

**Table 4-7:** Binding energy of elements in chemical functions of biochemical compounds [142].

	Element and function	Position (eV)	Reference compound
CARBON	<u>C</u> -(C,H)	284.8/285.0	Hydrocarbon, adventitious contamination
	<u>C</u> -N, O= <u>C</u> -N- <u>C</u>	286.1	Amine; amide, peptidic link
	<u>C</u> -O	286.3	Alcohol
	C- <u>C</u> -O	286.7	Polysaccharide
	O= <u>C</u> -O- <u>C</u>	286.8	Ester
	<u>C</u> =O, O- <u>C</u> -O	287.8	Aldehyde, (hemi)acetal
	O= <u>C</u> -N-C, O= <u>C</u> -O <sup>-</sup>	288.0	Amide, peptidic link; carboxylate
	C-O- <u>C</u> -O	288.1	Polysaccharide
	O= <u>C</u> -O-C	289.0	Ester
	O= <u>C</u> -OH	289.0	Carboxylic acid
OXYGEN	<u>O</u> =C-O <sup>-</sup>	531.1	Carboxylate
	<u>O</u> =C-N-C	531.3	Amide, peptidic link
	<u>O</u> =C-OH	531.8	Carboxylic acid
	<u>O</u> =C-O-C	531.9	Ester
	C- <u>O</u> H, C- <u>O</u> -C- <u>O</u> -C	532.6	Alcohol, (hemi)acetal
	C-C- <u>O</u>	532.9	Polysaccharide
	O=C- <u>O</u> -C	533.4	Ester
	O=C- <u>O</u> H	533.4	Carboxylic acid
	C- <u>O</u> -C-O	533.5	Polysaccharide
NITROGEN	C- <u>N</u> H <sub>2</sub>	399.3	Amine
	O=C- <u>N</u> H	399.8	Amide, peptidic link
	C- <u>N</u> H <sub>3</sub> <sup>+</sup>	401.3	Protonated amine

Figure 4-13(a) presents the plot of the molar concentration of carbon responsible for the C<sub>3</sub> component, located at 288.3 eV (O=C-N-C, or C-O-C-O or O=C-O<sup>-</sup>), as a function of the molar concentration of total organic nitrogen, N<sub>org</sub>. A 1:1 relation is expected for the amide function (HC-NH-(C=O)) forming the backbone of proteins (peptidic link). A deviation from this 1:1 line would indicate the presence of polysaccharides or any oxidized carbon of contaminants. As expected, the data are close to the 1:1 relation after 1 h of immersion of 70Cu-30Ni alloy in ASW with BSA in static conditions, evidencing the presence of adsorbed proteins on the surface. However, the organic layer after immersion in FNSW seem to contain other compounds than proteins.

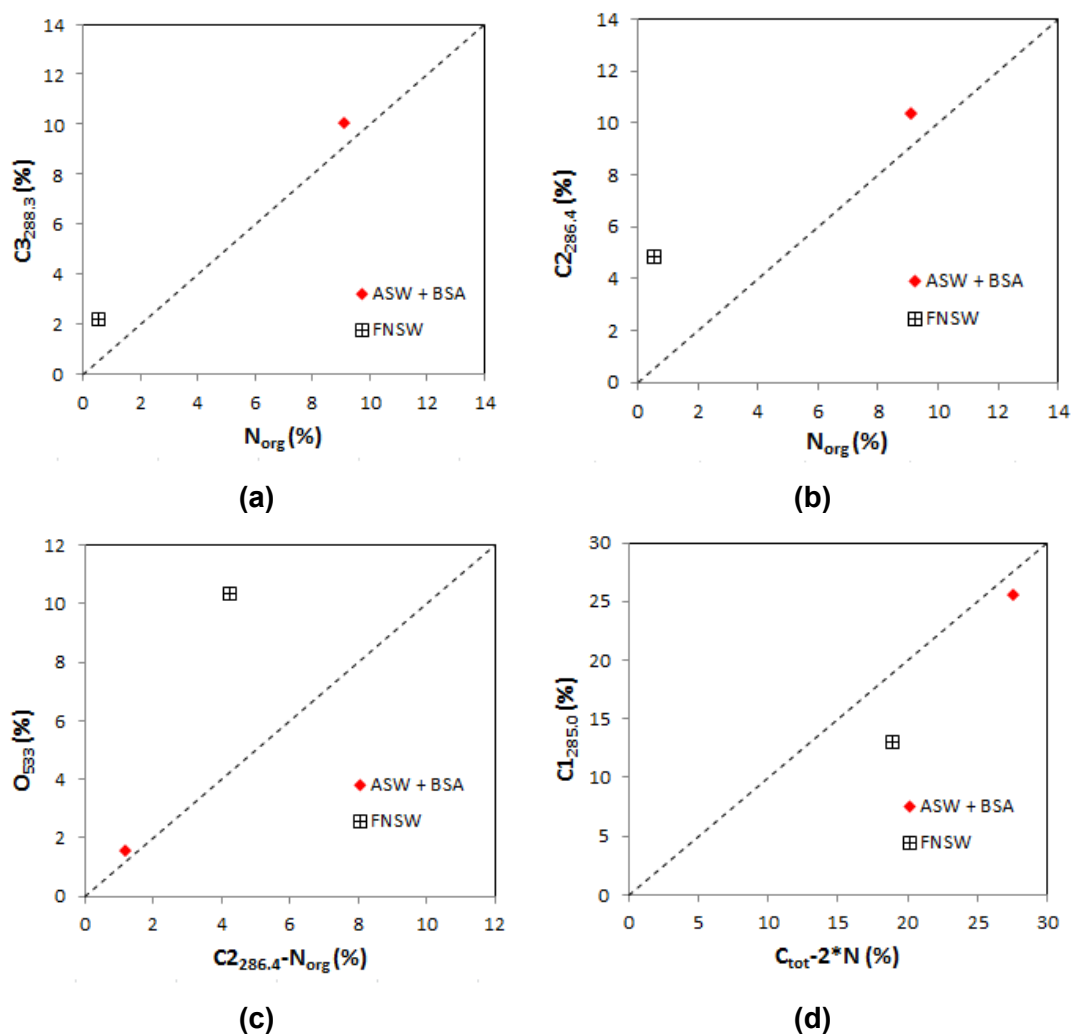


**Figure 4-13:** Plot of molar concentrations determined by XPS: (a)  $C_{3_{288.3}}$  vs  $N_{org}$ , (b)  $C_{2_{286.4}}$  vs  $N_{org}$ , c)  $O_{533}$  vs  $C_{2_{286.4}} - N_{org}$ , and d)  $C_{1_{285.0}}$  vs  $C_{tot} - 2 \cdot N_{org}$ . 70Cu-30Ni samples immersed 1 h at  $E_{corr}$ , in static aerated ASW with 20 mg.L<sup>-1</sup> of BSA (ASW + BSA) and FNSW. Dashed lines: 1:1 relation.

In Figure 4-13(b), the molar concentration of the carbon component located at a binding energy of 286.4 eV ( $C_2$  peak), which is due to carbon making a single bond with oxygen (in alcohol, polysaccharides, ester or ether) or nitrogen (in amine or amide), is plotted as a function of  $N_{org}$ . In this figure, the sample after immersion in FNSW presents high deviation from the 1:1 relation, which may be attributed to the presence of polysaccharides or oxygen-containing organic contaminants.

Figure 4-13(c) illustrates the O 1s near 533 eV (not shown in this manuscript), due to oxygen making one or two bonds with carbon, therefore, oxygen in polysaccharides, ester, alcohol or carboxyl groups, as a function of the difference between  $C_2$  and  $N_{org}$  ( $C_2 - N_{org}$ ). The total organic N is subtracted from  $C_2$  in order to remove the contribution of amide functions related to the presence of proteins. Therefore, 1:1 a relation is expected for alcohol,

ester and polysaccharides groups. For ASW+BSA, the experimental data are close to the 1:1 line. In the case of FNSW, the observed deviation may be due to the relatively low nitrogen concentration.

Figures 4-13(a) and 4-13(b) allow evidencing the presence of the amide function on the surface in ASW+BSA, but for FNSW other functions are present on the surface. This amide function is considered as a marker of proteins. However, the presence of other functional groups that can be associated to other biomolecules, such as polysaccharides or hydrocarbons (typical of lipids) is also evidenced. Polysaccharides frequently contain N-acetylated aminosugars in which nitrogen is also in the form of amide. Considering that all the  $N_{org}$  is in the form of amide ( $HC-NH-(C=O)$ ), the carbon which is not in the form of amide can be calculated by subtracting  $2*N_{org}$  from the total carbon ( $C_{tot} - 2*N_{org}$ ) [142, 188-190]. In Figure 4-13(d), the  $C_1$  carbon component, due to carbon only bound to carbon and hydrogen (hydrocarbon function, typical of lipids) is plotted as a function of the total carbon which is not in the form of amide ( $C_{tot} - 2*N_{org}$ ). The deviations from the 1:1 relation reflect the concentration of carbon which is neither in the form of hydrocarbon functions, nor in the form of amide. The sample after immersion in FNSW presents significant deviation from this 1:1 line.

Defining the composition of the organic adlayers is difficult due to the complexity of the biochemical compounds and the presence of organic contaminants on the surface. However, as shown in previous figures, the main biomolecules contributions can be distinguished and, therefore, the composition can be estimated in terms of these main components. In this work, the composition of the adsorbed layers is expressed in terms of 4 chemical entities: amide ( $HC-NH-(C=O)$ ) quantified by  $N_{org}$ ,  $CH_2$  quantified by the  $C_1$  component of the C 1s core level spectra, additional oxidized carbon quantified by  $C_{add} = C_{ox} - 2N_{org}$  and additional organic oxygen quantified by  $O_{add} = O_{org} - N_{org} = C_{ox} - 2N_{org}$  [143, 189], where  $C_{ox}$  is the oxidized carbon equal to:

$$C_{ox} = C_2 + C_3 = C_{tot} - C_1 \quad (4.14)$$

and  $O_{org}$  is the organic oxygen which can be approximated by:

$$O_{org} = C_{ox} + N_{org} \quad (4.15)$$

since for many organic functions (alcohol, primary amide or amine, ester, aldehyde, ketone), and mostly for those which are relevant in biosystems,  $C_{ox} = O_{org} + N_{org}$  (exceptions are the cases of ether, carboxylic acid or carboxylate functions).

Thus,  $C_{add}$  is the oxidized carbon in addition to the one present in the form of amide and  $O_{add}$  the organic oxygen in addition to the one present in the form of amide.

The elemental molar concentrations, obtained from XPS spectra, were converted into weight percentages of these chemical entities (g/100 g of adlayer), as explained in Annex A. Figure 4-14 illustrates the XPS results after conversion into weight percentages in the form of a ternary composition diagram. The corners of this triangle represent 100 wt % of amide, 100 wt % of  $\text{CH}_2$  and 100 wt % of additional carbon and oxygen ( $\text{C}_{\text{add}} + \text{O}_{\text{add}}$ ) [189]. This figure is convenient to represent the composition of surfaces and adlayers with respect to an amide pole, shared by proteins and N-acetylated functions of polysaccharides, a hydrocarbon pole, typical of lipids, and a pole representative of oxidized organic compounds, including polysaccharide moieties.

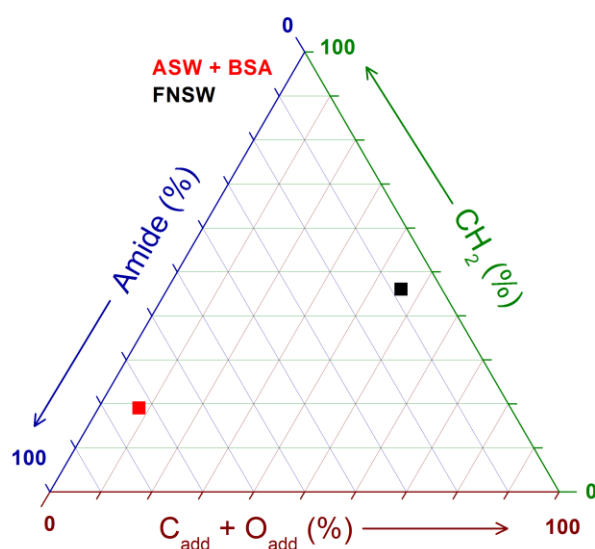


**Figure 4-14:** Composition of the biomolecules adsorbed on surface. Relative mass concentration of amide ( $\text{HC-NH-(C=O)}$ ), hydrocarbon  $\text{CH}_2$ , and other-oxygen-containing molecules ( $\text{C}_{\text{add}} + \text{O}_{\text{add}}$ ), including polysaccharides. 70Cu-30Ni samples immersed 1 h at  $E_{\text{corr}}$ , in static aerated ASW with 20  $\text{mg.L}^{-1}$  of BSA (ASW + BSA) and FNSW.

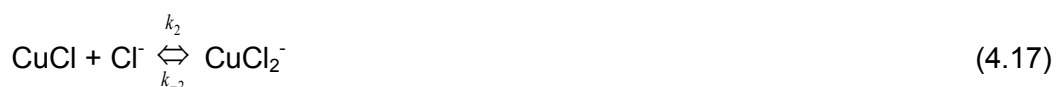
The ternary diagram has proved that proteins are the main compounds adsorbed on the surface after immersion in static ASW+BSA. This result is in agreement with the composition calculated by Y. Yang according to the aminoacid composition of BSA (70% amide + 30%  $\text{CH}_2$ ) [189]. After immersion in FNSW, the surface shows low protein concentration (10 % amide), but equal contribution of hydrocarbon (45 %  $\text{CH}_2$ ) and additional carbon and oxygen (45 %  $\text{C}_{\text{add}} + \text{O}_{\text{add}}$ ).

### 4.2.3 CORROSION MECHANISM

It is accepted by many authors that the corrosion of pure Cu is controlled by mass transport processes to and from corroding surfaces, involving  $O_2$ ,  $Cl^-$ ,  $OH^-$ ,  $Cu^+$  and  $CuCl_2^-$  species affecting both the anodic and the cathodic partial reactions [46, 127].

Four regions have been identified on the anodic polarization curve of pure Cu in acidic and neutral chloride solution for different rotation speeds: an active dissolution region close to the corrosion potential (apparent Tafel region) followed by a limiting-current region (current plateau), then a mixed-kinetics region appears up to a second limiting current region. The first two regions (active dissolution and first plateau) are attributed to the formation of  $Cu^+$  species, and the current increase beyond the first plateau accounts for copper dissolution as  $Cu^{2+}$  [191,192].

In the region of active dissolution close to the open circuit potential, the current is partially controlled by mass transport (mixed kinetics). Most of the authors agree that the anodic dissolution of Cu in chloride media occurs through a two-step sequence where CuCl is an insoluble specie [46,191,192]:



In this mechanism the soluble cuprous complex  $CuCl_2^-$  is the diffusing species and CuCl is the blocking species which is electrochemically formed in a first step (Eq. (4.16)) and chemically dissolved in a second step (Eq. (4.17)).

Therefore, in the anodic range, Cu is dissolved most likely as  $CuCl_2^-$  at low current densities and at sufficiently low chloride concentrations ( $< 1\text{ M}$ ) [193]. The mass transport/diffusion control of Cu electrodisolution has been ascribed by different authors either to the transport of  $Cl^-$  to the surface, or to the transport of  $CuCl_2^-$  from the surface to the bulk solution.

Deslouis *et al.* developed an expression (Eq. (4.18)) for low anodic current densities considering that: i) the first step (Eq. (4.16)) is no longer at quasi-equilibrium; ii) the coverage by CuCl is small; and iii) mass transport control is only due to  $CuCl_2^-$  diffusion from the surface [192].

$$\frac{F}{i} = \frac{1}{k_1[Cl^-]_\infty \exp\left(\frac{\alpha FE}{RT}\right)} + \frac{k_{-1} \exp\left(-\frac{FE}{RT}\right)}{k_1 k_2 [Cl^-]_\infty^2} + \frac{k_{-1} k_{-2} \delta_{CuCl_2} \exp\left(-\frac{FE}{RT}\right)}{k_1 k_2 [Cl^-]_\infty^2 D_{CuCl_2}} \quad (4.18)$$

On the other hand, the cathodic behavior of pure Cu is ascribed, in addition to O<sub>2</sub> reduction in aerated solution, to CuCl reduction and to Cu<sub>2</sub>O reduction. It has been established that on the cathodic plateau (transfer of 4 electrons) Cu<sub>2</sub>O does not interfere with O<sub>2</sub> reduction, and the interface may be considered as uniformly accessible for oxygen reduction. However, at less negative potentials (where some CuCl is also likely to be present), the cathodic partial reaction could be controlled by diffusion through a layer (Cu<sub>2</sub>O and/or CuCl) [46,192].

According to Pourbaix diagrams, insoluble corrosion products are expected to be formed on pure Cu surfaces at pH > 5.5. The presence of surface layers in neutral medium introduces additional complexity with respect to Cu corrosion in acidic chloride solution where corrosion products are soluble (oxide-free surface). Surface layers may partially block the metallic surface and/or may influence mass transport of either dissolved oxygen or oxidized Cu species [46,191].

Except for the effect of a surface layer, the model for the anodic electrodisolution may also explain qualitatively the behavior of Cu at the corrosion potential. At least, two different insoluble corrosion products are formed at  $E_{corr}$ , *i.e.* CuCl and Cu<sub>2</sub>O. At immersion times higher than 1 h, the surface layer consists mainly of Cu<sub>2</sub>O formed by hydrolysis of Cu<sup>+</sup> species. This hydrolytic reaction is competitive with the complexation of CuCl by Cl<sup>-</sup> and the removal of the produced CuCl<sub>2</sub><sup>-</sup> by mass transport [192]. Cu<sub>2</sub>O can also be formed from CuCl<sub>2</sub><sup>-</sup> as follows:

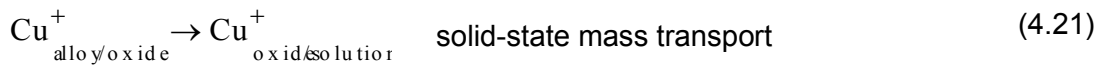
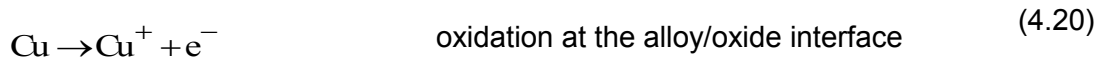


For pure Cu, only an effect of Cu<sub>2</sub>O as an insoluble product was claimed for low anodic currents, and the effect of the Cu<sub>2</sub>O layer on mass transport was considered. Thus, for the calculation of the corrosion current,  $I_{corr}$ , the anodic partial reaction was considered to be partially limited by the diffusion of CuCl<sub>2</sub><sup>-</sup> through both the Cu<sub>2</sub>O layer and the electrolyte (mixed control), while the cathodic partial reaction (oxygen reduction) was considered to be purely kinetic.

Two difficulties arise when comparing the corrosion behavior of Cu in acidic solution and that of 70Cu-30Ni alloy in seawater environments: a) the alloy is not pure Cu; and b) at pH 8, the alloy is covered by a corrosion product layer and, hence, there is a possible effect of the surface layers on the cathodic and the anodic mass transport.

Furthermore, it has been shown that the anodic behavior of 70Cu-30Ni alloy is predominated by that of copper (results not shown here).

From the mechanism shown for pure copper dissolution in chloride media at low anodic potential and in order to take into account the presence of an oxide layer as shown by surface analysis, a modified mechanism can be drawn for the anodic partial reaction of 70Cu-30Ni alloy at  $E_{corr}$  in ASW without and with biomolecules:



This mechanism involves four steps: 1) oxidation of Cu as  $\text{Cu}^+$  at the alloy/oxide interface, 2) mass transport of  $\text{Cu}^+$  by diffusion and migration in the solid phase from the alloy/oxide interface to the oxide/solution interface, 3) adsorption of chloride on a  $\text{Cu}^+$  surface site of the  $\text{Cu}_2\text{O}$  oxide at the oxide/solution interface, and 4) dissolution of copper as  $\text{CuCl}_2^-$  at the oxide/solution interface, followed by mass transport of  $\text{CuCl}_2^-$  by diffusion in the liquid phase from the oxide/solution interface to the bulk solution.

In aerated solution, the cathodic partial reaction is the reduction of dissolved oxygen that takes place at the oxide/solution interface.

#### 4.2.4 IMPEDANCE MODEL FOR 70Cu-30Ni AND EIS DATA FITTING

At  $E_{corr}$ , the anodic and the cathodic currents have the same magnitude and the net current is equal to zero. By principles of summation of currents, the Faradaic anodic and cathodic impedances must be in parallel (Figure 2-21). Both the anodic and the cathodic reactions are affected by mass transport. Therefore, the anodic Faradaic impedance can be depicted by a charge transfer resistance ( $R_t^a$ ) in series with an impedance that illustrates  $\text{Cu}^+$  and or  $\text{CuCl}_2^-$  mass transport and possible partial blocking effect by adsorbed species such as  $\text{CuCl}$  ( $Z_{\theta,D}^a$ ); whereas, the cathodic impedance can be depicted by a charge

transfer resistance ( $R_t^c$ ) in series with an impedance that illustrates  $O_2$  mass transport ( $Z_{\theta,D}^c$ ). A double layer capacitance  $C_{dl}$  is added in parallel with the anodic and the cathodic impedances. As the impedance response for electrochemical systems often reflects a distribution of reactivity that is commonly represented in equivalent electrical circuits as a constant-phase-element (CPE),  $C_{dl}$  is replaced here by  $CPE_{dl}$  which is a constant-phase-element related to the double layer. The CPE impedance equation is presented in Chapter 2, Eq. (2.20).

Thus, in a first approach, the 70Cu-30Ni/ASW and 70Cu-30Ni/FNSW systems can be modeled by the general equivalent electrical circuit illustrated in Figure 4-15(a), where  $R_e$  is the electrolyte resistance.

As the first current plateau for the reduction of dissolved oxygen is observed close to  $E_{corr}$  (Figure 4-1(a)), one hypothesis is that this plateau can be extrapolated down to  $E_{corr}$  (pure mass transport limitation for the cathodic partial reaction); thus,  $R_t^c$  can be neglected and the cathodic mass transport impedance is a Warburg impedance ( $W_c$ ) given by Eq. (2.25), presented in Chapter 2, with  $k_c$  expressed in  $s^{0.5} \cdot \Omega^{-1} \cdot cm^{-2}$ . Taking into account experimental cathodic polarization curves, the 70Cu-30Ni/ASW and 70Cu-30Ni/FNSW systems can be modeled by the simplified circuit presented in Figure 4-15(b).

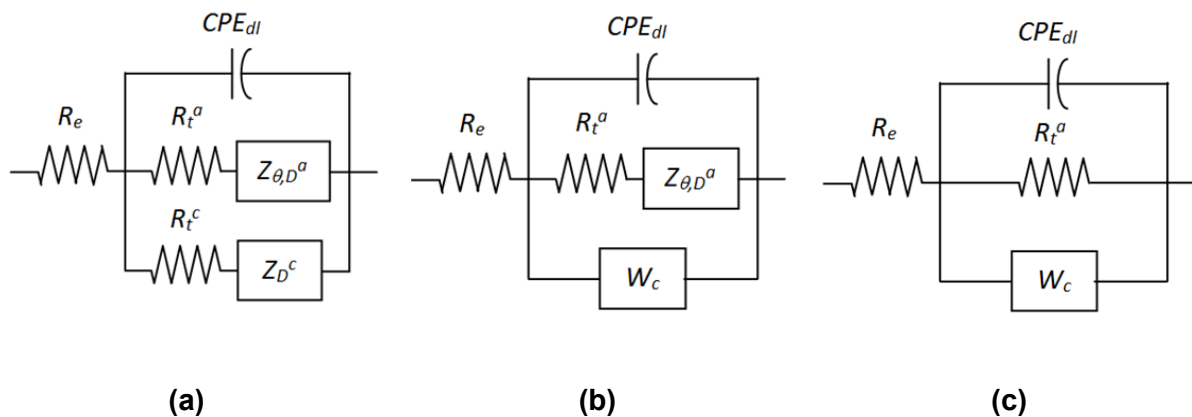


**Figure 4-15:** Equivalent electrical circuits to model the 70Cu-30Ni/ASW and 70Cu-30Ni/FNSW systems: (a) general circuit, (b) simplified circuit taking into account experimental cathodic polarization curves, and (c) circuit used to analyze the HF loop of experimental impedance diagrams.  $R_e$  is the electrolyte resistance,  $CPE_{dl}$  a constant-phase-element related to the double layer,  $R_t^a$  the anodic charge transfer resistance,  $Z_{\theta,D}^a$  an impedance that illustrates anodic mass transport and partial blocking effect by CuCl,  $R_t^c$  the cathodic charge transfer resistance,  $Z_D^c$  a cathodic impedance that illustrates  $O_2$  mass transport, and  $W_c$  the cathodic Warburg impedance.

For the same experimental impedance data as those presented in Figure 4-2 in the complex plane, the absolute value of the imaginary part of the impedance ( $|Z''|$ ) was plotted as a function of the frequency in logarithmic coordinates (Figure 4-16) [140].

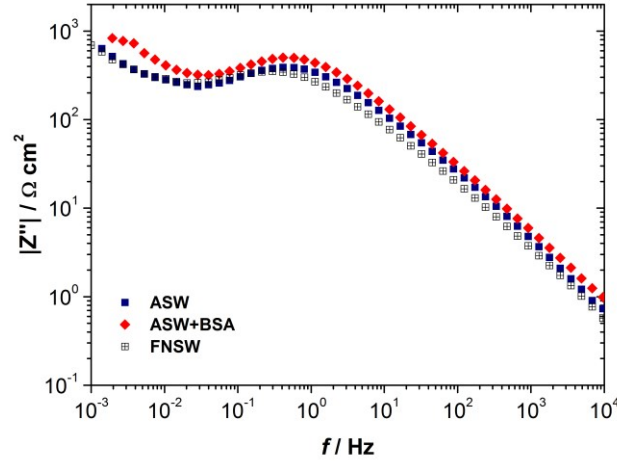


**Figure 4-16:** Experimental impedance data (imaginary part of the impedance as a function of frequency) of 70Cu-30Ni alloy obtained at  $E_{corr}$  after 1 h of immersion in static aerated artificial seawater (ASW) without and with BSA (20 mg.L<sup>-1</sup>), and filtered natural seawater (FNSW). Same data as in Figure 4-2.

In the HF range, a pseudo-straight line with a slope lower than 1 in absolute value but varying slightly with the frequency can be observed. This slope value lower than 1 suggests a CPE-like behavior (it should be equal to 1 in case of pure capacitive behavior). The CPE parameters  $\alpha$  and  $Q$  can be graphically obtained in the case of a R//CPE circuit, following the method presented by Orazem *et al.* [140]. The parameter  $\alpha$  is calculated from the slope of the  $\log |Z''|$  vs  $\log f$  curve in the HF range:

$$\alpha = \left| \frac{d \log |Z''(f)|}{d \log f} \right| \quad \text{at HF} \quad (4.24)$$

and  $Q$  is obtained from  $\alpha$  as follows:

$$Q = -\frac{1}{Z''(f)(2\pi f)^\alpha} \times \sin\left(\frac{\alpha\pi}{2}\right) \quad \text{at HF} \quad (4.25)$$

However, as the slope varies with the frequency, the HF loop of the impedance diagrams cannot be represented by a R//CPE circuit, and  $\alpha$  cannot be determined from Figure 4-16. To better visualize a possible constant value of the slope in a narrow frequency range, the  $d \log |Z''| / d \log f$  vs  $\log f$  curves were calculated from those presented in Figure

4-16 (derivative curves; Fig. 4-17). In the case of a R//CPE circuit, a plateau would be observed at HF corresponding to a value of  $-\alpha$ . In Figure 4-17, no plateau is clearly visible, in particular, at very HF, and again the value of  $\alpha$  cannot be graphically obtained. It can be concluded from Figure 4-17 that the HF loop of the experimental impedance diagrams cannot be modeled by a R//CPE circuit, and therefore that the CPE parameters  $\alpha$  and  $Q$  cannot be graphically estimated.

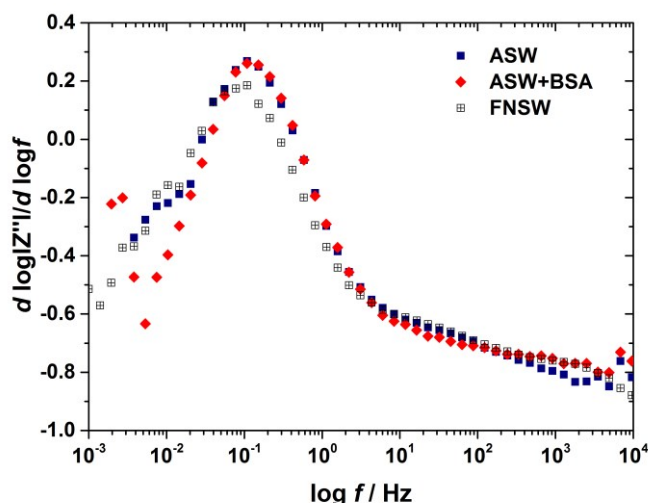


**Figure 4-17:** Experimental impedance data (derivative curves calculated from Figure 4-16) of 70Cu-30Ni alloy obtained at  $E_{corr}$  after 1 h of immersion in static aerated artificial seawater (ASW) without and with BSA ( $20 \text{ mg.L}^{-1}$ ), and filtered natural seawater (FNSW). Same data as in Figure 4-2.

In conclusion, the HF loop of experimental impedance diagrams corresponds to the  $CPE_{dl} // R_t^a // W_c$  equivalent circuit (Figure 4-15(c)); thus, it illustrates mainly the anodic charge transfer (diameter equal to  $R_t^a$ ), and its depressed shape is partly due to the CPE and partly due to the cathodic Warburg impedance in parallel. In all cases, since no plateau is clearly visible at very HF in Figure 4-17, the effect of  $W_c$  is not negligible compared to that of  $CPE_{dl}$  even at  $10^4$  Hz, and there is no clear frequency domain specifically assigned to each process.

The LF loop is related to the anodic mass transport and partial blocking effect by adsorbed species such as  $\text{CuCl}$  ( $Z_{\theta,D}^a$ ).

In the case of 70Cu-30Ni alloy, the impedance data show a minor effect of anodic mass transport and blocking effect by  $\text{CuCl}$  (LF loop of impedance diagrams described only by a few points). Indeed, the amount of  $\text{CuCl}$  which is formed on the surface depends on

potential and at  $E_{corr}$  this amount is low. This is in agreement with a very low amount of  $\text{Cl}^-$  compound evidenced by ToF-SIMS.

The circuits of Figure 4-15 take into account the presence of an oxide layer, as shown by surface analysis, through  $Z_{\theta,D}^a$  that partly illustrates  $\text{Cu}^+$  mass transport within that layer.

As the LF loop of impedance diagrams is not well defined, the single HF loop was analyzed by regression of the equivalent circuit presented in Figure 4-15(c), in which  $\text{CPE}_{dl}$ ,  $R_t^a$  and  $W_c$  are in parallel, using Simad® software developed at Laboratoire Interfaces et Systèmes Electrochimiques. The regression results are presented in Table 4-8 and Figure 4-18. The corresponding impedance equation is written as follows:

$$Z = R_e + \frac{1}{\frac{1}{R_t^a} + Q(j\omega)^\alpha + k_c \sqrt{j\omega}} \quad (4.26)$$

The experimental frequency range taken into account for the regression is indicated in Table 4-8, but the fitted curves in Figure 4-18 are shown in the whole frequency range (0.003-10<sup>5</sup> Hz), with parameters values corresponding to those given in Table 4-8.

If the CPE behavior is assumed to be associated with surface distributed time constants for charge-transfer reactions (time-constant distribution along the electrode surface), then it is possible to apply the equation derived by Brug *et al.*, (Eq. (2.22)), to calculate the effective capacitance associated with the CPE [138,139]. The capacitance values calculated from the impedance diagrams shown in Figure 4-18, taking for  $R_e$  and  $R_t^a$  the values extracted from the regression procedure (Table 4-8), are given in Table 4-8. These capacitance values are of the order of several tens of  $\mu\text{F} \cdot \text{cm}^{-2}$  in all cases; such values are typical of those for a double layer capacitance, which validates the equivalent electrical circuits proposed in Figure 4-15. Therefore, the HF loop illustrates mainly the anodic charge transfer and its diameter is equal to  $R_t^a$ .

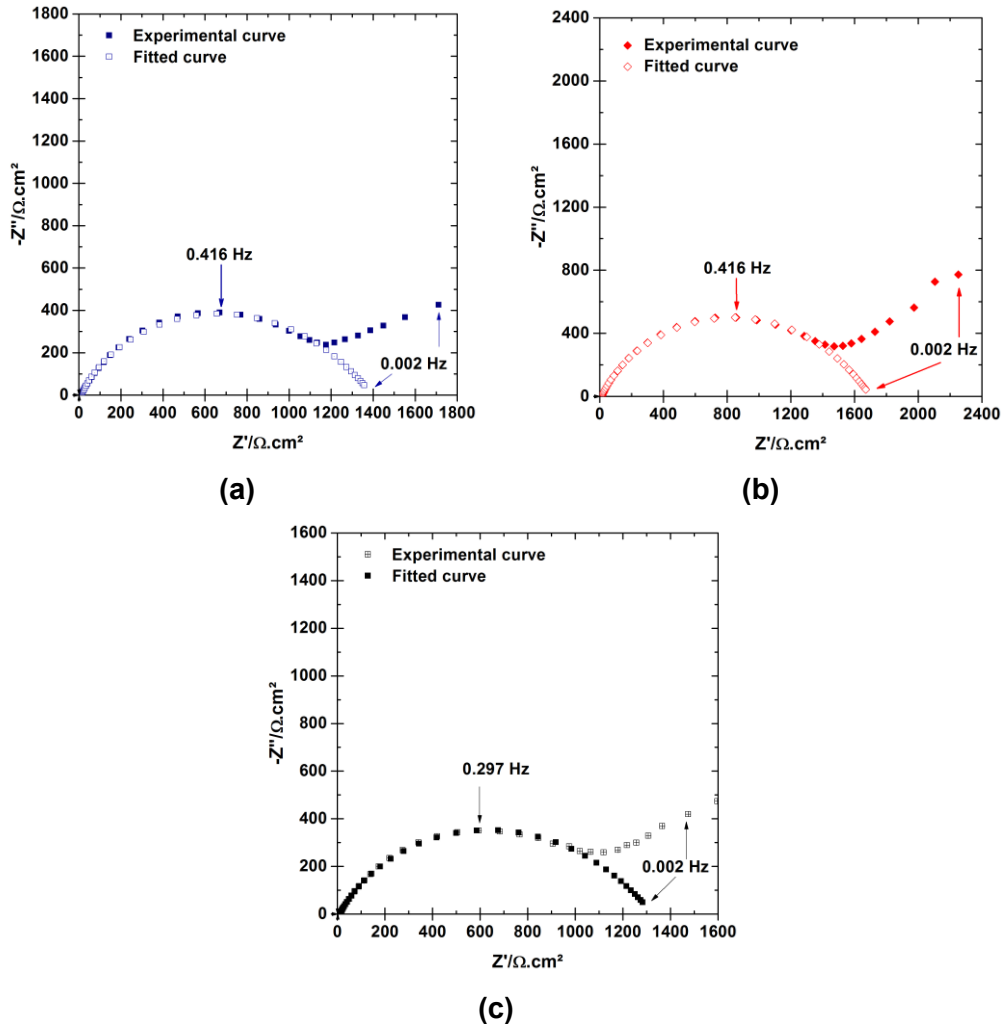


**Figure 4-18:** High frequency loops of Nyquist diagrams obtained for 70Cu-30Ni at  $E_{corr}$  after 1 h of immersion in static aerated: (a) ASW, (b) ASW with 20 mg.L<sup>-1</sup> of BSA, and (c) FNSW. Experimental curves and fit of the impedance model presented in Figure 4-15(c) to the data. Same data as in Figures 4-2.

**Table 4-8:** Experimental frequency range taken into account for the regression, parameters values (electrolyte resistance  $R_e$ , anodic charge transfer resistance  $R_t^a$ , constant of the cathodic Warburg impedance  $k_c$ , and CPE parameters  $\alpha$  and  $Q$  obtained from the regression of the equivalent circuit presented in Figure 4-15(c) to experimental impedance data shown in Figures 4-2, and effective capacitance  $C_{eff}$  associated with the CPE calculated from Eq. (2.22) presented in Chapter 2.

	Frequency range Hz	$R_e$ $\Omega.cm^2$	$R_t^a$ $\Omega.cm^2$	$k_c$ $s^{0.5}.\Omega^{-1}.cm^{-2}$	$\alpha$	$Q$ $F.cm^{-2}.s^{(\alpha-1)}$	$C_{eff}$ $\mu F.cm^{-2}$
ASW	$10^5$ - $5.6 \times 10^{-2}$	12	1390	$2.5 \times 10^{-04}$	0.78	$1.99 \times 10^{-04}$	37
ASW + BSA	$10^5$ - $1.1 \times 10^{-1}$	12	1690	$1.2 \times 10^{-04}$	0.76	$2.03 \times 10^{-04}$	30
FNSW	$10^5$ - $7.8 \times 10^{-2}$	12	1310	$3.5 \times 10^{-04}$	0.76	$2.90 \times 10^{-04}$	50

The  $C_{eff}$  value in the presence of 20 mg.L<sup>-1</sup> of BSA (30 μF.cm<sup>2</sup>) is lower than those calculated without protein (ASW) or with small amount of proteins (FNSW) (mean value: 42 μF.cm<sup>2</sup>). This may be explained by a blocking effect by the adsorbed proteins which decrease the active surface area ( $S_{act}$ ) where the electron transfer occurs. Thus, the  $C_{eff}$  ratio without and with biomolecules would be equal to the active surface ratio:

$$\frac{C_{eff}^{without}}{C_{eff}^{with}} = \frac{S_{act}^{without}}{S_{act}^{with}} \quad (4.27)$$

The mean value for this ratio is about 1.35.

Similar values are obtained for  $R_t^a$  in ASW and in FNSW, and  $R_t^a$  is ~ 22% higher in the presence of BSA.

The anodic charge-transfer resistance for a reaction dependent on potential and mass transport is defined in terms of kinetic parameters to be:

$$R_t^a = \frac{1}{Kbc_0e^{bV}} \quad (4.28)$$

$$\text{where } K = zFke^{-bV_0} \text{ and } b = \frac{\alpha zF}{RT}$$

with  $c_0$  the surface concentration of the diffusing species (CuCl<sub>2</sub><sup>-</sup>),  $z$  the number of transferred electrons,  $k$  the rate constant for the reaction,  $\alpha$  the symmetry factor,  $V$  the interfacial potential, and  $V_0$  the interfacial equilibrium potential.

Thus, mass transport influences charge transfer by means of the surface concentration.

In static conditions, changes in  $R_t^a$  value can be explained by three different effects: 1) a potential effect ( $V$  in Eq. (4.28)), 2) a kinetic effect ( $K$  in Eq. (4.28)), and 3) a blocking of surface effect induced by the adsorbed biomolecules. If we assume constant  $b$  and constant surface concentration of the diffusing species  $c_0$  without and with biomolecules, then Eq. (4.28) becomes:

$$\frac{R_t^a|^{with}}{R_t^a|^{without}} = \frac{K|^{without}}{K|^{with}} \times e^{b(E_{corr}^{without} - E_{corr}^{with})} \times \frac{S_{act}^{without}}{S_{act}^{with}} \quad (4.29)$$

where  $R_t^a$  is expressed in  $\Omega$ . Given Eq. (4.27), Eq. (4.29) can be written as:

$$\frac{K|^{without}}{K|^{with}} = \frac{R_t^a|^{with}}{R_t^a|^{without}} \times e^{b(E_{corr}^{with} - E_{corr}^{without})} \times \frac{C_{eff}^{with}}{C_{eff}^{without}} \quad (4.30)$$

The anodic partial reaction of 70Cu-30Ni alloy immersed at  $E_{corr}$  in seawater involves the dissolution of Cu as  $Cu^+$  species (modified mechanism drawn from that for pure copper dissolution in chloride media at low anodic potential; Eqs. (4.20) to (4.23)). Then, the number of transferred electrons  $z$  can be taken as 1. Moreover,  $\alpha$  is comprised between 0 and 1, and is usually assumed to be equal to 0.5. Therefore,  $b = \frac{\alpha z F}{RT} \approx 20$  and the numeral application of Eq. (4.30) gives  $\frac{k^{without}}{k^{with}}(BSA) = 1.7$ . The result  $K^{without} > K^{with}$  means that the anodic reaction is slowed down by the BSA and the effect of potential is compensated by a strong kinetic effect. Indeed, as  $E_{corr}$  is more anodic in the presence of BSA, a single effect of the potential would induce a decrease of  $R_t^a$  (Eq. (4.28)).

At the corrosion potential,  $E_{corr}$ , the overall current is equal to zero and the corrosion current density  $i_{corr}$  is given by:

$$i_{corr} = i_a = -i_c \quad (4.31)$$

where  $i_a$  is the anodic current density corresponding to the anodic partial reaction, and  $i_c$  is the cathodic current density corresponding to the cathodic partial reaction ( $i_c < 0$ ).

Under assumption of Tafel kinetics (pure kinetic control) for the anodic partial reaction,  $i_{corr}$  is related to  $R_t^a$  and the anodic Tafel slope  $\beta_a$  by:

$$i_{corr} = \frac{\beta_a}{2.303 R_t^a} \quad (4.32)$$

$$\text{with } \beta_a = \frac{2.303 RT}{\alpha z F}$$

The assumption of minor effect of anodic mass transport is reasonable since the LF loop related to the anodic mass transport (and partial blocking effect by CuCl) is described only by a few points.

Grubitsch *et al.* calculated  $i_{corr}$  as:

$$i_{corr} = \frac{B}{R_p} \quad (4.33)$$

where  $B = 0.019$  V and  $R_p$  is the polarization resistance [194]. The numerical value of the constant  $B$  was obtained by assuming a pure activation mechanism for both the anodic and the cathodic reactions (anodic and cathodic Tafel kinetics).

As mentioned before, the anodic partial reaction involves the dissolution of Cu as  $\text{Cu}^+$  species (Eqs. (4.20) to (4.23)). Therefore,  $z$  in Eq. (4.32) can be taken as 1.

Corrosion current densities were calculated from Eq. 4.32, with  $z = 1$  and  $\alpha = 0.5$ , and from Eq. (4.33) with  $R_p = R_t^a$ .

The calculated  $i_{corr}$  values are given in Table 4-9 and are compared to those deduced graphically from the cathodic polarization curves ( $i_{corr}$  being equal to the first plateau current density).

**Table 4-9:** Comparison of the corrosion current density values obtained from  $R_t^a$ , by application of Eqs. (4.32) and (4.33), and from the cathodic polarization curves (first plateau current density).

	$R_t^a / \Omega.\text{cm}^2$	$i_{corr} / \mu\text{A}.\text{cm}^{-2}$		
		Eq. (4.32)	Eq. (4.33)	Cathodic polarization curve
<b>ASW</b>	1390	36	14	12
<b>ASW + BSA</b>	1690	30	11	12
<b>FNSW</b>	1310	39	14	8

If comparing the corrosion current densities obtained from Eq. (4.32) to those deduced graphically from the cathodic polarization curves, there is a ratio of about 3-5 between the values that may be partly explained by a value of  $\alpha$  different from 0.5 and partly explained by the fact that polarization curves were plotted with a scan rate of  $0.5 \text{ mV}.\text{s}^{-1}$  (non steady-state curves).

Figure 4-19 allows to better visualize the differences in corrosion current density calculated from Eq. (4.32) (with  $z = 1$  and  $\alpha = 0.5$ ), for the different solutions in static conditions.

In static conditions, the corrosion current density of 70Cu-30Ni alloy is similar in ASW and in FNSW, and is slightly lower with BSA. In FNSW, the biomolecules concentration is not high enough to induce any corrosion inhibition effect. Therefore, these results show a small beneficial effect *i.e.* a small corrosion inhibition effect in the presence of BSA.

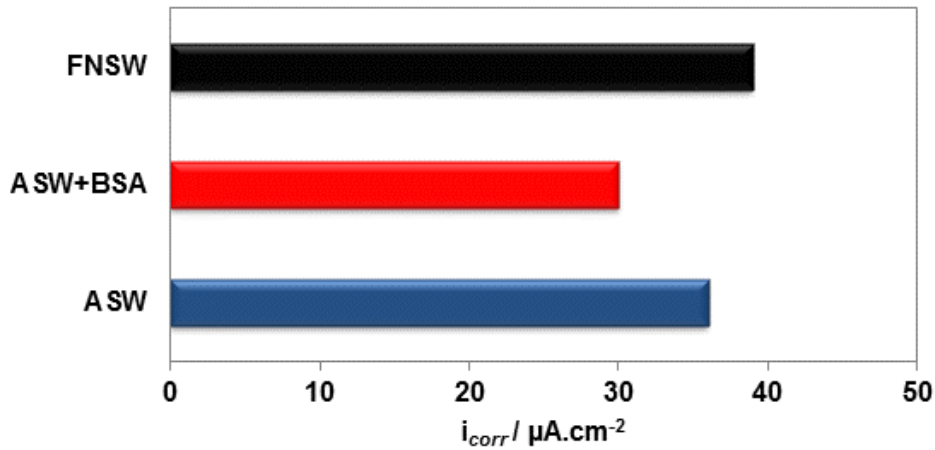


**Figure 4-19:** Comparison of the corrosion current density values calculated from Eq. (4.32) with  $z = 1$  and  $\alpha = 0.5$  for 70Cu-30Ni alloy after 1 h of immersion in static aerated ASW without and with 20 mg.L<sup>-1</sup> of BSA, and filtered natural seawater (FNSW).

### 4.3 CONCLUSIONS

The objective of this chapter was to study the influence of solution (FNSW vs ASW) and biomolecules (naturally present in seawater) concentration vs BSA on the electrochemical behavior and the surface chemical composition of 70Cu-30Ni alloy in seawater, in static conditions. For that purpose, electrochemical measurements performed after 1 h of immersion were combined to surface analyses.

From polarization curves, high anodic dissolution currents are shown (no passive current). A model is proposed to analyze electrochemical impedance data obtained at  $E_{corr}$ . The HF loop of the experimental diagrams illustrates mainly the anodic charge transfer, and its depressed shape is partly due to the CPE and partly due to the cathodic Warburg impedance in parallel; whereas, the LF loop is related to the anodic mass transport and partial blocking effect by adsorbed species such as CuCl. The BSA has a slight effect on the

electrochemical behavior of 70Cu-30Ni alloy. Thus,  $E_{corr}$  value after 1 h of immersion is ~ 30 mV more anodic with BSA, and EIS results indicate a small corrosion inhibition effect induced by the protein (decrease of the corrosion current density of  $\approx 20\%$ ).

From XPS and ToF-SIMS analyses, different surface chemical compositions of 70Cu-30Ni are shown in ASW without and with BSA, and in FNSW. In ASW without BSA, two oxidized layers can be observed: an outer layer mainly composed of copper oxide ( $\text{Cu}_2\text{O}$  redeposited layer) and an inner layer mainly composed of oxidized nickel, with a global thickness of ~ 30 nm. In ASW with BSA, the protein is detected on the surface and the thickness of the adsorbed layer is ~ 3 nm, corresponding to one monolayer. The presence of BSA leads to a mixed oxide layer ( $\text{CuO}$ ,  $\text{Cu}_2\text{O}$ , and  $\text{Ni}(\text{OH})_2$ ) with a lower thickness (~ 10 nm).

The thick duplex oxide layer is also observed in static FNSW, nevertheless, the oxidized Cu/oxidized Ni ratio is lower than in static ASW.

The combination of electrochemical measurements and surface analysis allows us to conclude that, in static conditions, the BSA induces a decrease of the dissolution rate at  $E_{corr}$ , and hence a decrease of the amount of redeposited  $\text{Cu}_2\text{O}$  and of the oxide layer thickness.

Similar electrochemical behavior and surface chemical composition of 70Cu-30Ni alloy are obtained in ASW and in FNSW, due to the low biomolecule concentration in FNSW.

As the water of cooling circuits is typically under flow and as the corrosion of copper is controlled by mass transport processes to and from corroding surfaces, electrochemical measurements in well-controlled hydrodynamics conditions, using a rotating electrode, have been performed. These experiments, which clarify the role of mass transport on the electrochemical behavior and strengthen the proposed impedance model, are the purpose of the next chapter.

## CHAPTER 5 – EFFECT OF HYDRODYNAMICS

This chapter is focused on the study of the effect of hydrodynamics on the corrosion behavior of 70Cu-30Ni and Al brass alloys after 1 h of immersion in aerated artificial seawater (ASW) and filtered natural seawater (FNSW). For that purpose, electrochemical measurements in static conditions, under flow and stirring, and in well-controlled hydrodynamic conditions, were combined to surface analysis (after immersion in static conditions and under flow and stirring). Two models deduced from a general one are proposed to analyze impedance data obtained with both alloys.

### 5.1 STATIC CONDITIONS VS UNDER FLOW AND STIRRING - RESULTS

As the water of cooling circuits is typically under flow and as the corrosion of copper in aerated solution is known to be controlled by mass transport processes to and from corroding surfaces [46], hydrodynamics is an important parameter to be studied. Therefore, in order to avoid the redeposition of  $\text{Cu}_2\text{O}$  (see Chapter 4) and to keep the same samples as in static conditions (disc electrodes), the effect of flow and stirring on the electrochemical behavior and the surface chemical composition of 70Cu-30Ni alloy was first investigated. For that, a volume 10 times higher than in static conditions was used inside the electrochemical cell (1 L instead of 100 mL); the solution was continuously renewed using a peristaltic pump, with a flow rate of  $\sim 0.27 \text{ mL.s}^{-1}$ , and the electrolyte inside the cell was stirred using a magnetic stirrer.

#### 5.1.1 ELECTROCHEMICAL MEASUREMENTS

After 1 hour of immersion in aerated artificial seawater, the corrosion potential  $E_{\text{corr}}$  reaches a steady-state value of  $-0.215 \pm 0.007 \text{ V vs SCE}$ . Thus, flow and stirring induce more anodic values compared to those found in static conditions ( $-0.230 \pm 0.009 \text{ V vs SCE}$ ).

The anodic behavior of 70Cu-30Ni alloy after 1h of immersion at  $E_{\text{corr}}$  in ASW under flow and stirring is compared to that obtained in static conditions in Figure 5-1. The shape of the anodic polarization curve is the same in both cases, showing very high dissolution currents, with a pseudo-plateau current density of  $\sim 2.5 \text{ mA.cm}^{-2}$  at around  $0.4 \text{ V vs SCE}$ . The two curves overlap at intermediate anodic potentials and small differences can be observed at high anodic potentials. Therefore, the anodic behavior does not depend strongly on hydrodynamics.

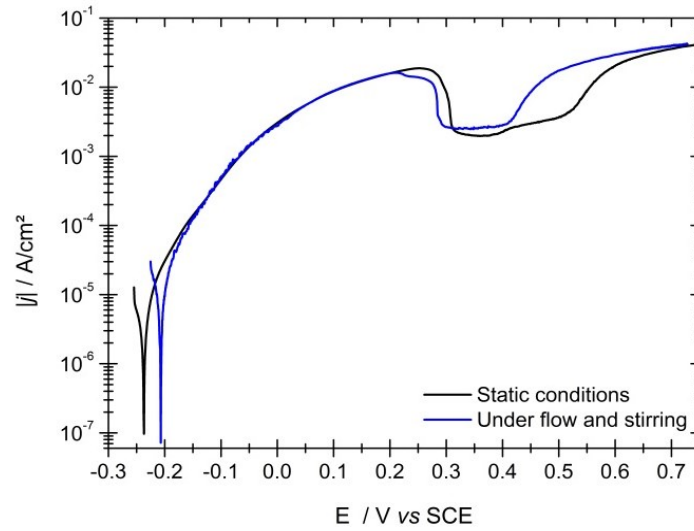


**Figure 5-1:** Anodic polarization curves of 70Cu-30Ni after 1 h of immersion at  $E_{corr}$  in aerated artificial seawater, in static conditions and under flow and stirring. Scan rate:  $0.5 \text{ mV.s}^{-1}$ .

Impedance diagrams in the complex plane, plotted at  $E_{corr}$  after 1 h of immersion in aerated artificial seawater, in static conditions and under flow and stirring, are presented in Figure 5-2. In both cases, the diagrams exhibit two capacitive loops: one high frequency (HF) depressed semi-circle, and a low frequency (LF) loop. The size of the HF loop is 2.5 times lower under flow and stirring. The decrease of the size of the high frequency loop when moving from static conditions to under flow and stirring (same electrode geometry) can be explained by additional mass transport and potential effects.

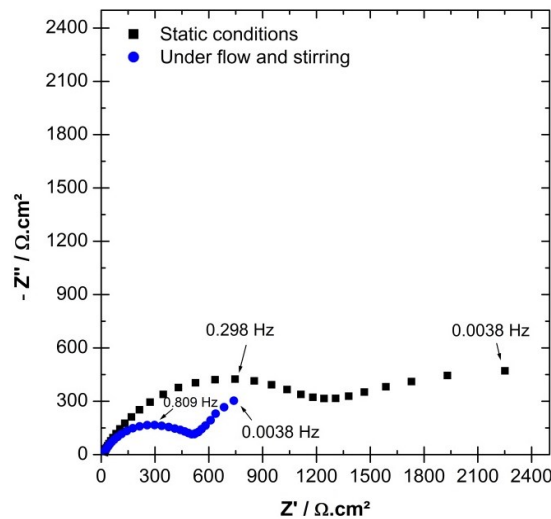


**Figure 5-2:** Experimental impedance diagrams in the complex plane (Nyquist diagrams) of 70Cu-30Ni plotted at  $E_{corr}$  after 1 h of immersion in aerated artificial seawater, in static conditions and under flow and stirring.

### 5.1.2 SURFACE ANALYSIS

Figure 5-3(a) illustrates the Cu  $2p_{3/2}$  core level spectrum for 70Cu-30Ni alloy in three different conditions: a) after polishing, b) in static ASW, and c) in ASW under flow and stirring. The Cu  $2p_{3/2}$  core level spectrum after immersion in ASW under flow and stirring indicates the presence of a first peak at a binding energy of 932.2 eV corresponding to  $\text{Cu}^0$  and/or  $\text{Cu}^+$ , and a second peak at a binding energy of 934.4 eV and the satellite at 943.4 eV associated to the presence of  $\text{Cu}^{2+}$ .

The Cu Auger line ( $L_3M_{45}M_{45}$ ) of 70Cu-30Ni alloy in ASW under flow and stirring (Figure 5-3(b)), located at a kinetic energy of 918.5 eV, demonstrates the presence of  $\text{Cu}^0$  as for the sample after polishing. This result allows us to conclude that the oxide layer formed on top of the alloy is very thin (compared to static conditions). Its thickness can be calculated from XPS data (see below).

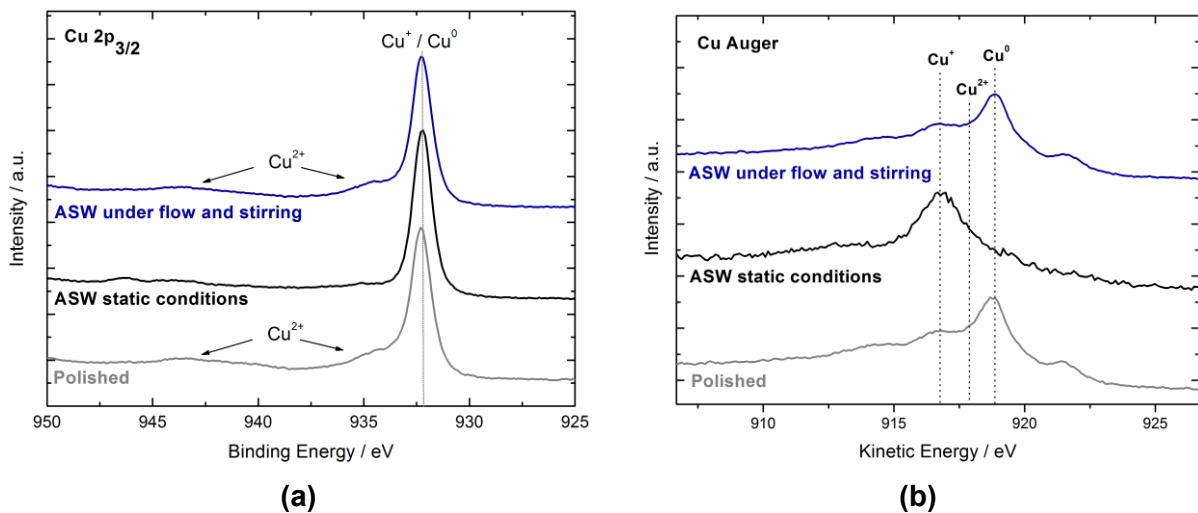


**Figure 5-3:** (a) X-ray photoelectron spectroscopy (XPS) Cu  $2p_{3/2}$  core level spectra, and (b) Cu  $L_3M_{45}M_{45}$  Auger lines of 70Cu-30Ni after polishing, after 1 h of immersion at  $E_{\text{corr}}$  in aerated artificial seawater in static conditions and under flow and stirring. The intensity is expressed in arbitrary unit (a.u.).

The Ni  $2p_{3/2}$  core level spectra obtained for 70Cu-30Ni alloy under flow and stirring exhibit one peak at 852.3 eV corresponding to  $\text{Ni}^0$ , which confirms that the oxide film formed on the surface is very thin. Another peak is observed at a binding energy of 855.7 eV as well as the satellite at 861.4 eV corresponding to  $\text{Ni}(\text{OH})_2$  (Figure 5-4).

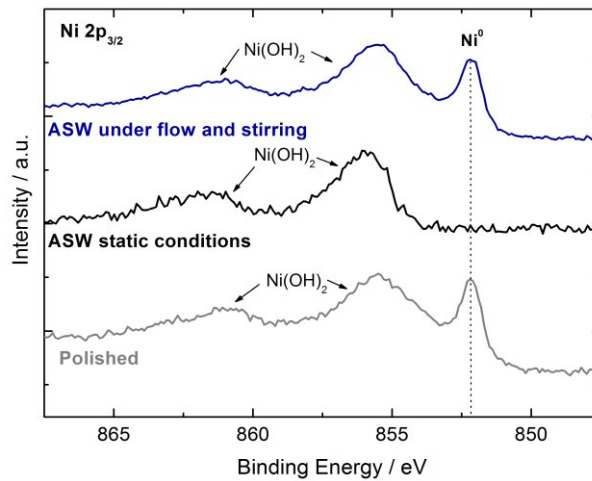


**Figure 5-4:** XPS Ni  $2p_{3/2}$  core level spectra of 70Cu-30Ni alloy after polishing, after 1 h of immersion at  $E_{corr}$  in aerated artificial seawater in static conditions and under flow and stirring. The intensity is expressed in arbitrary unit (a.u.).

The oxide layer is composed of 42 at. %  $\text{Cu}^+$ , 28 at. %  $\text{Cu}^{2+}$ , and 30 at. %  $\text{Ni(OH)}_2$  and its thickness, calculated from XPS data, is  $\sim 1.4$  nm. The composition of the alloy beneath the oxide layer is 67 at. % Cu and 33 at. % Ni. The atomic composition and the equivalent thickness of the oxide layer was calculated from XPS data for 70Cu-Ni alloy using the system of equations previously presented in Chapter 4 (Equations: (4.3) to (4.8)) and considering the intensities of copper and nickel in the metallic substrate.

Figure 5-5 shows a depth profile of 70Cu-30Ni alloy (negative ions) after 1h of immersion at  $E_{corr}$  in ASW under flow and stirring. This profile was obtained in the same conditions as the ones in static conditions (same sputtering rate and analysis area).

In this figure, two regions can be distinguished. In the first region, from 4 to  $\sim 13$  s, the  $35\text{Cl}^-$ ,  $90^{58}\text{NiO}_2^-$ ,  $95^{63}\text{CuO}_2^-$  and  $18^{18}\text{O}^-$  signals show their maximum intensity, and the  $116^{58}\text{Ni}_2^-$  signal continue increasing. At 13 s, the second region can be distinguished, where the  $90^{58}\text{NiO}_2^-$ ,  $95^{63}\text{CuO}_2^-$  and  $18^{18}\text{O}^-$  signals sharply decrease and the  $116^{58}\text{Ni}_2^-$  signal shows an intense and constant intensity. Therefore, the first zone corresponds to the oxide covering the alloy, whereas the second region corresponds to the metallic substrate. It should be noticed that between 13 s and 62 s, the  $35\text{Cl}^-$ ,  $90^{58}\text{NiO}_2^-$ ,  $95^{63}\text{CuO}_2^-$  and  $32\text{O}_2^-$  signals show an inflexion point forming a shoulder and subsequently decreasing, and the  $116^{58}\text{Ni}_2^-$  signal remains constant. This indicates that under the alloy/oxide interface, oxides are detected, which may result from the preparation of the samples (disk cut from real condenser tubes, and then flattened).

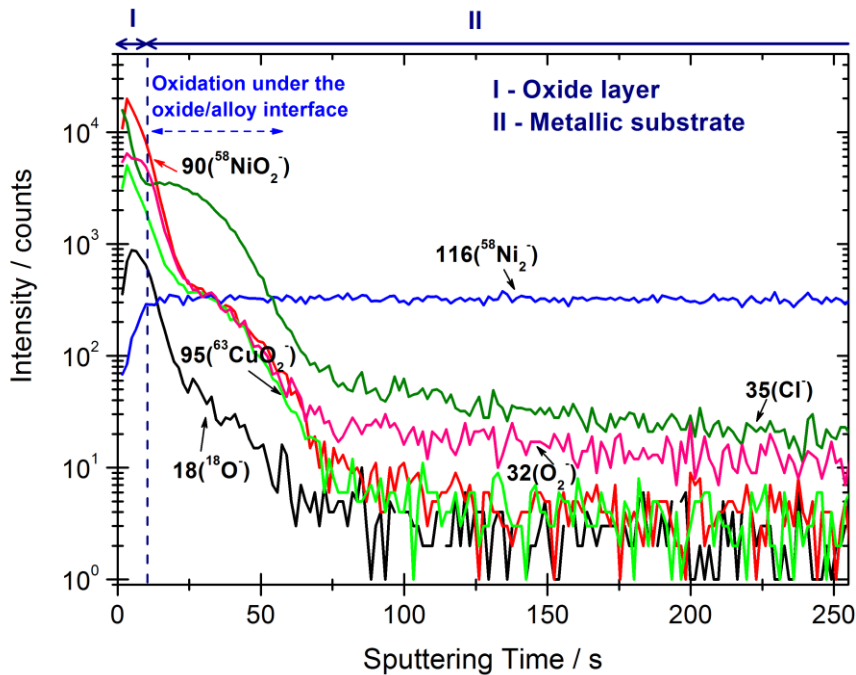


**Figure 5-5:** Characteristic time-of-flight secondary ions mass spectrometry (ToF-SIMS) negative depth profile of 70Cu-30Ni after 1 h of immersion at  $E_{corr}$  in aerated artificial seawater under flow and stirring.

If comparing the depth profiles after immersion in ASW in static conditions (previously presented in Chapter 4) and under flow and stirring, both profiles are different and the oxide layer is much thinner under flow and stirring. The profile under flow and stirring is more similar to the one obtained for the sample just after polishing, which confirms that flow and stirring avoid the redeposition of  $\text{Cu}_2\text{O}$ .

#### 5.1.2.1 SURFACE LAYERS MODELS (COMBINED XPS AND TOF-SIMS)

Figure 5-6 shows the surface layer model derived for the alloy after 1 h of immersion in ASW under flow and stirring. In this case, the oxide layer formed on top of the alloy is very thin and comparable to that obtained for the sample just after polishing (mixed oxide layer; see Figure 4-12(a)). Additionally, the amount of  $\text{Cu}_2\text{O}$  in the oxide layer is lower than that in static ASW but higher than that for the sample after polishing. This could indicate that both components are rarely dissolved; nevertheless, there is a preferential dissolution of  $\text{Cu}^+$ .

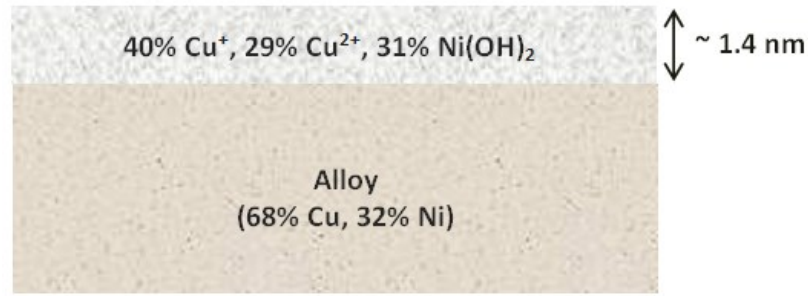


**Figure 5-6:** Model of the surface layers deduced from combined X-ray photoelectron spectroscopy (XPS) and time-of-flight secondary ions mass spectrometry (ToF-SIMS) results for 70Cu-30Ni after 1 h of immersion at  $E_{corr}$  in ASW under flow and stirring.

## 5.2 ELECTROCHEMICAL MEASUREMENTS USING A RRE

Electrochemical measurements in well-controlled hydrodynamic conditions were performed using a rotating ring electrode (RRE) at three different rotation speeds (40, 160, and 640 rpm).

### 5.2.1 THEORY FOR A ROTATING RING ELECTRODE

The first mathematical treatment of convection and diffusion towards a rotating electrode was given by Levich. The general mass transport equation for the flux of species  $j$ ,  $J_j$ , is given by:

$$J_j = -D_j \nabla C_j - \frac{z_j F}{RT} D_j C_j \nabla \phi + C_j \nu \quad (5.1)$$

where:

$D_j$  is the diffusion coefficient of the solution species  $j$  ( $\text{cm}^2 \cdot \text{s}^{-1}$ );

$C_j$  is the molar concentration of species  $j$  ( $\text{mol} \cdot \text{cm}^{-3}$ );

$\phi$  is the electrostatic potential;

$z_j$  is the number of transferred electrons;

$\nu$  is the hydrodynamic velocity vector and represents the motion of the solution; and

$\nabla$  is the vector of partial derivatives that defines the gradient operators.

The term  $-D_j \nabla C_j$  represents diffusion,  $-\frac{z_j F}{RT} D_j C_j \nabla \phi$  represents migration, and  $C_j \nu$  represents convection. For solutions containing an excess of supporting electrolyte, the ionic migration term can be neglected.

The variation of  $C_j$  with time is given by:

$$\frac{\partial C_j}{\partial t} = -\nabla J_j \quad (5.2)$$

Therefore, the general convective-diffusion equation is obtained by combining Eqs. (5.1) and (5.2), assuming that migration is absent and that  $D_j$  is not a function of the position:

$$\frac{\partial C_j}{\partial t} = D_j \nabla^2 C_j - \nu \cdot \nabla C_j \quad (5.3)$$

Under steady-state conditions ( $\frac{\partial C_j}{\partial t} = 0$ ), the convective-diffusion equation written in terms of cylindrical coordinates becomes:

$$\nu_r \frac{\partial C_j}{\partial r} + \nu_y \frac{\partial C_j}{\partial y} = D_j \left\{ \frac{\partial^2 C_j}{\partial r^2} + \frac{1}{r} \frac{\partial C_j}{\partial r} + \frac{\partial^2 C_j}{\partial y^2} \right\} \quad (5.4)$$

where:

$r$  is the radial flow direction;

$y$  is the flow direction normal to the surface ;

$\nu_r$  is the component of the velocity in the radial direction; and

$\nu_y$  is the component of the velocity normal to the electrode surface.

Let us consider a ring electrode with inner radius  $r_1$  and outer radius  $r_2$  (surface area =  $\pi(r_2^2 - r_1^2)$ ). When this electrode is rotated with an angular velocity (rotation speed),  $\Omega$ , then the steady-state, convective-diffusion equation that must be solved is:

$$\nu_r \frac{\partial C_j}{\partial r} + \nu_y \frac{\partial C_j}{\partial y} = D_j \frac{\partial^2 C_j}{\partial y^2} \quad (5.5)$$

Where mass transport by diffusion in the radial direction, represented by the terms  $D_j \left\{ \frac{\partial^2 C_j}{\partial r^2} + \frac{1}{r} \frac{\partial C_j}{\partial r} \right\}$ , is, for usual flow rates, small compared to mass transport by convection in the radial direction  $(\nu_r \left( \frac{\partial C_j}{\partial r} \right))$ , so that these terms can be neglected. The boundary conditions for the limiting ring current are:

$$\begin{array}{llll} C_j = C_j^* & \text{for} & y \rightarrow \infty & \text{where } C_j^* \text{ is the bulk concentration of species } j; \\ C_j = 0 & \text{at} & y = 0 & \text{for } r_1 \leq r < r_2; \\ \frac{\partial C_j}{\partial y} = 0 & \text{at} & y = 0 & \text{for } r < r_1; \\ C_j = C_j^* & \text{at} & y = 0 & \text{for } r < r_1; \end{array}$$

When the values of  $\nu_r$  and  $\nu_y$  velocities are introduced, Eq. (5.5) becomes:

$$r \left( \frac{\partial C_j}{\partial r} \right) - y \left( \frac{\partial C_j}{\partial y} \right) = \left( \frac{D_j}{B'} \right) \left( \frac{1}{y} \right) \left( \frac{\partial^2 C_j}{\partial y^2} \right) \quad (5.6)$$

where  $B' = 0.51 \Omega^{\frac{3}{2}} N^{-\frac{1}{2}}$  and  $N$  is the kinematic viscosity ( $10^{-2} \text{ cm}^2 \cdot \text{s}^{-1}$ ).

For the reduction reaction  $O + ne^- \rightarrow R$ , the current at the ring electrode is given by:

$$i_o = -zFD_o 2\pi \int_{r_1}^{r_2} \left( \frac{\partial C_o}{\partial y} \right)_{y=0} r dr \quad (5.7)$$

The solution to this equation yields the Levich expression for the cathodic limiting current:

$$i_{o,L} = -0.62zF\pi C_o^* D_o^{2/3} (r_2^3 - r_1^3)^{2/3} N^{-1/6} \Omega^{1/2} \quad (5.8)$$

where:

$F$  is the Faraday constant ( $96500 \text{ C} \cdot \text{mol}^{-1}$ );

$C_o^*$  is the bulk concentration of the oxidizing species O ( $\text{mol} \cdot \text{cm}^{-3}$ );

$D_o$  is the diffusion coefficient of the oxidizing species O ( $\text{cm}^2 \cdot \text{s}^{-1}$ ); and

$\Omega$  is the rotation speed ( $\text{s}^{-1}$ ).

This equation is comparable to the Levich equation presented by Tribollet [195] for the diffusion limiting current for a Newtonian fluid considering a thin ring ( $(r_2 - r_1) \ll r_1$ ):

$$i_{O,L} = -z \frac{F\pi}{\Gamma\left(\frac{4}{3}\right)} (3a_0)^{1/3} C_0^* D_0^{2/3} N^{-1/6} r_1^{4/3} (r_2 - r_1)^{2/3} \Omega^{1/2} \quad (5.9)$$

with  $\Gamma\left(\frac{4}{3}\right) \approx 0.893$ ,  $n = 1$ , and  $a_0 = 0.51021599$ .

## 5.2.2 RESULTS

### 5.2.2.1 70Cu-30Ni

#### 5.2.2.1.1 CORROSION POTENTIAL ( $E_{corr}$ ) VS TIME

The corrosion potential as a function of time ( $E_{corr}$  vs time) was followed for 1 h. In Table 5-1, the corrosion potential values obtained with the RRE in two different solutions (ASW and FNSW) are presented and compared with the values recorded in static conditions using a disc electrode. When using the rotating ring electrode, the corrosion potential ( $E_{corr}$ ) decreases when the rotation speed increases in the two solutions. However, in static ASW the corrosion potential values are similar to the ones obtained at 160 rpm.

**Table 5-1:** Corrosion potential values for 70Cu-30Ni alloy after 1 h of immersion in artificial seawater (ASW), and filtered natural seawater (FNSW), in static conditions and using a RRE at three different rotation speeds (40, 160 and 640 rpm).

	$E_{corr}$ / V vs SCE
<b>ASW static conditions</b>	$-0.230 \pm 0.009$
<b>ASW 40 rpm</b>	$-0.217 \pm 0.005$
<b>ASW 160 rpm</b>	$-0.233 \pm 0.006$
<b>ASW 640 rpm</b>	$-0.248 \pm 0.004$
<b>FNSW static conditions</b>	$-0.231 \pm 0.013$
<b>FNSW 40 rpm</b>	$-0.216 \pm 0.005$
<b>FNSW 160 rpm</b>	$-0.223 \pm 0.001$
<b>FNSW 640 rpm</b>	$-0.252 \pm 0.005$

### 5.2.2.1.2 CATHODIC POLARIZATION CURVES

The cathodic polarization curves of 70Cu-30Ni in artificial seawater plotted with the rotating ring electrode using a scan rate of  $0.5 \text{ mV.s}^{-1}$  are presented in Figure 5-7(a) and are compared to the curve obtained in static conditions. In static conditions, two cathodic plateaus can be observed, corresponding to the 2 steps of dissolved oxygen reduction, with a transfer of 2 or 4 electrons; the first plateau is observed close to  $E_{corr}$ .

The current densities in static conditions are lower than the current densities obtained with the rotating ring electrode. Furthermore, using the RRE, only one cathodic plateau (transfer of 4 electrons) is clearly visible and the plateau current density increases in absolute value with the rotation speed. This first current plateau observed close to  $E_{corr}$  in static conditions is replaced by an inflexion point.

Steady-state curves are reported in Figure 5-7(b). The curves plotted in steady-state conditions and with a scan rate of  $0.5 \text{ mV.s}^{-1}$  show similar shape and similar current densities.

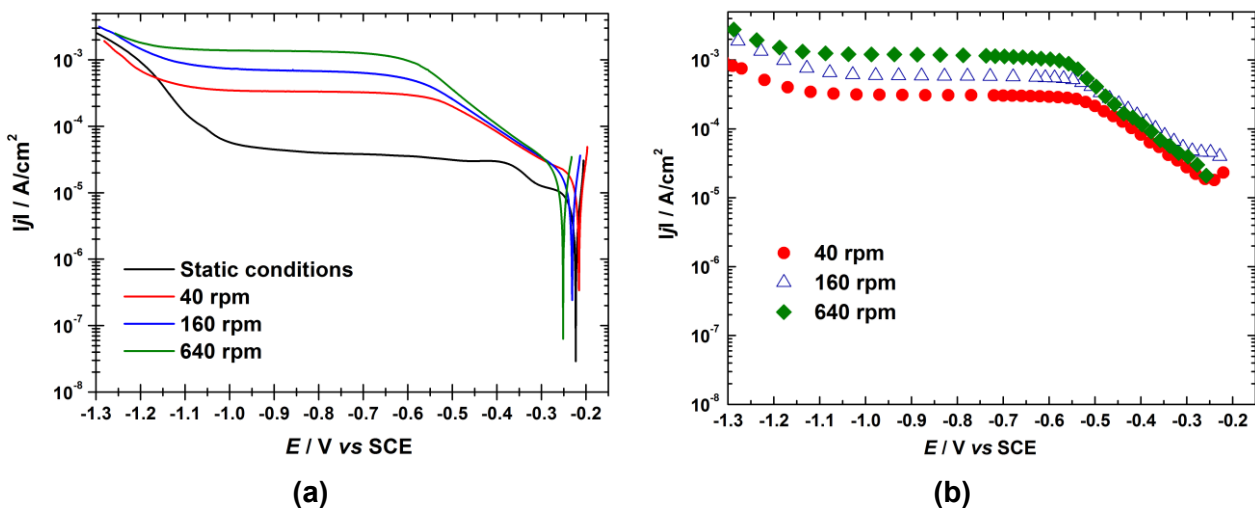


**Figure 5-7:** Cathodic polarization curves of 70Cu-30Ni after 1 h of immersion at  $E_{corr}$ , in aerated artificial seawater, in static conditions and using the rotating ring electrode at 40, 160 and 640 rpm: (a) Scan rate:  $0.5 \text{ mV.s}^{-1}$  and (b) steady-state curves.

In Table 5-2 the limiting current density values at  $-0.75 \text{ V vs SCE}$ , corresponding to the second plateau for the oxygen reduction reaction, are compared to the theoretical values calculated using Eq. (5.9). For that, the oxygen concentration in the solution was considered to be equal to 8 ppm ( $2.5 \times 10^{-5} \text{ mol.cm}^{-3}$ ) [175], and its diffusion coefficient equal to  $2 \times 10^{-5} \text{ cm}^2.\text{s}^{-1}$  at  $25^\circ\text{C}$  [3-5].

**Table 5-2:** Comparison between the limiting current densities at -0.75 V vs SCE (corresponding to the second step of dissolved oxygen reduction with transfer of 4 electrons), and  $0.5 \text{ mV.s}^{-1}$ , taken from Figure 5-7, and the theoretical values calculated from Eq. (5.9).

Limiting current densities ( $\mu\text{A.cm}^{-2}$ )				
		Experimental values taken from Figure 5-7(a) ( $0.5 \text{ mV.s}^{-1}$ )	Experimental values taken from Figure 5-7(b) (steady-state)	Theoretical values calculated from Eq. (5.9)
Static conditions		39	-	-
RRE	40 rpm	330	300	388
	160 rpm	662	600	777
	640 rpm	1314	1000	1554

The experimental limiting current densities recorded at  $0.5 \text{ mV.s}^{-1}$  are slightly higher than those recorded in steady-state conditions. However, all experimental limiting current densities are in good agreement with the theoretical ones. The differences between experimental and theoretical values can be explained by an oxygen bulk concentration slightly different from 8 ppm ( $C_o^*$  depends on salts concentrations and temperature) and/or by an oxygen diffusion coefficient comprised between  $1.87 \times 10^{-5}$  and  $2.60 \times 10^{-5} \text{ cm}^2.\text{s}^{-1}$  at  $25^\circ\text{C}$  [8].

To better compare steady-state and non-steady-state curves, the two curves, recorded in ASW at 160 rpm are superimposed in Figure 5-8, together with, the two curves obtained in FNSW at 160 rpm. The results show similar shape and current densities in the second plateau potential domain in all cases. However, the plateau current density in steady-state conditions is slightly lower compared to that recorded at  $0.5 \text{ mV.s}^{-1}$ . Moreover, some differences can be observed close to  $E_{corr}$ : the steady-state curve in ASW exhibits higher current densities than the curve plotted at  $0.5 \text{ mV.s}^{-1}$  in ASW.

It can be concluded from these curves that the cathodic behavior of 70Cu-30Ni alloy is the same in ASW and in FNSW.

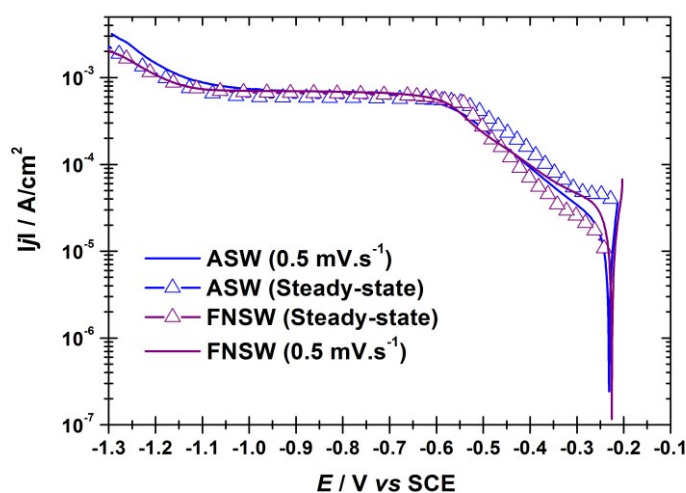


**Figure 5-8:** Cathodic polarization curves of 70Cu-30Ni rotating ring electrode at 160 rpm, after 1 h of immersion at  $E_{\text{corr}}$  in: i) aerated artificial seawater (scan rate:  $0.5 \text{ mV.s}^{-1}$ ), ii) aerated artificial seawater (steady-state curve), iii) filtered natural seawater (steady-state curve), and iv) filtered natural seawater (scan rate:  $0.5 \text{ mV.s}^{-1}$ ).

### 5.2.2.1.3 LEVICH AND KOUTECKY-LEVICH CURVES

From Figures 5-7 and 5-8, a limiting current plateau can be observed between -0.6 and  $\sim -1.1 \text{ V vs SCE}$ , where the oxygen reduction is under pure mass-transport control. In order to better understand what happens in that potential region, the steady-state limiting current density vs the square root of the RRE angular velocity was plotted at  $-0.8 \text{ V vs SCE}$  (Figure 5-9(a)).

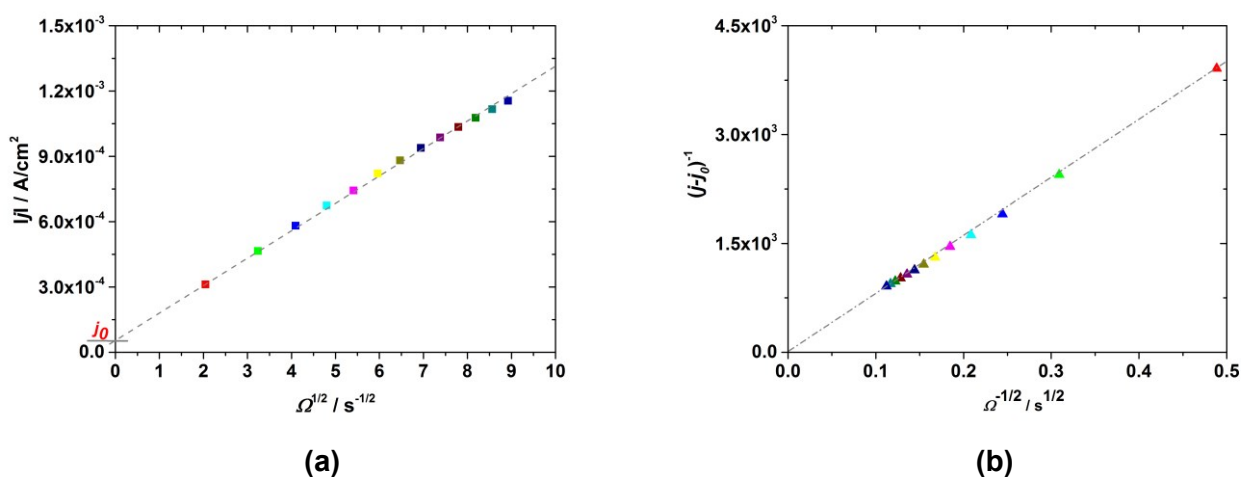


**Figure 5-9:** (a) Levich and (b) Koutecky-Levich curves of 70Cu-30Ni in aerated artificial seawater at  $-0.80 \text{ V vs SCE}$ .

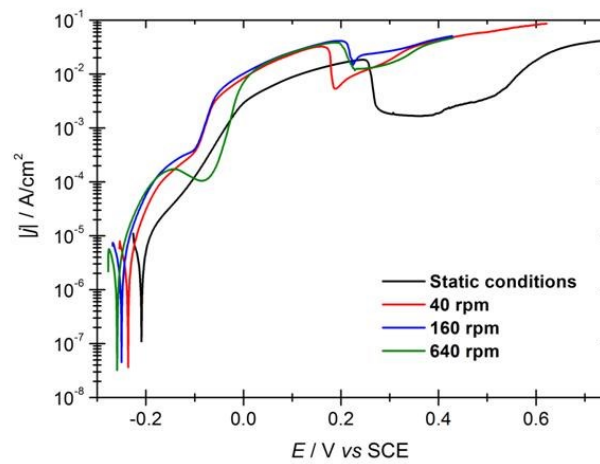
The Levich curve doesn't pass through zero and exhibits a slight curvature at high rotation speed, which shows a small contribution of a side reduction reaction of the solvent (corresponding to a non-diffusional current  $j_0$ , independent of  $\Omega$ ) and the reaction of  $O_2$  reduction not totally limited by mass transport, respectively. In that case, the Koutecky-Levich curve must be plotted  $((j-j_0)^{-1} \text{ vs } \Omega^{-1/2})$ ; Fig. 5-9(b)). The obtained curve is a straight line nearly passing through zero which demonstrates that the electronic transfer current is very high ( $O_2$  reduction is almost totally limited by mass transport).

From the slope of the Koutecky-Levich curve ( $C = s_{Lc}^{-1}$  with  $s_{Lc}$  given by Eq. (2.10)), in aerated artificial seawater, at room temperature,  $D_O$  was found to be equal to  $1.1 \times 10^{-5} \text{ cm}^2 \text{ s}^{-1}$ . This value is in agreement with that in the literature:  $D_O = 1.4 \times 10^{-5} \text{ cm}^2 \text{ s}^{-1}$  [7].

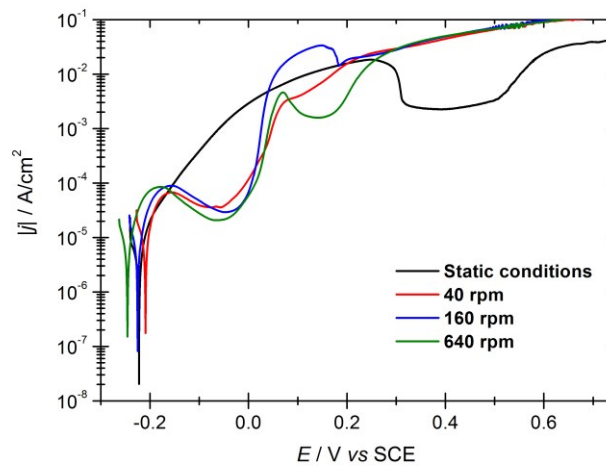
#### 5.2.2.1.4 ANODIC POLARIZATION CURVES

Figure 5-10 illustrates the anodic behavior of the alloy after 1 h of immersion in ASW and in FNSW (static conditions and using the RRE, at three different rotation speeds). The anodic polarization curves plotted in ASW with the rotating ring electrode present certain dissimilarities if compared to the curve obtained in static conditions (Figure 5-10(a)). Firstly, a current peak followed by a minimum current are observed between -0.15 and 0.05 V vs SCE with the RRE; this feature, which is not present in static conditions, becomes more evident with the increase of the rotation speed. Secondly, the current density is lower in static conditions than using the RRE at potentials higher than 0.05 V vs SCE. Furthermore, the wide plateau observed between 0.3 and 0.5 V vs SCE in static conditions is not well defined with the RRE. There is an influence of the rotation speed on the anodic polarization curves for potentials lower than 0.05 V vs SCE. However, the curves exhibit no anodic plateau at intermediate anodic potential (close to  $E_{corr}$ ) unlike pure copper in acidic or neutral chloride solution for which a limiting-current region can be observed around 0 V vs SCE [8, 9]. These results show partial mass transport limitation (*i.e.* mixed kinetics) for the anodic reactions.

Figure 5-10(b) illustrates the anodic polarization curves in FNSW. The current peak, followed by a minimum current observed with the RRE close to the corrosion potential in ASW, are also visible in FNSW; however, this feature is the same whatever the rotation speed of the RRE. Between 0.05 and 0.3 V vs SCE, there are significant changes of the current density with the rotation speed. Again the results show partial mass transport limitation (*i.e.* mixed kinetics) for the anodic reactions.



(a)



(b)

**Figure 5-10:** Anodic polarization curves of 70Cu-30Ni rotating ring electrode at three different rotation speeds (40, 160 and 640 rpm), after 1 h of immersion at  $E_{corr}$  in: (a) aerated artificial seawater, and (b) aerated filtered natural seawater. Scan rate:  $0.5 \text{ mV.s}^{-1}$ .

The anodic polarization curves plotted in ASW and FNSW at 160 rpm with a scan rate of  $0.5 \text{ mV.s}^{-1}$  were compared to steady-state curves obtained in both solutions at 160 rpm (Fig. 5-11(a)). The results show that the anodic behavior of 70Cu-30Ni alloy is the same in ASW and FNSW in steady-state conditions. The steady-state curves plotted in ASW at three different rotation speeds are presented in Figure 5-11(b). Contrary to what is observed in non steady-state conditions (Figure 5-10(a)); the effect of mass transport on the steady-state anodic behavior is small. From all these anodic polarization curves, it can be concluded that the anodic reactions of 70Cu-30Ni alloy in seawater environments are under mixed-kinetic control, but with a minor effect of mass transport.

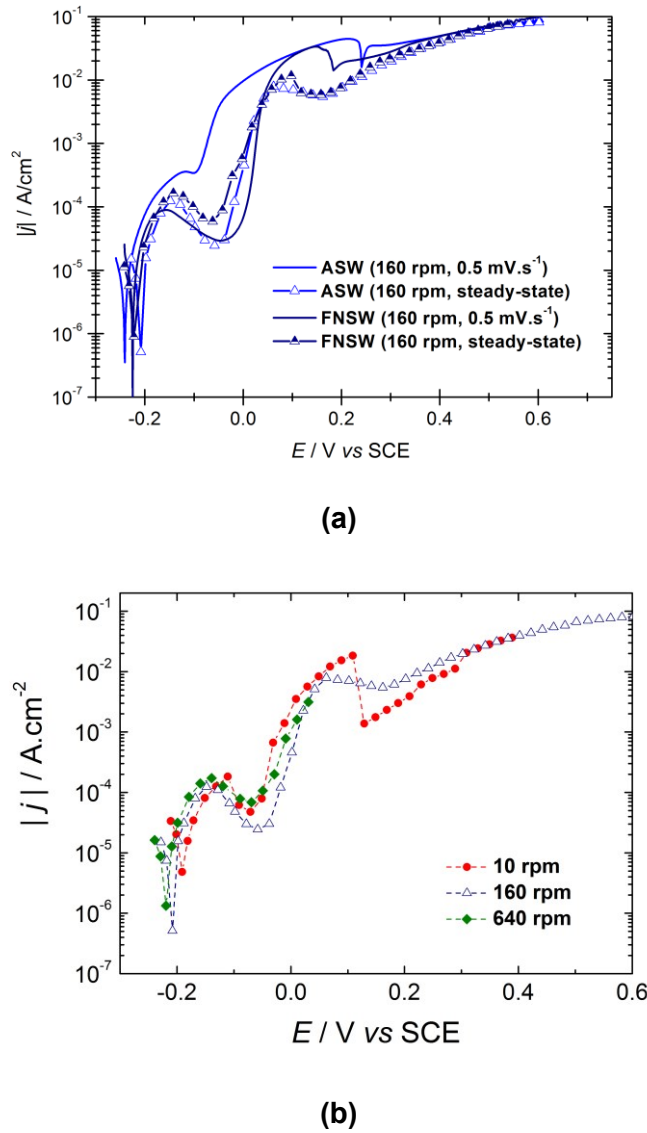


**Figure 5-11:** Anodic polarization curves of 70Cu-30Ni rotating ring electrode, after 1 h of immersion time at  $E_{\text{corr}}$  in: (a) aerated artificial seawater and filtered natural seawater, at 160 rpm, in steady-state conditions and with a scan rate of  $0.5 \text{ mV.s}^{-1}$  and (b) aerated artificial seawater in steady-state conditions at three different rotation speeds (10, 160 and 640 rpm).

#### 5.2.2.1.5 ELECTROCHEMICAL IMPEDANCE SPECTROSCOPY

Impedance diagrams were recorded at  $E_{\text{corr}}$  using the RRE at three different rotation speeds, and the results were compared to those obtained in static conditions (disk electrode) (Figure 5-12). The shape remains similar but the magnitude of the impedance, in particular the size of the high frequency loop depends on the hydrodynamic conditions. The low frequency loop is better defined in static conditions.

In ASW (Figure 5-12(a)), the size of the high frequency loop in static conditions is considerably higher than with the RRE. Nevertheless, comparing only the impedance diagrams obtained with the RRE, the magnitude of the high frequency loop increases with increasing rotation speed. Similar results are observed in FNSW (Figure 5-12(b)), but the variation with the rotation speed is less pronounced. Thus, there is an effect of hydrodynamics which is more important in ASW than in FNSW, which is in agreement with the anodic polarization curves (Figure 5-10).

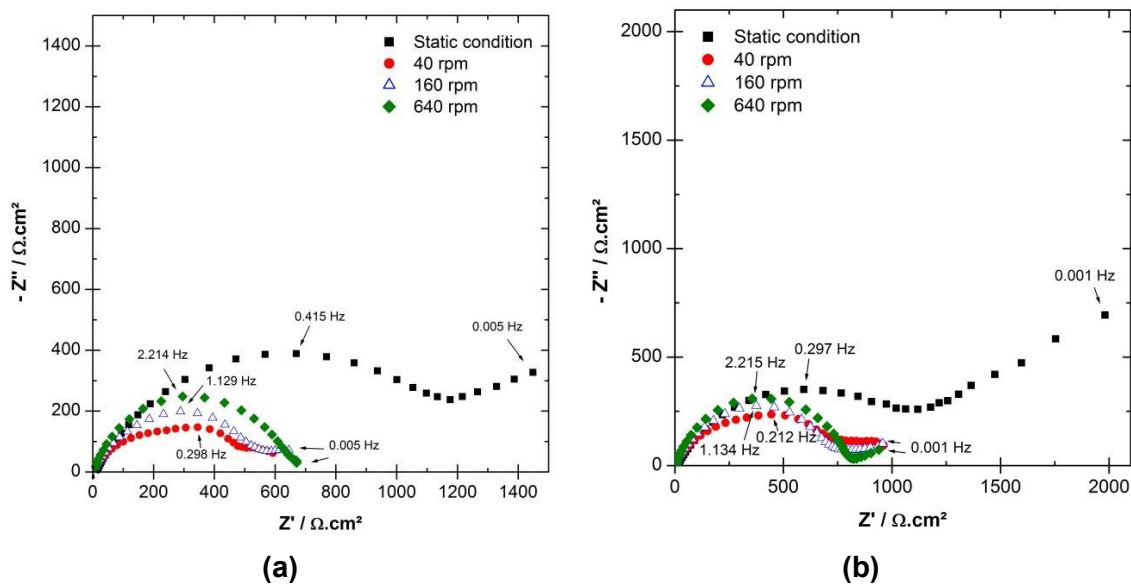


**Figure 5-12:** Experimental impedance diagrams in the complex plane (Nyquist diagrams) of 70Cu-30Ni rotating ring electrode at three different rotation speeds (40, 160 and 640 rpm), after 1 h of immersion at  $E_{\text{corr}}$  in: (a) aerated artificial seawater, and (b) aerated filtered natural seawater.

### 5.2.2.1.6 EIS DATA FITTING

In Chapter 4, an impedance model for 70Cu-30Ni alloy at  $E_{\text{corr}}$  in ASW and FNSW was developed. The bases of this model are the following:

a) the anodic partial reaction involves the dissolution of Cu as  $\text{Cu}^+$  species; a modified mechanism from that for pure copper dissolution in chloride media at low anodic potential was proposed, in order to take into account the presence of an oxide layer (Eqs. (4.20) to (4.23));

b) the cathodic partial reaction is the oxygen reduction reaction (aerated solutions);

c) the anodic and the cathodic partial reactions are affected by mass transport, with pure mass transport limitation for the cathodic partial reaction, and mixed kinetic control for the anodic partial reaction;

d) the anodic partial current is limited by mass transport of  $\text{Cu}^+$  in the solid phase and of  $\text{CuCl}_2^-$  in the electrolyte.

Figure 5-13 shows the absolute value of the imaginary part of the impedance ( $|Z''|$ ) plotted as a function of the frequency in logarithmic coordinates for the same experimental impedance data as those presented in Figure 5-12 [10].

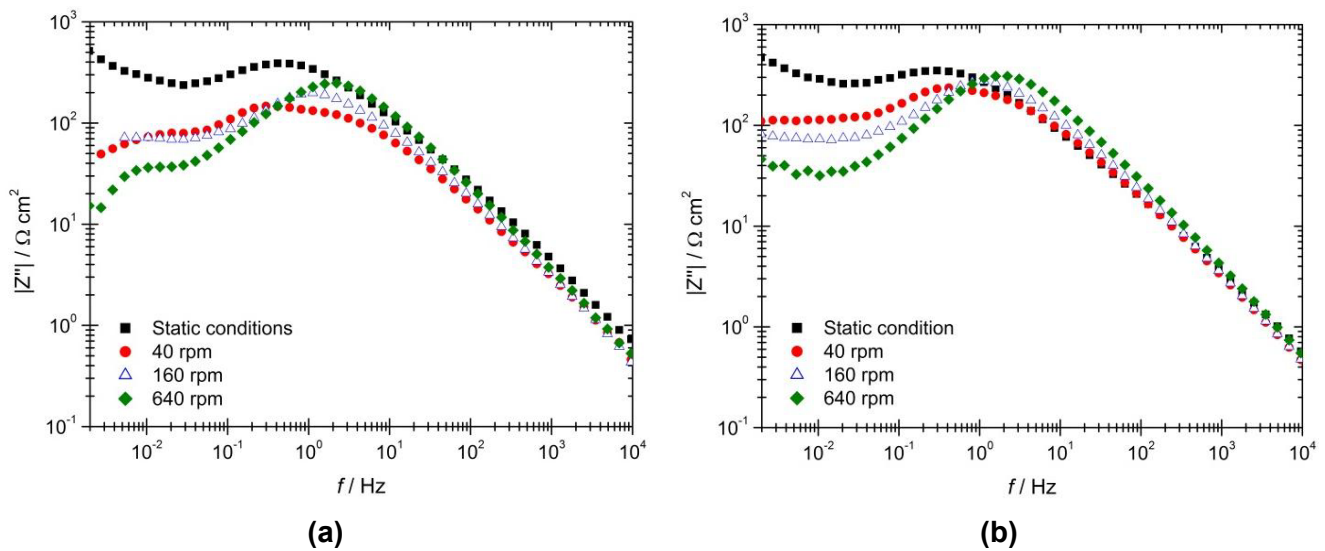


**Figure 5-13:** Experimental impedance data (imaginary part of the impedance as a function of frequency) of 70Cu-30Ni alloy obtained at  $E_{corr}$  after 1 h of immersion in aerated: (a) artificial seawater, and (b) filtered natural seawater, in static conditions and using the rotating ring electrode at three different rotation speeds (40, 160 and 640 rpm). Same data as in Figure 5-12.

In all cases, a pseudo-straight line with a slope lower than 1 in absolute value can be observed in the HF range. As this slope varies slightly with the frequency,  $\alpha$  cannot be determined graphically from Figure 5-13. Therefore, to better visualize a possible constant value of the slope in a narrow frequency range, the  $d \log |Z''| / d \log f$  vs  $\log f$  curves were calculated from those presented in Figure 5-13 (derivative curves; Figure 5-14). In Figure 5-14 (a) *i.e.* for the 70Cu-30Ni/ASW system, no plateau is visible at very HF, and again the value of  $\alpha$  cannot be graphically obtained. In Figure 5-14 (b) *i.e.* for the 70Cu-30Ni/FNSW system, a very narrow plateau can be distinguished at very HF ( $\sim 10^3$  Hz) in static conditions, corresponding to a slope of -0.76; using the RRE, a plateau is visible at very HF, corresponding to a slope of -0.87 V for the three rotation speeds. Therefore, for the latter

system, the value of  $\alpha$  can be graphically estimated ( $\alpha = 0.76$  in static conditions and  $\alpha = 0.87$  with the RRE), and the effect of  $W_c$  is negligible compared to that of  $CPE_{dl}$  at very HF.

The HF loop of the experimental impedance diagrams can be modelled by the  $CPE_{dl}/R_t^a/W_c$  equivalent circuit (Figure 4-15(c)), and the LF loop is related to the anodic mass transport and partial blocking effect by adsorbed species such as  $\text{CuCl}$  ( $Z_{\theta,D}^a$ ).

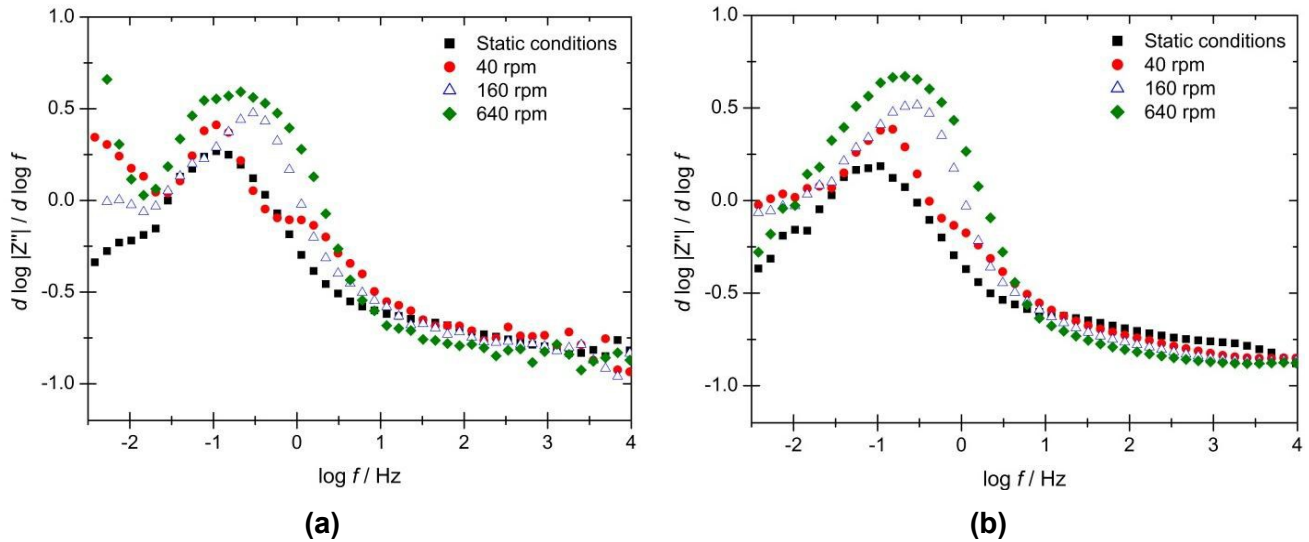


**Figure 5-14:** Experimental impedance data (derivative curves calculated from Figure 5-13) of 70Cu-30Ni alloy obtained at  $E_{corr}$  after 1 h of immersion in aerated: (a) artificial seawater, and (b) filtered natural seawater, in static conditions and using the rotating ring electrode at three different rotation speeds (40, 160 and 640 rpm). Same data as in Figure 5-12.

As only few points describe the LF loop, the single HF loop was analyzed by regression of the equivalent circuit presented in Figure 4-15(c), using Simad® software. The regression results are presented in Figure 5-15 and in Table 5-3. The experimental frequency range taken into account for the regression is indicated in Table 5-3 for each data set, but the fitted curves in Figure 5-15 are shown in the whole frequency range ( $0.003\text{-}10^5$  Hz), with parameters values corresponding to those given in Table 5-3.

**Table 5-3:** Experimental frequency range taken into account for the regression, parameters values (electrolyte resistance  $R_e$ , anodic charge transfer resistance  $R_t^a$ , constant of the cathodic Warburg impedance  $k_c$ , and CPE parameters  $\alpha$  and  $Q$ ) obtained from the regression of the equivalent circuit presented in Figure 4-15 (c) to experimental impedance data shown in Figure 5-12, and effective capacitance  $C_{eff}$  associated with the CPE calculated from Eq. (2.22).

	Frequency range Hz	$R_e$ $\Omega.cm^2$	$R_t^a$ $\Omega.cm^2$	$k_c$ $s^{0.5}.\Omega^{-1}.cm^{-2}$	$\alpha$	$Q$ $F.cm^{-2}.s^{(\alpha-1)}$	$C_{eff}$ $\mu F.cm^{-2}$
<b>ASW static</b>	$10^5-5.6\times 10^{-2}$	12	1390	$2.5\times 10^{-4}$	0.78	$1.99\times 10^{-4}$	37
<b>FNSW static</b>	$10^5-7.8\times 10^{-2}$	12	1310	$3.5\times 10^{-4}$	0.76	$2.90\times 10^{-4}$	50
<b>ASW RRE 40 rpm</b>	$10^5-1.52\times 10^{-1}$	4	590	$7.5\times 10^{-4}$	0.85	$1.54\times 10^{-4}$	42
<b>ASW RRE 160 rpm</b>	$10^5-2.98\times 10^{-1}$	3	650	$3.1\times 10^{-4}$	0.82	$2.21\times 10^{-4}$	45
<b>ASW RRE 640 rpm</b>	$10^5-1.52\times 10^{-1}$	4	660	$0.4\times 10^{-4}$	0.83	$1.92\times 10^{-4}$	44
<b>FNSW RRE 40 rpm</b>	$10^5-7.8\times 10^{-2}$	4	900	$5.4\times 10^{-4}$	0.87	$1.34\times 10^{-4}$	42
<b>FNSW RRE 160 rpm</b>	$10^5-1.08\times 10^{-1}$	3	810	$2.0\times 10^{-4}$	0.84	$1.78\times 10^{-4}$	42
<b>FNSW RRE 640 rpm</b>	$10^5-7.8\times 10^{-2}$	4	830	$0.5\times 10^{-4}$	0.85	$1.36\times 10^{-4}$	37

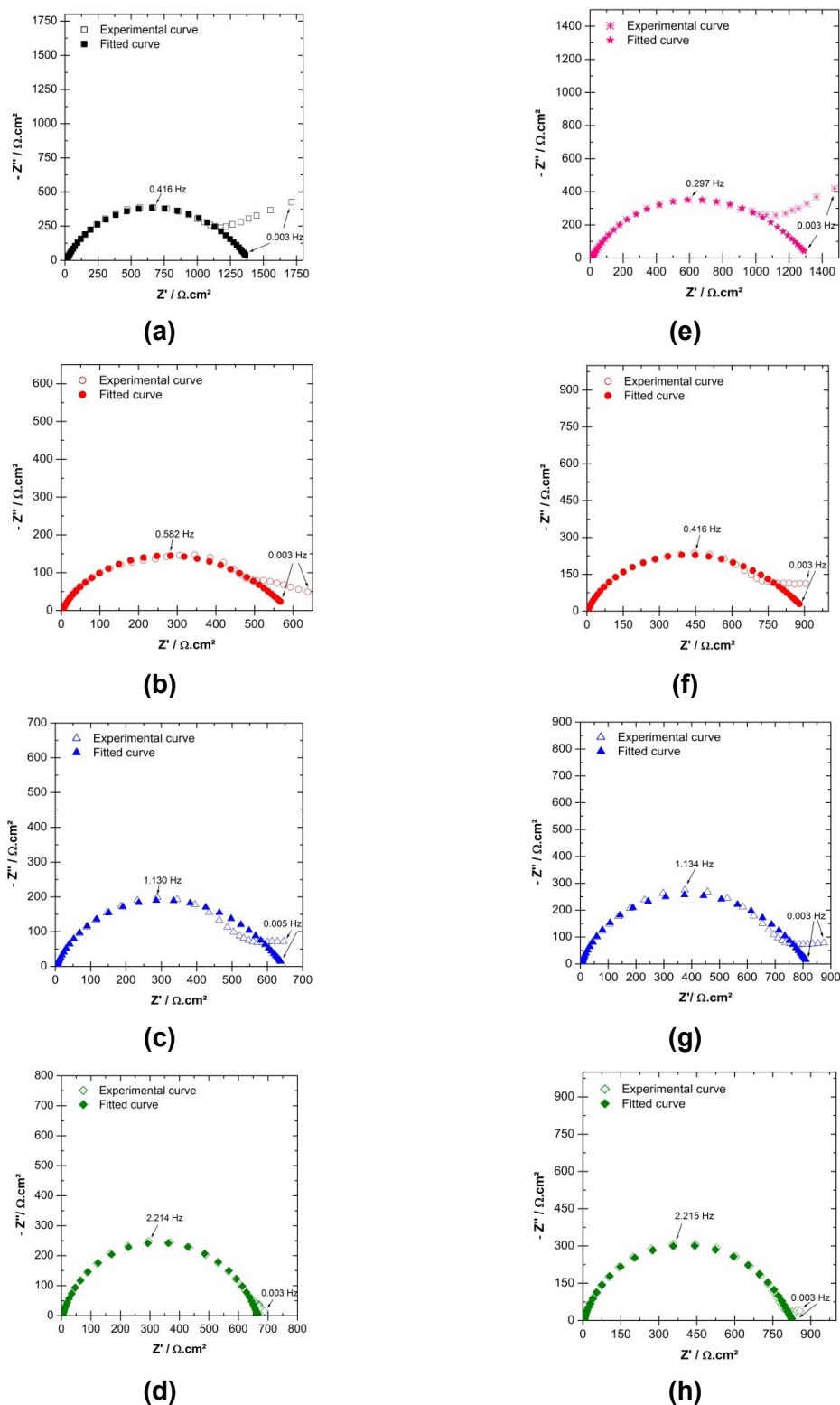


**Figure 5-15:** High frequency loops of Nyquist diagrams obtained for 70Cu-30Ni at  $E_{corr}$  after 1 h of immersion in aerated: (a) ASW in static conditions, (b) ASW with the RRE at 40 rpm, (c) ASW with the RRE at 160 rpm, (d) ASW with the RRE at 640 rpm, (e) FNSW in static conditions, (f) FNSW with the RRE at 40 rpm, (g) FNSW with the RRE at 160 rpm, and (h) FNSW with the RRE at 640 rpm. Experimental curves and fit of the impedance model presented in Figure 4-15 (c). Same data as in Figure 5-12.

When moving from static disk to the RRE, the apparent electrolyte resistance value changes from 12 to 3-4  $\Omega \cdot \text{cm}^2$ . This variation of  $R_e$  is not linked to a change of solution conductivity but to a change of electrode geometry.

The effective capacitance values calculated by the application of the equation derived by Brug *et al.* (Eq. (2.22)), taking for  $R_e$  and  $R_t^a$  the values extracted from the regression procedure (Table 5-3), are given in Table 5-3. These capacitance values are similar in all cases and are of the order of several tens of  $\mu\text{F} \cdot \text{cm}^{-2}$ ; typical of those for a double layer capacitance. In particular,  $C_{eff}$  is independent of the rotation speed, which confirms that it is a double layer capacitance.

Hence, the HF loop illustrates mainly the anodic charge transfer and its diameter is equal to  $R_t^a$ .

In order to explain the variations of  $R_t^a$  value when moving from the static disk to the RRE and when increasing the rotation speed of the RRE, theoretical considerations about  $R_t^a$  must be detailed.

The anodic charge-transfer resistance for a reaction dependent on potential and mass transport is given by Eq. (4.28). Thus, mass transport influences charge transfer by means of the surface concentration of the diffusing species  $c_0$ .

The anodic polarization curves plotted in static conditions and with the RRE show partial mass transport limitation. For mixed kinetics, the steady-state anodic current density can be written as:

$$i = Kc_0 e^{bV} \quad (5.10)$$

According to first Fick's law and assuming a linear concentration gradient in the diffusion layer of thickness  $\delta$ , the steady-state anodic current density can also be written as:

$$i = nFD \frac{c_\infty - c_0}{\delta} \quad (5.11)$$

with  $D$  the diffusion coefficient of the diffusing species ( $\text{CuCl}_2^-$ ), and  $c_\infty$  the bulk concentration of the diffusing species.

By Eqs. (5.10) and Eq. (5.11), the surface concentration of the diffusing species can be obtained:

$$c_0 = \frac{c_\infty}{1 + \frac{\delta}{D} k e^{b(V-V_0)}} \quad (5.12)$$

If comparing static disk and RRE, the electrode geometry (disk/ring) as well as the hydrodynamics of the solution are changed. The diffusion layer is thinner for a ring than for a disk, and its thickness is higher in static conditions than under rotation of the electrode.

Therefore, when moving from the static disk to the RRE at constant potential, the diffusion layer thickness decreases, which induces an increase of the surface concentration (Eq. (5.12)) and hence a decrease of the charge transfer resistance (Eq. (4.28)). On the other hand, a potential increase induces a decrease of  $R_t^a$  (Eq. (4.28)). Experimentally, when moving from the static disk to the RRE at 40 rpm in ASW as well as in FNSW, the corrosion potential increases (see Table 5-1) and  $R_t^a$  decreases (see Table 5-3). This decrease of  $R_t^a$  can be explained by additional mass transport ( $c_0$ ) effect and potential effect.

Experimentally, when increasing the rotation speed of the RRE from 40 to 640 rpm, the corrosion potential decreases in ASW as well as in FNSW (see Table 5-1) and  $R_t^a$  slightly increases in ASW and keeps constant in FNSW (see Figure 5-12 and Table 5-3). As the diffusion layer thickness is inversely proportional to the square root of the electrode rotation speed  $\Omega$  ( $\delta \propto \Omega^{-1/2}$ ), increase of  $\Omega$  would induce a decrease of  $\delta$  and hence a decrease of  $R_t^a$  (Eqs. (4.28) and (5.12)). Moreover, a decrease of the potential at constant  $\Omega$  would induce an increase of  $R_t^a$  (Eq. (4.28)). Therefore, the increase of  $R_t^a$  in ASW can be explained by a major effect of the potential, and the constant value of  $R_t^a$  in FNSW is due to compensated potential and mass transport effects.

Corrosion currents,  $i_{corr}$ , were calculated from Eqs. (4.32) and (4.33), assuming Tafel kinetics (pure kinetic control) for the anodic partial reaction, and using  $z = 1$  (dissolution of Cu as  $\text{Cu}^+$  species) and  $\alpha = 0.5$  in Eq. (4.32), and  $R_p = R_t^a$  in Eq. (4.33).

Table 5-4 compares the calculated  $i_{corr}$  values to those deduced graphically from the cathodic polarization curves, taking into account the first plateau current density in some cases or an extrapolation of the cathodic straight line down to  $E_{corr}$  in other cases.  $i_{corr}$  cannot be estimated graphically from the anodic polarization curves because they do not exhibit Tafel behavior (except in static ASW) or any current plateau. If comparing the corrosion current densities obtained from Eq. (4.32) to those deduced graphically from the cathodic polarization curves, there is a ratio of about 2-5 between the values that may be partly explained by a value of  $\alpha$  different from 0.5 and partly explained by the fact that polarization curves were plotted with a scan rate of  $0.5 \text{ mV.s}^{-1}$  (non steady-state curves). Thus, for the RRE at 160 rpm in ASW, the steady-state cathodic polarization curve yields a

first plateau current density of about  $50 \mu\text{A.cm}^{-2}$  (see Figure 5-8), which is much closer to the value of  $78 \mu\text{A.cm}^{-2}$  calculated from  $R_t^a$  (Eq. (4.32)).

Figure 5-16 allows to better visualize the differences in corrosion current density calculated from Eq. (4.32) (with  $z = 1$  and  $\alpha = 0.5$ ), for the two different solutions in static conditions and using the rotating ring electrode. In static conditions, the corrosion current density is similar in ASW and in FNSW. On the other hand,  $i_{corr}$  in ASW and FNSW is higher with the RRE than in static conditions (maximum ratio of 2). When increasing the rotation speed of the RRE, the corrosion current density slightly decreases in ASW and keeps constant in FNSW. As discussed before for  $R_t^a$  values, these results can be explained by combined potential and mass transport effect.

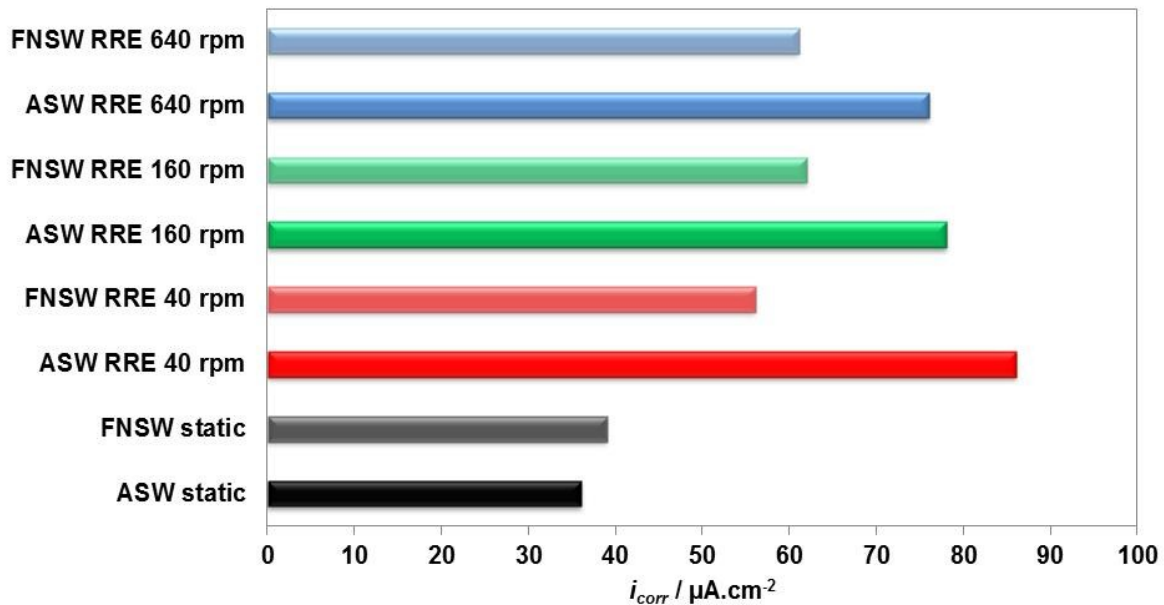


**Figure 5-16:** Comparison of the corrosion current density values calculated from Eq. (4.32) with  $z = 1$  and  $\alpha = 0.5$ , for 70Cu-30Ni alloy after 1h of immersion in ASW or FNSW, in static conditions and using the rotating ring electrode.

**Table 5-4:** Comparison of the corrosion current values obtained from  $R_t^a$ , by application of Eqs. (4.32) (with  $Z = 1$  and  $\alpha = 0.5$ ) and (4.33), and from the non steady-state cathodic polarization curves (first plateau current density or extrapolation to  $E_{corr}$  of the cathodic straight line).

	$R_t^a / \Omega.cm^2$	$i_{corr} / \mu A.cm^{-2}$		
		Eq. (4.32)	Eq. (4.33)	Cathodic polarization curve
<b>ASW static</b>	1390	36	14	12
<b>FNSW static</b>	1310	39	14	8
<b>ASW RRE 40 rpm</b>	590	86	32	26
<b>ASW RRE 160 rpm</b>	650	78	29	18
<b>ASW RRE 640 rpm</b>	660	76	29	20
<b>FNSW RRE 40 rpm</b>	900	56	21	-
<b>FNSW RRE 160 rpm</b>	810	62	23	30
<b>FNSW RRE 640 rpm</b>	830	61	23	-

## 5.2.2.2 AL BRASS

### 5.2.2.2.1 CORROSION POTENTIAL ( $E_{CORR}$ ) VS TIME

The corrosion potential as a function of time ( $E_{corr}$  vs time) was followed for 1 h. In Table 5-5, the corrosion potential values obtained with the RRE in FNSW are presented and compared with the value recorded in static conditions using a disk electrode. When using the rotating ring electrode, the corrosion potential ( $E_{corr}$ ) decreases when the rotation speed increases (as observed for 70Cu-30Ni alloy).

**Table 5-5:** Corrosion potential values for Al brass alloy after 1 h of immersion in filtered natural seawater (FNSW), in static conditions and using a RRE at three different rotation speeds (40, 160 and 640 rpm).

	$E_{corr} / V$ vs SCE
<b>FNSW static conditions</b>	$-0.247 \pm 0.002$
<b>FNSW 40 rpm</b>	$-0.301 \pm 0.009$
<b>FNSW 160 rpm</b>	$-0.299 \pm 0.016$
<b>FNSW 640 rpm</b>	$-0.325 \pm 0.001$

## 5.2.2.2.2 CATHODIC AND ANODIC POLARIZATION CURVES

The steady-state cathodic polarization curve of Al brass plotted in FNSW with the rotating ring electrode at 160 rpm is presented in Figure 5-17 (a) and is compared to that obtained in static conditions with a scan rate of  $0.5 \text{ mV.s}^{-1}$ . In static conditions and using the RRE, only one cathodic plateau is clearly visible, corresponding to the reduction of dissolved oxygen with transfer of 4 electrons. Close to  $E_{corr}$ , the steady-state curve exhibits Tafel behavior (*i.e.* pure charge transfer limitation), in the case of Al brass whereas a current plateau (*i.e.* pure mass transport limitation) can be observed in the case of 70Cu-30Ni (see Figure 5-8). Therefore, the kinetics of oxygen reduction depends on the alloying element (Zn or Ni).

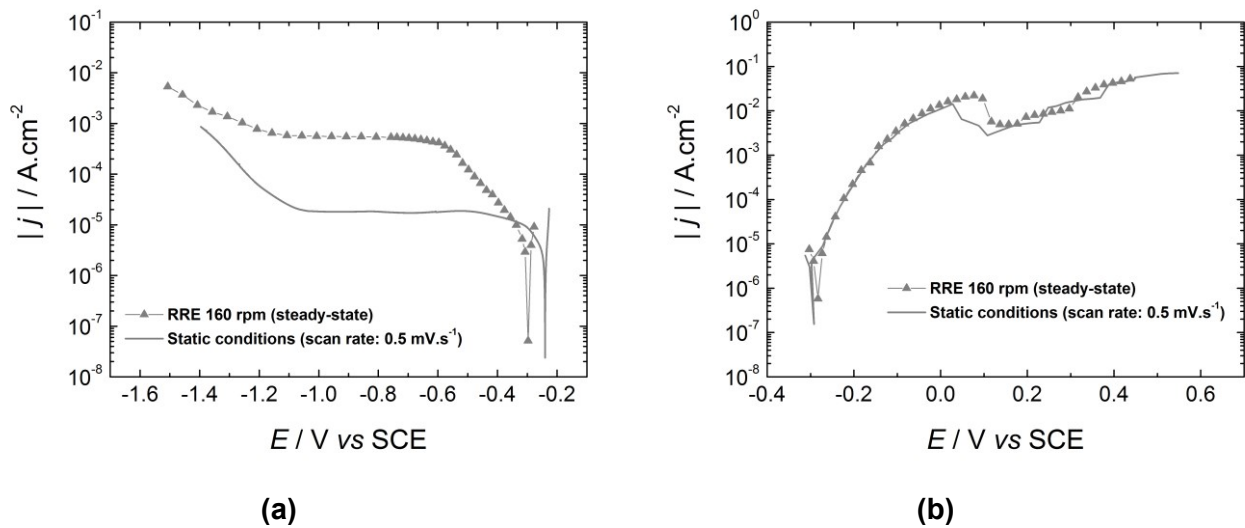


**Figure 5-17:** (a) Cathodic and (b) anodic polarization curves of Al brass after 1 h of immersion at  $E_{corr}$  in filtered natural seawater. RRE at 160 rpm in steady-state conditions and static conditions with a scan rate of  $0.5 \text{ mV.s}^{-1}$ .

The anodic behavior of the alloy after 1 h of immersion at  $E_{corr}$  in FNSW, in static conditions and using the RRE at 160 rpm is shown in Figure 5-17 (b). Both curves are very similar.

Figure 5-18 presents the anodic polarization curves of the two copper alloys used in this PhD, 70Cu-30Ni alloy and Al brass, obtained after 1 h of immersion at  $E_{corr}$  in FNSW in static conditions with a scan rate of  $0.5 \text{ mV.s}^{-1}$  and using a rotating ring electrode at 160 rpm in steady-state conditions. The similarity of the curves obtained for both alloys suggests that their anodic behavior is dominated by that of pure copper. This observation is in agreement with the work of Petetin *et al.* [11], who compared the anodic polarization curves of pure Cu,

pure Ni and 70Cu-30Ni alloy after 10 min of immersion at  $E_{corr}$  in a 3% NaCl solution; they showed that the anodic behavior of the alloy was more similar to that of pure Cu than to that of pure Ni.

However, if comparing the steady-state curves (Figure 5-18 (b)), the anodic behavior below 0.1 V vs SCE seems to depend on the alloying element (Ni or Zn): current peak followed by a pseudo-plateau for 70Cu-30Ni and continuous current increase for Al brass.

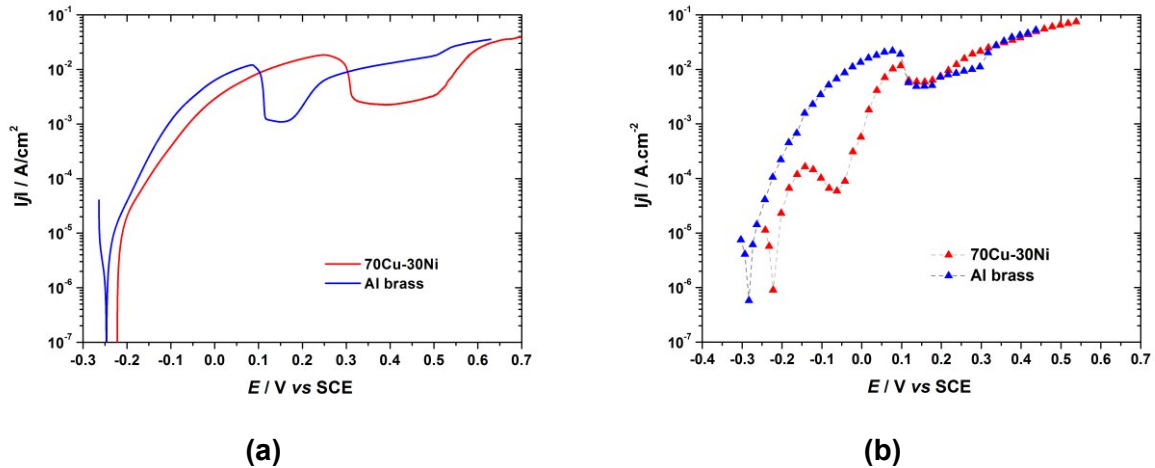


**Figure 5-18:** Anodic polarization curves of Al brass and 70Cu-30Ni alloy after 1 h of immersion at  $E_{corr}$  in FNSW. (a) Static conditions with a scan rate of  $0.5 \text{ mV.s}^{-1}$  and (b) rotating ring electrode at 160 rpm in steady-state conditions.

### 5.2.2.2.3 ELECTROCHEMICAL IMPEDANCE SPECTROSCOPY

Impedance diagrams of Al brass in FNSW were recorded at  $E_{corr}$  with the RRE at three different rotation speeds, and the results were compared to those obtained in static conditions (disk electrode) (Figure 5-19). The diagrams exhibit one single capacitive loop using the RRE whereas, in static conditions, two capacitive loops can be observed, similarly to what is found for 70Cu-30Ni. The LF linear region observed in static conditions disappears under rotation, indicating that this loop can be ascribed to mass transport phenomena. Similar results were obtained by Feng *et al.* with Cu at pH 5, in static conditions or with a rotating disk electrode (at 300, 1000 and 3000 rpm) [12].

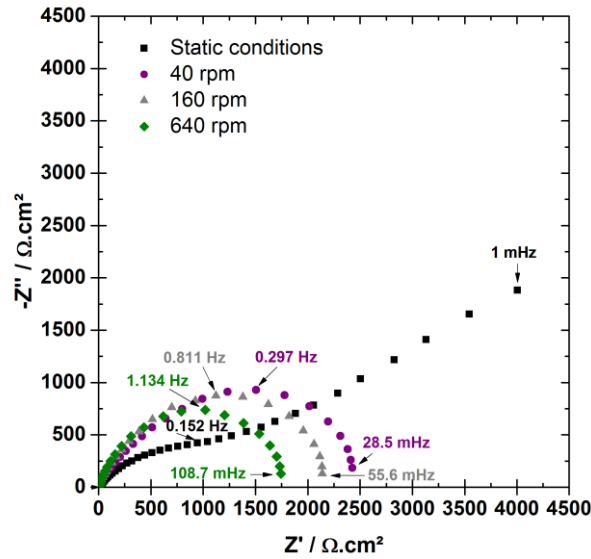


**Figure 5-19:** Experimental impedance diagrams in the complex plane (Nyquist diagrams) of Al brass plotted at  $E_{corr}$  after 1 h of immersion in aerated filtered natural seawater in static conditions and with a rotating ring electrode at three different rotation speeds (40, 160 and 640 rpm).

#### 5.2.2.2.4 IMPEDANCE MODEL FOR AL BRASS AND EIS DATA FITTING

For the same experimental impedance data as those presented in Figure 5-19, the absolute value of the imaginary part of the impedance ( $|Z''|$ ) was plotted as a function of the frequency in logarithmic coordinates (Figure 5-20(a)). In the HF range, a pseudo-straight line with a slope lower than 1 in absolute value, but varying slightly with the frequency, can be observed. This slope value lower than 1 suggests a CPE-like behavior. However, as the slope varies slightly with the frequency, the CPE parameter  $\alpha$  cannot be graphically estimated from Figure 5-20(a).

To better visualize a possible constant value of the slope in a narrow frequency range, the  $d \log |Z''| / d \log f$  vs  $\log f$  curves were calculated from those presented in Figure 5-20 (a) (derivative curves; Figure 5-20(b)). In all cases, a plateau is visible at very HF ( $10^3 < f < 10^{4.5}$  Hz), and the value of  $\alpha$  can be graphically estimated. The CPE parameters,  $\alpha$  and  $Q$ , deduced from Figure 5-20(b) and from Eq. (4.21), respectively, are presented in Table 5-6.

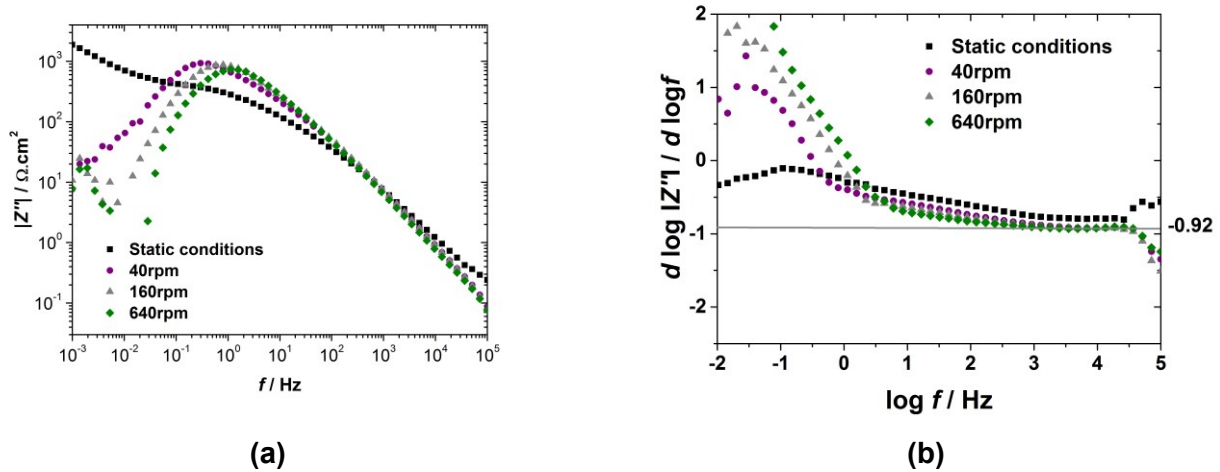


**Figure 5-20:** Experimental impedance data of Al brass obtained at  $E_{corr}$  after 1 h of immersion in aerated filtered natural seawater in static conditions and with a rotating ring electrode at three different rotation speeds (40, 160 and 640 rpm). (a) Imaginary part of the impedance as a function of frequency, and (b) derivative curves calculated from Figure 5-20(a) ( $d \log |Z''| / d \log f$  vs  $\log f$ ).

**Table 5-6:** Electrolyte resistance  $R_e$ , and CPE parameters,  $\alpha$  and  $Q$ , obtained graphically from experimental impedance data, and effective capacitance  $C_{eff}$  associated with the CPE calculated from Brug's formula for a blocking electrode (Eq. (2.23)).

	$R_e$ $\Omega.cm^2$	$\alpha$	$Q$ $\Omega^{-1}.cm^{-2}.s^\alpha$	$C_{eff}$ $\mu F.cm^{-2}$
<b>Static</b>	12	0.73	$2.33 \times 10^{-4}$	27
<b>RRE 40 rpm</b>	4	0.91	$4.68 \times 10^{-5}$	20
<b>RRE 160 rpm</b>	4	0.92	$4.25 \times 10^{-5}$	20
<b>RRE 640 rpm</b>	4	0.92	$4.98 \times 10^{-5}$	24

In static conditions, the Al brass/seawater system is very similar to the 70Cu-30Ni/seawater one. In particular, a pseudo-plateau can be observed close to  $E_{corr}$  on the cathodic polarization curve (Figure 5-17(a)). Therefore, the impedance model for Al brass in static seawater is the same as for 70Cu-30Ni in seawater (Figure 4-15(b) recalled in Figure 5-21(b)). Using the RRE, the impedance model for Al brass in FNSW is deduced from the same general model as for 70Cu-30Ni/seawater system (Figure 4-15 (a) recalled in Figure 5-21(a)). In the case of the Al brass RRE, the steady-state cathodic polarization curve shows Tafel behavior close to  $E_{corr}$  (Figure 5-17(a)), which corresponds to a very high value of  $R_t^c$ . Therefore, the cathodic branch in Figure 5-21(c) can be neglected with respect to the anodic

one. In the anodic branch,  $Z_{\theta,D}^a$ , illustrating mass transport and partial blocking effect by adsorbed CuCl is replaced by a capacitance  $C$  in parallel with a resistance  $R$  ( $R//C$  circuit) as for pure copper in chorine media (see Annex B). Therefore, the Al brass/seawater system can be modeled by the simplified circuit presented in Figure 5-21(c). Thus, the single capacitive loop of experimental diagrams illustrates both the anodic charge transfer and the anodic mass transport.

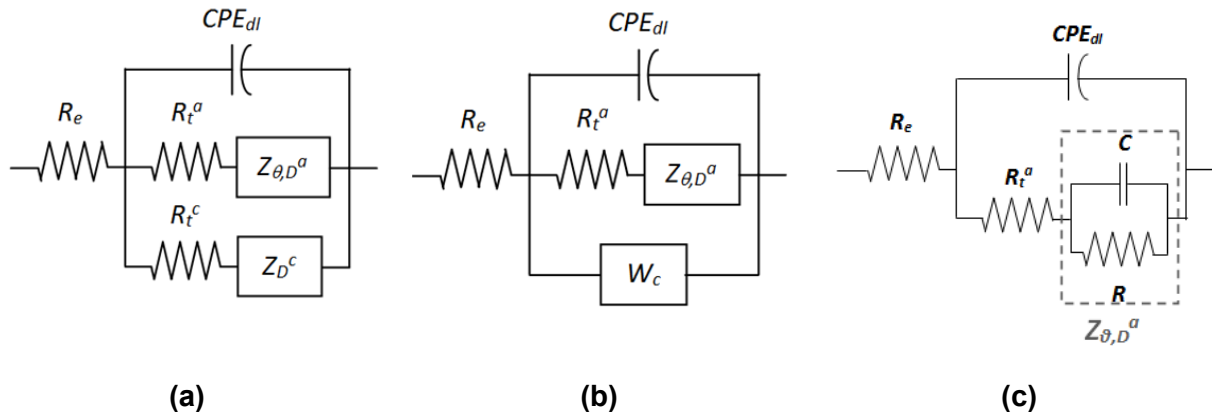


**Figure 5-21:** Simplified equivalent electrical circuits to model the Al brass/FNSW system: (a) general circuit, (b) simplified circuit in static conditions, and (c) simplified circuit using the RRE.  $R_e$  is the electrolyte resistance,  $CPE_{dl}$  a constant phase element related to the double layer,  $R_t^a$  the anodic charge transfer resistance,  $Z_D^c$  a cathodic impedance that illustrates  $O_2$  mass transport, and  $W_c$  the cathodic Warburg impedance,  $Z_{\theta,D}^a$  an impedance that illustrates anodic mass transport and partial blocking effect by CuCl shown to be a capacitance  $C$  in parallel with a resistance  $R$ ,  $R_t^c$  the cathodic charge transfer resistance.

In static conditions and as for the 70Cu-30Ni/seawater system, the single HF loop was analyzed by regression of the equivalent circuit presented in figure 4-15(c), using Simad® software developed at Laboratoire Interfaces et Systèmes Electrochimiques. Experimental diagrams were first analyzed by regression of the general circuit with both the anodic and cathodic branches, i.e. circuit of Figure 5-21(a) in which  $Z_{\theta,D}^a$  is replaced by  $R//C$  (results not presented here).

For experiments carried out with the RRE, the single loop was analyzed by regression of the equivalent circuit presented in figure 5-21(c) using Simad® software. In this circuit, only the anodic branch is taken into account.

The regression results are presented in Table 5-7 and in Figure 5-22. In static conditions, the corresponding impedance equation is given by Eq. (4.22), and for the RRE it is written as follows:

$$Z = R_e + \frac{1}{Q(j\omega)^\alpha + \frac{1}{R_t^a + \frac{R}{(1 + j\omega RC)}}} \quad (5.13)$$

The experimental frequency range taken into account for the regression of each data set is indicated in Table 5-7, but the fitted curves in Figure 5-22 are shown in the whole frequency range ( $10^{-3}$ - $10^5$  Hz), with parameters values corresponding to those given in Table 5-7.

**Table 5-7:** Regression results for the Al brass/FNSW system. Experimental frequency range taken into account for the regression, parameters values (electrolyte resistance  $R_e$ , anodic charge transfer resistance  $R_t^a$ , constant of the cathodic Warburg impedance  $k_c$ , resistance  $R$ , capacitance  $C$ , and CPE parameters  $\alpha$  and  $Q$ ), obtained from the regression of the equivalent circuit presented in Figure 4-15(c) (static conditions) or 5-30(c) (RRE) to experimental impedance data shown in Figure 5-19, and effective capacitance  $C_{eff}$  associated with the CPE calculated from Eq. (2.22).

	<b>Frequency Range /</b> <b>Hz</b>	<b><math>R_e</math> /</b> <b><math>\Omega \cdot \text{cm}^2</math></b>	<b><math>R_t^a</math> /</b> <b><math>\Omega \cdot \text{cm}^2</math></b>	<b><math>k_c</math> /</b> <b><math>\text{s}^{0.5} \cdot \Omega^{-1} \cdot \text{cm}^{-2}</math></b>	<b><math>R</math> /</b> <b><math>\Omega \cdot \text{cm}^2</math></b>	<b><math>C</math> /</b> <b><math>\mu\text{F} \cdot \text{cm}^{-2}</math></b>	<b><math>\alpha</math></b>	<b><math>Q</math> /</b> <b><math>\text{F} \cdot \text{cm}^{-2} \cdot \text{s}^{(\alpha-1)}</math></b>	<b><math>C_{eff}</math> /</b> <b><math>\mu\text{F} \cdot \text{cm}^{-2}</math></b>
<b>Static</b>	$10^5$ - $5.8 \times 10^{-1}$	12	1800	$6.1 \times 10^{-4}$	-	-	0.93	$2.5 \times 10^{-5}$	14
<b>RRE 40 rpm</b>	$10^5$ - $2.04 \times 10^{-2}$	3	820	-	1640	144	0.82	$1.01 \times 10^{-4}$	18
<b>RRE 160 rpm</b>	$10^5$ - $5.56 \times 10^{-2}$	4	740	-	1440	58	0.86	$7.2 \times 10^{-5}$	19
<b>RRE 640 rpm</b>	$10^5$ - $1.1 \times 10^{-3}$	4	770	-	1010	39	0.89	$6.7 \times 10^{-5}$	24

The effective capacitance values calculated from the impedance diagrams shown in Figure 5-22, taking for  $R_e$  and  $R_t^a$  the values extracted from the regression procedure (Table 5-7), are also given in Table 5-7. As for 70Cu-30Ni in seawater, these  $C_{eff}$  values, are typical of those for a double layer capacitance, and do not depend on the rotation speed.

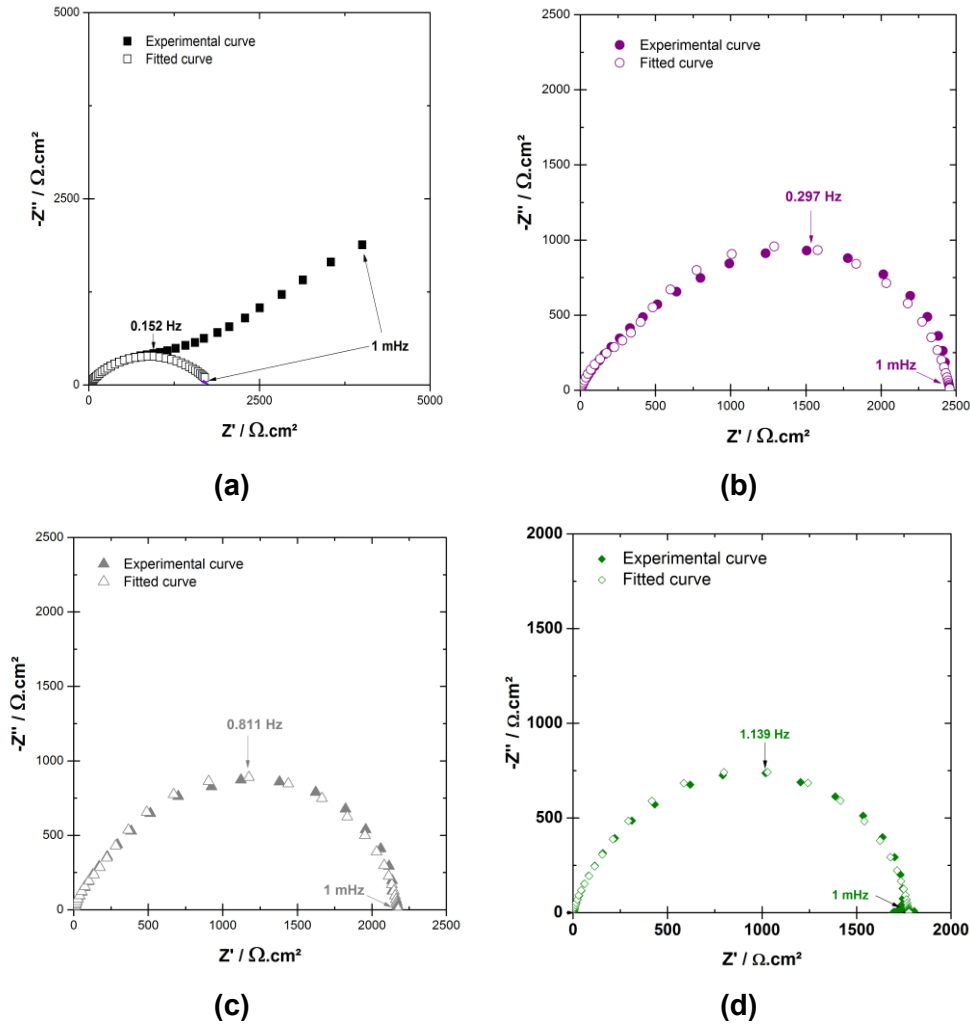


**Figure 5-22:** Nyquist diagrams obtained for Al brass at  $E_{corr}$  after 1 h of immersion in aerated filtered natural seawater: (a) in static conditions, (b) with the RRE at 40 rpm, (c) with the RRE at 160 rpm, and (d) with the RRE at 640 rpm. Experimental curves and fit of the impedance model presented in Figure 4-15(c) (static conditions) or 5-30(c) (RRE) to the data. Same data as in Figure 5-19.

As for 70Cu-30Ni in FNSW,  $E_{corr}$  decreases (Table 5-5) and  $R_t^a$  remains constant (Table 5-7) when increasing the rotation speed of the RRE from 40 to 640 rpm. This constant value of  $R_t^a$  and hence of  $i_{corr}$  is due to compensated potential and mass transport effects. The application of Eq. (4-32) at 160 rpm, with  $z = 1$  and  $\alpha = 0.5$ , yields  $j_{corr} = 68 \mu\text{A.cm}^{-2}$ . Unlike 70Cu-30Ni in FNSW, these values are not in agreement with that deduced graphically from the steady-state cathodic polarization curve plotted at 160 rpm; indeed, the extrapolation of the Tafel straight line down to  $E_{corr}$  yields  $i_{corr} = 5\text{--}6 \mu\text{A.cm}^{-2}$  (Figure 5-17(a)). This ratio of about 12 between both values may be explained by the fact that the cathodic polarization curve plotted in Figure 5-17(a) is not a real steady-state curve near to the

corrosion potential due to the presence of an oxide layer (a longer time should have been waited at each point close to  $E_{corr}$ ).

When increasing the rotation speed *i.e.* when decreasing  $E_{corr}$  value,  $C$  value decreases and  $RxC$  varies as  $\Omega^{-1/2}$ . These results are in agreement with the theoretical equations demonstrated for pure copper in chloride media (see the Annex B, Eqs. (5.34) and (5.35)).

If considering the RRE and comparing both copper alloys, the effect of mass transport on the anodic partial reaction is more important in the case of Al brass since the single capacitive loop illustrates both the anodic charge transfer and the anodic mass transport; whereas, in the case of 70Cu-30Ni, the HF loop illustrates mainly the anodic charge transfer and the LF loop of impedance diagrams, which is related to the anodic mass transport, is defined only by a few points.

### 5.3 CONCLUSIONS

In this chapter, the corrosion behavior of two copper alloys, 70Cu-30Ni alloy and Al brass were studied after short-term immersion in ASW and/or FNSW in different hydrodynamic conditions (static, under flow and stirring, using a RRE), by combined electrochemical measurements and surface analysis.

Surface analysis by XPS and ToF-SIMS performed with 70Cu-30Ni alloy after 1 h of immersion in static ASW shows the formation of a thick duplex oxide layer, with an outer layer mainly composed of  $\text{Cu}_2\text{O}$ . However, under flow and stirring, this thick duplex oxide layer is no longer observed; a mixed oxide layer is obtained, with a thickness similar to that for the sample just after polishing. The  $\text{Cu}_2\text{O}$ -rich outer layer formed in static ASW is formed by redeposition due to the saturation of the solution in  $\text{Cu}^+$  ions. The thick duplex oxide layer is also observed in static FNSW, nevertheless the oxidized Cu/oxidized Ni ratio is lower than in static ASW.

From Levich and Koutecky-Levich curves, the oxygen diffusion coefficient in aerated filtered natural seawater was calculated and found to be equal to  $1.1 \times 10^{-5} \text{ cm}^2 \cdot \text{s}^{-1}$  (at room temperature).

For 70Cu-30Ni, the experimental impedance diagrams exhibit two capacitive loops: one HF depressed semi-circle, and a not well defined LF loop; whereas for Al brass, one single capacitive loop is observed.

The same impedance model can be used for the two copper alloys immersed at the corrosion potential in seawater. This model assumes for the anodic branch the same mechanism as that for pure copper dissolution in chloride media at low anodic potential. At  $E_{corr}$ , the kinetic parameters of the cathodic partial reaction are different for the two alloys. In the case of 70Cu-30Ni, the cathodic polarization curves show pure mass transport limitation and the cathodic impedance is represented by a Warburg impedance; whereas in the case of Al brass, Tafel behavior is evidenced and the cathodic impedance which is very large can be neglected with respect to the anodic one. In the case of 70Cu-30Ni, the HF loop of experimental impedance diagrams corresponds to the  $CPE_{dl}/R_t^a/W_c$  equivalent circuit and illustrates mainly the anodic charge transfer (diameter equal to the anodic charge transfer resistance  $R_t^a$ ); its depressed shape is partly due to the CPE and partly due to the cathodic Warburg impedance in parallel. The LF loop is related to the anodic mass transport and partial blocking effect by adsorbed species such as CuCl. In the case of Al brass, the single experimental loop illustrates both anodic charge transfer and anodic mass transport plus partial blocking effect. The impedance that illustrates anodic mass transport and partial blocking effect,  $Z_{\theta,D}^a$ , can be approximated by an R/C circuit, as for pure copper in chloride media.

The anodic polarization curves and impedance diagrams show mixed kinetics for the anodic partial reaction, with major effect of mass transport for Al brass and minor effect of mass transport for 70Cu-30Ni.

The  $R_t^a$  values were used to calculate the corrosion current  $i_{corr}$ , assuming Tafel kinetics for the anodic partial reaction. For both alloys in FNSW,  $R_t^a$  and hence  $i_{corr}$  are independent of the rotation speed, due to compensated potential and mass transport effects.

## CHAPTER 6 – EFFECT OF PH

In the absence of biofilms, waters with low pH may increase the solubility of the protective layer formed on internal copper pipe surfaces [202]. When MIC occurs, microorganisms cause a decrease of the pH at the copper/solution interface, increasing the dissolution of the protective layer [203]. The decrease of pH at the copper/solution interface is the main factor controlling MIC of copper [204].

The effect of pH on the electrochemical behavior of 70Cu-30Ni and Al brass alloys in filtered natural seawater (FNSW) at different pH (ranging from 3.7 to 8.0, adding HCL (0.1 M)), and on the surface chemical composition of oxide layers is presented in this chapter.

For that purpose, electrochemical measurements, performed after 1 h of immersion, were combined to surface analysis.

### 6.1 70Cu-30Ni

#### 6.1.1 ELECTROCHEMICAL MEASUREMENTS

Electrochemical measurements presented here, were performed in static conditions.

##### 6.1.1.1 CORROSION POTENTIAL ( $E_{corr}$ ) VS TIME

Before each experiment, the corrosion potential was followed as a function of time ( $E_{corr}$  vs time). During the first hour of immersion, the corrosion potential decreases till reaching a steady-state value of  $-0.231 \pm 0.013$  V vs SCE for pH 8.0,  $-0.220 \pm 0.010$  V vs SCE for pH 6.0 and  $-0.224 \pm 0.007$  V vs SCE for pH 3.7.

There is no significant change in  $E_{corr}$  value with pH. This is in agreement with King's results who studied the dependence of copper corrosion potential in  $0.5 \text{ mol.L}^{-1}$  chloride solution as a function of pH [58]. According to this study, below  $\sim$  pH 8,  $E_{corr}$  is independent of pH and is determined by the relative reaction rates of the anodic dissolution of Cu as  $\text{CuCl}_2^-$  ions and of  $\text{O}_2$  reduction.

##### 6.1.1.2 CATHODIC POLARIZATION CURVES

Figure 6-1(a) shows the cathodic polarization curves obtained in static FNSW for the three different pH values. Two current plateaus, illustrating mass transport limited reactions, can be clearly observed for all curves. The short plateau at around  $-0.30$  V vs SCE ( $|j| \sim 10$

$\mu\text{A}\cdot\text{cm}^{-2}$ ) illustrates the first step of dissolved oxygen reduction with production of  $\text{H}_2\text{O}_2$ . The second plateau current density seems to be lower at pH 3.7 but this may also be induced by a difference in natural convection from one experiment to another. The wide plateau observed for potentials ranging from -0.40 down to -1.00 V vs SCE corresponds to the second step of dissolved oxygen reduction with transfer of 4 electrons. The current increase (in absolute value) observed below -1.00 V vs SCE illustrates water reduction (hydrogen evolution reaction).

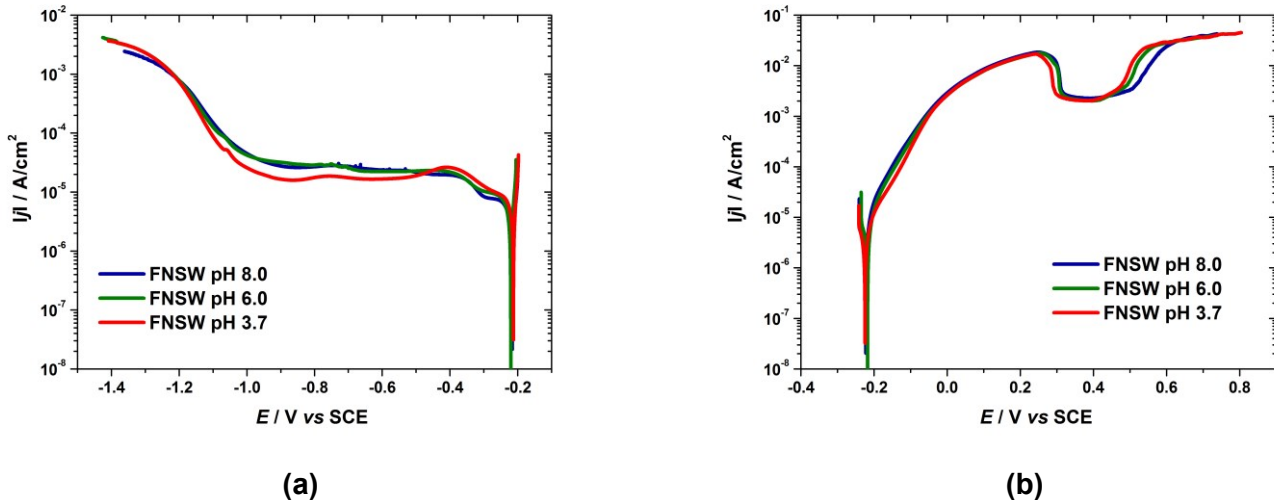


**Figure 6-1:** (a) Cathodic and (b) anodic polarization curves of 70Cu-30Ni after 1 h of immersion at  $E_{\text{corr}}$  in static aerated filtered natural seawater at three different pH values: 8.0, 6.0 and 3.7. Scan rate:  $0.5 \text{ mV}\cdot\text{s}^{-1}$ .

### 6.1.1.3 ANODIC POLARIZATION CURVES

The anodic polarization curves obtained in static FNSW for the three different pH values are presented in Figure 6-1(b). These curves show very high dissolution currents. In particular, a pseudo-plateau, corresponding to a current density of  $\sim 2.5 \text{ mA}\cdot\text{cm}^{-2}$ , can be observed at around 0.4 V vs SCE; therefore, this plateau current is not a passive current, and hence the oxide film formed on the surface is not a passive layer. The pH has no effect on the anodic polarization curves.

### 6.1.1.4 ELECTROCHEMICAL IMPEDANCE SPECTROSCOPY

Figure 6-2 shows the impedance diagrams in the complex plane (Nyquist diagrams) plotted at  $E_{\text{corr}}$  after 1 h of immersion in static FNSW for the three different pH values. The diagrams exhibit two capacitive loops: one high-frequency (HF) depressed semi-circle, and a

not well defined low-frequency (LF) loop. The size of the HF loop is similar at pH 8.0 and 3.7, but is higher at pH 6.0.

After impedance measurements, there is no sign of pitting corrosion on the electrode surface.

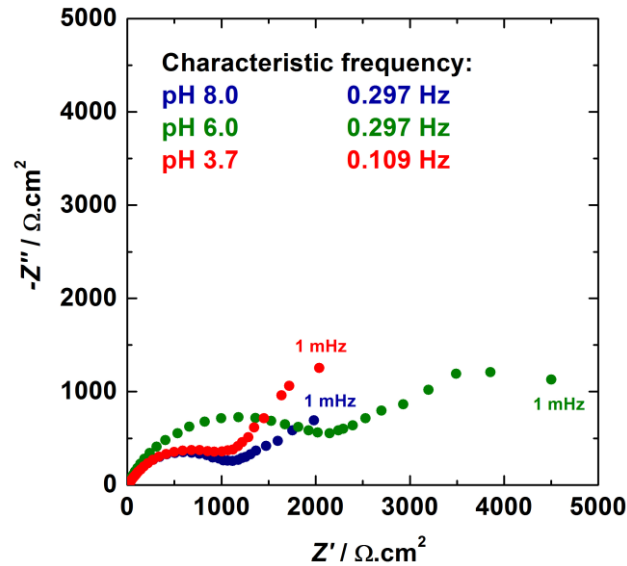


**Figure 6-2:** Experimental impedance diagrams in the complex plane (Nyquist diagrams) of 70Cu-30Ni plotted at  $E_{corr}$  after 1 h of immersion in static aerated filtered natural seawater at three different pH values: 8.0, 6.0 and 3.7.

#### 6.1.1.5 EIS DATA FITTING

In Chapter 4, an impedance model for 70Cu-30Ni alloy at  $E_{corr}$  in ASW and FNSW was developed. The bases of this model are the following:

- a) the anodic partial reaction involves the dissolution of Cu as  $\text{Cu}^+$  species; modified mechanism drawn from that for pure copper dissolution in chloride media at low anodic potential, in order to take into account the presence of an oxide layer (Eqs. (4.20) to (4.23));
- b) the cathodic partial reaction is the oxygen reduction reaction (aerated solutions);
- c) the anodic and the cathodic partial reactions are affected by mass transport, with pure mass transport limitation for the cathodic partial reaction, and mixed kinetic control for the anodic partial reaction;
- d) the anodic partial current is limited by mass transport of  $\text{Cu}^+$  in the solid phase and of  $\text{CuCl}_2^-$  in the electrolyte.

Figure 6-3 shows the absolute value of the imaginary part of the impedance ( $|Z''|$ ) plotted as a function of the frequency in logarithmic coordinates for the same experimental impedance data as those presented in Figure 6-2.

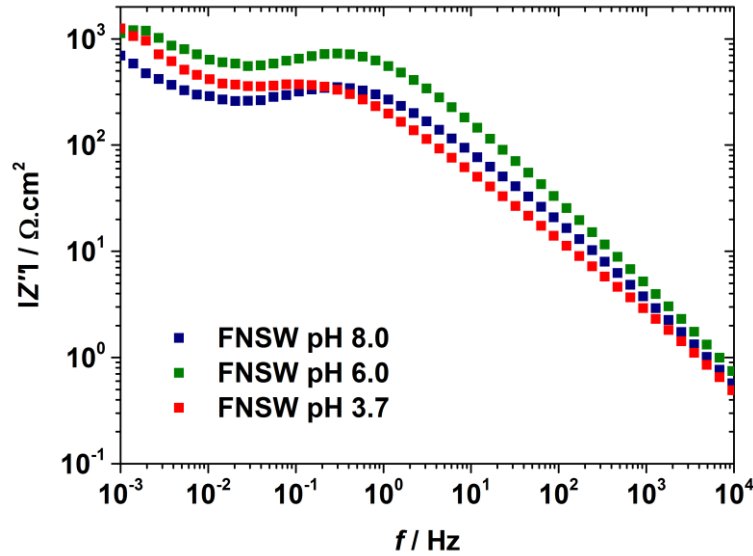


**Figure 6-3:** Experimental impedance data (imaginary part of the impedance as a function of frequency) of 70Cu-30Ni alloy obtained at  $E_{corr}$  after 1 h of immersion in static aerated filtered natural seawater at three different pH values: 8.0, 6.0 and 3.7. Same data as in Figure 6-2.

In all cases, a pseudo-straight line with a slope lower than 1 in absolute value can be observed in the HF range. Similarly to what is observed in ASW (Chapter 4), this slope varies with the frequency, and hence  $\alpha$  cannot be determined graphically from Figure 6-3. Therefore, to better visualize a possible constant value of the slope in a narrow frequency range, the  $d \log |Z''| / d \log f$  vs  $\log f$  curves were calculated from those presented in Figure 6-3 (derivative curves; Figure 6-4).

At pH 8.0 a very narrow plateau can be distinguished at very HF ( $\sim 10^3$  Hz), corresponding to a slope of -0.74. For the other pH values, a plateau is visible at HF, corresponding to a slope of -0.81 at pH 6.0 and of -0.67 at pH 3.7.

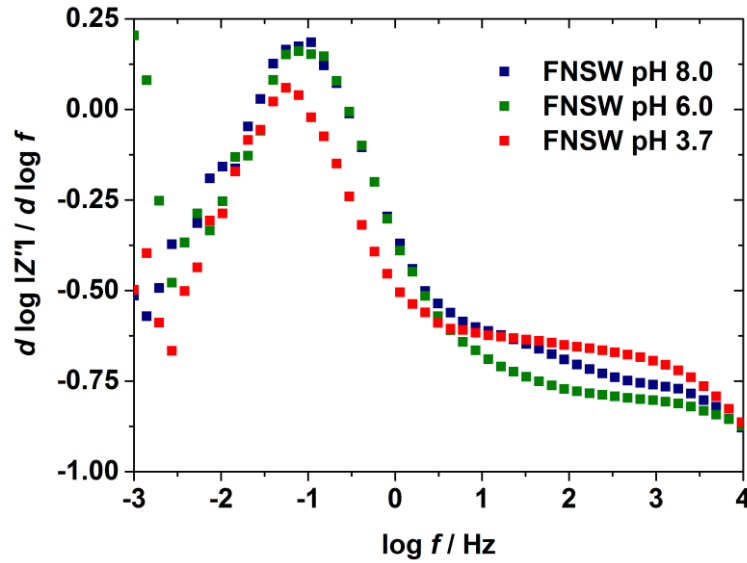


**Figure 6-4:** Experimental impedance data (derivative curves calculated from Figure 6-3) of 70Cu-30Ni alloy obtained at  $E_{corr}$  after 1 h of immersion in filtered natural seawater at three different pH values: 8.0, 6.0 and 3.7. Same data as in Figure 6-2.

The HF loop of the experimental impedance diagrams can be modelled by the  $CPE_{dl} // R_t^a // W_c$  equivalent circuit (Figure 4-15(c)), and the LF loop is related to the anodic mass transport and partial blocking effect by adsorbed species such as  $\text{CuCl}$  ( $Z_{\theta,D}^a$ ). As only few points describe the LF loop, the single HF loop was analyzed by regression of the equivalent circuit presented in Figure 4-15(c), using Simad® software. The regression results are presented in Table 6-1 and in Figure 6-5.

The experimental frequency range taken into account for the regression is indicated in Table 6-1 for each data set, but the fitted curves in Figure 6-5 are shown in the whole frequency range (1 mHz -  $10^5$  Hz), with parameters values corresponding to those given in Table 6-1.

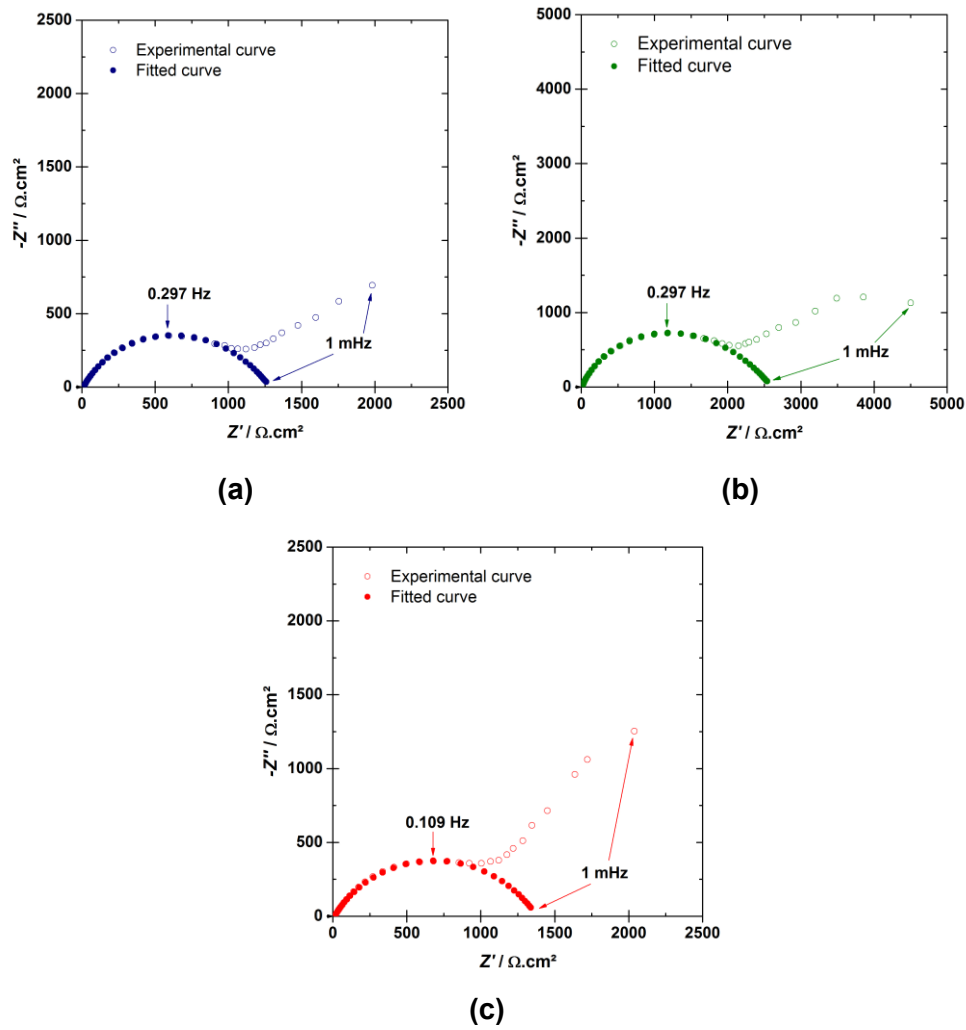


**Figure 6-5:** High frequency loops of Nyquist diagrams obtained for 70Cu-30Ni at  $E_{corr}$  after 1 h of immersion in static aerated filtered natural seawater at three different pH values: (a) 8.0, (b) 6.0 and (c) 3.7. Experimental curves and fit of the impedance model presented in Figure 4-15(c). Same data as in Figure 6-2.

**Table 6-1:** Experimental frequency range taken into account for the regression, parameters values (electrolyte resistance  $R_e$ , anodic charge transfer resistance  $R_t^a$ , constant of the cathodic Warburg impedance  $k_c$ , and CPE parameters  $\alpha$  and  $Q$ ) obtained from the regression of the equivalent circuit presented in Figure 4-15(c) to experimental impedance data shown in Figure 6-2, and effective capacitance  $C_{eff}$  associated with the CPE calculated from Eq. (2.22).

FNSW	Frequency range Hz	$R_e$ $\Omega \cdot \text{cm}^2$	$R_t^a$ $\Omega \cdot \text{cm}^2$	$k_c$ $\text{s}^{0.5} \cdot \Omega^{-1} \cdot \text{cm}^{-2}$	$\alpha$	$Q$ $\text{F} \cdot \text{cm}^{-2} \cdot \text{s}^{(\alpha-1)}$	$C_{eff}$ $\mu\text{F} \cdot \text{cm}^{-2}$
pH 8.0	$10^5 - 7.8 \times 10^{-2}$	12	1310	$3.5 \times 10^{-4}$	0.76	$2.90 \times 10^{-4}$	50
pH 6.0	$10^5 - 7.8 \times 10^{-2}$	13	2600	$1.9 \times 10^{-4}$	0.83	$1.30 \times 10^{-4}$	40
pH 3.7	$10^5 - 4.0 \times 10^{-2}$	12	1370	$2.1 \times 10^{-4}$	0.68	$7.70 \times 10^{-4}$	85

The capacitance values calculated from the impedance diagrams shown in Figure 6-5 by application of Brug's formula (Eq. 2.22)), taking for  $R_e$  and  $R_t^a$  the values extracted from the regression procedure (Table 6-1), are given in Table 6-1. These capacitance values, of the order of several tens of  $\mu\text{F}.\text{cm}^{-2}$ , are typical of those for a double layer capacitance.

$C_{\text{eff}}$  seems to be higher at pH 3.7. Compared to the value obtained at pH 8.0,  $R_t^a$  is similar at pH 3.7 and is  $\sim 100\%$  higher at pH 6.0.

In static conditions, changes in  $R_t^a$  value can be explained by a potential effect, a kinetic effect, and a surface effect (see Eq. (4.28)). As  $E_{\text{corr}}$  is independent of the pH, the application of Eq. (4.30), with  $R_t^a$  and  $C_{\text{eff}}$  values obtained at the three pH, yields  $K|^{pH8.0} \sim 1.6 K|^{pH6.0}$ ,  $K|^{pH8.0} \sim 1.8 K|^{pH3.7}$  and  $K|^{pH6.0} \sim 1.1 K|^{pH3.7}$ . Therefore, the rate of the anodic reaction is the highest at pH 8.0 and is similar at pH 6.0 and 3.7. In other words, the anodic reaction is slow down at acidic pH.

Corrosion currents,  $i_{\text{corr}}$ , were calculated from Eqs. (4.32) and (4.33), assuming Tafel kinetics (pure kinetic control) for the anodic partial reaction, and using  $z = 1$  (dissolution of Cu as  $\text{Cu}^+$  species) and  $\alpha = 0.5$  in Eq. (4.32), and  $R_p = R_t^a$  in Eq. (4.33).

Table 6-2 compares the calculated  $i_{\text{corr}}$  values to those deduced graphically from the cathodic polarization curves ( $i_{\text{corr}}$  being equal to the first plateau current density). If comparing the corrosion current densities obtained from Eq. (4.32) to those deduced graphically, there is a ratio of about 2-5 between the values that may be partly explained by a value of  $\alpha$  different from 0.5 and partially explained by the fact that polarization curves were plotted with a scan rate of  $0.5 \text{ mV}.\text{s}^{-1}$  (non steady-state curves). From this results, it can be concluded that  $i_{\text{corr}}$  is similar for pH 8.0 and 3.7, and is lower at pH 6.0 (divided by  $\sim 2$ ).

**Table 6-2:** Comparison of the corrosion current values obtained from  $R_t^a$ , by application of Eqs. (4.32) (with  $z=1$  and  $\alpha=0.5$ ) and (4.33), and from the cathodic polarization curves (first plateau current density).

FNSW	$R_t^a / \Omega.\text{cm}^2$	$i_{corr} / \mu\text{A}.\text{cm}^{-2}$		
		Eq. (4.32)	Eq. (4.33)	Cathodic polarization curve
pH 8.0	1310	39	14	8
pH 6.0	2600	19	7	10
pH 3.7	1370	37	14	10

## 6.1.2 SURFACE ANALYSIS

Surface analysis presented here was performed after immersion in FNSW under flow and stirring.

### 6.1.2.1 RESULTS

Figure 6-6(a) illustrates the Cu  $2p_{3/2}$  core level spectra for 70Cu-30Ni alloy after polishing and after 1 h immersion at the corrosion potential in FNSW at pH 8.0, pH 6.0 and pH 3.7, under flow and stirring.

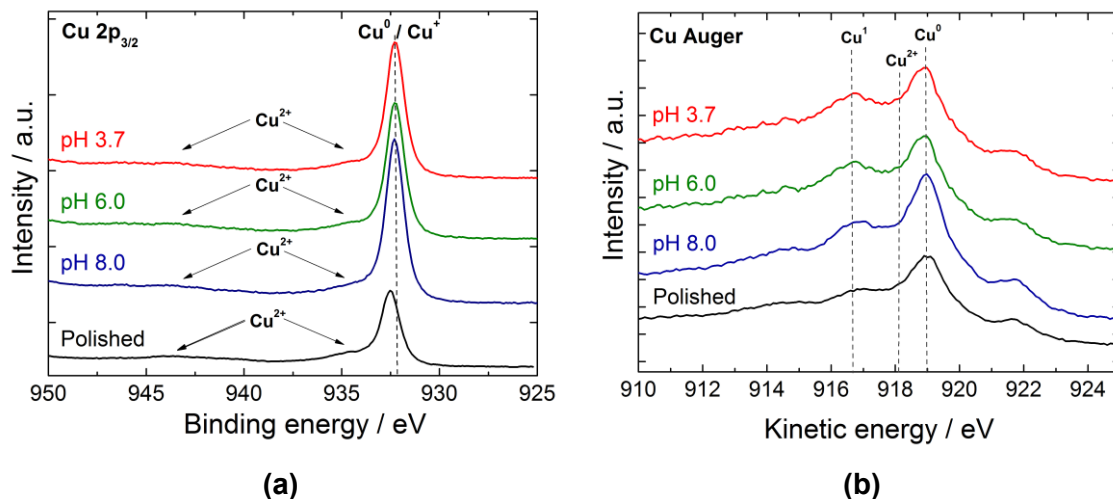


**Figure 6-6:** (a) X-ray photoelectron spectroscopy (XPS) Cu  $2p_{3/2}$  core level spectra, and (b) Cu  $L_{3}M_{45}M_{45}$  Auger lines of 70Cu-30Ni after polishing and after 1 h of immersion at  $E_{corr}$  in aerated filtered natural seawater at pH 8.0, 6.0 and 3.7, under flow and stirring. The intensity is expressed in arbitrary unit (a.u.).

Results related to the sample after polishing were previously presented in Chapter 4.

After immersion in FNSW under flow and stirring at different pH values, the Cu  $2p_{3/2}$  core level spectrum indicates the presence of a first peak at a binding energy of 932.3 eV corresponding to  $\text{Cu}^0$  and/or  $\text{Cu}^+$  (Figure 6-6(a)). A second peak is visible at 933.7 eV with a satellite at higher binding energy (943.2 eV) corresponding to  $\text{Cu}^{2+}$ , however, this  $\text{Cu}^{2+}$  contribution is very low and can be neglected (Figure 6-6(a)).

The Cu Auger line ( $L_3M_{45}M_{45}$ ) located at a kinetic energy of 918.9 eV demonstrates the presence of  $\text{Cu}^0$ , as previously recorded for the sample after polishing (Figure 6-6(b)). Thus, the oxide layer formed on top of the alloy is very thin and its thickness can be calculated from XPS data. However, for the four samples, the position of the Auger line ( $L_3M_{45}M_{45}$ ) at a kinetic energy of 916.7 eV, also indicates the presence of  $\text{Cu}^+$ .

The Ni  $2p_{3/2}$  core level spectra, obtained for 70Cu-30Ni alloy at different pH values, exhibit one peak at 852.2 eV, independently of the pH value. This peak corresponds to  $\text{Ni}^0$ , which confirms that the oxide film formed on the surfaces is very thin. Another peak is observed at a binding energy of 855.7 eV, as well as the satellite at  $\sim 861.4$  eV, corresponding to  $\text{Ni}(\text{OH})_2$  (Figure 6-7).

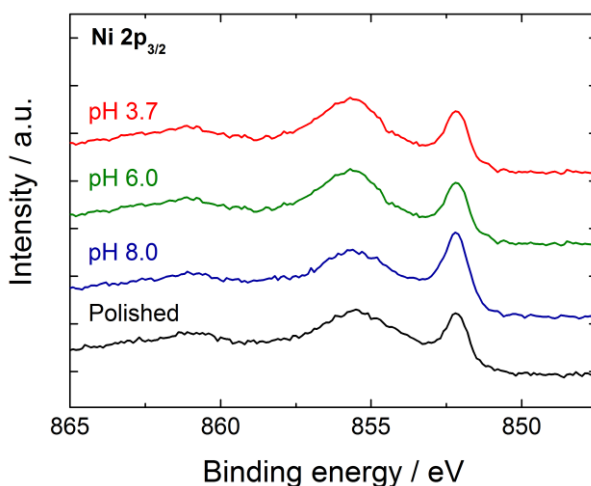


**Figure 6-7:** X-ray photoelectron spectroscopy (XPS) Ni  $2p_{3/2}$  core level spectra of 70Cu-30Ni alloy after polishing and after 1 h of immersion at  $E_{corr}$  in aerated filtered natural seawater at pH 8.0, 6.0 and 3.7, under flow and stirring. The intensity is expressed in arbitrary unit (a.u.).

As previous mentioned in Chapter 4, a major symmetric peak, centered at 400.2 eV at the N 1s spectrum is expected for the amine or amide groups of BSA. The N 1s spectrum

recorded after immersion in FNSW under flow and stirring at different pH values (Figure 6-8(a)) exhibits this symmetric peak, thus, for the three different pH values, low amount of adsorbed proteins are adsorbed. The C 1s signal obtained in the same conditions is shown in Figure 6-8(b). As already mentioned in Chapter 4, it can be fitted with three contributions corresponding to well identified carbon bonds present in the BSA molecule. From the N 1s and C 1s signals, different “nitrogen/carbon” or “carbon/carbon” atomic ratios were calculated and the values obtained for the 70Cu-30Ni alloy immersed in FNSW, under flow and stirring, at the three different pH values, are presented in Table 6-3.

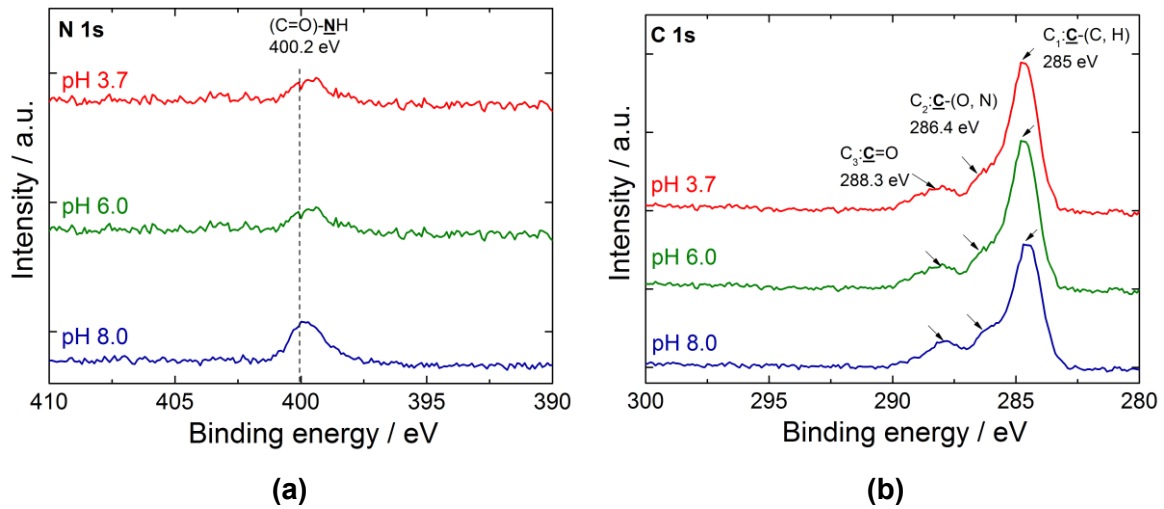


**Figure 6-8:** (a) N 1s core level spectra, and (b) C 1s core level spectra of 70Cu-30Ni after 1 h of immersion at  $E_{corr}$ , under flow and stirring, in aerated filtered natural seawater at pH 8.0, pH 6.0, and pH 3.7. The intensity is expressed in counts per second (CPS).

**Table 6-3:** Atomic ratios calculated from the XPS N 1s and C 1s core level spectra recorded for 70Cu-30Ni after 1 h of immersion at  $E_{corr}$ , under flow and stirring, in aerated filtered natural seawater at pH 8.0, pH 6.0, and pH 3.7.

	$N/C_{total}^*$	$N/(C_2+C_3)^*$	$C_1/C_{total}^*$	$C_2/C_{total}^*$	$C_3/C_{total}^*$
pH 8.0	0.07	0.20	0.66	0.19	0.15
pH 6.0	0.02	0.06	0.67	0.18	0.10
pH 3.7	0.02	0.10	0.75	0.20	0.06

<sup>(a)</sup>The atomic ratio X/Y is given by:

$$X/Y = I_X \sigma_Y \lambda_Y^{BSA} T_Y / I_Y \sigma_X \lambda_X^{BSA} T_X$$

where  $I_{X,Y}$  is the intensity of the peak (peak surface area) associated to element X or Y (X and Y equal to N or C),  $\lambda_{X,Y}^{BSA}$  the attenuation length of photoelectrons emitted by the X or Y core level in the BSA

layer,  $\sigma_{X,Y}$  the photoionisation cross-section of X or Y, and  $T_{X,Y}$  the transmission factor of X or Y. The C 1s signal is fitted with three contributions  $C_1$ ,  $C_2$  and  $C_3$ , corresponding to well identified carbon bonds present in the BSA molecule.

The “nitrogen/carbon” and “carbon/carbon” ratios are similar at the different pH values. The  $C_1/C_{\text{total}}$  ratio is very high at the 3 pH values, illustrating the high amount of hydrocarbons present on the surface. Moreover, the  $N/(C_2+C_3)$  ratio is low compared to the theoretical value of 0.5 corresponding to the peptidic link (HC-NH-(C=O)), showing that the amount of adsorbed proteins is low whatever the pH. However, that amount of proteins is higher at pH 8 ( $N/(C_2+C_3) = 0.20$ ) than at acidic pH ( $N/(C_2+C_3) = 0.06$  to  $0.10$ ).

The atomic composition and the equivalent thickness of the oxide layers were calculated from XPS data, using the system of equations previously presented in Chapter 4 (Eqs. (4.3) to (4.8)) and considering the intensities of copper and nickel in the metallic substrate and in the mixed oxide layer formed on the alloy. These data are presented in Table 6-4.

**Table 6-4:** Atomic composition of the oxide layer and equivalent thickness of the surface layers calculated from XPS data for 70Cu-Ni alloy after 1 h of exposure at  $E_{\text{corr}}$  to FNSW at three different pH values (8.0, 6.0 and 3.7).

		pH		
		8.0	6.0	3.7
Oxide layer (at. %)	Cu <sup>+</sup>	21.9	11.8	9.4
	Ni <sup>2+</sup>	78.1	88.2	90.6
Surface layer thickness (nm)	Oxide layer	0.8	1.0	1.5
	Organic layer	0.6	0.3	0.4

The results show an enrichment in Ni in the oxide layer that increases with decreasing pH, and an increase of the oxide film thickness with the pH decrease. Cu<sup>+</sup> content decreases and Ni<sup>2+</sup> content increases with decreasing pH. This enrichment in Ni in the oxide layer can be explained by an increased dissolution of Cu and passivating properties of Ni in acidic electrolytes [206]. Thus, Cu follows the predictions of the Pourbaix diagram (Figure 1-5); its passive behavior is determined by the solubility of its oxide, *i.e.*

exclusively by thermodynamic data. Contrary to Cu, Ni shows also passivity in strongly acidic electrolytes, which is controlled by the extremely slow dissolution rate of its oxide or hydroxide layers, *i.e.* by its kinetic characteristics. From XPS results, it seems that the oxide layer thickness increases with decreasing pH (about two times higher at pH 3.7 compared to pH 8.0).

The organic layer equivalent thickness, calculated from the  $\frac{I_N^{org}}{I_{Cu}^{ox}}$  ratio (Eq. 4.13)), is very thin (few Å) and similar for the different pH values (Table 6-4). In fact, the amount of nitrogen-containing molecules (including proteins) on the surface is very low and the surface layer formed on the top of the oxide layer is mainly composed of hydrocarbons, corresponding to the carbonaceous contamination layer (C<sub>1</sub> peak at 285.0 eV; Figure 6-8(b)). The evolution with pH of the organic layer equivalent thickness seems to follow that of the N/(C<sub>2</sub>+C<sub>3</sub>) atomic ratio, *i.e.* it is higher at pH 8 than at acidic pH, but with a lower amplitude of variation.

A characteristic ToF-SIMS (negative ions) depth profile obtained with 70Cu-30Ni alloy immersed during 1 h at  $E_{corr}$  in FNSW at pH 8.0 is presented in Figure 6-9(a). This profile allows evidencing a possible stratification of the different compounds on the alloy surface. It shows four regions. A first one that extends from 0 s to 3 s of sputtering characterized by an increase of all signals and corresponding to the time necessary to reach a steady-state. After 3 s, one enters the second region that extends up to 7 s of sputtering. In this region, the  $35\text{Cl}^-$ ,  $90^{58}\text{NiO}_2^-$ ,  $95^{63}\text{CuO}_2^-$  and  $18^{18}\text{O}^-$  signals, that are at their maximums, decrease sharply, and the  $116^{58}\text{Ni}_2^-$  signal increases, indicating a compact oxide layer covering the whole surface. In the second region, the  $26\text{CN}^-$  signal, characteristic of organic compounds, is at maximum value; this may suggest that the surface of the oxide layer is partly covered by an organic film. In fact, it seems that the oxide film is very thin and that the thickness is not homogeneous on the whole surface. After 7 s, the metallic surface has been reached. However, from 7 to 40 s, a third region can be distinguished for which the  $35\text{Cl}^-$ ,  $90^{58}\text{NiO}_2^-$ ,  $95^{63}\text{CuO}_2^-$  and  $18^{18}\text{O}^-$  signals present a shoulder. This could be assigned to an oxide film non covered by the organic layer. As the organic layer is very thin and due to the fact that we sputtered with a "sufficiently high" current to go through the oxide film thickness in an appropriate time, it could be possible that we cannot distinguish the organic layer of the oxide film (the peaks on the  $95^{63}\text{CuO}_2^-$ ,  $90^{58}\text{NiO}_2^-$ ,  $26\text{CN}^-$  and  $35\text{Cl}^-$  are over imposed in the 3-10s region). Thus, from this point, it is also possible that the organic layer covers the whole oxide layer and not only the thickest part of the oxide. The fourth region starts at 40 s, when  $35\text{Cl}^-$ ,  $90^{58}\text{NiO}_2^-$ ,  $95^{63}\text{CuO}_2^-$  and  $18^{18}\text{O}^-$  signals decrease again and the  $116^{58}\text{Ni}_2^-$  signal reaches its

maximum intensity, describing a plateau. This indicates that the alloy/oxide interface is reached. The depth profiles show one mixed oxide layer (oxidized copper and nickel) with a thickness of  $\sim 1.5$  nm.

A similar behavior is observed for the samples immersed in FNSW at pH 6.0 (Figure 6-8(b)) and pH 3.7 (Figure 6-8(c)). Moreover, the thickness of the oxide film (regions 2+3) seems independent of the pH, contrary to what is concluded from XPS data. One explanation would be the difficulty of estimating low surface layer thickness from ToF-SIMS data.

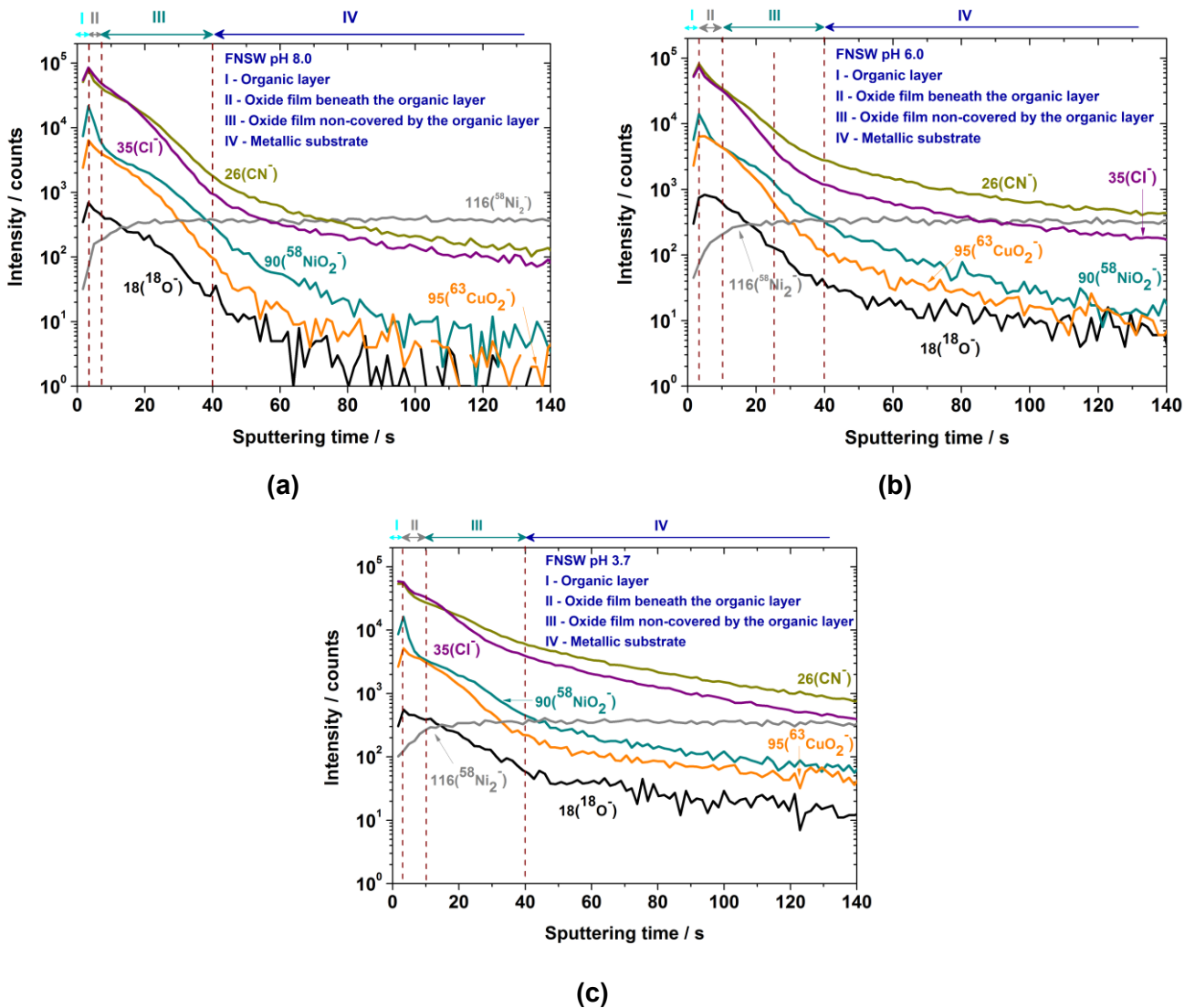


**Figure 6-9:** Characteristic time-of-flight secondary ions mass spectrometry (ToF-SIMS) negative depth profiles of 70Cu-30Ni after 1 h of immersion at  $E_{\text{corr}}$ , under flow and stirring, in aerated filtered natural seawater at (a) pH 8.0, (b) pH 6.0, and (c) pH 3.7.

### 6.1.2.2 SURFACE LAYERS MODELS (COMBINED XPS AND TOF-SIMS)

The surface layer model deduced from combined XPS and ToF-SIMS data for 70Cu-30Ni alloy after 1 h of immersion at  $E_{corr}$ , under flow and stirring, in FNSW at pH 8.0, 6.0 and 3.7 is shown in Figure 6-10. This model shows that the oxide layer formed on top of the alloy is very thin and presents heterogeneous thickness (maximum thickness  $\sim 1.5$  nm). An organic layer with a thickness of  $\sim 0.5$  nm covers the whole oxide layer.

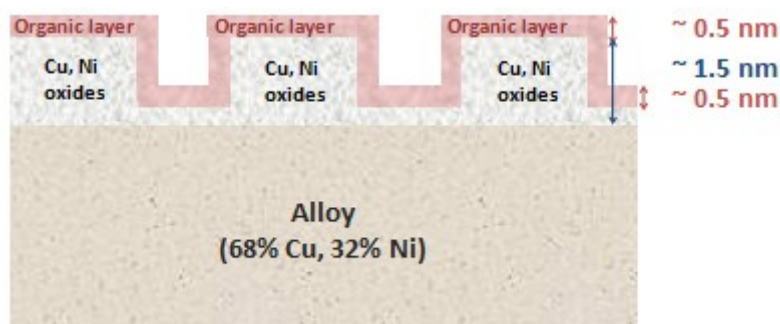


**Figure 6-10:** Model of the surface layers deduced from combined X-ray photoelectron spectroscopy (XPS) and time-of-flight secondary ions mass spectrometry (ToF-SIMS) results for 70Cu-30Ni after 1 h of immersion at  $E_{corr}$ , under flow and stirring, in FNSW at pH 8.0, 6.0 and 3.7.

### 6.1.2.3 COMPOSITION OF THE ORGANIC LAYERS (XPS)

Within seconds, surfaces immersed in water become covered by macromolecules, such as polysaccharides and proteins, which are present in natural seawater. As in chapter 4, correlations between spectral XPS data (C 1s, N 1s and O 1s) were used to generate information about the organic layer formed in FNSW at different pH values. As for the analysis of data in Chapter 4, the C 1s peak was decomposed into three contributions.

Figure 6-11(a) presents the plot of the molar concentration of carbon responsible for the C<sub>3</sub> component, located at 288.3 eV (O=C-N-C, O=C-O or C-O-C-O), as a function of the molar concentration of total organic nitrogen, N<sub>org</sub>. A 1:1 relation is expected for the amide function (HC-NH-(C=O)) forming the backbone of proteins (peptidic link). A deviation from this 1:1 line would indicate the presence of polysaccharides or any oxidized carbon of contaminants. This graph indicates that the organic layers after immersion in FNSW (pH 8.0, 6.0 and 3.7) seem to contain other compounds than proteins.

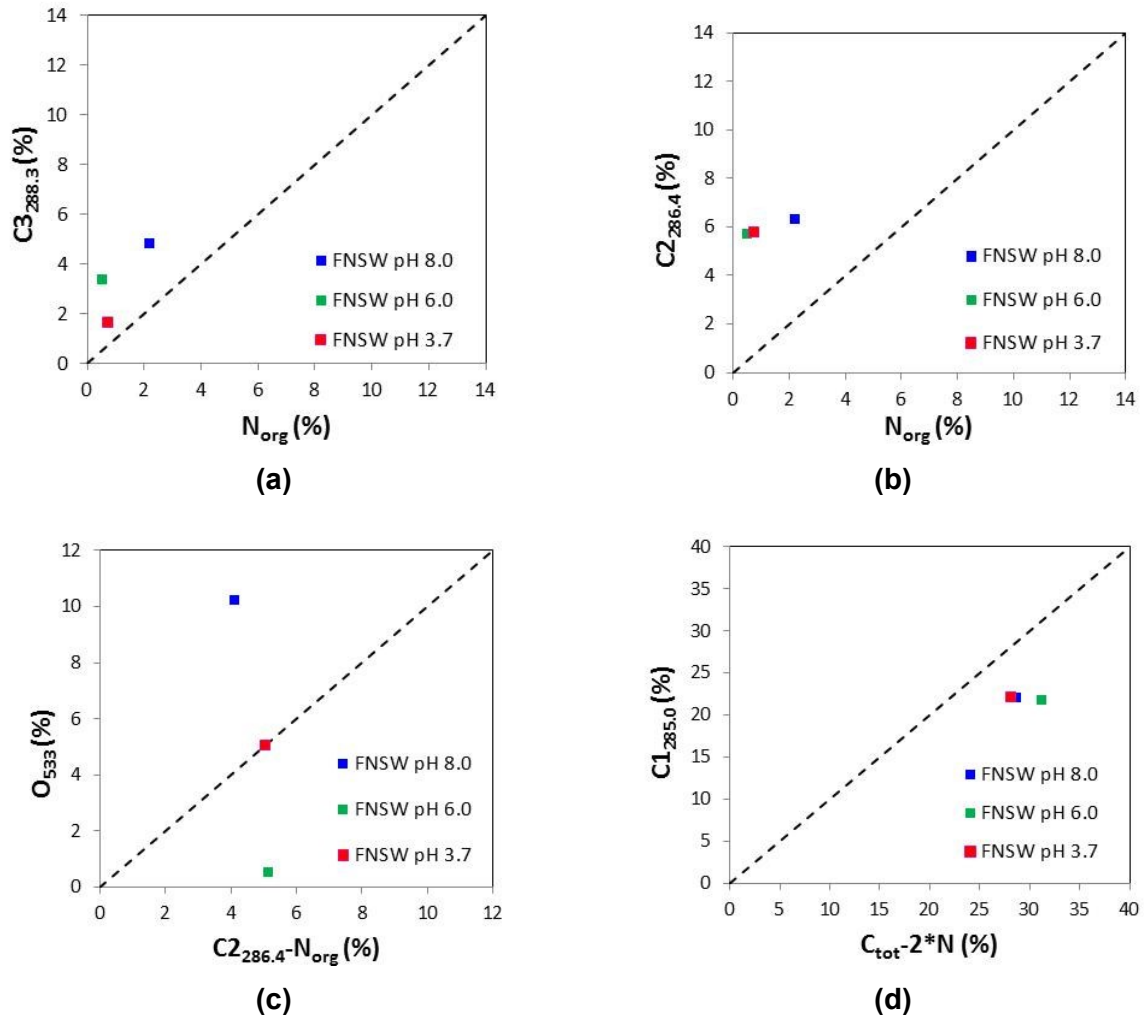


**Figure 6-11:** Plot of molar concentrations determined by XPS: (a)  $C3_{288.3}$  vs  $N_{org}$ , (b)  $C2_{286.4}$  vs  $N_{org}$ , c)  $O_{533}$  vs  $C2_{286.4} - N_{org}$ , and d)  $C1_{285.0}$  vs  $C_{tot} - 2*N_{org}$ . 70Cu-30Ni samples immersed 1 h at  $E_{corr}$ , under flow and stirring, in FNSW at pH 8.0, 6.0 and 3.7. Dashed lines: 1:1 relation.

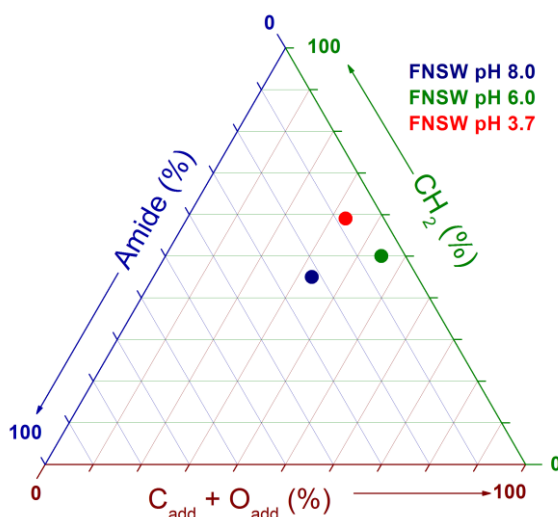
In Figure 6-11(b), the molar concentration of the carbon component located at a binding energy of 286.4 eV ( $C_2$  peak), which is due to carbon making a single bond with oxygen (in alcohol, polysaccharides, ester or ether) or nitrogen (in amine or amide), is plotted as a function of  $N_{org}$ . In this figure, all samples after immersion in FNSW at different pH values present high deviation from the 1:1 relation, which may be attributed to the presence of polysaccharides or oxygen-containing organic contaminants.

Figure 6-11(c) illustrates the O 1s at 533.4 eV, due to oxygen in ester or ether groups or in polysaccharides, as a function of the difference between  $C_2$  and  $N_{org}$  ( $C_2 - N_{org}$ ). The total organic N is subtracted from  $C_2$  in order to remove the contribution of amide functions related to the presence of proteins. Therefore, a 1:1 relation is expected for esters and polysaccharides. In the case of FNSW, at pH 3.7, the experimental data are close to the 1:1 line, but at pH 8.0 and 6.0, this is not true. This means that at pH 3.7 esters and or

polysaccharides are detected on the surface but at more alkaline pH, other species can be found (more oxidized species at pH 8.0 and more carbonated species at pH 6.0).

Figures 6-11(a) and 6-11(b) allow evidencing low content of the amide function on the surface in FNSW (at different pH values). This amide function is considered as a marker of proteins. However, the presence of other functional groups that can be associated to other biomolecules, such as polysaccharides or hydrocarbons (typical of lipids) is also evidenced. Polysaccharides frequently contain N-acetylated aminosugars in which nitrogen is also in the form of amide. Considering that all the  $N_{org}$  is in the form of amide ( $HC-NH-(C=O)$ ), the carbon which is not in the form of amide can be calculated by subtracting  $2*N_{org}$  from the total carbon ( $C_{tot} - 2*N_{org}$ ). In Figure 6-11(d), the  $C_1$  carbon component, due to carbon only bound to carbon and hydrogen (hydrocarbon function, typical of lipids) is plotted as a function of the total carbon which is not in the form of amide ( $C_{tot} - 2*N_{org}$ ). The deviations from the 1:1 relation reflect the concentration of carbon which is neither in the form of hydrocarbon functions, nor in the form of amide. All samples after immersion in FNSW, independently of pH, present significant deviations from this 1:1 line.

Defining the composition of the organic adlayers is difficult due to the complexity of the biochemical compounds and the presence of organic contaminants on the surface. However, as shown in previous figures, the main biomolecules contributions can be distinguished and, therefore, the composition can be estimated in terms of these main components. The elemental molar concentrations, obtained from XPS spectra, were converted into weight percentages of these chemical entities (g/100 g of adlayer), as explained in Annex A of Chapter 4. Figure 6-12 illustrates the XPS results after conversion into weight percentages in the form of a ternary composition diagram. The corners of this triangle represent 100 wt % of amide, 100 wt % of  $CH_2$  and 100 wt % of additional carbon and oxygen ( $C_{add} + O_{add}$ ). This figure is convenient to represent the composition of surface layers and adlayers with respect to an amide pole, shared by proteins and N-acetylated functions of polysaccharides, a hydrocarbon pole, typical of lipids, and a pole representative of oxidized organic compounds, including polysaccharide moieties.



**Figure 6-12:** Composition of adsorbed biomolecules on the surface. Relative mass concentration of amide ( $\text{HC-NH-(C=O)}$ ), hydrocarbon  $\text{CH}_2$ , and other oxygen-containing molecules ( $\text{C}_{\text{add}} + \text{O}_{\text{add}}$ ), including polysaccharides. 70Cu-30Ni samples immersed 1 h at  $E_{\text{corr}}$ , under flow and stirring, in FNSW at pH 8.0, 6.0 and 3.7.

After 1 h immersion in FNSW at pH 8.0, the surface show low protein concentration (22 % amide), 45 % of hydrocarbon ( $\text{CH}_2$ ) and 33 % of additional carbon and oxygen ( $\text{C}_{\text{add}} + \text{O}_{\text{add}}$ ). At pH 6.0 and 3.7, the surface show lower protein concentration (5 % and 8 % amide respectively), higher hydrocarbon contribution (50 % and 59 % respectively), and higher or equal contribution of additional carbon and oxygen (45% and 33%  $\text{C}_{\text{add}} + \text{O}_{\text{add}}$ , respectively). Whatever the pH value, the organic layer is mainly composed of hydrocarbon and the quantity of proteins is low. This result confirms that, in fact, what is called “organic layer” is mainly the carbonaceous contamination layer.

Proteins are small biomolecules composed by a number of amino acids. Due to the great variety of physical and chemical properties among the amino acids, including charge, hydrophobicity, and acid/base character, proteins also exhibit great variation in physical and chemical characteristics. The environment in which the amino acids are present plays a key role. In particular, the pH is an important parameter [205]. Amino acids are characterized by the presence of both acidic (carboxylic acid) and basic (amine) functional groups. These groups undergo the same type of equilibrium reactions that all weak acids and bases undergo, and the relative amount of each form can be altered by adjusting the pH of the solution. This could explain the decrease of protein concentration with the decrease of pH from 8.0 to 6.0 (22 % to 5 %), or from 8.0 to 3.7 (22% to 8%), but not from 6.0 to 3.7 (5 % to 8 %). Our results indicate that pH is not the key parameter in protein adsorption.

## 6.2 AL BRASS

### 6.2.1 ELECTROCHEMICAL MEASUREMENTS

Electrochemical measurements presented here were performed in static conditions.

#### 6.2.1.1 CORROSION POTENTIAL ( $E_{corr}$ ) VS TIME

The corrosion potential as a function of time ( $E_{corr}$  vs time) was followed for 1 h.  $E_{corr}$  values obtained in static FNSW, at three different pH values (8.0, 6.0 and 3.7), are presented in Table 6-5. As for 70Cu-30Ni there is no significant change in  $E_{corr}$  value with pH.

**Table 6-5:** Corrosion potential values for Al brass alloy after 1 h of immersion in static filtered natural seawater (FNSW), at three different pH values (8.0, 6.0 and 3.7).

	$E_{corr}$ / V vs SCE
FNSW pH 8.0	$-0.247 \pm 0.002$
FNSW pH 6.0	$-0.246 \pm 0.001$
FNSW pH 3.7	$-0.249 \pm 0.006$

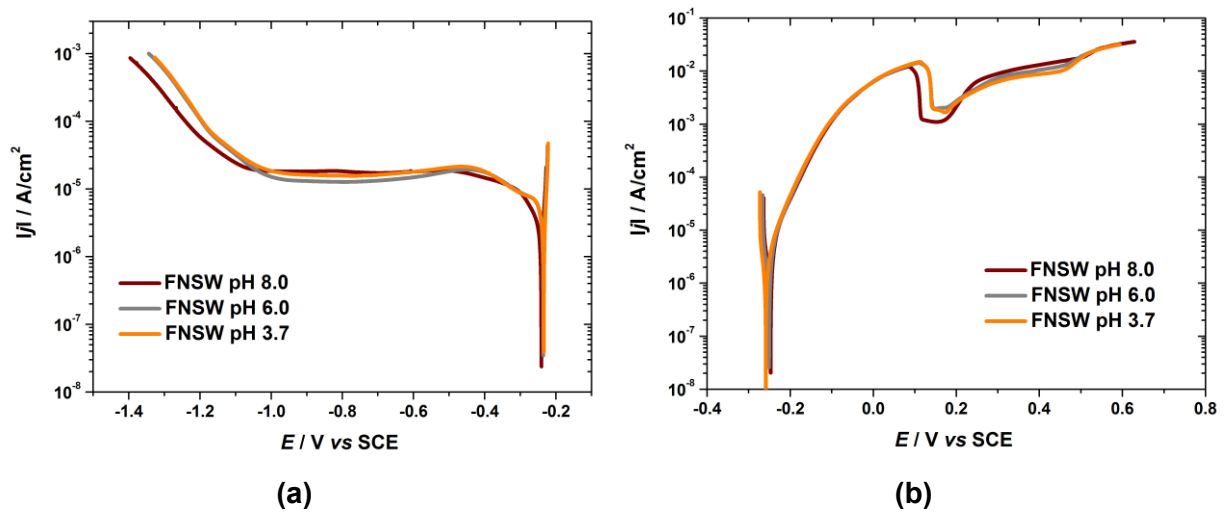
#### 6.2.1.2 CATHODIC POLARIZATION CURVES

Figure 6-13(a) shows the cathodic polarization curves obtained in static FNSW for the three different pH values. Two current plateaus illustrating mass transport limited reactions can be observed at pH 6.0 and 3.7, with the short plateau at around -0.30 V vs SCE ( $|j| \sim 8 \mu\text{A}\cdot\text{cm}^{-2}$ ) illustrating the first step of dissolved oxygen reduction with production of  $\text{H}_2\text{O}_2$ . This first plateau is not clearly visible at pH 8.0. The wide plateau observed for potentials ranging from -0.50 down to -1.00 V vs SCE corresponds to the second step of dissolved oxygen reduction with a transfer of 4 electrons. The current increase (in absolute value) observed below -1.00 V vs SCE illustrates water reduction (hydrogen evolution reaction). The pH does not seem to have a great effect on the cathodic polarization curves.

#### 6.2.1.3 ANODIC POLARIZATION CURVES

The anodic polarization curves obtained in static FNSW for the three different pH values are presented in Figure 6-13(b). Similar anodic behavior is observed for the 3 pH.

The electrochemical behavior of Al brass was investigated in both 3.5% NaCl and seawater by M.M. Osman [207]. At active potential, the alloy is dissolved directly or through an adsorbed metastable CuCl layer. At higher applied anodic potential, the active–passive transition leads to the formation of a thicker and more stable CuCl salt layer. With further increase of the anodic potential, the formation of CuO and/or Cu(OH)<sub>2</sub> will take place. Three anodic peaks can be observed on the potentiodynamic polarization curves, corresponding to the formation of Cu<sub>2</sub>O, CuCl and CuO and/or Cu(OH)<sub>2</sub> for increasing potential [8].



**Figure 6-13:** (a) Cathodic and (b) anodic polarization curves of Al brass after 1 h of immersion at  $E_{corr}$  in static aerated filtered natural seawater at three different pH values: 8.0, 6.0 and 3.7. Scan rate: 0.5 mV.s<sup>-1</sup>.

#### 6.2.1.4 ELECTROCHEMICAL IMPEDANCE SPECTROSCOPY

Figure 6-14 shows the impedance diagrams in the complex plane (Nyquist diagrams) plotted at  $E_{corr}$  after 1 h of immersion in static FNSW for the three different pH values. The diagrams exhibit two loops: one HF capacitive loop and a LF straight line, forming an angle with the X-axis lower than 45° (this angle increases with decreasing pH). The HF loop is less defined for Al brass compared to 70Cu-30Ni.

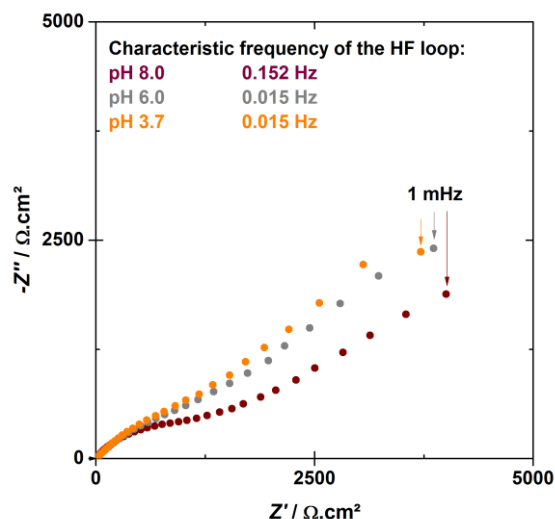


**Figure 6-14:** Experimental impedance diagrams in the complex plane (Nyquist diagrams) of Al brass plotted at  $E_{corr}$  after 1 h of immersion in static filtered natural seawater at three different pH values: 8.0, 6.0 and 3.7.

### 6.2.1.5 EIS DATA FITTING

In Chapter 4, an impedance model for 70Cu-30Ni alloy in ASW and in FNSW was developed. On the other hand, in Chapter 5, it was shown that for Al brass/FNSW system under static conditions, the impedance model was the same as that for 70Cu-30Ni.

Figure 6-15 shows the absolute value of the imaginary part of the impedance ( $|Z''|$ ) plotted as a function of the frequency in logarithmic coordinates for the same experimental impedance data as those presented in Figure 6-14.

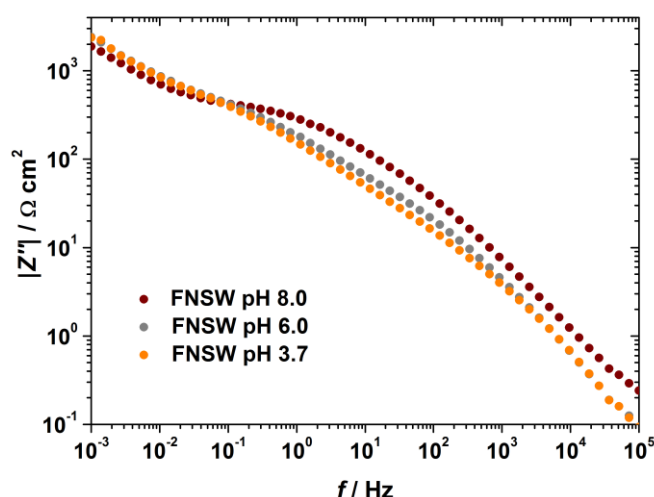


**Figure 6-15:** Experimental impedance data (imaginary part of the impedance as a function of frequency) of Al brass alloy obtained at  $E_{corr}$  after 1 h of immersion in static filtered natural seawater at three different pH values: 8.0, 6.0 and 3.7. Same data as in Figure 6-14.

Two domains can be distinguished in the HF range ( $f > 10^3$  Hz) and in the medium frequency (MF) range ( $1 \leq f \leq 10^3$  Hz). A straight line with a slope lower than 1 in absolute value can be observed in the HF range; this slope value lower than 1 suggests a CPE-like behavior. A straight line with a slope equal to -0.5 can be observed in the MF range, especially at pH 6.0 and 3.7; this slope equal to -0.5 suggests a Warburg-like behavior.

In order to better visualize a possible constant value of the slope in a narrow frequency range, the  $d \log |Z''| / d \log f$  vs  $\log f$  curves were calculated from those presented in Figure 6-15 (derivative curves; Figure 6-16). At pH 8.0, a plateau corresponding to a value of about -0.8 can be observed in the very HF range ( $f > 2000$  Hz). This HF plateau shows a CPE behavior, with a value of  $\alpha$  equal to 0.8. No plateau corresponding to a value of about -0.5 is visible in the MF range. At pH 6.0 and 3.7, a plateau corresponding to a value of about -0.5 can be observed in the MF range ( $2 < f < 20$  Hz). This MF plateau is in agreement with a Warburg-like behavior. No plateau is visible at very high frequency. Therefore, the HF loop of the experimental impedance diagrams can be modelled by the  $CPE_{dl} // R_t^a // W_c$  equivalent circuit (Figure 4-15(c)). At the 3 pH, there is no clear frequency domain specifically assigned to each process (charge transfer at very HF and mass transport at MF). The LF loop is related to the anodic mass transport and partial blocking effect by CuCl ( $Z_{\theta,D}^a$ ).

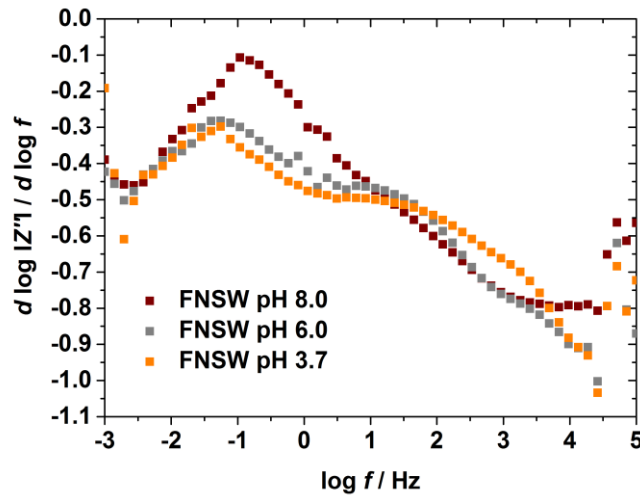


**Figure 6-16:** Experimental impedance data (derivative curves calculated from Figure 6-14) of Al brass alloy obtained at  $E_{corr}$  after 1 h of immersion in static filtered natural seawater at three different pH values: 8.0, 6.0 and 3.7. Same data as in Figure 6-14.

As only few points describe the LF loop, the single HF loop was analyzed by regression of the equivalent circuit presented in Figure 4-15(c), using Simad® software. The regression results are presented in Figure 6-17 and in Table 6-6.

The experimental frequency range taken into account for the regression is indicated in Table 6-6 for each data set, but the fitted curves in Figure 6-16 are shown in the whole frequency range (1 mHz -  $10^5$  Hz), with parameters values corresponding to those given in Table 6-6.

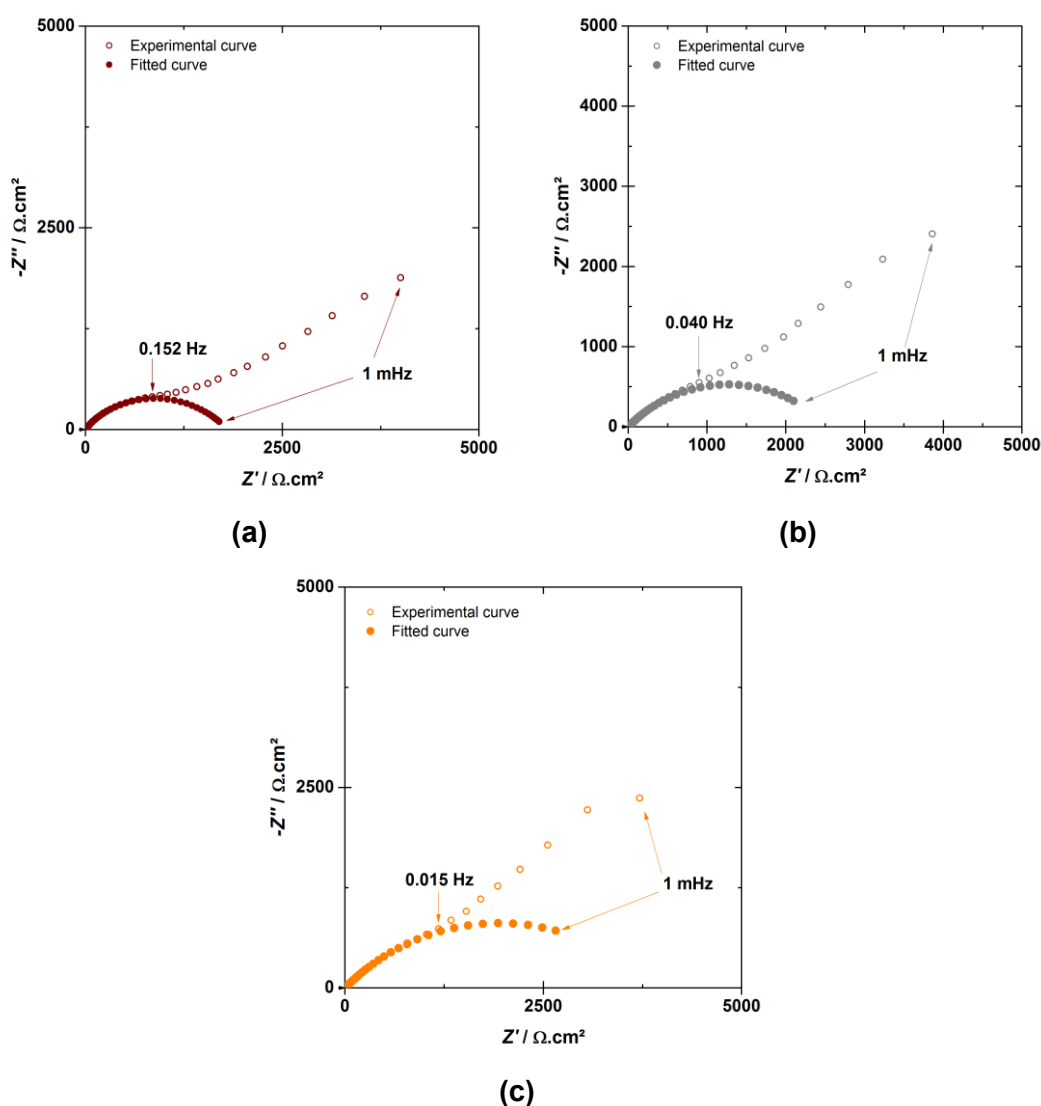


**Figure 6-17:** High frequency loops of Nyquist diagrams obtained for Al brass at  $E_{corr}$  after 1 h of immersion in static filtered natural seawater at three different pH values: (a) 8.0, (b) 6.0 and (c) 3.7. Experimental curves and fit of the impedance model presented in Figure 4-15(c). Same data as in Figure 6-14.

**Table 6-6:** Regression results for the Al brass/FNSW system, in static conditions, at three different pH. Experimental frequency range taken into account for the regression, parameters values (electrolyte resistance  $R_e$ , anodic charge transfer resistance  $R_t^a$ , constant of the cathodic Warburg impedance  $k_c$ , and CPE parameters  $\alpha$  and  $Q$ ) obtained from the regression of the equivalent circuit presented in Figure 4-15(c) to experimental impedance data shown in Figure 6-14, and effective capacitance  $C_{eff}$  associated with the CPE calculated from Eq. (2.22).

FNSW	Frequency range Hz	$R_e$ $\Omega.cm^2$	$R_t^a$ $\Omega.cm^2$	$k_c$ $s^{0.5}.\Omega^{-1}.cm^{-2}$	$\alpha$	$Q$ $F.cm^{-2}.s^{(\alpha-1)}$	$C_{eff}$ $\mu F.cm^{-2}$
pH 8.0	$10^5-5.8 \times 10^{-1}$	12	1800	$6.1 \times 10^{-4}$	0.93	$2.5 \times 10^{-5}$	14
pH 6.0	$10^5-1.5 \times 10^{-1}$	12	2530	$1.3 \times 10^{-3}$	0.99	$2.0 \times 10^{-5}$	20
pH 3.7	$10^5-2.9 \times 10^{-2}$	12	3880	$1.7 \times 10^{-3}$	0.94	$3.1 \times 10^{-5}$	19

The effective capacitance values calculated from the impedance diagrams shown in Figure 6-17, taking for  $R_e$  and  $R_t^a$  the values extracted from the regression procedure (Table 6-6), are given in Table 6-6. These capacitance values are similar for all pH values and are typical of those for a double layer capacitance.

$R_t^a$  increases with decreasing pH; compared to the value obtained at pH 8.0,  $R_t^a$  is  $\sim 1.4$  higher at pH 6.0 and  $\sim 2.2$  higher at pH 3.7. Changes in  $R_t^a$  value can be explained by a potential effect, a kinetic effect, and a surface effect (see Eq. (4.28)). As  $E_{corr}$  is independent of the pH, the application of Eq. (4.30), with  $R_t^a$  and  $C_{eff}$  values obtained at the three pH, yields  $K|^{pH8.0} \sim 2.0 K|^{pH6.0}$ ,  $K|^{pH8.0} \sim 2.9 K|^{pH3.7}$  and  $K|^{pH6.0} \sim 1.4 K|^{pH3.7}$ . Therefore, for the Al brass/FNSW system, the more acidic the pH, the slower the anodic reaction.

Corrosion currents,  $i_{corr}$ , were calculated from Eqs. (4.32) and (4.33), assuming Tafel kinetics (pure kinetic control) for the anodic partial reaction, and using  $z = 1$  (dissolution of Cu as  $Cu^+$  species) and  $\alpha = 0.5$  in Eq. (4.32), and  $R_p = R_t^a$  in Eq. (4.33). The  $i_{corr}$  values are presented in Table 6-7. For pH 6.0 and 3.7, Table 6-7 compares the calculated  $i_{corr}$  values to those deduced graphically from the cathodic polarization curves ( $i_{corr}$  being equal to the first plateau current density). For pH 8.0, it was impossible to extract  $i_{corr}$  value from the cathodic polarization curve. If comparing the corrosion current densities obtained from Eq. (4.32) to those deduced graphically, there is a ratio of  $\sim 2$ -2.5 between the values that may be partly explained by a value of  $\alpha$  different from 0.5 and partly explained by the fact that polarization curves were plotted with a scan rate of  $0.5 \text{ mV.s}^{-1}$  (non steady-state curves).

From these results, it can be concluded that the corrosion current density decreases with decreasing the pH, and is of the same order of magnitude as that calculated for the 70Cu-30Ni/FNSW system.

**Table 6-7:** Comparison of the corrosion current values obtained from  $R_t^a$ , by application of Eqs. (4.32) and (4.33) and from the cathodic polarization curves (first plateau current density).

FNSW	$R_t^a / \Omega.cm^2$	$i_{corr} / \mu A.cm^{-2}$		
		Eq. (4.32)	Eq. (4.33)	Cathodic polarization curve
pH 8.0	1800	28	11	-
pH 6.0	2530	20	8	8
pH 3.7	3880	13	5	7

## 6.2.2 SURFACE ANALYSIS

Surface analysis presented here was performed after immersion in FNSW under flow and stirring.

### 6.2.2.1 INTRODUCTION

As indicated in Chapter 2, from SEM micrographs it is possible to observe a homogeneous distribution of Cu, Zn and Al along the Al brass sample surface.

If a continuous mixed oxide layer covering the metallic alloy is assumed (Figure 6-18), the composition and the equivalent thickness of the oxide layer ( $d_{ox}$ ) can be calculated from XPS data using the following system of equations, in which the intensities of copper, zinc and aluminum in the metallic substrate and in the oxide layer are considered:

$$\text{Metallic copper (Cu}^m\text{)} \quad I_{Cu}^m = k\sigma_{Cu}\lambda_{Cu}^m D_{Cu}^m T_{Cu} \left( \exp\left(-\frac{d_{ox}}{\lambda_{Cu}^{ox}}\right) \right) \quad (6.1)$$

$$\text{Copper oxide (Cu}^{ox}\text{)} \quad I_{Cu}^{ox} = k\sigma_{Cu}\lambda_{Cu}^{ox} D_{Cu}^{ox} T_{Cu} \left( 1 - \exp\left(-\frac{d_{ox}}{\lambda_{Cu}^{ox}}\right) \right) \quad (6.2)$$

$$\text{Metallic zinc (Zn}^m\text{)} \quad I_{Zn}^m = k \sigma_{Zn} \lambda_{Zn}^m D_{Zn}^m T_{Zn} \left( \exp \left( -\frac{d_{ox}}{\lambda_{Zn}^{ox}} \right) \right) \quad (6.3)$$

$$\text{Zinc oxide (Zn}^{ox}\text{)} \quad I_{Zn}^{ox} = k \sigma_{Zn} \lambda_{Zn}^{ox} D_{Zn}^{ox} T_{Zn} \left( 1 - \exp \left( -\frac{d_{ox}}{\lambda_{Zn}^{ox}} \right) \right) \quad (6.4)$$

$$\text{Metallic aluminum (Al}^m\text{)} \quad I_{Al}^m = k \sigma_{Al} \lambda_{Al}^m D_{Al}^m T_{Al} \left( \exp \left( -\frac{d_{ox}}{\lambda_{Al}^{ox}} \right) \right) \quad (6.5)$$

$$\text{Aluminum oxide (Al}^{ox}\text{)} \quad I_{Al}^{ox} = k \sigma_{Al} \lambda_{Al}^{ox} D_{Al}^{ox} T_{Al} \left( 1 - \exp \left( -\frac{d_{ox}}{\lambda_{Al}^{ox}} \right) \right) \quad (6.6)$$

where:

$\theta$  is the take-off angle of the photoelectrons with respect to the sample surface. It is  $90^\circ$  in this work;

$k$  is the spectrometer specific constant;

$\sigma_{Cu}$ ,  $\sigma_{Zn}$ ,  $\sigma_{Al}$  are the photo-ionization cross-sections of Cu, Zn and Al, respectively;

$\lambda_{Cu}^m, \lambda_{Cu}^{ox}, \lambda_{Zn}^m, \lambda_{Zn}^{ox}, \lambda_{Al}^m, \lambda_{Al}^{ox}$  are the inelastic mean free paths (IMFP) of the photoelectrons emitted by the Cu core level in the metallic alloy and in the oxide, by the Zn core level in the metallic alloy and in the oxide and by the Al core level in the metallic alloy and in the oxide, respectively;

$T_{Cu}$ ,  $T_{Zn}$ ,  $T_{Al}$  are the transmission functions for elements Cu, Zn and Al, respectively;

$D_{Cu}^m, D_{Cu}^{ox}, D_{Zn}^m, D_{Zn}^{ox}, D_{Al}^m, D_{Al}^{ox}$  are the densities of element Cu in the metallic alloy and in the oxide, Zn in the metallic alloy and in the oxide and Al in the metallic alloy and in the oxide.

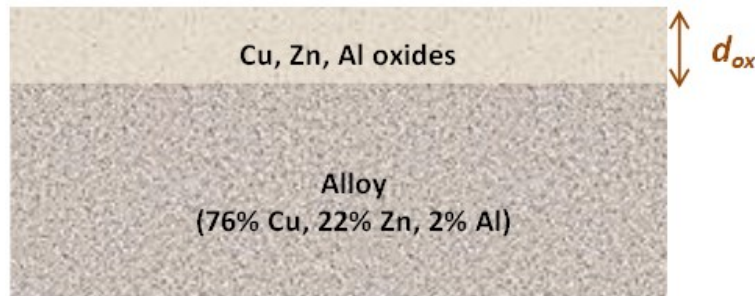


**Figure 6-18:** Layer model assumed for the analysis of XPS data (mixed oxide layer covering the metallic substrate).

Considering that:

$$D_{Cu}^m + D_{Zn}^m + D_{Al}^m = 1 \quad (6.7)$$

$$D_{Cu}^{ox} + D_{Zn}^{ox} + D_{Al}^{ox} = 1 \quad (6.8)$$

the concentrations of copper, zinc and aluminum in the oxide layer and beneath the oxide layer, as well as the oxide layer thickness can be calculated by solving the system of eight equations (Eqs. (6.1) to (6.8)) with eight unknowns ( $D_{Cu}^m, D_{Zn}^m, D_{Al}^m, D_{Cu}^{ox}, D_{Zn}^{ox}, D_{Al}^{ox}, d_{oxide}$  and  $k$ ).

The calculated values for the transmission function T are listed in Table 6-8.

**Table 6-8:** Transmission functions  $T(E_{kin})$  of the Escalab 250 energy analyzer, provided by Thermo Electron Corporation.

$T(E_{kin})$	Cu Auger line $L_3M_{45}M_{45}$	Cu $2p_{3/2}$	Zn $2p_{3/2}$	Zn Auger line $L_3M_{45}M_{45}$	Al $2p_{3/2}$
	3492	4265	4523	3372	2832

As mentioned in Chapter 2, the inelastic mean free path ( $\lambda$ ) values were taken from the QUASES-IMFP-TPP2M, a database for calculation of IMFPs by the TPP2M-formula, which is part of the QUASES-Tougaard method. For Cu, these values are listed in Table 4-2 and for Zn and Al they are presented in Table 6-9.

**Table 6-9:** Inelastic mean free paths  $\lambda$  in nm – Taken from the QUASES-IMFP-TPP2M.

$\lambda$ (nm)					
$\lambda_{Cu\ Auger}^{Albrass}$	$\lambda_{Cu\ Auger}^{ox}$	$\lambda_{Al}^{Albrass}$	$\lambda_{Al\ 2p_{3/2}}^{Al^{+2}}$	$\lambda_{Zn\ Auger}^{Albrass}$	$\lambda_{Zn\ Auger}^{ox}$
15.0	23.6	20.7	32.8	15.8	25.0

The photo-ionization cross-section  $\sigma_x$  at 1486.6 eV for Al  $2p_{3/2}$  is equal to 0.5371.

Although with the previous equations, it is possible to calculate the equivalent thickness and the composition of the oxide layer formed on the Al brass alloy, the decomposition of the Cu  $2p_{3/2}$  and Zn  $2p_{3/2}$  XPS peaks presents an important difficulty. The approach adopted for Cu and previously described in Chapter 4 was also applied for Zn. Thus, the Zn Auger line was used to obtain information about the relative contributions of ZnO and metallic Zn. For that purpose, the decomposition was performed with the software "CASA", using the reference spectra of ZnO and metallic Zn. The results provide the relative

proportions of these compounds at the alloy surface, considering that only these species are present. However, this is not fully correct, due to the fact that other Zn species may be part of the surface film, such as  $\text{Zn(OH)}_2$ ,  $3\text{Zn(OH)}_2 \cdot 2\text{ZnCO}_3$  or other Zn complexes, leading to an overestimation of the percentages of Zn in the Auger line ( $\text{L}_{3\text{M}_{45}\text{M}_{45}}$ ).

The decomposition of the Al  $2p_{3/2}$  peaks also presents an important difficulty. When using the standard aluminum X-ray anodes, the only aluminum photoelectric peaks available for measuring the amount of aluminum in the sample are Al 2s and Al 2p. Both aluminum peaks (Al 2s = 118 eV and Al 2p = 73 eV) appear at almost the same binding energies as the Cu 3s and Cu 3p peaks (Cu 3s = 123 eV; Cu  $3p_{1/2}$  = 77 eV and Cu  $3p_{3/2}$  = 75 eV).

**Table 6-10:** Binding energy and kinetic energy of Zn  $2p_{3/2}$  XPS peak and Auger line, respectively, for Zn species.

Compound	Zn $2p_{3/2}$	$\text{L}_{3\text{M}_{45}\text{M}_{45}}$ Zn Auger line
	binding energy / eV	kinetic energy / eV
Zn	$1022.0 \pm 0.1$	$991.9 \pm 0.1$
ZnO	$1021.5 \pm 0.1$	$988.6 \pm 0.1$
$\text{Zn(OH)}_2$	$1022.1 \pm 0.1$	$987.7 \pm 0.1$

For experiments performed with FNSW, the composition and the equivalent thickness of the oxide layer ( $d_{ox}$ ) formed in the presence of biomolecules were calculated from XPS data, using the system of equations previously presented (Eqs: (6.1) to (6.8)) and considering the intensities of copper, zinc and aluminum in the metallic substrate and in the mixed oxide layer formed on the alloy. In case of a continuous organic layer, each equation

(Eqs. (6.1) to (6.8)) is multiplied by a term:  $\exp\left(-\frac{d_{org}}{\lambda_{Cu,Zn,Al}^{org}}\right)$ . Figure 6-19 illustrates the

layer model used for the analysis of XPS data of a metallic material after immersion in a solution containing biomolecules that adsorb on the surface, forming a continuous organic film on top of the oxide layer, with an equivalent thickness  $d_{org}$ .

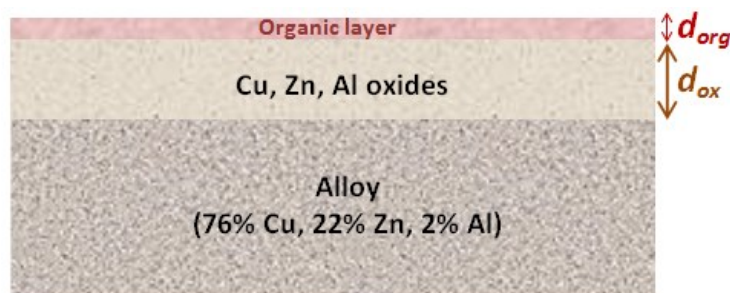


**Figure 6-19:** Layer model assumed for the analysis of XPS data (organic layer covering the mixed oxide layer formed on the metallic substrate).

The thickness  $d_{org}$  can be calculated from the  $\frac{I_N^{org}}{I_{Cu}^{Oxide}}$  intensity ratio, as previously explained in Chapter 4.

During the XPS measurements, the following core levels were recorded: Cu 2p (and Auger lines), Zn 2p (and Auger lines), Al 2p, O 1s, C 1s, and N 1s.

### 6.2.2.2 RESULTS

Figure 6-20(a) illustrates the Cu 2p<sub>3/2</sub> core level spectra for Al brass after polishing and after 1 h immersion at the corrosion potential, under flow and stirring conditions, in FNSW at pH 8.0, pH 6.0, and pH 3.7.

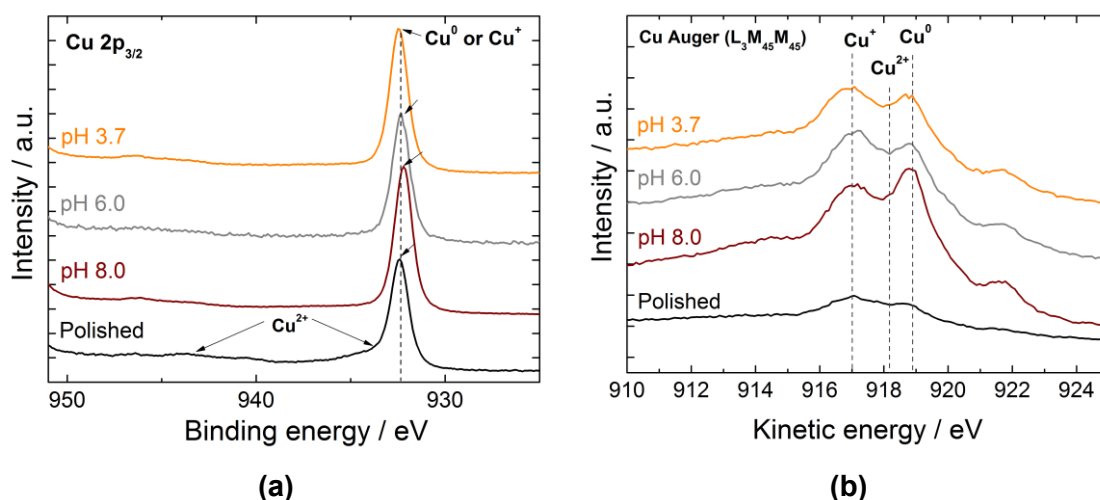


**Figure 6-20:** (a) X-ray photoelectron spectroscopy (XPS) Cu 2p<sub>3/2</sub> core level spectra, and (b) Cu L<sub>3</sub>M<sub>45</sub>M<sub>45</sub> Auger lines of Al brass after polishing and after 1 h of immersion at  $E_{corr}$  in aerated filtered natural seawater at pH 8.0, 6.0 and 3.7, under flow and stirring. The intensity is expressed in arbitrary unit (a.u.).

The XPS Cu  $2p_{3/2}$  core level peak with a binding energy located at 932.2 eV (pH 8.0) and 932.4 (pH 6.0 and 3.7) (Figure 6-20(a)) and the Cu Auger line ( $L_3M_{45}M_{45}$ ) at a kinetic energy of 918.8 eV (all pH values) (Figure 6-20(b)) demonstrate the presence of  $Cu^0$ , also observed for the sample after polishing and for 70Cu-30Ni alloy in the same conditions. A second peak is visible at 933.7 eV with a satellite at higher binding energy (943.2 eV) corresponding to  $Cu^{2+}$ , for the sample after polishing. However, this  $Cu^{2+}$  contribution is very low and can be neglected (Figure 6-20(a)).

The Cu Auger line ( $L_3M_{45}M_{45}$ ) located at a kinetic energy of 918.9 eV demonstrates the presence of  $Cu^0$  (Figure 6-20(b)). Thus, the oxide layer formed on top of the alloy is very thin and its thickness can be calculated from XPS data. However, for the four samples, the position of the Auger line ( $L_3M_{45}M_{45}$ ) at a kinetic energy of 916.7 eV, also indicates the presence of  $Cu^+$ .

The Zn  $2p_{3/2}$  core level spectra, obtained for Al brass at different pH values and presented in figure 6-21(a), exhibit one peak at 1022.0 eV for the polished sample, pH 6.0 and pH 3.7. A peak at 1021.3 eV is observed for pH 8.0. These peaks are attributed to  $Zn^0$  or  $Zn^{2+}$ . The Zn Auger line ( $L_3M_{45}M_{45}$ ) at a kinetic energy of 992 eV (all pH values) shows the presence of  $Zn^0$ , which confirms that the oxide film formed on the surface is very thin (Figure 6-21(b)). In XPS measurements, it is difficult to distinguish various chemical states of Zn-based materials by measuring  $2p_{3/2}$  line alone due to close binding energy values between  $Zn^{2+}$  and  $Zn^0$  states. However, the peaks visible in Figure 6-21(b), with corresponding Auger peak value of 987.6 eV ( $Zn(OH)_2$ ) and 988.5 eV (ZnO), strongly suggests the existence of ZnO and  $Zn(OH)_2$  for the samples after polishing and at the 3 pH values.

For Al XPS spectra (Figure 6-21(c)), only the peak located at ~73 eV was taken in to account for metallic Al in Al brass and that at 75.2 eV for Al in the oxide layer.

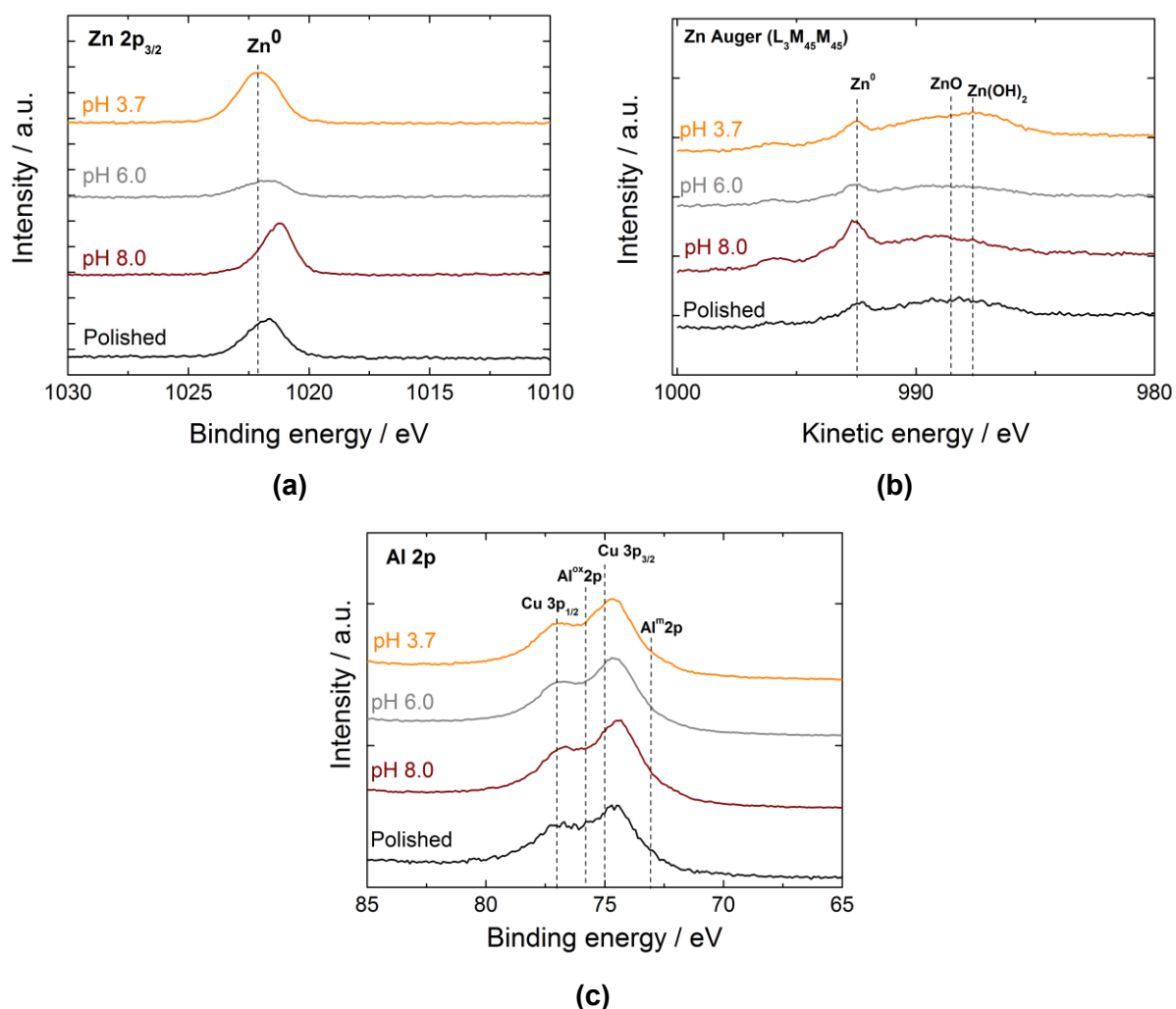


**Figure 6-21:** X-ray photoelectron spectroscopy (XPS): (a) Zn 2p<sub>3/2</sub>, (b) Zn L<sub>3</sub>M<sub>45</sub>M<sub>45</sub> Auger lines and (c) Al 2p core level spectra of Al brass after polishing and after 1 h of immersion at  $E_{corr}$  in aerated filtered natural seawater at pH 8.0, 6.0 and 3.7, under flow and stirring. The intensity is expressed in arbitrary unit (a.u.).

The N 1s spectrum recorded after immersion in FNSW under flow and stirring at different pH values (Figure 6-22(a)) exhibits a major symmetric peak, centered at 400.2 eV, thus, for the three different pH values, low amount of proteins are adsorbed. The C 1s signal obtained in the same conditions is shown in Figure 6-22(b). From the N 1s and C 1s signals, different “nitrogen/carbon” or “carbon/carbon” atomic ratios were calculated and the values obtained for the Al brass immersed in FNSW, under flow and stirring, at the three different pH values, are presented in Table 6-11.

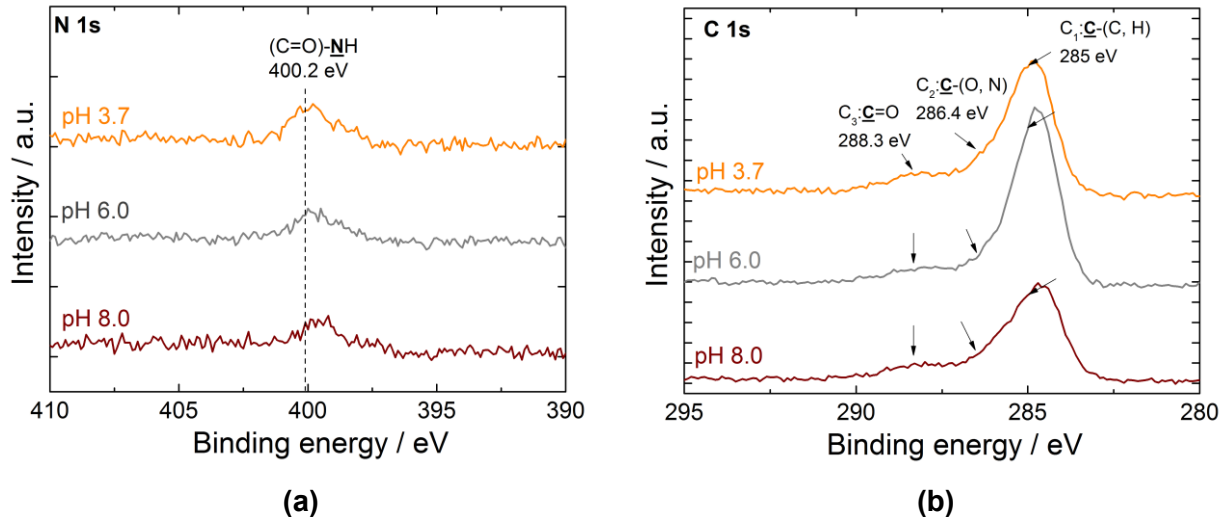


**Figure 6-22:** (a) N 1s core level spectra, and (b) C 1s core level spectra of Al brass after 1 h of immersion at  $E_{corr}$ , under flow and stirring, in aerated filtered natural seawater at pH 8.0, pH 6.0, and pH 3.7. The intensity is expressed in counts per second (CPS).

**Table 6-11:** Atomic ratios calculated from the XPS N 1s and C 1s core level spectra recorded for Al brass after 1 h of immersion at  $E_{corr}$ , under flow and stirring, in aerated filtered natural seawater at pH 8.0, pH 6.0, and pH 3.7.

	N/C <sub>total</sub> <sup>*</sup>	N/(C <sub>2</sub> +C <sub>3</sub> ) <sup>*</sup>	C <sub>1</sub> /C <sub>total</sub> <sup>*</sup>	C <sub>2</sub> /C <sub>total</sub> <sup>*</sup>	C <sub>3</sub> /C <sub>total</sub> <sup>*</sup>
pH 8.0	0.07	0.21	0.69	0.18	0.13
pH 6.0	0.03	0.16	0.79	0.12	0.08
pH 3.7	0.05	0.20	0.73	0.16	0.11

<sup>(a)</sup>The atomic ratio X/Y is given by:

$$X/Y = I_X \sigma_Y \lambda_Y^{BSA} T_Y / I_Y \sigma_X \lambda_X^{BSA} T_X$$

where  $I_{X,Y}$  is the intensity of the peak (peak surface area) associated to element X or Y (X and Y equal to N or C),  $\lambda_{X,Y}^{BSA}$  the attenuation length of photoelectrons emitted by the X or Y core level in the BSA layer,  $\sigma_{X,Y}$  the photoionisation cross-section of X or Y, and  $T_{X,Y}$  the transmission factor of X or Y. The C 1s signal is fitted with three contributions C<sub>1</sub>, C<sub>2</sub> and C<sub>3</sub>, corresponding to well identified carbon bonds present in the BSA molecule.

As for the 70Cu-30Ni alloy, the C<sub>1</sub>/C<sub>total</sub> ratio is very high at the 3 pH values, illustrating the high amount of hydrocarbons present on the surface. Moreover, the N/(C<sub>2</sub>+C<sub>3</sub>) ratio is low compared to the theoretical value of 0.5 corresponding to the peptidic link (HC-NH-(C=O)), showing that the amount of adsorbed proteins is low whatever the pH. Contrary to the conclusion drawn for 70Cu-30Ni, that amount of proteins is independent of the pH.

The atomic composition and the equivalent thickness of the oxide layers were calculated from XPS data, using the system of equations previously presented (Eqs. (6.1) to (6.8)) and considering the intensities of copper, zinc and aluminum in the metallic substrate and in the oxide layer formed on the alloy. These data are presented in Table 6-12.

**Table 6-12:** Atomic composition of the oxide layer and equivalent thickness of the surface layers calculated from XPS data for Al brass after 1 h of exposure at  $E_{corr}$  to FNSW at three different pH values (8.0, 6.0 and 3.7).

		pH			After polishing
		8.0	6.0	3.7	
Oxide layer (at. %)	$\text{Cu}^+$	35.1	84.0	57.6	78.0
	$\text{Zn}^{2+}$	6.4	6.4	13.1	11.8
	$\text{Al}^{3+}$	58.5	9.6	29.3	10.2
Surface layer thickness (nm)	Oxide layer	1.2	1.4	1.6	1.3
	Organic layer	0.1	0.1	0.1	-

These data indicate an enrichment in Al and a decrease of  $\text{Cu}^+$  concentration in the oxide layer for pH 8.0 and 3.7 compared to the sample after polishing. From these results, the oxide film is very thin and its thickness seems to be independent of the pH. This very low thickness would mean that the oxide layer is not continuous. An organic layer was also detected and its thickness is very low (1 Å) and is lower than for the 70Cu-30Ni/FNSW system.

A characteristic ToF-SIMS (negative ions) depth profile obtained with Al brass after polishing is presented in Figure 6-23(a). This profile allows evidencing a stratification of the different compounds on the alloy surface. It shows three regions. A first one that extends from 0 s to ~ 3 s of sputtering characterized by an increase of all signals and corresponding to the time necessary to reach a steady-state. After 3 s, one enters the second region that extends up to ~ 9 s of sputtering. In this region, the  $35\text{Cl}^-$ ,  $79^{64}\text{ZnO}_2^-$ ,  $58\text{AlO}_2^-$ ,  $95^{63}\text{CuO}_2^-$  and  $18^{18}\text{O}^-$  signals reach their maximum intensity. After 9 s of sputtering, all oxidized signals sharply decrease, whereas  $129\text{Zn}_2^-$  and  $125^{63}\text{Cu}_2^-$  reach a plateau. This indicates that a mixed Cu, Al and Zn outer oxide layer covers the metallic substrate (region 3) with a thickness of about ~ 2 nm. This result is in agreement with the thickness estimated by XPS (see Table 6-12). After closer examination of the oxide signals, one can observe that the  $95^{63}\text{CuO}_2^-$  signal reaches its maximum intensity before the  $79^{64}\text{ZnO}^-$  signal and the later

before the  $58\text{AlO}_2^-$  signal, indicating a stratification of the oxide with the following stack: an outer Cu oxide layer, a middle Zn oxide layer and an inner Al oxide layer.

A characteristic ToF-SIMS negative depth profile obtained with Al brass immersed during 1 h at  $E_{\text{corr}}$  in FNSW at pH 8.0 is presented in Figure 6-23(b). It shows three regions. A first one that extends from 0 s to  $\sim 3$  s of sputtering characterized by an increase of all signals and corresponding to the time necessary to reach a steady-state. After 3 s, one enters the second region that extends up to  $\sim 10$  s of sputtering. In this region the  $35\text{Cl}^-$ ,  $79^{64}\text{ZnO}^-$ ,  $58\text{AlO}_2^-$ ,  $95^{63}\text{CuO}_2^-$  and  $18^{18}\text{O}^-$  signals reach their maximum intensity. After  $\sim 10$  s of sputtering, similarly to the profile obtained after polishing, all the oxidized signals decrease, whereas  $129\text{Zn}_2^-$  and  $125^{63}\text{Cu}_2^-$  signals reach their maximum intensity, meaning that the metal/oxide interface is reached. Thus, a compact oxide layer covers the metallic surface with a thickness of about  $\sim 1$  nm. This result is in agreement with the thickness estimated by XPS (see Table 6-12). It can also be observed that the intensity of the  $26\text{CN}^-$  signal, characteristic of organic compounds, is maximal from the extreme surface, suggesting that the oxide scale is covered by an organic layer with a thickness of about  $\sim 0.5$  nm. This result is not in agreement with the thickness estimated by XPS, but the difference between ToF-SIMS and XPS values can be explained by the fact that the organic layer equivalent thickness was calculated from the N 1s XPS signal ( $\frac{I_N^{\text{org}}}{I_{\text{Cu}}^{\text{Oxide}}}$  ratio), whereas what is called “organic layer” is, in fact, the carbonaceous contamination layer. Again, after closer examination of the oxide scale, the stratification of the oxide is observed with a Cu oxide outer layer covering a Zn oxide middle layer and an Al oxide inner layer.

The same behavior is observed for the samples immersed in FNSW at pH 6.0 (Figure 6-23(c)) and pH 3.7 (Figure 6-23(d)). The thickness structure and composition of the oxide layer is unmodified whatever the pH, according to the ToF-SIMS profiles.

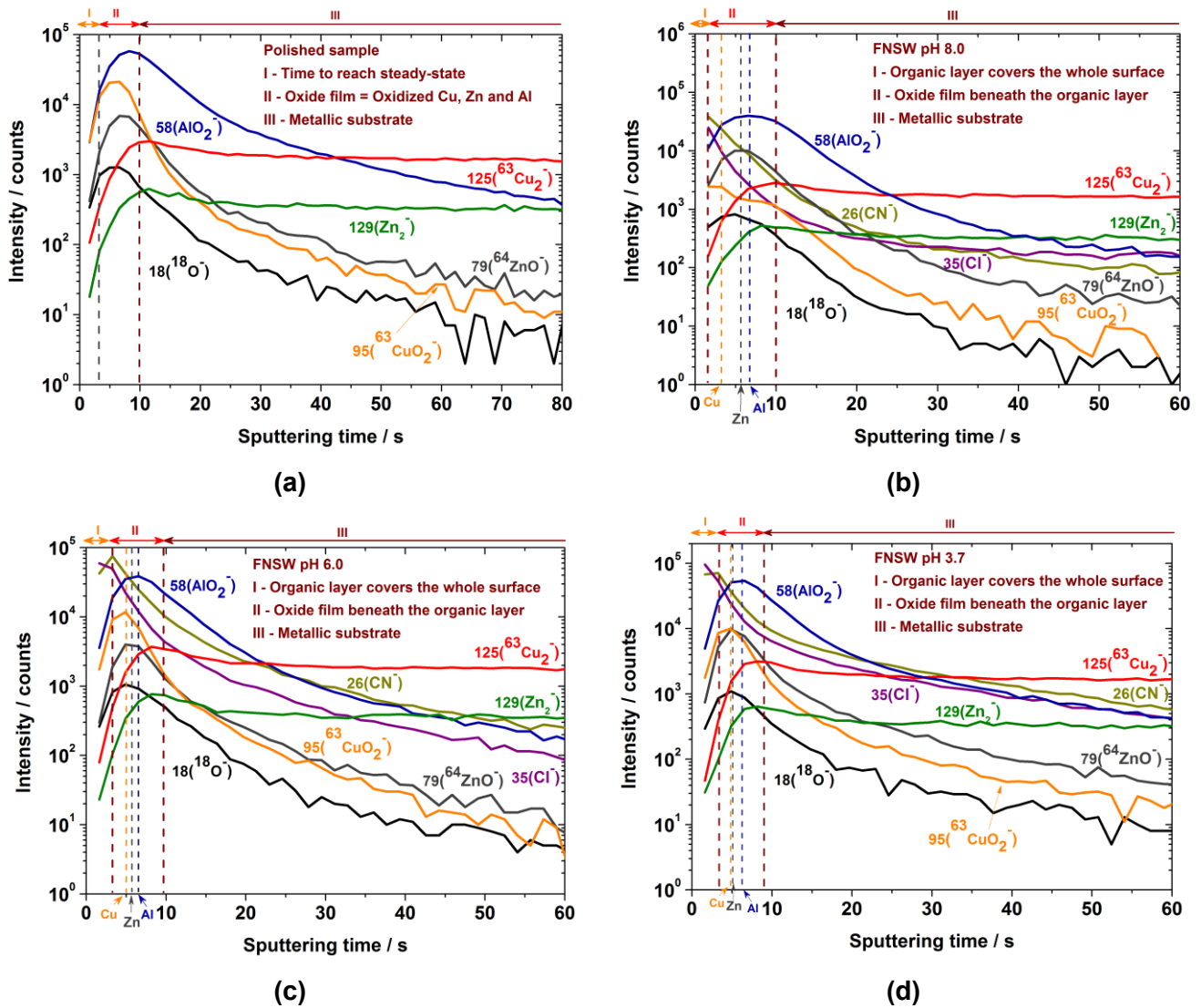


**Figure 6-23:** Characteristic time-of-flight secondary ions mass spectrometry (ToF-SIMS) negative ions depth profiles of Al brass after (a) polishing and after 1 h of immersion at  $E_{\text{corr}}$ , under flow and stirring, in aerated filtered natural seawater at (b) pH 8.0, (c) pH 6.0, and (d) pH 3.7.

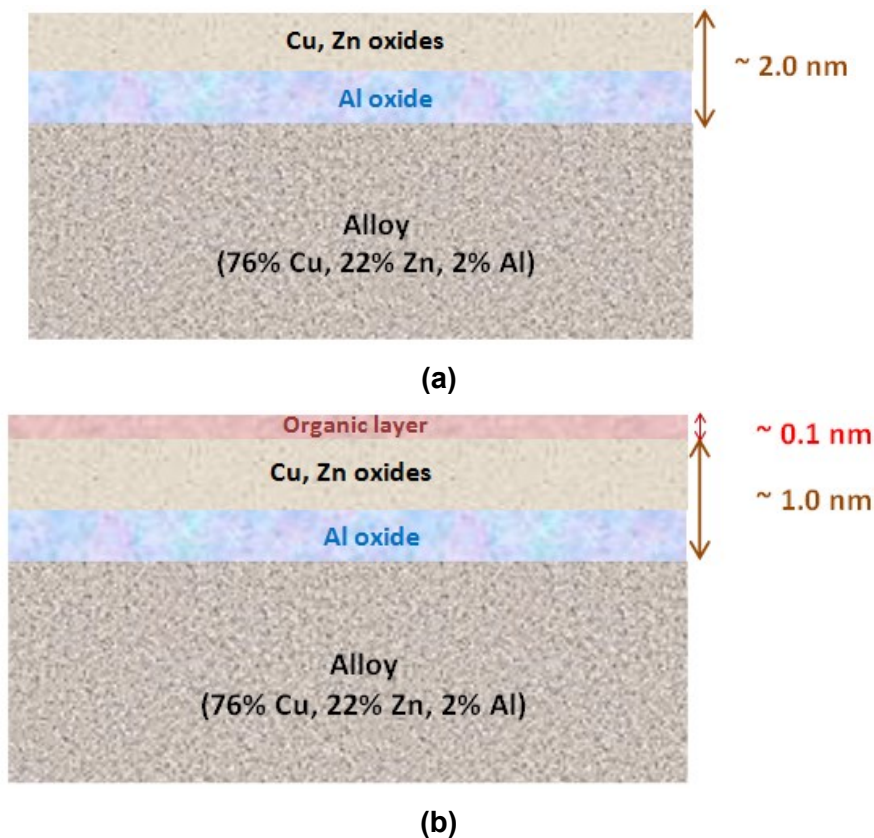
### 6.2.2.3 SURFACE LAYERS MODELS (COMBINED XPS AND TOF-SIMS)

Figure 6-24 illustrates the surface layer models deduced from the surface analysis of Al brass just after polishing and after 1 h of immersion at  $E_{\text{corr}}$  in FNSW at pH 8.0, 6.0 and 3.7.

For the sample after polishing (Figure 6-24(a)), one compact oxide layer, made up of Cu, Zn and Al oxides covers the whole surface. This oxide layer is stratified with a mixed Cu

and Zn oxide outer layer covering an Al oxide inner layer. The thickness of the oxide layer is  $\sim 2.0$  nm.

Figure 6-24(b)) presents the model for the surface layers formed on the samples after 1 h of exposure to FNSW at pH 8.0, 6.0 and 3.7. A compact mixed oxide layer, as the one observed for the sample after polishing (Figure 6-24(a)) is observed, but, in this case, the thickness is lower and is of  $\sim 1$  nm. The oxide scale is covered by a very thin organic layer ( $\sim 0.1$  nm).



**Figure 6-24:** Models of the surface layers deduced from combined X-ray photoelectron spectroscopy (XPS) and time-of-flight secondary ions mass spectrometry (ToF-SIMS) results for Al brass (a) after polishing and (b) after 1 h immersion at  $E_{corr}$ , under flow and stirring, in FNSW at pH 8.0, 6.0 and 3.7.

### 6.3 CONCLUSIONS

In this chapter, the corrosion behavior of 70Cu-30Ni and Al brass alloy was studied after short-term immersion in FNSW at different pH values (8.0, 6.0 and 3.7), by combined electrochemical measurements (in static conditions) and surface analysis (under flow and stirring).

From corrosion potential values and polarization curves recorded for both alloys in static conditions, there is no significant difference in electrochemical behavior with seawater pH change. Impedance data were fitted with the impedance model previously described for the 70Cu-30Ni/seawater system. The  $R_t^a$  values were used to calculate the corrosion current density  $i_{corr}$ , assuming Tafel kinetics for the anodic partial reaction. In the case of 70Cu-30Ni alloy, compared to the value obtained at pH 8.0,  $i_{corr}$  is similar at pH 3.7 and is  $\sim 100\%$  lower at pH 6.0. The rate constant of the anodic reaction is the highest at pH 8.0 and is similar at pH 6.0 and 3.7; in other words, the anodic reaction is slowed down at acidic pH (kinetic effect). In the case of Al brass,  $i_{corr}$  decreases with decreasing pH, i.e. there is a corrosion inhibition effect at acidic pH; moreover, the more acidic the pH, the slower the anodic reaction.

For 70Cu-30Ni, the surface analysis after 1 h of immersion in FNSW, under flow and stirring, at different pH values, shows the formation of a mixed oxide layer (oxidized copper and nickel) that presents a heterogeneous thickness (maximum thickness =  $\sim 1.5$  nm). An organic layer is detected on the surface and the equivalent thickness of the adsorbed layer is  $\sim 0.5$  nm. For the Al brass sample just after polishing, one compact oxide layer, made up of Cu, Zn and Al oxides covers the whole surface. This oxide layer is stratified with a mixed Cu and Zn oxide outer layer covering an Al oxide inner layer. The total thickness of the oxide layer is  $\sim 2.0$  nm. Independent of FNSW pH value, a compact mixed oxide layer, as the one observed for the sample after polishing is observed, but, in this case, the oxide thickness is lower ( $\sim 1$  nm). The oxide scale is covered by an organic layer with a thickness of about  $\sim 0.1$  nm.

In the case of 70Cu-30Ni alloy, the oxide layer thickness increases with decreasing pH, whereas for Al brass it is independent of the pH. The atomic composition of the oxide layers formed on 70Cu-30Ni samples shows a  $\text{Cu}^+$  content decrease and a  $\text{Ni}^{2+}$  content increase with decreasing pH. This Ni enrichment is due to an increased dissolution of Cu and passivating properties of Ni in acidic electrolytes. For Al brass samples, the composition at pH 6.0 is similar to that of the sample after polishing; at pH 8.0 and 3.7, an enrichment in Al and a decrease of  $\text{Cu}^+$  concentration compared to the sample after polishing can be observed.

For both Cu alloys, the amount of hydrocarbons present on the surface is high and that of adsorbed proteins, illustrated by the  $\text{N}/(\text{C}_2+\text{C}_3)$  atomic ratio, is low whatever the pH. In fact, what is called the “organic layer” is mainly the carbonaceous contamination layer. At pH 8.0, the  $\text{N}/(\text{C}_2+\text{C}_3)$  ratio is the same for both materials and is equal to  $\sim 0.2$ ; whereas, at acidic pH (6.0 and 3.7), the  $\text{N}/(\text{C}_2+\text{C}_3)$  ratio is about two times lower for 70Cu-30Ni ( $\sim 0.1$ ). Therefore, the chemical composition of the oxide layer seems to have an effect on the

amount of adsorbed proteins. The calculated organic layer equivalent thickness is very low (few Å for 70Cu-30Ni and 1 Å for Al brass); it seems to be higher at pH 8.0 than at acidic pH for 70Cu-30Ni alloy, whereas it is independent of pH for Al brass.

## GENERAL CONCLUSIONS

Power plants require cooling circuits with seawater or fresh water as the cooling agent. Tubes are the basic components of heat exchangers; they provide the heat transfer surface between one fluid (liquid or gas) flowing inside the tubes and other fluid (liquid or gas) flowing outside the tubes. In marine environments, copper and copper alloys are commonly used in condensers and heat exchangers due to their high thermal conductivity, and good mechanical workability. However, these materials may be affected by corrosion and biocorrosion induced by biofilm formation.

The main objectives of this work were to study firstly, the corrosion behavior of 70Cu-30Ni alloy and aluminum brass in seawater environments under real industrial conditions and secondly, the influence of different parameters such as solution (filtered natural seawater (FNSW) vs artificial seawater (ASW)), biomolecule (biomolecules naturally present in seawater vs a model protein, the bovine serum albumin (BSA)) concentration, hydrodynamics and pH on the electrochemical behavior and the surface chemical composition of these two copper alloys. The experimental work was divided into two parts: field experiments and laboratory experiments.

From field experiments, the relevant role of biofouling against the formation of protective oxide layers on the surface of copper alloys exposed to seawater, and the positive influence of chlorination treatments on the formation of these protective oxide layers are confirmed. For the 70Cu-30Ni alloy, when biofilm starts growing on new samples exposed to seawater, a quite constant and low value of the corrosion rate ( $V_{corr}$ ) can be observed with chlorination,; whereas, high values of the corrosion rate are recorded without chlorination. These corrosion rates monitored with the LPR probe are in agreement with weight loss measurements. The quite stable base line value of the BIOX signal confirms that chlorination treatments are enough to strictly control the biofilm growth. For aluminum brass, if increasing the concentration of ferrous ions in order to promote alloy passivity, the time necessary for reaching the passivity ( $V_{corr} < 20 \mu\text{m/y}$ ) is reduced to few weeks. For both alloys, microbiological and molecular analysis indicates what kinds of bacterial species can be found in biofilms formed on copper alloys exposed to seawater; these species are: *Marinobacter*, *Alteromonas* and *Pseudomonas*.

Controlling the adsorption of biomolecules, which is the first step in biofilm formation, by modifying the surface properties of the material may represent a good strategy for inhibiting microbial growth. Thus, the first part of the work performed in laboratory was focused on the influence of solution (FNSW vs ASW) and biomolecules (naturally present in

seawater vs BSA) concentration on the electrochemical behavior and the surface chemical composition of 70Cu-30Ni alloy in seawater, in static conditions. Surface analysis after 1 h of immersion in static ASW shows the formation of a thick duplex oxide layer ( $\sim 30$  nm), with an outer layer mainly composed of cuprous oxide ( $\text{Cu}_2\text{O}$ ) and an inner layer mainly composed of oxidized nickel. In ASW with BSA, the protein is detected on the surface and the equivalent thickness of the adsorbed layer is  $\sim 3$  nm, corresponding to one monolayer. The presence of BSA leads to a mixed oxide layer ( $\text{CuO}$ ,  $\text{Cu}_2\text{O}$ , and  $\text{Ni}(\text{OH})_2$ ) with a lower thickness ( $\sim 10$  nm). In static FNSW, the thick duplex oxide layer is also observed; nevertheless, the oxidized Cu/oxidized Ni ratio is lower than in static ASW. This cuprous oxide-rich outer layer evidenced in static conditions is formed by redeposition due to the saturation of the solution in copper ions. On the other hand, from the mechanism shown for pure copper dissolution in chloride media at low anodic potential and in order to take into account the presence of an oxide layer as shown by surface analysis, a modified mechanism is proposed for the anodic partial reaction of 70Cu-30Ni alloy at the corrosion potential ( $E_{\text{corr}}$ ) in seawater. An impedance model is proposed to analyze the impedance data obtained at  $E_{\text{corr}}$ . This model is deduced from a general model based on the experimental observation that the electrochemical behavior of the alloy is dominated by that of pure copper, and that both the anodic and the cathodic partial reactions are affected by mass transport. Pure mass transport limitation is considered for the cathodic partial reaction, and mixed kinetics for the anodic partial reaction. This impedance model shows that the HF loop of experimental impedance diagrams corresponds to the  $CPE_{dl}/R_t^a/W_c$  equivalent circuit, with  $CPE_{dl}$  the constant phase element related to the double layer,  $R_t^a$  the anodic charge transfer resistance and  $W_c$  the cathodic Warburg impedance. Therefore, the HF loop illustrates mainly the anodic charge transfer (diameter equal to  $R_t^a$ ), and its depressed shape is partly due to the CPE and partly due to the cathodic Warburg impedance in parallel. The LF loop of experimental diagrams is related to the anodic mass transport and partial blocking effect by adsorbed species, such as  $\text{CuCl}$ . Additionally, corrosion currents were calculated from  $R_t^a$  values and assuming Tafel kinetics for the anodic partial reaction. In static conditions, the corrosion current density  $i_{\text{corr}}$  of 70Cu-30Ni alloy is similar in ASW and in FNSW ( $i_{\text{corr}} \sim 10 \mu\text{A}\cdot\text{cm}^{-2}$ ). The BSA has a slight effect on the electrochemical behavior of 70Cu-30Ni alloy. Thus,  $E_{\text{corr}}$  value after 1 h of immersion is  $\sim 30$  mV more anodic with BSA, and EIS results indicate a small corrosion inhibition effect induced by the protein (decrease of the corrosion current density of  $\sim 20\%$ ).

As the water of cooling circuits is typically under flow and as the corrosion of copper in aerated solution is known to be controlled by mass transport processes to and from corroding surfaces, hydrodynamics is an important parameter to be studied. Therefore, the

corrosion behavior of 70Cu-30Ni alloy and aluminum brass after short-term immersion in ASW and/or FNSW was studied, by combined electrochemical measurements and surface analysis, for different hydrodynamic conditions: static conditions, under flow and stirring, and in well-controlled hydrodynamic conditions using a rotating ring electrode (RRE). Under flow and stirring, the thick duplex oxide layer previously detected with 70Cu-30Ni alloy in static ASW is no longer observed; a mixed Cu and Ni oxide layer is obtained, with a thickness similar to that for the sample just after polishing ( $\sim 1.5$  nm). From Levich and Koutecky-Levich curves plotted with the RRE, the oxygen diffusion coefficient in aerated FNSW can be calculated and is found to be equal to  $1.1 \times 10^{-5} \text{ cm}^2 \cdot \text{s}^{-1}$  (at room temperature). In static conditions, the experimental impedance diagrams of 70Cu-30Ni and Al brass immersed at the corrosion potential in seawater exhibit two capacitive loops (a HF depressed semi-circle, and a not well defined LF loop); the same impedance model, described above, can be used for the two copper alloys. Using the RRE, two capacitive loops can be observed for 70Cu-30Ni alloy, whereas one single capacitive loop is visible for Al brass. The impedance model for the Al brass RRE in FNSW is deduced from the same general model as for the 70Cu-30Ni/seawater system. At  $E_{\text{corr}}$ , the kinetic parameters of the cathodic partial reaction are different for the two alloys. In the case of the 70Cu-30Ni RRE, the cathodic polarization curves show pure mass transport limitation and the cathodic impedance is represented by a Warburg impedance; whereas in the case of the Al brass RRE, Tafel behavior is evidenced and the cathodic impedance which is very large can be neglected with respect to the anodic one. Moreover, for the Al brass RRE, the impedance in the anodic branch that illustrates mass transport and partial blocking effect can be approximated by an R//C circuit, as for pure copper in chloride media; thus, the single experimental loop illustrates both anodic charge transfer and anodic mass transport plus partial blocking effect. The anodic polarization curves and impedance diagrams show mixed kinetics for the anodic partial reaction, with major effect of mass transport for Al brass and minor effect of mass transport for 70Cu-30Ni (LF loop defined only by a few points). For both alloys, the anodic charge transfer resistance and hence the corrosion current are independent of the rotation speed of the RRE, due to compensated potential and mass transport effects.

Since the decrease of pH at the copper/solution interface might be the main factor controlling the biocorrosion of copper alloys, the corrosion behavior of 70Cu-30Ni and Al brass alloy was studied after short-term immersion in FNSW at different pH values (8.0, 6.0 and 3.7), by combined electrochemical measurements (in static conditions) and surface analysis (under flow and stirring). For 70Cu-30Ni, the surface analysis after 1 h of immersion in FNSW, under flow and stirring, at different pH values, shows the formation of a mixed oxide layer (oxidized copper and nickel) that presents a heterogeneous thickness (maximum

thickness =  $\sim 1.5$  nm). An organic layer is detected on the surface and the equivalent thickness of the adsorbed layer is  $\sim 0.5$  nm. For the Al brass sample just after polishing, one compact oxide layer, made up of Cu, Zn and Al oxides covers the whole surface. This oxide layer is stratified with a mixed Cu and Zn oxide outer layer covering an Al oxide inner layer. The total thickness of the oxide layer is  $\sim 2.0$  nm. Independent of FNSW pH value, a compact mixed oxide layer, as the one observed for the sample after polishing is observed, but, in this case, the oxide thickness is lower ( $\sim 1$  nm). The oxide scale is covered by an organic layer with a thickness of about  $\sim 0.1$  nm. In the case of 70Cu-30Ni alloy, the oxide layer thickness increases with decreasing pH, whereas for Al brass it is independent of the pH. The atomic composition of the oxide layers formed on 70Cu-30Ni samples shows a  $\text{Cu}^+$  content decrease and a  $\text{Ni}^{2+}$  content increase with decreasing pH. This Ni enrichment is due to an increased dissolution of Cu and passivating properties of Ni in acidic electrolytes. For Al brass samples, the composition at pH 6.0 is similar to that of the sample after polishing; at pH 8.0 and 3.7, an enrichment in Al and a decrease of  $\text{Cu}^+$  concentration compared to the sample after polishing can be observed. For both Cu alloys, the amount of hydrocarbons present on the surface is high and that of adsorbed proteins, illustrated by the  $\text{N}/(\text{C}_2+\text{C}_3)$  atomic ratio, is low whatever the pH. In fact, what is called the “organic layer” is mainly the carbonaceous contamination layer. At pH 8.0, the  $\text{N}/(\text{C}_2+\text{C}_3)$  ratio is the same for both materials and is equal to  $\sim 0.2$ ; whereas, at acidic pH (6.0 and 3.7), the  $\text{N}/(\text{C}_2+\text{C}_3)$  ratio is about two times lower for 70Cu-30Ni ( $\sim 0.1$ ). Therefore, the chemical composition of the oxide layer seems to have an effect on the amount of adsorbed proteins. The calculated organic layer equivalent thickness is very low (few Å for 70Cu-30Ni and 1 Å for Al brass); it seems to be higher at pH 8.0 than at acidic pH for 70Cu-30Ni alloy, whereas it is independent of pH for Al brass. From corrosion potential values and polarization curves recorded for both alloys in static conditions, there is no significant difference in electrochemical behavior with seawater pH change. Impedance data were fitted with the impedance model previously described for the 70Cu-30Ni/seawater system. The  $R_t^a$  values were used to calculate the corrosion current density  $i_{\text{corr}}$ , assuming Tafel kinetics for the anodic partial reaction. In the case of 70Cu-30Ni alloy, compared to the value obtained at pH 8.0,  $i_{\text{corr}}$  is similar at pH 3.7 and is  $\sim 100\%$  lower at pH 6.0. The rate constant of the anodic reaction is the highest at pH 8.0 and is similar at pH 6.0 and 3.7; in other words, the anodic reaction is slowed down at acidic pH (kinetic effect). In the case of Al brass,  $i_{\text{corr}}$  decreases with decreasing pH, i.e. there is a corrosion inhibition effect at acidic pH; moreover, the more acidic the pH, the slower the anodic reaction.

From field experiments, *Marinobacter*, *Alteromonas* and *Pseudomonas* bacterial species were found in biofilms formed on copper alloys exposed to seawater. Studying the

interactions of these species with copper alloys is necessary, in order to better understand the influence of cell adhesion and biofilm formation on the corrosion behavior of 70Cu-30Ni alloy and Al brass in seawater. Tightly bound (TB) and loosely bound (LB) extracellular polymeric substances (EPS), that play a fundamental role in the different stages of biofilm formation, maturation and maintenance, have already been extracted from *Pseudomonas NCIMB 2021* marine strain, and their effects on oxide layers developed on 70Cu-30Ni alloy in seawater environments have been evaluated [208]. The results show a slow-down of the anodic reaction in the presence of TB EPS and LB EPS, and a corrosion inhibition effect by LB EPS. No detrimental effect is evidenced with TB EPS.

In addition, laboratory experiments were performed after short-time immersion in seawater environments; future work must aim at testing both copper alloys during long-term exposure, in order to better approximate field conditions.

## REFERENCES

- [1] G. H. Koch, M. P. H. Brongers, N. G. Thompson, Y. Paul Virmani, J. H. Payer, Corrosion Costs and Preventive Strategies in the United States, Supplement to Materials Performance (2002) 4-9.
- [2] M. G. Fontana, N. D. Greene, Corrosion Forms, Corrosion Engineering, McGraw-Hill, New York (1967) 41 – 44.
- [3] N. W. Polan, Copper and Copper Alloy, ASM handbook - Corrosion, ASM International (1987) 610 – 616.
- [4] B. C. Syrett, O. Jonas, J. M. Mancini, Corrosion in the condensate-feedwater system, ASM Handbook 13C (2006) 447-460.
- [5] H. A. Jenner, J. W. Whitehouse, C. J. L. Taylor, M. Khalanski, Cooling water management in European power stations, biology and control of fouling, Hydroécologie Appliquée (1998) 1–225.
- [6] R. K. Shah, B. Thonon, D. M. Benforado, Opportunities for heat exchanger applications in environmental systems, Applied Thermal Engineering, 20 (2000) 631–650.
- [7] [http://media.johnwiley.com.au/product\\_data/excerpt/10/04713217/0471321710.pdf](http://media.johnwiley.com.au/product_data/excerpt/10/04713217/0471321710.pdf).
- [8] G. Bianchi, G. Fiori, P. Longhi, F. Mazza, Horse shoe - corrosion of copper alloys in flowing sea water: mechanism, and possibility of cathodic protection of condenser tubes in power stations, Corrosion 34 (1978) 396–406.
- [9] Seawater circuits treatments and materials, Chambre syndicale de la recherche et de la production du pétrole et du gaz naturel. Comité des techniciens, Editions Technip, Paris (1998).
- [10] H. Richaud-Minier, P. Gerard, H. Marchebois, Titanium and super stainless steel welded tubing solutions for seawater cooled heat exchangers, Materials Technology 24 (2009) 191-200.
- [11] B. Feng, J. Weng, B. C. Yang, J. Y. Chen, J. Z. Zhao, L. He, S. K. Qi, X. D. Zhang, Surface characterization of titanium and adsorption of bovine serum albumin, Materials Characterization 49 (2002) 129–137.
- [12] Y. Bao, W. Wang, B. He, M. Wang, Y. Yin, L. Liang, L. Xu, G. Xu, EIS analysis of hydrophobic and hydrophilic TiO<sub>2</sub> film, Electrochimica Acta 54 (2008) 611–615.
- [13] J. A. Mountford, Titanium-properties, advantages and applications solving the corrosion problems in marine service, NACE International (2002).
- [14] B. Little, P. Wagner, Microbiologically influenced corrosion of metals and alloys, International Materials Reviews 36 (1991) 253-272.
- [15] L. Lartundo-Rojas, Influence de l'adsorption de protéine (BSA) sur le comportement électrochimique et la composition de surface d'un alliage Fe-17Cr en solution aqueuse, University of Paris 6 (2007).
- [16] C. O. Olsson, D. Landolt, Passive films on stainless steels - chemistry, structure and growth, Electrochimica Acta 48 (2003) 1093–1104.
- [17] Č. Donik, A. Kocijan, J. T. Grant, M. Jenko, A. Drenik, B. Pihlar, XPS study of duplex stainless steel oxidized by oxygen atoms, Corrosion Science 51 (2009) 827–832.
- [18] D. Thierry, W. Sand, Microbially Influenced Corrosion, Corrosion Mechanisms in Theory and Practice (2011) 737–776.

- [19] C. A. Powell, H. T. Michels, Copper-Nickel alloys for seawater corrosion resistance and antifouling - A state of the art review, NACE Corrosion (2000).
- [20] H. H. Strehblow, V. Maurice, P. Marcus, Passivity of Metals, Corrosion Mechanisms in Theory and Practice (2011) 235–326.
- [21] A. M. Alfantazi, T. M. Ahmed, D. Tromans, Corrosion behavior of copper alloys in chloride media, Materials & Design 30 (2009) 2425–2430.
- [22] J. M. Cieslewicz, P.A. Schweitzer, Copper and Copper Alloys, Corrosion and Corrosion Protection Handbook (1989) 125 – 152.
- [23] H. Videla, Prevention and control of biocorrosion, International Biodeterioration & Biodegradation 49 (2002) 259–270.
- [24] T. Y. Soror, Scale and Corrosion Prevention in Cooling Water Systems - Part I: Calcium Carbonate, The Open Corrosion Journal 2 (2009) 45–50.
- [25] S. G. Choudhary, Emerging microbial control issues in cooling water systems, Hydrocarbon processing 77 (1998) 91–102.
- [26] G. J. Licina, MIC in the Power Industry, Microbiologically Influenced Corrosion, NACE International (1993).
- [27] P. Cristiani, U. Giancola, Prevention of fouling and microbial corrosion in power stations using seawater as a coolant, Heat Exchanger Fouling Mitigation and Cleaning Technologies, H. Muller-Steinhagen ed., Publico, Publ., Essen (D) (2000) 334-349.
- [28] Reference Document on the application of Best Available Techniques to Industrial Cooling Systems, European Commission, Integrated Pollution Prevention and Control (2001) [www.jrc.es](http://www.jrc.es).
- [29] P. Cristiani, Solutions To Fouling In Power Station Condensers, Applied Thermal Engineering Journal 25 (2005) 2630-2640.
- [30] B. Todd, J. Oldfield, Corrosion and Chlorination in Materials for Offshore Seawater Systems - Chlorination of Seawater Systems and its Effect on Corrosion, Society of Chemical Industry (1986).
- [31] C. A. Powell, Corrosion and biofouling resistance of copper-nickel in offshore and other marine applications, UK Corrosion & Eurocorr (1994).
- [32] G. A. Mansoori, Physicochemical Basis of Arterial Blockage Fouling - Prediction and Prevention, Journal of the Chinese Institute of Chemical Engineers 33 (2002) 25-31.
- [33] A. G. Howell, Xcel Energy Under Deposit Corrosion Mechanisms in Boilers, CORROSION (2006) 12-16.
- [34] <http://www.fresmetal.dk/uploads/media/pub-80-aluminium-bronze-corrosion-resistance.pdf>
- [35] R. A. Minear, G. L. Amy, Disinfection By-Products in Water Treatment, The Chemistry of their Formation and Control, Boca Raton (FL) US, Lewis Publishers (1995) 91-130.
- [36] R. L. Jolley, G. Jones, W. W. Pitt, J. E. Thompson, Chlorination of organics in cooling waters and process effluents, The environmental impact of water chlorination, Tennessee US, Oak Ridge National Laboratory (1976) 115-152.
- [37] ASCE/AWWA, Water treatment plant design 2nd ed., New York, McGraw-Hill (1990).
- [38] H. J. L. Jenner, C. Taylor, M. Van Donk, M. Khalanski, Chlorination by-products in chlorinated cooling water of some European coastal power stations, Marine Environmental Research 43 (1997) 279-293.

- [39] P. Cristiani, Electrochemical Technologies For Antifouling Treatments of Cooling Circuits, Chan J and Wong S, Biofouling, Types, Impact and Anti-Fouling, Nova Science Publishers (2010).
- [40] M. Khalanski, Organic products generated by the chlorination of cooling water at marine power stations, Journées d'Etudes du Cebedeau, Tribune de l'Eau (2002) 24–39, 619–621.
- [41] B. S. Syrett, Cost of Corrosion in the Electric Power Industry, EPRI Report 1004662 (2002).
- [42] P. Cristiani, G. Bianchi, ENEL Experience in microbial corrosion prevention, Aspects of microbially induced corrosion, The institute of materials - European Federation of Corrosion Publications 22 (1997).
- [43] M. Pourbaix, Establishment and Interpretation of Potential – pH Equilibrium Diagrams, Atlas of Electrochemical Equilibria in Aqueous Solutions, National Association of Corrosion Engineers, (1974) 384 – 392.
- [44] G. Bianchi, P. Longhi, Copper in Sea-Water, Potential-pH Diagrams, Corrosion Science 13 (1973) 853 – 864.
- [45] G. Kear, B. D. Barker, F. C. Walsh, Electrochemical corrosion of unalloyed copper in chloride media – a critical review, Corrosion Science 46 (2004) 109-135.
- [46] C. Deslouis, B. Tribollet, G. Mengoli, M. M. Musiani, Electrochemical behavior of copper in neutral aerated chloride solution. I Steady-state investigation, Journal of Applied Electrochemistry 18 (1988) 374-383.
- [47] G. Kear, C. P. Albarran, F. C. Walsh, Reduction of dissolved oxygen at a copper rotating-disc electrode, Chemical Engineering Education (2005) 14-21.
- [48] A. H. Tuthill, B. Todd, J. Oldfield, Experience With Copper Alloy Tubing Waterboxes and Piping in MSF Desalination Plants, Proceedings of world congress on desalination and water re-use (1997) 251-270.
- [49] H. P. Hack, H. Shih, H. W. Pickering, Role of the Corrosion Product Film in the Corrosion Protection of Cu-Ni Alloys in-Saltwater, Surfaces, Inhibition, and Passivation, E. McCafferty and J. Brodd, eds., Proceedings 86-7, The Electrochemical Society (1986).
- [50] H. P. Hack, Role of the Corrosion Product Film in the Corrosion Protection of Cu-Ni Alloys in Saltwater, Naval Surface Warfare Center (1987) DTNSRDC/SME-87-22.
- [51] M. S. Parvizi, A. Aladjem, J. E. Castle, Behavior of 90-10 Cupronickel in Seawater, International materials preview 33 (1988) 169-199.
- [52] The Application of Copper-Nickel Alloys in Marine Systems, CDA Inc. Seminar-Technical Report (1996) 7044-1919.
- [53] J. Castle, D. Epler., ESCA Investigation of Iron-Rich Protective Films on Aluminum Brass Condenser Tubes, Corrosion Science 16 (1976) 145-157.
- [54] R. Francis, Effects of Cooling Water Treatment on Ships, Condenser Tubes. BNF Research Report 1945 (1979).
- [55] C. Kato, B. G. Ateya, J. E. Castle, H. W. Pickering, On the mechanism of corrosion of Cu-9.4Ni-1.7Fe alloy in air saturated aqueous NaCl solution: I. Kinetic Investigations, Journal of the Electrochemical Society 127 (1980) 1890-1896.
- [56] C. Kato, J. E. Castle, B. G. Ateya, H. W. Pickering, On the Mechanism of Corrosion of Cu-9.4Ni-1.7Fe Alloy in Air Saturated Aqueous NaCl Solution: II . Composition of the Protective Surface Layer, Journal of the Electrochemical Society 127 (1980) 1897-1903.

- [57] Engineering Properties and Service Characteristics, ASM Specialty Handbook - Copper and Copper Alloys, ASM International (2001) 385 – 418.
- [58] F. King, Corrosion of copper in alkaline chloride environments, Swedish Nuclear Fuel and Waste Management Company Report (2002) TR-02-25.
- [59] J.L. Chen , Z. Li, Y.Y. Zhao, Corrosion characteristic of Ce Al brass in comparison with As Al brass, Materials and Design 30 (2009) 1743–1747.
- [60] A. U. Malik, P. C. M. Kuty, Corrosion and material selection in desalination plants, Proceeding of the seminar on operation and maintenance of desalination plant, Saline Water Conversion Corporation (1992) 274-307.
- [61] [http://www.copper.org/applications/marine/cuni/txt\\_MSF.html](http://www.copper.org/applications/marine/cuni/txt_MSF.html)
- [62] B. C. Syrett, D. D. Macdonald, S. Wing, Corrosion of copper nickel alloys in seawater polluted with sulphide and sulphide oxidation products, Corrosion 35 (1979) 409-22.
- [63] M. Valilappan, M. Natesan, G. Venkatachari, K. Balakrishnan, Effect of sulfide ions on the corrosion behavior of marine alloys in synthetic sea water, Bulletin of Electrochemistry 6 (1990) 213-214.
- [64] R. J. K. Woods, S. P. Hutton, Mass transfer effects of non-cavitating seawater on the corrosion of Cu and 70Cu-30Ni, Corrosion Science 30 (1990) 1177–1181, 1183–1201.
- [65] B. C. Syrett, The mechanism of accelerated corrosion of copper-nickel alloys in sulphide-polluted seawater, Corrosion Science 21 (1981) 187-209.
- [66] A. M. Beccaria, G. Poggi, P. Traverso, M. Ghiazza, A study of the de-alloying of 70Cu-30Ni commercial alloy in sulphide polluted and unpolluted sea water, Corrosion Science 32 (1991) 1263-1275.
- [67] L. E. Eiselstein, B. C. Syrett, S. S. Wing, R. D. Caligiuri, The accelerated corrosion of Cu-Ni alloys in sulphide-polluted seawater: Mechanism no. 2, Corrosion Science 23 (1983) 223–239.
- [68] B. C. Syrett, S. S. Wing, Effect of flow on corrosion of copper-nickel alloys in aerated seawater and in sulphide-polluted seawater, Corrosion 36 (1980) 73-85.
- [69] G. Bianchi, G. Fiori, P. Longhi, F. Mazza, Horse shoe corrosion of copper alloys in flowing sea water: mechanism, and possibility of cathodic protection of condenser tubes in power stations. Corrosion 34 (1978) 396–406.
- [70] C. Powell, Corrosion and Biofouling Resistance Evaluation of 90/10 Copper-Nickel, Eurocorr 2004, European Federation of Corrosion, Nice (2004).
- [71] Microbial Corrosion in Fossil-Fired Power Plants, EPRI CS-5495 final report (1987).
- [72] Microbial Corrosion: 1988 Workshop, EPRI ER-6345 proceedings of San Jose (CA)(1989).
- [73] G. G. Geesey, M. Mittelman, T. Iwaoka, P. R. Griffiths, Role of bacteria exopolymers in the determination of metallic copper surfaces, Materials Performance 2 (1986) 37-40.
- [74] R. Mitchell, Mechanisms of biofilm formation in seawater, Proceedings Ocean Thermal Energy Conversion, Biofouling and corrosion symposium (1977) 45-49.
- [75] A. K. Tiller, Metallic corrosion and microbes, Proceedings 2nd EFC Workshop on microbial corrosion, EFC Publication 8, The institute of materials (1992) 1-8.
- [76] A. Mollica, Biofilm and corrosion on active–passive alloys in seawater, International Biodeterioration and Biodegradation 29 (1992) 213.

- [77] P. Chandrasekaram, S. C. Dexter, Factor Contributing to Ennoblement of Passive Metals Due to Biofilm in Seawater, Proceedings 12th International Corrosion Congress, NACE 493 (1993) 3696-3707.
- [78] P. Angell, A. H. L. Chamberlain, The role of extracellular products in copper colonization, International Biodeterioration 27 (1991) 135–143.
- [79] P. Arens, G. J. Tuschewitzki, M. Wollmann, H. Follner, H. Jacobi, Indicators for microbiologically induced corrosion of copper pipes in a cold-water plumbing system, International Journal of Hygiene and Environmental Medicine 196 (1995) 444–454.
- [80] B. J. Webster, D. B. Wells, P. J. Bremer, The influence of potable water on copper corrosion, Proceedings of NACE Corrosion 294 (1996) 1–13.
- [81] M. M. Critchley, H. J. Fallowfield, The effect of distribution system bacterial biofilms on copper concentrations in drinking water, Water Science and Technology: Water Supply 1 (2001), 247–252.
- [82] G. Muyzer, T. Brinkhoff, U. Nubel, C. Santegoeds, H. Schafer, C. Wawer, Denaturing gradient gel electrophoresis (DGGE) in microbial ecology, Molecular Microbial Ecology Manual (1998) 1-27.
- [83] D. J. Schiffrin, S. R. De Sanchez, The Effect of Pollutants and Bacterial Microfouling on the Corrosion of Copper Base Alloys in Seawater, Corrosion 41 (1985) 31-38.
- [84] S. J. Yuan, A. M. F. Choong, S. O. Pehkonen, The influence of marine aerobic *Pseudomonas* strain on the corrosion of 70/30 Cu-Ni alloy, Corrosion Science 49 (2007) 4352-4385.
- [85] R. Konečná, S. Fintová, Copper and copper alloys: casting, classification and characteristic microstructures, [http://cdn.intechopen.com/pdfs/30472/InTech-Copper\\_and\\_copper\\_alloys\\_casting\\_classification\\_and\\_characteristic\\_microstructures.pdf](http://cdn.intechopen.com/pdfs/30472/InTech-Copper_and_copper_alloys_casting_classification_and_characteristic_microstructures.pdf), accessed online on April 2014.
- [86] V. Calcut, Copper alloys in marine environments, Metallurgia 55 (1988) 38-40.
- [87] U. R. Evans, The corrosion and oxidation of metals, scientific principals and practical applications, C. Arnold, London (1960) 585.
- [88] A. M. Shams El Din, Copper Alloys for Desalination Plants, Desalination 93 (1993) 499-516.
- [89] G. L. Bailey, Copper-Nickel-Iron Alloys Resistance to Seawater Corrosion, Journal of the Institute of Metals 79 (1951) 243-292.
- [90] P.T. Gilbert, A Review of Recent Work on Corrosion Behavior of Copper Alloys in Seawater, Materials Performance 21 (1982) 47-53.
- [91] G. Kear, F. C. Walsh, D. B. Barker, K. S. Stokes, Electrochemical corrosion characteristics of copper in filtered and artificial seawater as a function of mass transfer conditions, EuroCorr 2000, Institute of Corrosion, Leighton Buzzard, UK (2000).
- [92] K. C. Bendall, A Longer Life in the Ocean Waves, Materials world 5 (1997) 711-713.
- [93] K. D. Efird, The Synergistic Effect of Ni and Fe on the Seawater Corrosion of Copper Alloys, Corrosion 33 (1977) 347-350.
- [94] G. Faita, G. Fiori, D. Salvatore, Copper behaviour in acid and alkaline brines - I Kinetics of anodic dissolution in 0.5M NaCl and free-corrosion rates in the presence of oxygen, Corrosion Science 15 (1975) 383–392.
- [95] J. M. Popplewell, R. J. Hart, J. A. Ford, The effect of iron on the corrosion characteristics of 90-10 cupro nickel in quiescent 3.4%NaCl solution, Corrosion Science 13 (1973) 295–298.

- [96] R. W. Ross, David B. Anderson, Hot Seawater Corrosion of Copper-Base Alloys, *Materials Performance* 14 (1975) 27-32.
- [97] F. P. Ijsseling, L. J. P. Drolenga, B. H. Kolster, Influence of Temperature on Corrosion Product Film Formation on CuNi 1 OFe in the Low Temperature Range. 1. Corrosion rate as a function of temperature in well aerated sea water, *British Corrosion Journal* 17 (1982) 162-167.
- [98] Y. Feng, K. S. Siow, W. K. Teo, K. L. Tan, A. K. Hsieh, Corrosion Mechanisms and Products of Copper in Aqueous Solutions at Various pH Values, *Corrosion* 53 (1997) 389-398.
- [99] P. Cristiani, F. Mazza, G. Rocchini, Influence of metal-biofilm interface pH on aluminum brass corrosion in seawater, *Proceedings of the 3rd international EFC workshop* 15 (1995) 243-260.
- [100] L. Knutsson, E. Mattsson, B. E. Ramberg, Erosion-corrosion in copper water tubing, *British Corrosion Journal* 7 (1972) 208.
- [101] B. C. Syrett, Erosion-Corrosion of Copper-Nickel Alloys in Seawater and Other Aqueous Environments -A Literature Review, *Corrosion* 32 (1976) 242-252.
- [102] D. C. Vreeland, Review of Corrosion Experience With Copper-Nickel Alloys in Seawater Piping Systems, *Materials Performance* 15 (1976) 38-41.
- [103] J. P. Gudas, H. P. Hack, Sulphide induced corrosion of copper nickel alloys', *Corrosion* 35 (1979) 67-73.
- [104] J. N. Alhajji, M. R. Reda, The Conflicting Roles of Complexing Agents on the Corrosion of Copper-Nickel Alloys in Sulphide Polluted Seawater, *Journal Electrochemical Society* 141 (1994) 1432-1438.
- [105] D. B. Anderson, F. A. Badia, Chromium modified copper-nickel alloys for improved seawater impingement resistance, *Journal of Engineering for Power* 95 (1973) 132- 135.
- [106] L. Giuliani, A. Tamba, C. Modena, Electrochemical Characterization of Some Cu Alloys in NaCl Solutions, *Corrosion Science* 11 (1971) 485 – 498.
- [107] K. D. Efird, Effect of Fluid Dynamics on the Corrosion of Copper-Base Alloys in Seawater, *Corrosion* 33 (1977) 3-8.
- [108] S. Sato, K. Nagata, Factors Affecting Corrosion and Fouling of Metal Condenser Tubes of Copper Alloys and Titanium, Sumitomo light metal technical reports 19 (1978) 83.
- [109] T. W. Bostwick, Reducing Corrosion of Power Plant Condenser Tubing with Ferrous Sulfate, *Corrosion* 17 (1961) 12-15.
- [110] P. T. Gilbert, Use of Ferrous Sulphate Treatment For Combating Condenser Tube Corrosion, *Supplement to Chemistry and Industry* (1977).
- [111] R. F. North, M. J. Pryor, The protection of Cu by ferrous sulphate additions, *Corrosion Science* 8 (1968) 149-157.
- [112] D. B. Anderson, B. R. Richards, Chlorination of Seawater - effects on Fouling and Corrosion', *Journal of Engineering for Gas Turbines and Power* 88 (1966) 203-208.
- [113] P. A. Klein, R. A. Hays, R. J. Ferrara, The Effect of Electrolytic Chlorination on the Crevice Corrosion Behavior of 70/30 Copper-Nickel and 102 Nickel-Copper Alloy 400, *Proceedings Corrosion/91* (1991) 509-15.
- [114] E. Heitz, Chemo-Mechanical Effects of Flow on Corrosion, *Corrosion* 47 (1991) 135-145.

- [115] K. C. Goretta, R. C. Arroyo, C. T. Wu, J. L. Routbort, Erosion of Work-Hardened Copper, Nickel and 304 Stainless Steel, *Wear* 147 (1991) 145-154.
- [116] B. Little, J. Jacobus, L. Janus, Evaluation of Microbiologically Induced corrosion in an estuary, *Estuaries* 12 (1989) 138-141.
- [117] E. M. Pinto, D. M. Soares, C. M. A. Brett, Interaction of BSA protein with copper evaluated by electrochemical impedance spectroscopy and quartz crystal microbalance, *Electrochimica Acta* 53 (2008) 7460-7466.
- [118] C. W. Svare, G. Belton, E. Korostoff, The role of organics in metallic passivation, *Journal of Biomedical Materials Research* 4 (1970) 457-467.
- [119] G. C. F. Clark, D. F. Williams, The effects of proteins on metallic corrosion, *Journal of Biomedical Materials Research* 16 (1982) 125-134.
- [120] P. Cristiani, G. Perboni, Monitoring of the negative influence of biofilm and the positive effect of chlorination on surface passivation of CuNi70/30 condenser tubes, *Proceedings of Eurocorr 2009, Nice* (2009) 6-10.
- [121] C. Gabrielli, Identification of electrochemical processes by frequency response analysis, Solartron (1998), technical report number 004/83.
- [122] M. Stern, A.L. Geary, Electrochemical polarization curves, *Journal of the Electrochemical Society* 104 (1957) 56.
- [123] G. Rastogi, R. K. Sani, Molecular Techniques to Assess Microbial Community Structure, Function and Dynamics in the Environment, *Microbes and Microbial Technology* (2011) 29-57.
- [124] P. Hugenholtz, Exploring prokaryotic diversity in the genomic era, *Genome Biology* 3 (2002).
- [125] G. Muyzer, Genetic fingerprinting of microbial communities – present status and future perspectives, *Methods of microbial community analysis, Proceedings of the 8th international symposium on microbial Ecology, Atlantic Canada Society for Microbial Ecology, Halifax, Canada* (1999).
- [126] G. Muyzer, E.C.D. Waal, A.G. Uitterlinden, Profiling of complex microbial populations by denaturing gradient gel electrophoresis analysis of polymerase chain reaction-amplified genes coding for 16S rRNA. *Applied Environmental Microbiology* 53 (1993) 695-700.
- [127] F. B. Mansfeld, G. Liu, H. Xiao, C. H. Tsai, B. J. Little, The corrosion behavior of copper alloys, stainless steels and titanium in seawater, *Corrosion Science* 36 (1994) 2063-2095.
- [128] J.P. Diard, B. Le Gorrec, C. Montella, *Cinétique électrochimique*, Hermann (1996).
- [129] O. Reynolds, An experimental investigation of the circumstances which determine whether the motion of water shall be direct or sinuous, and of the law of resistance in parallel channels, *Philosophical Transactions of the Royal Society* 174 (1883) 935-982.
- [130] M. Potter, D.C. Wiggert, *Fluid Mechanics, Schaum's Series* (2008).
- [131] C. Deslouis, M. Keddam, Emploi d'électrodes a anneau tournant a l'étude du transport de matiere dans un fluide en regime hydrodynamique laminaire ou turbulent, *International Journal of Heat Mass Transfer* 16 (1973) 1763-1775.
- [132] V. G. Levich, *Physicochemical Hydrodynamics*, Prentice-Hall, Englewood Cliffs, NJ (1962) 72.
- [133] B. Robertson, B. Tribollet, C. Deslouis, Measurement of diffusion-coefficients by DC and EHD electrochemical methods, *Journal of the Electrochemical Society* 135 (1988) 2279-2284.

- [134] J. R. MacDonald, *Impedance Spectroscopy: Emphasizing Solid Materials and Systems*, John Wiley & Sons, New York (1987).
- [135] A. Lasia, R. E. White, B. E. Conway, *Modern Aspects of Electrochemistry*, J. O. M. Bockris (Eds.), Plenum Press, New York, 32 (1999) 143.
- [136] M.E. Orazem and B. Tribollet, *Electrochemical Impedance Spectroscopy*, The Electrochemical Society Series, John Wiley & Sons, Inc., Hoboken, NJ, 2008.
- [137] V. M. W. Huang, V. Vivier, M. E. Orazem, N. Pébère, B. Tribollet, The apparent constant-phase-element behavior of an ideally polarized blocking electrode: a global and local impedance analysis, *Journal of the Electrochemical Society* 154 (2007) 81-88.
- [138] G. J. Brug, A. L. G. van den Eeden, M. Sluyters-Rehbach, J. H. Sluyters, The analysis of electrode impedances complicated by the presence of a constant phase element, *Journal of Electroanalytical Chemistry and Interfacial Electrochemistry* 176 (1984) 275–295.
- [139] B. Hirschorn, M. E. Orazem, B. Tribollet, V. Vivier, I. Frateur, M. Musiani, Determination of effective capacitance and film thickness from constant-phase-element parameters, *Electrochimica Acta* 55 (2010) 6218–6227.
- [140] M. E. Orazem, N. Pébère, B. Tribollet, Enhanced graphical representation of electrochemical impedance data, *Journal Electrochemical Society* 153 (2006) 129–B136.
- [141] *Practical Surface Analysis: Volume 1 – Auger and X-ray Photoelectron Spectroscopy* (2nd edn.), D. Briggs and M. P. Seah (eds), John Wiley & Sons Ltd (1990).
- [142] M. Genet, C. C. Dupont-Gillain, P. Rouxhet, *XPS analysis of biosystems and biomaterials, Medical Applications of Colloids*, E. Matijevic, Ed. Springer, New York (2008) 177–307.
- [143] A. J. Wikiel, *Role of extracellular polymeric substances on biocorrosion initiation or inhibition*, Universität Duisburg-Essen, PhD thesis (2013).
- [144] S. Brunner, *Surface analytical and electrochemical characterization of biomaterial surfaces*, Friedrich-Alexander University (2006).
- [145] I. Frateur, J. Lecoœur, S. Zanna, C. O. A. Olsson, D. Landolt, P. Marcus, Adsorption of BSA on passivated chromium studied by a flow-cell EQCM and XPS, *Electrochimica Acta* 52 (2007) 7660-7669.
- [146] Ithurbide, I. Frateur, A. Galtayries, P. Marcus, XPS and flow-cell EQCM study of albumin adsorption on passivated chromium surfaces: Influence of potential and pH, *Electrochimica Acta* 53 (2007) 1336–1345.
- [147] A. M. Belu, D. J. Graham, D. G. Castner, Time-of-flight secondary ion mass spectrometry: techniques and applications for the characterization of biomaterial surfaces, *Biomaterials* 24 (2003) 3635–3653.
- [148] V. Payet, S. Brunner, A. Galtayries, I. Frateur, P. Marcus, Cleaning of albumin-contaminated Ti and Cr surfaces: an XPS and QCM study, *Surface and Interface Analysis* 40 (2008) 215–219.
- [149] Y. C. Ee, Z. Chen, S.B. Law, S. Xud, N.L. Yakovlev, M.Y. Lai, Copper diffusion in Ti–Si–N layers formed by inductively coupled plasma implantation, *Applied Surface Science* 253 (2006) 530–534.
- [150] S. Hofmann, Ultimate Depth Resolution and Profile Reconstruction in Sputter Profiling with AES and SIMS, *Surface and Interface Analysis* 30 (2000) 228-233.
- [151] S. Hofmann, Sputter depth profile analysis of interfaces, *Reports on Progress in Physics* 61 (1998) 827.

- [152] P. Cristiani, G. Perboni, A. Debenedetti, Effect of chlorination on the corrosion of Cu/Ni 70/30 condenser tubing, *Electrochimica Acta* 54 (2008) 100–107.
- [153] T. J. Marchesani, J.A. Ellor, G. A. Gehring Jr, Effect of Target Chlorination on the Corrosion Behavior of Copper-Nichel Condenser Tubing, EPRI TR-101405, Ocean City Research Corporation, Final Report (1992).
- [154] R. J. Ferrara, E. Taschenberg, P. J. Moran, The effect of chlorinated seawater on galvanic corrosion behavior of alloys used in seawater piping systems, *CORROSION85*, Boston, MA, Paper 211 (1985).
- [155] A. Mollica, Biofilm and corrosion on active-passive alloys in seawater, *International Biodeterioration and Biodegradation Journal* 29 (1992) 213-229.
- [156] A. Mollica, P. Cristiani, On-line biofilm monitoring by “BIOX” electrochemical probe, *Water Science and Technology* 47 (2003) 45–49.
- [157] R. M. Park, A guide to understanding reference electrode readings, *Materials Performance* 48 (2009) 32-36.
- [158] P. Cristiani, Corrosion monitoring in microbial environments in: *Techniques for corrosion monitoring*, L. Yang (Ed.), Woodhead publishing limited, Cambridge (2008) 347-387.
- [159] G. Pavanello, M. Faimali, M. Pittore, A. Mollica, A. Mollica, A. Mollica, Exploiting a new electrochemical sensor for biofilm monitoring and water treatment optimization, *Water Research* 45 (2011) 1651–1658.
- [160] C. Barry, J. Syrett, J. M. Mancini, *Corrosion: Environments and Industries*, ASM Handbook Volume 13 (2006) 447-460.
- [161] K. Abouswa, F. Elshawesh, O. Elragei, A. Elhood, , Corrosion investigation of Cu–Ni tube desalination plant, *Desalination* 205 (2007) 140–146.
- [162] J. N. Wardell, A. L. Chamberlain, *Microbial Corrosion Proceedings of the 3rd EFC Workshop*, EFC Publication, The Institute of Materials 15 (1995) 49.
- [163] A. K. Tiller, *Microbial Corrosion Proceedings of the 2nd EFC Workshop*, EFC Publication, The Institute of Materials 8 (1992) 1.
- [164] H.C. Flemming, J. Wingender, The biofilm matrix *Nature Reviews Microbiology* 8 (2010) 623-633.
- [165] E. Singer, E. A. Webb, W. C. Nelson, J. F. Heidelberg, N. Ivanova, A. Pati, K. J. Edwards, Genomic Potential of *Marinobacter aquaeolei*, a Biogeochemical “Opportunitroph”, *Applied Environmental Microbiology* 1 (2011) 2763–2771.
- [166] M. Loaëc, R. Olier, J. Guezennec, Chelating properties of bacterial exopolysaccharides from deep-sea hydrothermal vents, *Carbohydrate Polymers* 35 (1998) 65–70.
- [167] L. Bozzi, M. Milas, M. Rinaudo, Characterization and solution properties of a new exopolysaccharide excreted by the bacterium *Alteromonas* sp. strain 1644, *International Journal of Biological Macromolecules* 18 (1996) 9-17.
- [168] G. Raguenees, P. Pignet, G. Gauthier, A. Peres, R. Christen, H. Rougeaux, G. Barbier, J. Guezennec, Description of a new polymer-secreting bacterium from a deep-sea hydrothermal vent, *Alteromonas macleodii* subsp. *fijiensis*, and preliminary characterization of the polymer, *Applied Environmental Microbiology* 62 (1996) 67-73.
- [169] H. Rougeaux, P. Talaga, R. W. Carlson, J. Guezennec, Structural studies of an exopolysaccharide produced by *Alteromonas macleodii* subsp. *fijiensis* originating from a deep-sea hydrothermal vent, *Carbohydrate Research* 312 (1998) 53-9.

- [170] G. G. Geesey, L. Jang, J. G. Jolley, M. R. Hankins, T. Iwaoka, P. R. Griffiths, Binding of metal ions by extracellular polymers of biofilm bacteria, *Water and Wastewater Microbiology*, D. Jenkins and B. H. Olson eds. 20 (1988) 161-165.
- [171] P. V. Bhaskar, N. B. Bhosle, Bacterial extracellular polymeric substance (EPS): a carrier of heavy metals in the marine food-chain, *Environment International* 32 (2006) 191-198.
- [172] M. Loaëc, R. Olier, J. Guezennec, Uptake of lead, cadmium and zinc by a novel bacterial exopolysaccharide, *Water Research* 31 (1997) 1171-1179.
- [173] T. Peters, Serum albumin, *Advances in Protein Chemistry* 37 (1985) 161-245.
- [174] D. C. Carter, J. X. Ho, Structure of serum albumin, *Advances in Protein Chemistry* 45 (1994) 153-205.
- [175] I. Frateur, Incidence de la corrosion des matériaux ferreux sur la demande en chlore libre en réseaux de distribution d'eau potable, Université Pierre et Marie Curie, Paris 6 (1997).
- [176] C. D. Wagner, W. M. Riggs, L. E. Davis, J. F. Moulder, *Handbook of X-ray Photoelectron Spectroscopy*, Perkin-Elmer Corporation (1979) 192.
- [177] S. K. Chawla, N. Sankarraman, J. H. Payer, Diagnostic spectra for XPS analysis of Cu-O-S-H compounds, *Journal of Electron Spectroscopy and Related Phenomena* 61 (1992) 1-18.
- [178] M. C. Biesinger, L. W. M. Lau, A. R. Gerson, R. S. C. Smart, Resolving surface chemical states in {XPS} analysis of first row transition metals, oxides and hydroxides: Sc, Ti, V, Cu and Zn, *Applied Surface Science* 257 (2010) 887-898.
- [179] G. Deroubaix, P. Marcus, X-ray photoelectron spectroscopy analysis of copper and zinc oxides and sulphides, *Surface and Interface Analysis* 18 (1992) 39-46.
- [180] Y. Z. Wang, A. M. Beccaria, G. Poggi, The effect of temperature on the corrosion behaviour of a 70/30 Cu-Ni commercial alloy in seawater, *Corrosion Science* 36 (1994) 1277-1288.
- [181] A. Galtayries, J. Grimblot, J.P. Bonnelle, Interaction of SO<sub>2</sub> with different polycrystalline Cu, Cu<sub>2</sub>O and CuO surfaces, *Surface and Interface Analysis* 24 (1996) 345-354.
- [182] A. Galtayries, J. P. Bonnelle, XPS and ISS studies on the interaction of H<sub>2</sub>S with polycrystalline Cu, Cu<sub>2</sub>O and CuO surfaces, *Surface and Interface Analysis* 23 (1995) 171-179.
- [183] H. Ayoub, V. Lair, S. Griveau, A. Galtayries, P. Brunswick, F. Bedioui, M. Cassir, Ageing of nickel used as sensitive material for early detection of sudomotor dysfunction, *Applied Surface Science* 258 (2012) 2724-2731.
- [184] Y. F. Dufrêne, T. G. Marchal, P. G. Rouxhet, Probing the organization of adsorbed protein layers: complementary of atomic force microscopy, X-ray photoelectron spectroscopy and radiolabeling, *Applied Surface Science* 144-145 (1999) 638-643.
- [185] R. Souchet, F. Danoix, A. D'huysser, M. Lenglet, APFIM and XPS study of the first stages of low temperature air oxidation of industrial CuNi alloys, *Applied Surface Science* 87-88 (1995) 271-278.
- [186] R. Souchet, M. Lenglet, P. Miche, S. Weber, and S. Scherrer, Study of copper-nickel alloy oxidation by FTIR and SIMS, *Analisis* 21 (1993) 173-176.
- [187] A. M. Beccaria, J. Crousier, Dealloying of Cu-Ni alloys in natural sea water, *British Corrosion Journal* 24 (1989) 49-52.

- [188] P. G. Rouxhet, N. Mozes, P. B. Dengis, Y. F. Dufrêne, P. A. Gerin, M. J. Genet, Application of X-ray photoelectron spectroscopy to microorganisms, *Colloids Surfaces Biointerfaces* 2 (1994) 347–369.
- [189] Y. Yang, Biofouling of metal surfaces: study of adsorbed biomolecules and prevention strategy based on a renewable copolymer layer, PhD, Université Catholique de Louvain, Belgium (2013).
- [190] F. Ahimou, C. J. P. Boonaert, Y. Adriaensen, P. Jacques, P. Thonart, M. Paquot, P. G. Rouxhet, {XPS} analysis of chemical functions at the surface of *Bacillus subtilis*, *Journal of Colloid and Interface Science* 309 (2007) 49–55.
- [191] E. D'Elia, O. E. Barcia, O. R. Mattos, N. Pébère, B. Tribollet, High-Rate Copper Dissolution in Hydrochloric Acid Solution, *Journal Electrochemical Society* 143 (1996) 961–967.
- [192] C. Deslouis, O. R. Mattos, M. M. Musiani, B. Tribollet, Comments on mechanisms of copper electrodisolution in chloride media, *Electrochimica Acta* 38 (1993) 2781–2783.
- [193] W. H. Smyrl, Digital Impedance for Faradaic Analysis: II . Electrodisolution of Cu, *Journal of the Electrochemical Society* 132 (1985) 1555–1562.
- [194] H. Grubitsch, F. Hilbert, R. Sammer, Auswertung von potentiokinetischen Strom-Spannungsmessungen an Cu-Ni-Legierungen, Kupfer und Messung in Meerwasser, *Materials and Corrosion* 17 (1966) 760–765.
- [195] B. Tribollet, “Applications des méthodes électrochimiques a l'étude des solutions de polymère en écoulement, PhD, Université Pierre et Marie Curie, Paris 6 (1978).
- [196] P. Han, D. M. Bartels, Temperature dependence of oxygen diffusion in H<sub>2</sub>O and D<sub>2</sub>O, *The Journal of Physical Chemistry* 100 (1996) 5597–5602.
- [197] E. L. Cussier, Diffusion, mass transfer in fluid systems, 2nd edition, New york, Cambridge University Press (1997) 580.
- [198] F. C. Tse, O. C. Sandall, Diffusion coefficients for oxygen and carbon dioxide in water at 25°C by unsteady state desorption from a quiescent liquid, *Chemical Engineering Communications* 3 (1979) 147–153.
- [199] S.R. de Sanchez, D.J. Schiffrin, The use of high speed rotating disc electrodes for the study of erosion-corrosion of copper base alloys in sea water, *Corrosion Science* 28 (1988) 141–151.
- [200] O. E. Barcia, O. R. Mattos, N. Pébère, B. Tribollet, Mass Transport Study for the Electrodisolution of Copper in 1M Hydrochloric Acid Solution by Impedance, *Journal of the Electrochemical Society* 140 (1993) 2825–2832.
- [201] S. Petetin, J. Crousier, J. P. Crousier, Comportement de l'alliage Cuivre-Nickel 7030 dans une solution de NaCl A 3%, *Materials Chemistry and Physics* 10 (1984) 317–329.
- [202] M. Edwards, J. F. Ferguson, S. H. Reiber, The pitting corrosion of copper, *Journal of American Water Works Association* 86 (1994) 74–90.
- [203] D. Davidson, B. Beheshti, M. W. Mittelman, Effects of *Arthrobacter* sp., *Acidovorax delafieldii*, and *Bacillus megaterium* colonization on copper solvency in a laboratory reactor, *Biofouling* 9 (1996) 279–292.
- [204] B. J. Webster, S. E. Werner, D. B. Wells, P. J. Bremer, Microbiologically influenced corrosion of copper in potable water systems - pH effects, *Corrosion Science* 56 (2000) 942–950.

- [205] K. Rechendorff, The influence of surface roughness on protein adsorption, University of Aarhus, Denmark (2006).
- [206] P. Druska, H.-H. Strehblow, Surface analytical examination of passive layers on Cu-Ni alloys Part II. Acidic solutions, *Corrosion Science* 38 (8) (1996) 1369-1383.
- [207] M.M Osman, Corrosion inhibition of aluminium–brass in 3.5% NaCl solution and sea water, *Materials Chemistry and Physics* 71 (2001) 12–16.
- [208] B. TORRES BAUTISTA, Effect of biomolecules adsorption on oxide layers developed on metallic materials used in cooling water systems, PhD, Université Pierre et Marie Curie in Paris, France (2014).

## ANNEX A – CHAPTER 4

Table A-1 presents the scheme of the procedure used for converting the elemental molar concentrations, obtained by XPS spectra, into weight percentages of chemical entities (g/100 g of adlayer).

The chemical entities considered were amide [HC-NH-(C=O)] quantified by  $N_{org}$  as a marker,  $CH_2$  quantified by  $C_{285/284.8}$  component, additional carbon C quantified by  $[C_{284.8}-2N_{org}]$  and additional organic oxygen  $O_{org}$  quantified by  $[O_{org} - N_{org} = C_{ox} - 2*N_{org}]$ . Multiplying the molar concentration of marker (X, mol/100 mol) by the molar mass (MM) of the relevant model constituent provides its concentration W, in g/100 mol. Dividing W of each compound by the sum of W for all compounds (Tot) and multiplying by 100 finally gives the mass concentration in % of the constituent in the volume probed by XPS.

**Table A-1:** Computation scheme used for converting the elemental molar concentrations, obtained by XPS spectra, into weight percentages of chemical entities (g/100 g of adlayer).

Model constituent		Marker	W=X*MM <sup>(c)</sup>	W*100/Tot constituent concentration [mass%]
Nature	MM <sup>(a)</sup>	Name and concentration X <sup>(b)</sup>		
Amide	56.08	$N_{org}$	...	...
$CH_2$	14.01	$C_{285/284.8}$	...	...
Extra C	12.01	$C_{284.8}-2N_{org}$	...	...
Extra $O_{org}$	16.00	$C_{ox}-2N_{org}$	...	...
Total	-	-	Tot=...	100

(a) Molar mass of constituent

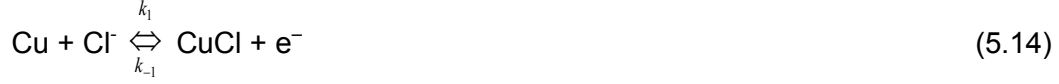
(b) Name of marker, concentration X deduced from XPS spectra (mole / 100 moles excluding hydrogen)

(c) In gram of constituent / 100 moles of elements other than hydrogen

... From measurements

## ANNEX B – CHAPTER 5

As already mentioned in Chapter 4, the mechanism of anodic dissolution of pure copper in acidic and neutral chloride solutions is given by the following two-step sequence:



where CuCl represents an intermediate cuprous chloride species which is adsorbed onto the copper electrode surface (surface coverage:  $\delta$ ) and  $\text{CuCl}_2^-$  a soluble cuprous complex which is the diffusing species.

The steady-state faradaic current may be obtained from the equation:

$$\frac{i}{F} = k_1 [\text{Cl}^-]_0 (1 - \gamma) \exp\left(\frac{\alpha FV}{RT}\right) - k_{-1} \Gamma \gamma \exp\left(-\frac{(1 - \alpha) FV}{RT}\right) \quad (5.16)$$

where  $[\text{Cl}^-]_0$  is the chloride concentration at the electrode surface and  $\Gamma$  the total number of sites available for adsorption.

The conservation equation for the adsorbed intermediate yields:

$$\Gamma \frac{d\gamma}{dt} = k_1 [\text{Cl}^-]_0 (1 - \gamma) \exp\left(\frac{\alpha FV}{RT}\right) - k_{-1} \Gamma \gamma \exp\left(-\frac{(1 - \alpha) FV}{RT}\right) - k_2 \Gamma \gamma [\text{Cl}^-]_0 + k_{-2} [\text{CuCl}_2^-]_0 \quad (5.17)$$

where  $[\text{CuCl}_2^-]_0$  represents the  $\text{CuCl}_2^-$  concentration at the electrode surface.

As mass transport limitation is due to  $\text{CuCl}_2^-$ ,  $[\text{Cl}^-]_0 = [\text{Cl}^-]_\infty$  in Eqs. (5.16) and (5.17), with  $[\text{Cl}^-]_\infty$  the chloride concentration in bulk solution, the steady-state flux of  $\text{CuCl}_2^-$  at the surface is related to the current as follows:

$$\frac{\bar{i}}{F} = D \frac{[\text{CuCl}_2^-]_0}{\delta} \quad (5.18)$$

with  $D$  and  $\delta$  the diffusion coefficient and diffusion layer thickness, respectively, of  $\text{CuCl}_2^-$ .

At steady-state,  $\frac{d\delta}{dt} = 0$ ; thus, the combination of Eqs. (5.16), (5.17) and (5.18)

yields:

$$\frac{\bar{i}}{F} = k_2 \Gamma \bar{\gamma} [Cl^-]_{\infty} - k_{-2} \frac{\bar{i}\delta}{FD} \quad (5.19)$$

and finally:

$$\frac{\bar{i}}{F} \left( 1 + k_2 \frac{\delta}{D} \right) = k_2 \Gamma \bar{\gamma} [Cl^-]_{\infty} \quad (5.20)$$

If it is assumed that  $\gamma \ll 1$ , then Eq. (5.16) becomes:

$$\frac{i}{F} = k_1 [Cl^-]_{\infty} \exp(bV) - k_{-1} \Gamma \bar{\gamma} \exp(-bV) \quad (5.21)$$

where  $b = \frac{\alpha F}{RT} > 0$  with  $\alpha = 0.5$ .

The combination of Eqs. (5.20) and (5.21) yields:

$$\Gamma \bar{\gamma} = \frac{k_1 [Cl^-]_{\infty} \exp(bV) \left( 1 + k_{-2} \frac{\delta}{D} \right)}{k_2 [Cl^-]_{\infty} + k_{-1} \exp(-bV) \left( 1 + k_{-2} \frac{\delta}{D} \right)} \quad (5.22)$$

The combination of Eqs. (5.20) and (5.22) finally gives:

$$\frac{F}{\bar{i}} = \frac{1}{k_1 [Cl^-]_{\infty} \exp(bV)} + \frac{k_{-1} \exp(-2bV)}{k_1 k_2 [Cl^-]_{\infty}^2} \left( 1 + \frac{k_{-2} \delta}{D} \right) \quad (5.23)$$

Under a sinusoidal perturbation, Eqs. (5.21) and (5.17) become:

$$\tilde{i} = R_t^{-1} \tilde{V} - F k_{-1} \Gamma \exp(-bV) \tilde{\gamma} \quad (5.24)$$

$$j\omega \Gamma \tilde{\gamma} = \frac{\tilde{V}}{FR_t} - \left( k_{-1} \exp(-bV) + k_2 [Cl^-]_{\infty} \right) \Gamma \tilde{\gamma} + k_{-2} [Cu\tilde{Cl}_2^-]_0 \quad (5.25)$$

$$\text{with } R_t^{-1} = F \left\{ k_1 [Cl^-]_{\infty} b \exp(bV) + k_{-1} \Gamma \bar{\gamma} b \exp(-bV) \right\} \quad (5.26)$$

Eqs. (5.24) and (5.25) are written in terms of four oscillating variables:  $\tilde{V}, \tilde{i}, \tilde{\gamma}, [Cu\tilde{Cl}_2^-]_0$ . An additional equation is needed to allow calculation of transfer functions.

Eq. (5.19) may be expressed as:

$$-D \frac{\partial [Cu\tilde{Cl}_2^-]}{\partial y} \Big|_0 = k_2 [Cl^-]_\infty \Gamma \tilde{\gamma} - k_{-2} [Cu\tilde{Cl}_2^-]_0 \quad (5.27)$$

According to the theory of diffusion impedance:

$$\frac{[Cu\tilde{Cl}_2^-]_0}{\frac{\partial [Cu\tilde{Cl}_2^-]}{\partial y} \Big|_0} = -\delta \times \left( \frac{-1}{\theta'(0)} \right) \quad (5.28)$$

where  $-1/\theta'(0)$  is the dimensionless diffusion impedance for  $CuCl_2^-$  depending only on the dimensionless frequency  $\frac{\omega \times \delta^2}{D}$  [136].

With Eqs. (5.24), (5.25), (5.27) and (5.28), we have a set of four equations with four

unknowns:  $\frac{\tilde{i}}{\tilde{V}}$ ,  $\frac{\tilde{\gamma}}{\tilde{V}}$ ,  $\frac{[Cu\tilde{Cl}_2^-]_0}{\tilde{V}}$  and  $\frac{\frac{\partial [Cu\tilde{Cl}_2^-]}{\partial y} \Big|_0}{\tilde{V}}$ .

The solution for the Faradaic impedance  $Z_f$  is:

$$\frac{1}{Z_f} = \frac{\tilde{i}}{\tilde{V}} = R_t^{-1} - \frac{k_{-1} \exp(-bV)}{R_t \left( j\omega + k_{-1} \exp(-bV) + k_2 [Cl^-]_\infty \left( \frac{\frac{D}{\delta} \left( -\frac{1}{\theta'(0)} \right)}{k_{-2} + \frac{D}{\delta} \left( -\frac{1}{\theta'(0)} \right)} \right) \right)} \quad (5.29)$$

and finally:

$$Z_f = R_t + \frac{R_t k_{-1} \exp(-bV)}{j\omega + k_2 [Cl^-]_\infty \left( \frac{(D/\delta)(-1/\theta'(0))}{(D/\delta)(-1/\theta'(0)) + k_{-2}} \right)} \quad (5.30)$$

For  $\Omega \rightarrow \infty$ , then  $\delta \rightarrow 0$  and hence:

$$Z_f = R_t + \frac{R_t k_{-1} \exp(-bV)}{j\omega + k_2 [Cl^-]_\infty} \quad (5.31)$$

For  $\Omega \rightarrow 0$ , then  $\delta \rightarrow \infty$  and hence:

$$Z_f = R_t + \frac{R_t k_{-1} \exp(-bV)}{j\omega} \quad (5.32)$$

With a rotating ring electrode (RRE), the diffusion layer thickness is smaller than for a rotating disk electrode (RDE); therefore, in the low frequency range,  $\frac{\omega \times \delta^2}{D} \ll 1$  and  $-1/\theta'(0)$  can be considered as equal to 1 and then independent of the frequency. Thus, Equation (5.30) can be written as:

$$Z_f = R_t + \frac{R}{1 + j\omega RC} \quad (5.33)$$

in which the second term corresponds to the impedance of an R/C circuit, with the resistance R and the capacitance C given by:

$$R \times C = \frac{1}{k_2 [Cl^-]_\infty \left( \frac{(D/\delta)}{(D/\delta) + k_{-2}} \right)} = \frac{1}{k_2 [Cl^-]_\infty} \times \left( 1 + \frac{k_{-2}\delta}{D} \right) \quad (5.34)$$

and

$$C = \frac{1}{R_t k_{-1} \exp(-bV)} \quad (5.35)$$

Thus, the anodic dissolution of pure copper can be modeled by the equivalent circuit given in Figure B-1(a), in which C depends on potential only,  $R \times C$  depends on the rotation speed only via  $\delta$ , and R depends on both potential and rotation speed. As  $\delta$  varies as  $\Omega^{-1/2}$  for a RDE or a RRE [195],  $R \times C$  varies as  $\Omega^{-1/2}$  (Eq. (5.34)). The corresponding simulated impedance diagrams are shown in Figure B-1(b) for different rotation speeds. These diagrams are composed of two semi-circles, the HF one illustrating charge transfer and the LF one illustrating mass transport and partial blocking effect by CuCl.

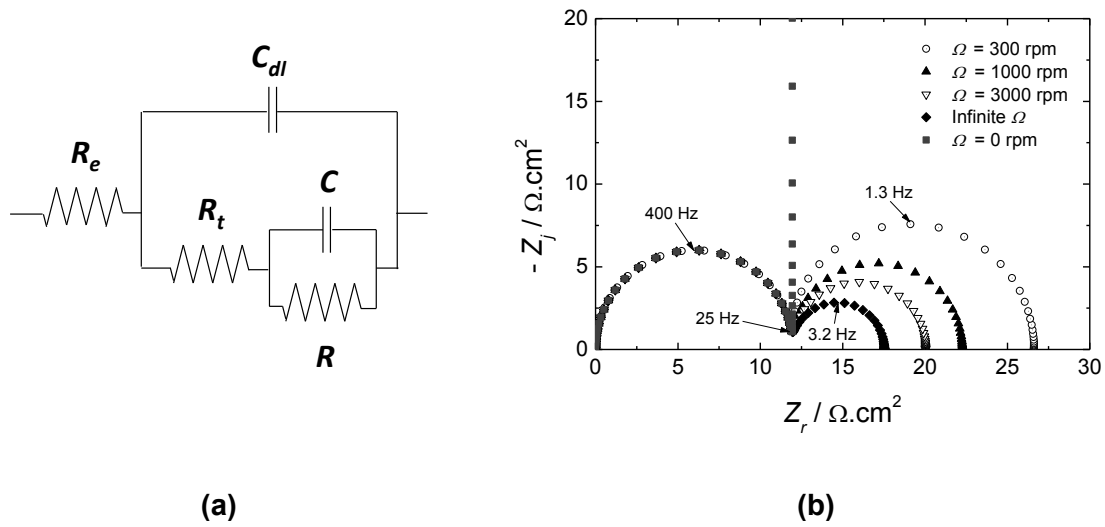


**Figure B-1:** (a) Equivalent electrical circuit for the anodic dissolution of pure copper and (b) corresponding simulated impedance diagrams at different rotation speeds, with  $C_{dl} = 30 \mu\text{F} \cdot \text{cm}^{-2}$ ,  $R_t = 12 \Omega \cdot \text{cm}^2$ ,  $R_t k_{-1} \exp(-bV) = 100$ ,  $k_2[\text{Cl}^-]_\infty = 20$ ,  $k_{-2} = 0.2$ ,  $D/\delta = 0.0006 \times \Omega^{1/2}$ .

This simulation is in good agreement with the experimental data presented in Figure 3 of Ref. [200].

## LIST OF FIGURES

### CHAPTER 1

Figure 1-1: Open circuit power plant.....	1
Figure 1-2: Classification of heat exchangers according to flow arrangements (a) and example of single and multiple pass heat exchangers (b) (adapted from John Willey [7]).....	3
Figure 1-3: Distribution of $\text{CO}_2$ , $\text{HCO}_3^-$ and $\text{CO}_3^{2-}$ concentrations as a function of pH. Seawater has a pH value around 8.2.....	4
Figure 1-4: Principal steps in the biofilm development: 1) Initial reversible attachment of free swimming micro-organisms to surface, 2) Permanent chemical attachment, single layer, bacteria begin making slime, 3) Early vertical development, 4) Multiple towers with channels between, maturing biofilm, 5) Mature biofilm with seeding/dispersal of more free swimming micro-organisms (Graphic by Peg Dirckx and David Davies, 2003 Center for Biofilm Engineering Montana State University). ....	8
Figure 1-5: Pourbaix diagram for the Cu-H <sub>2</sub> O system at 25 °C [43]. ....	14
Figure 1-6: Pourbaix diagram for copper in seawater at 25 °C [44]. ....	15
Figure 1-7: Typical anodic polarization curve of copper in aqueous chloride solution (adapted from Kear <i>et al.</i> [45]). ....	16
Figure 1-8: Steps involved during the reduction of oxygen consisting of mass transport to and from the electrode surface and electron transfer reaction (adapted from Kear <i>et al.</i> [47]). ....	17
Figure 1-9: Critical local flow velocity. ....	23
Figure 1-10: Scheme for microbial corrosion (metal under a microbial colony). ....	24
Figure 1-11: (a) Variation of oxide film thickness with pH estimated from electrochemical methods (EC) or weight loss method (WL); (b) corrosion current density of copper in solutions of various pH calculated from polarization curves or weight loss measurements. Copper immersed during 24 h in simulated tap water at 30°C (adapted from Feng <i>et al.</i> [98]). ....	28
Figure 1-12: Outline of the thesis and objective of each chapter. This also illustrates the BIOCOR project approach: from the field, through the lab, to the field (NSW = Natural seawater without chlorination; TNSW = Treated natural seawater, with chlorination; FNSW = Filtered natural seawater; ASW = Artificial seawater; ASW+BSA = Artificial seawater with 20 mg.L <sup>-1</sup> of bovine serum albumin; XPS = X-ray photoelectron spectroscopy and ToF-SIMS = time-of-flight secondary ion mass spectrometry).....	35

### CHAPTER 2

Figure 2-1: Experimental methods and places where the measurements were performed. (RSE SpA = Ricerca sul Sistema Energetico, Milan, Italy; UoP = University of Portsmouth, Portsmouth, UK; LPCS = Laboratoire de Physico-Chimie des Surfaces, Paris, France; LISE = Laboratoire Interfaces et Systèmes Electrochimiques, Paris, France; $E_{corr}$ = corrosion potential; LPR = linear polarization resistance; EIS = electrochemical impedance spectroscopy; XPS = X-ray photoelectron spectroscopy and ToF-SIMS = time-of-flight secondary ion mass spectrometry). ....	36
Figure 2-2: (a) Heat exchanger inside a power plant facility, (b) condenser tubes and (c) samples cut from condenser tubes. ....	37
Figure 2-3: SEM micrographs of a 70Cu-30Ni polished sample: (a) surface overview (secondary electrons; scale: 2µm), (b) Cu and Ni distribution (scale: 60 µm), (c) Cu distribution (scale: 60 µm) and (d) Ni distribution (scale: 60 µm). ....	38

Figure 2-4: SEM micrographs of an Al brass polished sample: (a) surface overview (secondary electrons; scale: 60µm), (b) Cu, Zn and Al distribution (scale: 60 µm).....	39
Figure 2-5: Five tubular electrodes used for the corrosion rate determination: (a) outside and (b) inside a plastic tube.....	40
Figure 2-6: Sample holder used for electrochemical tests in static conditions.....	41
Figure 2-7: Rotating Ring Electrode (RRE) for the measurements in well-controlled hydrodynamic conditions. ....	42
Figure 2-8: Three-electrode electrochemical cell. ....	44
Figure 2-9: Electrochemical cell used for the corrosion rate determination by the Linear Polarization Resistance (LPR) method: (a) schema of the LPR method and (b) image of the electrochemical cell inserted in a test line.....	45
Figure 2-10: Electrodes configuration for the measurement of the corrosion potential vs a Zn electrode during field experiments (on-line measurements).....	46
Figure 2-11: Microorganisms identification: molecular biology steps.....	48
Figure 2-12: Electrochemical cells used for experiments carried with ASW (without or with BSA) and FNSW in: (a), (b) static conditions and (c) under flow and stirring. ....	52
Figure 2-13: Electrochemical cell used for experiments carried out with a RRE in ASW and FNSW. ....	53
Figure 2-14: Flow behavior through a pipe: a) laminar and b) turbulent behavior.....	54
Figure 2-15: Flow movement induced by a rotating disk electrode. ....	56
Figure 2-16: Levich plot ( $I = f(\Omega^{1/2})$ ). ....	58
Figure 2-17: Koutecky-Levich plot ( $(I - A)^{-1} = f(\Omega^{-1/2})$ ). ....	58
Figure 2-18: Sinusoidal current response of a linear system. ....	59
Figure 2-19: Origin of Lissajous Figure.....	61
Figure 2-20: EIS representation: (a) Nyquist plot with impedance vector (b) Bode plots (with one time constant).....	61
Figure 2-21: Equivalent electrical circuit of the interfacial impedance at the corrosion potential, where $i_{di}$ represents the charging current, $i_F^a$ the anodic Faradaic current and $i_F^c$ the cathodic Faradaic current (the electrolyte resistance is omitted).....	66
Figure 2-22: Schematic diagrams of (a) photoelectron emission, and (b) Auger electron emission.....	67
Figure 2-23: Schematic drawing of the secondary particles emission process initiated by the impact of the primary ion. Positive and negative ions, electrons and neutral particles are emitted. In ToF-SIMS measurements, only ions can be analyzed. ....	72
Figure 2-24: SIMS depth profile of Cu, Ti, Si and N after annealing for 30 min at 650°C. Copper diffused into Ti-Si-N film. (Adapted from Y.C. Ee <i>et al.</i> [149]) .....	72

### CHAPTER 3

Figure 3-1: Pictures of the Piombino power plant: power plant view (left side) and outlet of seawater in the pool (right side).....	77
Figure 3-2: Schema of the two hydraulic test lines (control and treated) in the cooling circuit bypass (DPD = N,N-diethyl-p-phenyldiamine; LPR = linear polarization resistance).....	78
Figure 3-3: Pictures of the heat exchanger at Servola power plant: inlet (left side) and outlet (right side). ....	78
Figure 3-4: Monitoring system: a) Inside view of the experimental circuit, (b) computer display and (c) two hydraulic lines (Control and Treated) with 70Cu-30Ni specimens and probes....	79

Figure 3-5: Evolution of the overall cathodic curve during the gradual development of biofilm on a stainless steel surface exposed to aerated natural seawater (adapted from G. Pavanello <i>et al.</i> [159]).	81
Figure 3-6: Biofilm growth. (a) Schema of the electrochemical sensor, (b) Evolution of the bacteria population density on SS surfaces obtained from SEM count of settled bacteria and (c) signal provided by an electrochemical probe in a test performed in flowing natural seawater [156].	82
Figure 3-7: Biofilm growth. (a) BIOX system, (b) typical trend of BIOX signal (chlorine dosages and biofilm growth).	84
Figure 3-8: BIOX and chlorination treatments: (a) BIOX signal trend and residual oxidant concentration in seawater measured with the on-line instrumentation based on DPD colorimetric method, (b) AMI Codes (SWAN) colorimetric device.	85
Figure 3-9: Corrosion potential ( $E_{corr}$ ) vs SCE of three 70Cu-30Ni samples (new and old) exposed to natural seawater (NSW) or treated natural seawater (TNSW) for a period of 210 days.	87
Figure 3-10: Monitoring system results. (a) Corrosion rate ( $V_{corr}$ ) of 70Cu-30Ni exposed to the chlorinated seawater (Treated line) and non-chlorinated seawater (Control line), and (b) BIOX signal (left side scale) and chlorine concentration (right side scale) for the 70Cu-30Ni/TNSW system in the period 22 August – 30 November 2010.	88
Figure 3-11: Monitoring system results. (a) Corrosion rate ( $V_{corr}$ ) (left side scale) and BIOX signal (right side scale) of 70Cu-30Ni exposed to chlorinated seawater in the period January-March 2011, and (b) BIOX signal (left side scale) and chlorine concentration (right side scale).	89
Figure 3-12: Monitoring system results. Corrosion rate ( $V_{corr}$ ) of 70Cu-30Ni exposed to chlorinated seawater (Treated Line) and non-chlorinated seawater (Control Line) in the period (a) April-June 2011 and (b) October-December 2011.	90
Figure 3-13: BIOX signal (left side scale) and chlorinated seawater (Treated Line) red-ox potential (right side scale) from end December 2011 to end February 2012.	91
Figure 3-14: Monitoring system results. (a) Seawater red-ox potential in the treated line (left side scale) and in the control line (right side scale); (b) BIOX signal for the treated line (left side scale) and for the control line (right side scale), from end December 2011 to middle March 2012.	92
Figure 3-15: Monitoring system results. (a) seawater temperature in the treated line (left side scale) and in the control line (right side scale); (b) seawater turbidity for the treated line. Period from the end December 2011 to middle March 2012.	93
Figure 3-16: Longitudinal view of Al brass stepped specimens.	94
Figure 3-17: Monitoring results in treated natural seawater (TNSW). (a) Antifouling treatment monitored by the BIOX probe and (b) Al brass corrosion rate ( $V_{corr}$ ), estimated with two probes: probe 1 with smooth specimens; probe 2 with smooth and stepped specimens.	95
Figure 3-18: Monitoring results. Corrosion rate trends of Al brass specimens in treated natural seawater: non stepped specimen (old) and stepped specimen (new).	96
Figure 3-19: Corrosion rate trend of new Al brass stepped and smoothed (not stepped) specimens immersed in natural seawater with $\text{FeSO}_4$ dosages ( $0.5 \text{ mg.L}^{-1} \text{ Fe}^{2+}$ , 1 h/day).	97
Figure 3-20: Corrosion rate trend of new Al brass stepped and smoothed (not stepped) specimens with $\text{FeSO}_4$ dosages ( $0.5 \text{ mg.L}^{-1} \text{ Fe}^{2+}$ , 1 h/day + $1 \text{ mg.L}^{-1} \text{ Fe}^{2+}$ , 1 h/week).	97
Figure 3-21: 70Cu-30Ni samples extracted from the hydraulic lines after 80 days of operation: A24 and A9 samples were exposed to TNSW, and A1 and T16 ones to NSW. (a,c) Before and (b, d) after acidic cleaning.	98

Figure 3-22: Off-line measurements. 70Cu-30Ni corrosion probes extracted from the hydraulic lines after 405 days of operation in treated natural seawater (TNSW) or natural seawater (NSW).	100
Figure 3-23: Six percent DGGE gel showing biodiversity data from 70Cu30Ni and Al brass samples exposed to LTTNSW (long time (one year) to treated natural seawater), LTNSW (long time to natural seawater) and 2DNSW (2 days to natural seawater). Lanes 1 and 2: 70Cu30Ni/LTTNSW; lanes 3, 4 and 5: 70Cu30Ni/LTTNSW; lanes 6 and 7: Al brass/2DNSW; lane 8: Al brass/LTNSW; and lane 9 70Cu30 Ni 2D/NSW.	102
Figure 3-24: Bacterial 16S rRNA gene (550 bp); 70Cu30Ni and Al brass samples on 0.9% agarose gel exposed previously to LTTNSW (long time (one year) to treated natural seawater), LTNSW (long time to natural seawater) and 2DNSW (2 days to natural seawater). Lanes 1 and 2: 70Cu30Ni/LTTNSW; lanes 3, 4 and 5: 70Cu30Ni/LTTNSW; lanes 6 and 7: Al brass/2DNSW; lane 8 Al brass/LTNSW; lane 9 70Cu30Ni/2DNSW; lane 10 <i>D. alaskensis</i> (positive control); lane 11 negative control (PCR water); and lane 12 100 bp DNA ladder.	103

## CHAPTER 4

Figure 4-1: (a) Cathodic and (b) anodic polarization curves of 70Cu-30Ni after 1 h of immersion at $E_{corr}$ in static aerated filtered natural seawater (FNSW), artificial seawater (ASW) without BSA and with 20 mg.L <sup>-1</sup> of BSA. Scan rate: 0.5 mV.s <sup>-1</sup>	106
Figure 4-2: Experimental impedance diagrams in the complex plane (Nyquist diagrams) of 70Cu-30Ni plotted at $E_{corr}$ after 1 h of immersion in static aerated filtered natural seawater (FNSW), artificial seawater (ASW) without and with 20 mg.L <sup>-1</sup> of BSA.	108
Figure 4-3: Layer model assumed for the analysis of XPS data (mixed oxide layer covering the metallic substrate).	109
Figure 4-4: Layer model assumed for the analysis of XPS data (organic layer covering the mixed oxide layer formed on the metallic substrate).	112
Figure 4-5: (a) X-ray photoelectron spectroscopy (XPS) Cu 2p <sub>3/2</sub> core level spectra and (b) Cu L <sub>3</sub> M <sub>45</sub> M <sub>45</sub> Auger lines of 70Cu-30Ni after polishing and after 1 h of immersion at $E_{corr}$ in static aerated filtered natural seawater (FNSW) and artificial seawater (ASW) without and with 20 mg.L <sup>-1</sup> of BSA. The intensity is expressed in arbitrary unit (a.u.).	114
Figure 4-6: X-ray photoelectron spectroscopy (XPS) Ni 2p <sub>3/2</sub> core level spectra of 70Cu-30Ni after 1 h of immersion at $E_{corr}$ in static aerated filtered natural seawater (FNSW) and artificial seawater (ASW) without and with 20 mg.L <sup>-1</sup> of BSA. The intensity is expressed in arbitrary unit (a.u.).	116
Figure 4-7: Characteristic time-of-flight secondary ions mass spectrometry (ToF-SIMS) negative depth profile of 70Cu-30Ni after 1 h of immersion at $E_{corr}$ in static aerated artificial seawater (ASW).	117
Figure 4-8: Characteristic time-of-flight secondary ions mass spectrometry (ToF-SIMS) negative depth profile of 70Cu-30Ni after 1 h of immersion at $E_{corr}$ in static aerated filtered natural seawater (FNSW).	118
Figure 4-9: Characteristic time-of-flight secondary ions mass spectrometry (ToF-SIMS) negative depth profile of 70Cu-30Ni after 1 h of immersion at $E_{corr}$ in static aerated artificial seawater with 20 mg.L <sup>-1</sup> of BSA.	119
Figure 4-10: (a) N 1s core level spectra of 70Cu-30Ni after 1 h of immersion at $E_{corr}$ in static aerated filtered natural seawater (FNSW) and artificial seawater (ASW) without and with 20 mg.L <sup>-1</sup> of BSA, and (b) C 1s core level spectra of 70Cu-30Ni after 1 h of immersion at $E_{corr}$ in static aerated artificial seawater with 20 mg.L <sup>-1</sup> of BSA. Solid line: experimental spectra; dashed line: peak decomposition. The intensity is expressed in counts per second (CPS).	120

Figure 4-11: Model of the surface layers deduced from combined X-ray photoelectron spectroscopy (XPS) and time-of-flight secondary ions mass spectrometry (ToF-SIMS) results for 70Cu-30Ni just after polishing. ....	121
Figure 4-12: Models of the surface layers deduced from combined X-ray photoelectron spectroscopy (XPS) and time-of-flight secondary ions mass spectrometry (ToF-SIMS) results for 70Cu-30Ni after 1 h of immersion at $E_{corr}$ in static (a) ASW, (b) FNSW and c) ASW with 20 mg.L <sup>-1</sup> of BSA (ASW + BSA). ....	123
Figure 4-13: Plot of molar concentrations determined by XPS: (a) C <sub>3288.3</sub> vs N <sub>org</sub> , (b) C <sub>2286.4</sub> vs N <sub>org</sub> , c) O <sub>533</sub> vs C <sub>2286.4</sub> - N <sub>org</sub> , and d) C <sub>1285.0</sub> vs C <sub>tot</sub> - 2*N <sub>org</sub> . 70Cu-30Ni samples immersed 1 h at $E_{corr}$ , in static aerated ASW with 20 mg.L <sup>-1</sup> of BSA (ASW + BSA) and FNSW. Dashed lines: 1:1 relation. ....	125
Figure 4-14: Composition of the biomolecules adsorbed on surface. Relative mass concentration of amide (HC-NH-(C=O)), hydrocarbon CH <sub>2</sub> , and other-oxygen-containing molecules (C <sub>add</sub> + O <sub>add</sub> ), including polysaccharides. 70Cu-30Ni samples immersed 1 h at $E_{corr}$ , in static aerated ASW with 20 mg.L <sup>-1</sup> of BSA (ASW + BSA) and FNSW. ....	127
Figure 4-15: Equivalent electrical circuits to model the 70Cu-30Ni/ASW and 70Cu-30Ni/FNSW systems: (a) general circuit, (b) simplified circuit taking into account experimental cathodic polarization curves, and (c) circuit used to analyze the HF loop of experimental impedance diagrams. $R_e$ is the electrolyte resistance, $CPE_{dl}$ a constant-phase-element related to the double layer, $R_t^a$ the anodic charge transfer resistance, $Z_{\theta,D}^a$ an impedance that illustrates anodic mass transport and partial blocking effect by CuCl, $R_t^c$ the cathodic charge transfer resistance, $Z_D^c$ a cathodic impedance that illustrates O <sub>2</sub> mass transport, and $W_c$ the cathodic Warburg impedance. ....	131
Figure 4-16: Experimental impedance data (imaginary part of the impedance as a function of frequency) of 70Cu-30Ni alloy obtained at $E_{corr}$ after 1 h of immersion in static aerated artificial seawater (ASW) without and with BSA (20 mg.L <sup>-1</sup> ), and filtered natural seawater (FNSW). Same data as in Figure 4-2. ....	132
Figure 4-17: Experimental impedance data (derivative curves calculated from Figure 4-16) of 70Cu-30Ni alloy obtained at $E_{corr}$ after 1 h of immersion in static aerated artificial seawater (ASW) without and with BSA (20 mg.L <sup>-1</sup> ), and filtered natural seawater (FNSW). Same data as in Figure 4-2. ....	133
Figure 4-18: High frequency loops of Nyquist diagrams obtained for 70Cu-30Ni at $E_{corr}$ after 1 h of immersion in static aerated: (a) ASW, (b) ASW with 20 mg.L <sup>-1</sup> of BSA, and (c) FNSW. Experimental curves and fit of the impedance model presented in Figure 4-15(c) to the data. Same data as in Figures 4-2. ....	135
Figure 4-19: Comparison of the corrosion current density values calculated from Eq. (4.32) with $z = 1$ and $\alpha = 0.5$ for 70Cu-30Ni alloy after 1 h of immersion in static aerated ASW without and with 20 mg.L <sup>-1</sup> of BSA, and filtered natural seawater (FNSW). ....	139

## CHAPTER 5

Figure 5-1: Anodic polarization curves of 70Cu-30Ni after 1 h of immersion at $E_{corr}$ in aerated artificial seawater, in static conditions and under flow and stirring. Scan rate: 0.5 mV.s <sup>-1</sup> . ...	142
Figure 5-2: Experimental impedance diagrams in the complex plane (Nyquist diagrams) of 70Cu-30Ni plotted at $E_{corr}$ after 1 h of immersion in aerated artificial seawater, in static conditions and under flow and stirring. ....	142
Figure 5-3: (a) X-ray photoelectron spectroscopy (XPS) Cu 2p <sub>3/2</sub> core level spectra, and (b) Cu L <sub>3</sub> M <sub>45</sub> M <sub>45</sub> Auger lines of 70Cu-30Ni after polishing, after 1 h of immersion at $E_{corr}$ in aerated artificial seawater in static conditions and under flow and stirring. The intensity is expressed in arbitrary unit (a.u.). ....	143

Figure 5-4: XPS Ni 2p <sub>3/2</sub> core level spectra of 70Cu-30Ni alloy after polishing, after 1 h of immersion at $E_{corr}$ in aerated artificial seawater in static conditions and under flow and stirring. The intensity is expressed in arbitrary unit (a.u.).	144
Figure 5-5: Characteristic time-of-flight secondary ions mass spectrometry (ToF-SIMS) negative depth profile of 70Cu-30Ni after 1 h of immersion at $E_{corr}$ in aerated artificial seawater under flow and stirring.	145
Figure 5-6: Model of the surface layers deduced from combined X-ray photoelectron spectroscopy (XPS) and time-of-flight secondary ions mass spectrometry (ToF-SIMS) results for 70Cu-30Ni after 1 h of immersion at $E_{corr}$ in ASW under flow and stirring.	146
Figure 5-7: Cathodic polarization curves of 70Cu-30Ni after 1 h of immersion at $E_{corr}$ in aerated artificial seawater, in static conditions and using the rotating ring electrode at 40, 160 and 640 rpm: (a) Scan rate: 0.5 mV.s <sup>-1</sup> and (b) steady-state curves.	150
Figure 5-8: Cathodic polarization curves of 70Cu-30Ni rotating ring electrode at 160 rpm, after 1 h of immersion at $E_{corr}$ in: i) aerated artificial seawater (scan rate: 0.5 mV.s <sup>-1</sup> ), ii) aerated artificial seawater (steady-state curve), iii) filtered natural seawater (steady-state curve), and iv) filtered natural seawater (scan rate: 0.5 mV.s <sup>-1</sup> ).	152
Figure 5-9: (a) Levich and (b) Koutecky-Levich curves of 70Cu-30Ni in aerated artificial seawater at -0.80 V vs SCE.	152
Figure 5-10: Anodic polarization curves of 70Cu-30Ni rotating ring electrode at three different rotation speeds (40, 160 and 640 rpm), after 1 h of immersion at $E_{corr}$ in: (a) aerated artificial seawater, and (b) aerated filtered natural seawater. Scan rate: 0.5 mV.s <sup>-1</sup> .	154
Figure 5-11: Anodic polarization curves of 70Cu-30Ni rotating ring electrode, after 1 h of immersion time at $E_{corr}$ in: (a) aerated artificial seawater and filtered natural seawater, at 160 rpm, in steady-state conditions and with a scan rate of 0.5 mV.s <sup>-1</sup> and (b) aerated artificial seawater in steady-state conditions at three different rotation speeds (10, 160 and 640 rpm).	155
Figure 5-12: Experimental impedance diagrams in the complex plane (Nyquist diagrams) of 70Cu-30Ni rotating ring electrode at three different rotation speeds (40, 160 and 640 rpm), after 1 h of immersion at $E_{corr}$ in: (a) aerated artificial seawater, and (b) aerated filtered natural seawater.	156
Figure 5-13: Experimental impedance data (imaginary part of the impedance as a function of frequency) of 70Cu-30Ni alloy obtained at $E_{corr}$ after 1 h of immersion in aerated: (a) artificial seawater, and (b) filtered natural seawater, in static conditions and using the rotating ring electrode at three different rotation speeds (40, 160 and 640 rpm). Same data as in Figure 5-12.	157
Figure 5-14: Experimental impedance data (derivative curves calculated from Figure 5-13) of 70Cu-30Ni alloy obtained at $E_{corr}$ after 1 h of immersion in aerated: (a) artificial seawater, and (b) filtered natural seawater, in static conditions and using the rotating ring electrode at three different rotation speeds (40, 160 and 640 rpm). Same data as in Figure 5-12.	158
Figure 5-15: High frequency loops of Nyquist diagrams obtained for 70Cu-30Ni at $E_{corr}$ after 1 h of immersion in aerated: (a) ASW in static conditions, (b) ASW with the RRE at 40 rpm, (c) ASW with the RRE at 160 rpm, (d) ASW with the RRE at 640 rpm, (e) FNSW in static conditions, (f) FNSW with the RRE at 40 rpm, (g) FNSW with the RRE at 160 rpm, and (h) FNSW with the RRE at 640 rpm. Experimental curves and fit of the impedance model presented in Figure 4-15 (c). Same data as in Figure 5-12.	160
Figure 5-16: Comparison of the corrosion current density values calculated from Eq. (4.32) with $z = 1$ and $\alpha = 0.5$ , for 70Cu-30Ni alloy after 1h of immersion in ASW or FNSW, in static conditions and using the rotating ring electrode.	163

Figure 5-17: (a) Cathodic and (b) anodic polarization curves of Al brass after 1 h of immersion at $E_{corr}$ in filtered natural seawater. RRE at 160 rpm in steady-state conditions and static conditions with a scan rate of $0.5 \text{ mV.s}^{-1}$ .	165
Figure 5-18: Anodic polarization curves of Al brass and 70Cu-30Ni alloy after 1 h of immersion at $E_{corr}$ in FNSW. (a) Static conditions with a scan rate of $0.5 \text{ mV.s}^{-1}$ and (b) rotating ring electrode at 160 rpm in steady-state conditions.	166
Figure 5-19: Experimental impedance diagrams in the complex plane (Nyquist diagrams) of Al brass plotted at $E_{corr}$ after 1 h of immersion in aerated filtered natural seawater in static conditions and with a rotating ring electrode at three different rotation speeds (40, 160 and 640 rpm).	167
Figure 5-20: Experimental impedance data of Al brass obtained at $E_{corr}$ after 1 h of immersion in aerated filtered natural seawater in static conditions and with a rotating ring electrode at three different rotation speeds (40, 160 and 640 rpm). (a) Imaginary part of the impedance as a function of frequency, and (b) derivative curves calculated from Figure 5-20(a) ( $d \log  Z''  / d \log f$ vs $\log f$ ).	168
Figure 5-21: Simplified equivalent electrical circuits to model the Al brass/FNSW system: (a) general circuit, (b) simplified circuit in static conditions, and (c) simplified circuit using the RRE. $R_e$ is the electrolyte resistance, $CPE_{dl}$ a constant phase element related to the double layer, $R_t^a$ the anodic charge transfer resistance, $Z_D^c$ a cathodic impedance that illustrates $O_2$ mass transport, and $W_c$ the cathodic Warburg impedance, $Z_{\theta D}^a$ an impedance that illustrates anodic mass transport and partial blocking effect by CuCl shown to be a capacitance $C$ in parallel with a resistance $R$ , $R_t^c$ the cathodic charge transfer resistance.	169
Figure 5-22: Nyquist diagrams obtained for Al brass at $E_{corr}$ after 1 h of immersion in aerated filtered natural seawater: (a) in static conditions, (b) with the RRE at 40 rpm, (c) with the RRE at 160 rpm, and (d) with the RRE at 640 rpm. Experimental curves and fit of the impedance model presented in Figure 4-15(c) (static conditions) or 5-30(c) (RRE) to the data. Same data as in Figure 5-19.	171
<b>CHAPTER 6</b>	
Figure 6-1: (a) Cathodic and (b) anodic polarization curves of 70Cu-30Ni after 1 h of immersion at $E_{corr}$ in static aerated filtered natural seawater at three different pH values: 8.0, 6.0 and 3.7. Scan rate: $0.5 \text{ mV.s}^{-1}$ .	175
Figure 6-2: Experimental impedance diagrams in the complex plane (Nyquist diagrams) of 70Cu-30Ni plotted at $E_{corr}$ after 1 h of immersion in static aerated filtered natural seawater at three different pH values: 8.0, 6.0 and 3.7.	176
Figure 6-3: Experimental impedance data (imaginary part of the impedance as a function of frequency) of 70Cu-30Ni alloy obtained at $E_{corr}$ after 1 h of immersion in static aerated filtered natural seawater at three different pH values: 8.0, 6.0 and 3.7. Same data as in Figure 6-2.	177
Figure 6-4: Experimental impedance data (derivative curves calculated from Figure 6-3) of 70Cu-30Ni alloy obtained at $E_{corr}$ after 1 h of immersion in filtered natural seawater at three different pH values: 8.0, 6.0 and 3.7. Same data as in Figure 6-2.	178
Figure 6-5: High frequency loops of Nyquist diagrams obtained for 70Cu-30Ni at $E_{corr}$ after 1 h of immersion in static aerated filtered natural seawater at three different pH values: (a) 8.0, (b) 6.0 and (c) 3.7. Experimental curves and fit of the impedance model presented in Figure 4-15(c). Same data as in Figure 6-2.	179
Figure 6-6: (a) X-ray photoelectron spectroscopy (XPS) Cu $2p_{3/2}$ core level spectra, and (b) Cu $L_{3/2}M_{45}M_{45}$ Auger lines of 70Cu-30Ni after polishing and after 1 h of immersion at $E_{corr}$ in aerated filtered natural seawater at pH 8.0, 6.0 and 3.7, under flow and stirring. The intensity is expressed in arbitrary unit (a.u.).	181

Figure 6-7: X-ray photoelectron spectroscopy (XPS) Ni 2p <sub>3/2</sub> core level spectra of 70Cu-30Ni alloy after polishing and after 1 h of immersion at $E_{corr}$ in aerated filtered natural seawater at pH 8.0, 6.0 and 3.7, under flow and stirring. The intensity is expressed in arbitrary unit (a.u.).	182
Figure 6-8: (a) N 1s core level spectra, and (b) C 1s core level spectra of 70Cu-30Ni after 1 h of immersion at $E_{corr}$ , under flow and stirring, in aerated filtered natural seawater at pH 8.0, pH 6.0, and pH 3.7. The intensity is expressed in counts per second (CPS).	183
Figure 6-9: Characteristic time-of-flight secondary ions mass spectrometry (ToF-SIMS) negative depth profiles of 70Cu-30Ni after 1 h of immersion at $E_{corr}$ , under flow and stirring, in aerated filtered natural seawater at (a) pH 8.0, (b) pH 6.0, and (c) pH 3.7.	186
Figure 6-10: Model of the surface layers deduced from combined X-ray photoelectron spectroscopy (XPS) and time-of-flight secondary ions mass spectrometry (ToF-SIMS) results for 70Cu-30Ni after 1 h of immersion at $E_{corr}$ , under flow and stirring, in FNSW at pH 8.0, 6.0 and 3.7.	187
Figure 6-11: Plot of molar concentrations determined by XPS: (a) C <sub>3288.3</sub> vs N <sub>org</sub> , (b) C <sub>2286.4</sub> vs N <sub>org</sub> , c) O <sub>533</sub> vs C <sub>2286.4</sub> - N <sub>org</sub> , and d) C <sub>1285.0</sub> vs C <sub>tot</sub> - 2*N <sub>org</sub> . 70Cu-30Ni samples immersed 1 h at $E_{corr}$ , under flow and stirring, in FNSW at pH 8.0, 6.0 and 3.7. Dashed lines: 1:1 relation.	188
Figure 6-12: Composition of adsorbed biomolecules on the surface. Relative mass concentration of amide (HC-NH-(C=O)), hydrocarbon CH <sub>2</sub> , and other oxygen-containing molecules (C <sub>add</sub> + O <sub>add</sub> ), including polysaccharides. 70Cu-30Ni samples immersed 1 h at $E_{corr}$ , under flow and stirring, in FNSW at pH 8.0, 6.0 and 3.7.	190
Figure 6-13: (a) Cathodic and (b) anodic polarization curves of Al brass after 1 h of immersion at $E_{corr}$ in static aerated filtered natural seawater at three different pH values: 8.0, 6.0 and 3.7. Scan rate: 0.5 mV.s <sup>-1</sup> .	192
Figure 6-14: Experimental impedance diagrams in the complex plane (Nyquist diagrams) of Al brass plotted at $E_{corr}$ after 1 h of immersion in static filtered natural seawater at three different pH values: 8.0, 6.0 and 3.7.	193
Figure 6-15: Experimental impedance data (imaginary part of the impedance as a function of frequency) of Al brass alloy obtained at $E_{corr}$ after 1 h of immersion in static filtered natural seawater at three different pH values: 8.0, 6.0 and 3.7. Same data as in Figure 6-14.	193
Figure 6-16: Experimental impedance data (derivative curves calculated from Figure 6-14) of Al brass alloy obtained at $E_{corr}$ after 1 h of immersion in static filtered natural seawater at three different pH values: 8.0, 6.0 and 3.7. Same data as in Figure 6-14.	194
Figure 6-17: High frequency loops of Nyquist diagrams obtained for Al brass at $E_{corr}$ after 1 h of immersion in static filtered natural seawater at three different pH values: (a) 8.0, (b) 6.0 and (c) 3.7. Experimental curves and fit of the impedance model presented in Figure 4-15(c). Same data as in Figure 6-14.	195
Figure 6-18: Layer model assumed for the analysis of XPS data (mixed oxide layer covering the metallic substrate).	198
Figure 6-19: Layer model assumed for the analysis of XPS data (organic layer covering the mixed oxide layer formed on the metallic substrate).	201
Figure 6-20: (a) X-ray photoelectron spectroscopy (XPS) Cu 2p <sub>3/2</sub> core level spectra, and (b) Cu L <sub>3</sub> M <sub>45</sub> M <sub>45</sub> Auger lines of Al brass after polishing and after 1 h of immersion at $E_{corr}$ in aerated filtered natural seawater at pH 8.0, 6.0 and 3.7, under flow and stirring. The intensity is expressed in arbitrary unit (a.u.).	201
Figure 6-21: X-ray photoelectron spectroscopy (XPS): (a) Zn 2p <sub>3/2</sub> , (b) Zn L <sub>3</sub> M <sub>45</sub> M <sub>45</sub> Auger lines and (c) Al 2p core level spectra of Al brass after polishing and after 1 h of immersion at $E_{corr}$ in aerated filtered natural seawater at pH 8.0, 6.0 and 3.7, under flow and stirring. The intensity is expressed in arbitrary unit (a.u.).	203

Figure 6-22: (a) N 1s core level spectra, and (b) C 1s core level spectra of Al brass after 1 h of immersion at $E_{corr}$ , under flow and stirring, in aerated filtered natural seawater at pH 8.0, pH 6.0, and pH 3.7. The intensity is expressed in counts per second (CPS). .....	204
Figure 6-23: Characteristic time-of-flight secondary ions mass spectrometry (ToF-SIMS) negative ions depth profiles of Al brass after (a) polishing and after 1 h of immersion at $E_{corr}$ , under flow and stirring, in aerated filtered natural seawater at (b) pH 8.0, (c) pH 6.0, and (d) pH 3.7. ....	207
Figure 6-24: Models of the surface layers deduced from combined X-ray photoelectron spectroscopy (XPS) and time-of-flight secondary ions mass spectrometry (ToF-SIMS) results for Al brass (a) after polishing and (b) after 1 h immersion at $E_{corr}$ , under flow and stirring, in FNSW at pH 8.0, 6.0 and 3.7.....	208

## ANNEX B

Figure B-1: (a) Equivalent electrical circuit for the anodic dissolution of pure copper and (b) corresponding simulated impedance diagrams at different rotation speeds, with $C_{dl} = 30 \mu\text{F}.\text{cm}^{-2}$ , $R_t = 12 \Omega.\text{cm}^2$ , $R_t k_{-1} \exp(-bV) = 100$ , $k_2[\text{Cl}^-]_{\infty} = 20$ , $k_2 = 0.2$ , $D/\delta = 0.0006 \times \Omega^{1/2}$ . ...	233
--	-----

## LIST OF TABLES

### CHAPTER 1

Table 1-1: Application fields of copper and its alloys (adapted from Cieslewicz and Schweitzer [22]).....	6
Table 1-2: Corrosion mechanisms that have caused problems in power plant cooling water systems under certain conditions (adapted from Syrett <i>et al.</i> [4]).....	8
Table 1-3: Anodic partial reactions of pure copper in chloride media. ....	15
Table 1-4: Recommended maximum water flow velocities for condenser tube alloys in seawater. Adapted from [9].....	23
Table 1-5: Corrosion products, controlling mechanisms and corrosion rate of copper in aqueous solutions at various pH.....	28

### CHAPTER 2

Table 2-1: Chemical composition of the 70Cu-30Ni (wt. %) alloy.....	37
Table 2-2: 70Cu-30Ni samples geometry, as a function of performed tests. ....	38
Table 2-3: Al brass samples geometry as a function of performed tests. ....	39
Table 2-4: Tafel constants for pure copper in aerated chloride media.....	54
Table 2-5: Common electrical elements, equations for their current vs voltage relationship, their impedance, their characteristics and their Nyquist representation. ....	63

### CHAPTER 3

Table 3-1: Off-line measurements. Weight loss measurements performed with 70Cu-30Ni samples exposed to treated natural sweater. ....	99
Table 3-2: Off-line measurements. Weight loss measurements performed with 70Cu-30Ni samples exposed to natural sweater. ....	99

### CHAPTER 4

Table 4-1: Transmission functions $T(E_{kin})$ of the Escalab 250 energy analyzer, provided by Thermo Electron Corporation. ....	110
Table 4-2: Inelastic mean free paths $\lambda$ in nm – Taken from the QUASES-IMFP-TPP2M. ...	110
Table 4-3: Photo-ionization cross sections $\sigma_x$ at 1486.6 eV. ....	110
Table 4-4: Binding energy of Cu 2p <sub>3/2</sub> XPS peak and kinetic energy of L <sub>3</sub> M <sub>45</sub> M <sub>45</sub> Cu Auger line for different Cu species [176-182].....	111
Table 4-5: Inelastic mean free paths $\lambda$ in nm – Taken from the QUASES-IMFP-TPP2M. ...	113
Table 4-6: Atomic ratios calculated from the XPS N 1s and C 1s core level spectra recorded for the BSA powder and for 70Cu-30Ni after 1 h of immersion at $E_{corr}$ in static aerated artificial seawater without and with 20 mg.L <sup>-1</sup> of BSA and filtered natural seawater. ....	120
Table 4-7: Binding energy of elements in chemical functions of biochemical compounds [142]. ....	124
Table 4-8: Experimental frequency range taken into account for the regression, parameters values (electrolyte resistance $R_e$ , anodic charge transfer resistance $R_t^a$ , constant of the cathodic Warburg impedance $k_c$ , and CPE parameters $\alpha$ and $Q$ obtained from the regression of the equivalent circuit presented in Figure 4-15(c) to experimental impedance data shown in Figures 4-2, and effective capacitance $C_{eff}$ associated with the CPE calculated from Eq. (2.22) presented in Chapter 2.....	135

Table 4-9: Comparison of the corrosion current density values obtained from $R_t^a$ , by application of Eqs. (4.32) and (4.33), and from the cathodic polarization curves (first plateau current density).....	138
--	-----

## CHAPTER 5

Table 5-1: Corrosion potential values for 70Cu-30Ni alloy after 1 h of immersion in artificial seawater (ASW), and filtered natural seawater (FNSW), in static conditions and using a RRE at three different rotation speeds (40, 160 and 640 rpm). ....	149
--	-----

Table 5-2: Comparison between the limiting current densities at -0.75 V vs SCE (corresponding to the second step of dissolved oxygen reduction with transfer of 4 electrons), and $0.5 \text{ mV.s}^{-1}$ , taken from Figure 5-7, and the theoretical values calculated from Eq. (5.9). ....	151
---	-----

Table 5-3: Experimental frequency range taken into account for the regression, parameters values (electrolyte resistance $R_e$ , anodic charge transfer resistance $R_t^a$ , constant of the cathodic Warburg impedance $k_c$ , and CPE parameters $\alpha$ and $Q$ ) obtained from the regression of the equivalent circuit presented in Figure 4-15 (c) to experimental impedance data shown in Figure 5-12, and effective capacitance $C_{eff}$ associated with the CPE calculated from Eq. (2.22). ....	159
---	-----

Table 5-4: Comparison of the corrosion current values obtained from $R_t^a$ , by application of Eqs. (4.32) (with $Z = 1$ and $\alpha = 0.5$ ) and (4.33), and from the non steady-state cathodic polarization curves (first plateau current density or extrapolation to $E_{corr}$ of the cathodic straight line).....	164
---	-----

Table 5-5: Corrosion potential values for Al brass alloy after 1 h of immersion in filtered natural seawater (FNSW), in static conditions and using a RRE at three different rotation speeds (40, 160 and 640 rpm).....	164
---	-----

Table 5-6: Electrolyte resistance $R_e$ , and CPE parameters, $\alpha$ and $Q$ , obtained graphically from experimental impedance data, and effective capacitance $C_{eff}$ associated with the CPE calculated from Brug's formula for a blocking electrode (Eq. (2.23)). ....	168
--	-----

Table 5-7: Regression results for the Al brass/FNSW system. Experimental frequency range taken into account for the regression, parameters values (electrolyte resistance $R_e$ , anodic charge transfer resistance $R_t^a$ , constant of the cathodic Warburg impedance $k_c$ , resistance $R$ , capacitance $C$ , and CPE parameters $\alpha$ and $Q$ ), obtained from the regression of the equivalent circuit presented in Figure 4-15(c) (static conditions) or 5-30(c) (RRE) to experimental impedance data shown in Figure 5-19, and effective capacitance $C_{eff}$ associated with the CPE calculated from Eq. (2.22). ....	170
--	-----

## CHAPTER 6

Table 6-1: Experimental frequency range taken into account for the regression, parameters values (electrolyte resistance $R_e$ , anodic charge transfer resistance $R_t^a$ , constant of the cathodic Warburg impedance $k_c$ , and CPE parameters $\alpha$ and $Q$ ) obtained from the regression of the equivalent circuit presented in Figure 4-15(c) to experimental impedance data shown in Figure 6-2, and effective capacitance $C_{eff}$ associated with the CPE calculated from Eq. (2.22). ....	179
---	-----

Table 6-2: Comparison of the corrosion current values obtained from $R_t^a$ , by application of Eqs. (4.32) (with $z=1$ and $\alpha=0.5$ ) and (4.33), and from the cathodic polarization curves (first plateau current density). ....	181
--	-----

Table 6-3: Atomic ratios calculated from the XPS N 1s and C 1s core level spectra recorded for 70Cu-30Ni after 1 h of immersion at $E_{corr}$ , under flow and stirring, in aerated filtered natural seawater at pH 8.0, pH 6.0, and pH 3.7. ....	183
---	-----

Table 6-4: Atomic composition of the oxide layer and equivalent thickness of the surface layers calculated from XPS data for 70Cu-Ni alloy after 1 h of exposure at $E_{corr}$ to FNSW at three different pH values (8.0, 6.0 and 3.7).....	184
Table 6-5: Corrosion potential values for Al brass alloy after 1 h of immersion in static filtered natural seawater (FNSW), at three different pH values (8.0, 6.0 and 3.7). ....	191
Table 6-6: Regression results for the Al brass/FNSW system, in static conditions, at three different pH. Experimental frequency range taken into account for the regression, parameters values (electrolyte resistance $R_e$ , anodic charge transfer resistance $R_t^a$ , constant of the cathodic Warburg impedance $k_c$ , and CPE parameters $\alpha$ and $Q$ ) obtained from the regression of the equivalent circuit presented in Figure 4-15(c) to experimental impedance data shown in Figure 6-14, and effective capacitance $C_{eff}$ associated with the CPE calculated from Eq. (2.22).....	196
Table 6-7: Comparison of the corrosion current values obtained from $R_t^a$ , by application of Eqs. (4.32) and (4.33) and from the cathodic polarization curves (first plateau current density).....	197
Table 6-8: Transmission functions $T(E_{kin})$ of the Escalab 250 energy analyzer, provided by Thermo Electron Corporation. ....	199
Table 6-9: Inelastic mean free paths $\lambda$ in nm – Taken from the QUASES-IMFP-TPP2M. ...	199
Table 6-10: Binding energy and kinetic energy of Zn 2p <sub>3/2</sub> XPS peak and Auger line, respectively, for Zn species. ....	200
Table 6-11: Atomic ratios calculated from the XPS N 1s and C 1s core level spectra recorded for Al brass after 1 h of immersion at $E_{corr}$ , under flow and stirring, in aerated filtered natural seawater at pH 8.0, pH 6.0, and pH 3.7.....	204
Table 6-12: Atomic composition of the oxide layer and equivalent thickness of the surface layers calculated from XPS data for Al brass after 1 h of exposure at $E_{corr}$ to FNSW at three different pH values (8.0, 6.0 and 3.7).....	205

## ANNEX A

Table A-1: Computation scheme used for converting the elemental molar concentrations, obtained by XPS spectra, into weight percentages of chemical entities (g/100 g of adlayer). ....	228
--	-----

## Corrosion d'alliages de cuivre en eau de mer naturelle - Effets de l'hydrodynamique et du pH

**Résumé :** Cette thèse, réalisée en étroite collaboration avec le partenaire industriel RSE S.p.A (Italie), s'inscrit dans le cadre du projet européen BIOCOR ITN. Les alliages de cuivre habituellement utilisés dans les circuits de refroidissement de centrales électriques peuvent être affectés par la biocorrosion induite par la formation d'un biofilm. L'objectif de ce travail était d'étudier le comportement à la corrosion de l'alliage 70Cu-30Ni et d'un laiton contenant 2% d'aluminium en milieu marin, dans des conditions industrielles réelles (expériences sur le terrain) et en laboratoire. L'influence de différents paramètres, tels que la solution (eau de mer naturelle filtrée (FNSW) vs eau de mer artificielle (ASW)), la concentration en biomolécules (biomolécules naturellement présentes dans l'eau de mer vs une protéine modèle, l'albumine de sérum bovin (BSA)), l'hydrodynamique (conditions statiques, sous circulation et agitation, électrode à anneau tournant) et le pH (8,0 ; 6,0 et 3,7), a été évaluée. Sur le terrain, le comportement global à la corrosion et les traitements antifouling ont été suivis en utilisant des techniques électrochimiques (potentiel de corrosion  $E_{corr}$  vs temps, LPR), gravimétriques (pertes de masse) et génétiques. En laboratoire, des mesures électrochimiques ( $E_{corr}$  vs temps, courbes de polarisation, spectroscopie d'impédance électrochimique), réalisées pendant les toutes premières étapes de formation des couches d'oxydes (1 h d'immersion), ont été combinées à des analyses de surface par XPS et ToF-SIMS. A partir des expériences sur le terrain, l'analyse microbiologique et moléculaire des biofilms formés sur les deux alliages de cuivre dans l'eau de mer naturelle montre la présence des espèces bactériennes *Marinobacter*, *Alteromonas* et *Pseudomonas*. A partir des expériences en laboratoire, des modèles sont proposés pour analyser les données d'impédance obtenues à  $E_{corr}$ . Dans le cas de 70Cu-30Ni, la boucle HF illustre principalement le transfert de charge anodique (diamètre égal à  $R_t^a$ ) ; alors que la boucle BF est liée au transport de matière anodique et au blocage partiel de la surface par CuCl. Dans le cas du laiton, la seule boucle expérimentale illustre à la fois le transfert de charge anodique et le transport de matière anodique. Le comportement électrochimique et la composition chimique de surface de l'alliage 70Cu-30Ni sont similaires dans ASW et dans FNSW statiques, du fait de la faible concentration en biomolécules dans FNSW. En comparaison de l'alliage 70Cu-30Ni dans ASW statique sans biomolécules, pour lequel une couche duplex épaisse (couche externe de  $Cu_2O$  redéposé et couche interne de nickel oxydé) est montrée, la présence de BSA conduit à une couche mixte d'oxydes de Cu et de Ni d'épaisseur plus faible ; les résultats montrent aussi un ralentissement de la réaction anodique et un faible effet d'inhibition de la corrosion en présence de BSA. Sous circulation et agitation, une couche mixte d'oxydes de Cu et de Ni, de très faible épaisseur, est obtenue. Pour les deux alliages dans FNSW, le courant de corrosion  $i_{corr}$  estimé à partir de  $R_t^a$  est indépendant de la vitesse de rotation de l'électrode tournante, du fait de la compensation des effets du potentiel et du transport de matière. Pour 70Cu-30Ni dans FNSW statique, la réaction anodique est ralentie à pH acide (effet cinétique). Pour le laiton, un effet d'inhibition de la corrosion est montré à pH acide, et plus le pH est acide, plus la réaction anodique est lente. Pour 70Cu-30Ni, l'épaisseur de la couche d'oxyde augmente avec la diminution du pH, dans le cas du laiton il est indépendante du pH. La composition chimique de la couche d'oxyde semble avoir un effet sur la quantité de protéines adsorbées et l'épaisseur équivalente calculée de la couche organique est très faible (quelques Å pour 70Cu-30Ni et 1 Å pour laiton).

**Mots-clés :** alliage 70Cu-30Ni, laiton, eau de mer, biocorrosion, BSA, EIS, XPS, ToF-SIMS

## Corrosion of copper alloys in natural seawater – Effects of hydrodynamics and pH

**Abstract:** This thesis was carried out in the frame of the BIOCOR ITN European project, in close collaboration with the industrial partner RSE S.p.A. (Italy). Copper alloys commonly used in cooling systems of power plants may be affected by biocorrosion induced by biofilm formation. The main objective of this work was to study the corrosion behavior of 70Cu-30Ni alloy and aluminum brass in seawater environments, under real industrial conditions (field experiments) and in laboratory. The influence of different parameters, such as the solution (filtered natural seawater (FNSW) vs artificial seawater (ASW)), the concentration of biomolecules (biomolecules naturally present in seawater vs a model protein, the bovine serum albumin (BSA)), hydrodynamics (static conditions, under flow and stirring, rotating ring electrode (RRE)) and pH (8.0, 6.0 and 3.7), was evaluated. In field, the overall corrosion behavior and antifouling treatments were monitored using electrochemical (corrosion potential  $E_{corr}$  vs time, LPR), gravimetric (weight losses) and genetic techniques. In lab, electrochemical measurements ( $E_{corr}$  vs time, polarization curves, EIS), performed during the very first steps of oxide layers formation (1 h immersion time), were combined to surface analysis by XPS and ToF-SIMS. From field experiments, microbiological and molecular analysis of biofilms formed on both copper alloys in natural seawater indicates the presence of *Marinobacter*, *Alteromonas* and *Pseudomonas* bacterial species. From lab experiments, models are proposed to analyze impedance data obtained at  $E_{corr}$ . In the case of 70Cu-30Ni, the HF loop illustrates mainly the anodic charge transfer (diameter equal to  $R_t^a$ ); whereas the LF loop is related to the anodic mass transport and partial blocking effect by CuCl. In the case of Al brass, the single experimental loop illustrates both anodic charge transfer and anodic mass transport. Similar electrochemical behavior and surface chemical composition of 70Cu-30Ni alloy are obtained in static ASW and FNSW, due to the low biomolecule concentration in FNSW. Compared to 70Cu-30Ni in static ASW without biomolecules, for which a thick duplex oxide layer (outer redeposited  $Cu_2O$  layer and inner oxidized nickel layer) is shown, the presence of BSA leads to a mixed Cu and Ni oxide layer with a lower thickness; the results also show a slow-down of the anodic reaction and a small corrosion inhibition effect in the presence of BSA. Under flow and stirring, a very thin mixed Cu and Ni oxide layer is obtained. For both alloys in FNSW, the corrosion current  $i_{corr}$  estimated from  $R_t^a$  is independent of the rotation speed of the RRE, due to compensated potential and mass transport effects. For 70Cu-30Ni in static FNSW, the anodic reaction is slowed down at acidic pH (kinetic effect). For Al brass, there is a corrosion inhibition effect at acidic pH, and the more acidic the pH, the slower the anodic reaction. In the case of 70Cu-30Ni alloy, the oxide layer thickness increases with decreasing pH, whereas for Al brass it is independent of the pH. The chemical composition of the oxide layer seems to have an effect on the amount of adsorbed proteins and the calculated organic layer equivalent thickness is very low (few Å for 70Cu-30Ni and 1 Å for Al brass).

**Key words:** 70Cu-30Ni alloy, aluminum brass, seawater, biocorrosion, BSA, EIS, XPS, ToF-SIMS